

AD _____

Award Number: W81XWH-10-1-0923

TITLE: Lightweight Portable Plasma Medical Device - Plasma
Engineering Research Laboratory

PRINCIPAL INVESTIGATOR: Dr. Magesh Thiyagarajan, Ph.D.

CONTRACTING ORGANIZATION:
TEXAS A&M UNIVERSITY-CORPUSCHRISTI

CORPUSCHRISTI TX 78412-5503

REPORT DATE: October 2012

TYPE OF REPORT: Annual

PREPARED FOR: U.S. Army Medical Research and Materiel Command
Fort Detrick, Maryland 21702-5012

DISTRIBUTION STATEMENT:

☒ Approved for public release; distribution unlimited

The views, opinions and/or findings contained in this report are those of the author(s) and should not be construed as an official Department of the Army position, policy or decision unless so designated by other documentation.

REPORT DOCUMENTATION PAGE			Form Approved OMB No. 0704-0188		
Public reporting burden for this collection of information is estimated to average 1 hour per response, including the time for reviewing instructions, searching existing data sources, gathering and maintaining the data needed, and completing and reviewing this collection of information. Send comments regarding this burden estimate or any other aspect of this collection of information, including suggestions for reducing this burden to Department of Defense, Washington Headquarters Services, Directorate for Information Operations and Reports (0704-0188), 1215 Jefferson Davis Highway, Suite 1204, Arlington, VA 22202-4302. Respondents should be aware that notwithstanding any other provision of law, no person shall be subject to any penalty for failing to comply with a collection of information if it does not display a currently valid OMB control number. PLEASE DO NOT RETURN YOUR FORM TO THE ABOVE ADDRESS.					
1. REPORT DATE (DD-MM-YYYY) 01-10-2012		2. REPORT TYPE Annual		3. DATES COVERED (From - To) 1 Oct 2011 - 30 SEP 2012	
4. TITLE AND SUBTITLE Lightweight Portable Plasma Medical Device Plasma Engineering Research Laboratory			5a. CONTRACT NUMBER		
			5b. GRANT NUMBER W81XWH-10-1-0923		
			5c. PROGRAM ELEMENT NUMBER		
6. AUTHOR(S) Dr. Magesh Thiagarajan magesh@tamucc.edu			5d. PROJECT NUMBER		
			5e. TASK NUMBER		
			5f. WORK UNIT NUMBER		
7. PERFORMING ORGANIZATION NAME(S) AND ADDRESS(ES) TEXAS A&M UNIVERSITY-CORPUSCHRISTI CORPUSCHRISTI TX 78412-5843			8. PERFORMING ORGANIZATION REPORT NUMBER		
9. SPONSORING / MONITORING AGENCY NAME(S) AND ADDRESS(ES) U.S. Army Medical Research and Materiel Command Fort Detrick, Maryland 21702-5012			10. SPONSOR/MONITOR'S ACRONYM(S)		
			11. SPONSOR/MONITOR'S REPORT NUMBER(S)		
12. DISTRIBUTION / AVAILABILITY STATEMENT Approved for public release; distribution unlimited					
13. SUPPLEMENTARY NOTES					
14. ABSTRACT We have established a state-of-the-art plasma research facility which is capable of conducting various interdisciplinary research projects. We have completed the setup of DC RBD plasma system, 13.56 MHz RF DBD plasma system, laser induced breakdown plasma system, plasma shadowgraphy system and optical emission spectroscopy diagnostics, two color laser interferometry diagnostics. We have completed the design and construction of the portable plasma source. We have made significant progress in testing and characterization and biological testing of the portable plasma source and the research will be continued to make progress.					
15. SUBJECT TERMS Plasma, laser, shadowgraphy, bacteria, cancer					
16. SECURITY CLASSIFICATION OF:			17. LIMITATION OF ABSTRACT UU	18. NUMBER OF PAGES ~204	19a. NAME OF RESPONSIBLE PERSON USAMRMC
a. REPORT U	b. ABSTRACT U	c. THIS PAGE U			19b. TELEPHONE NUMBER (include area code)

Standard Form 298 (Rev. 8-98)
Prescribed by ANSI Std. Z39.18

Table of Contents

	<u>Page</u>
Introduction.....	4
Body.....	5
Key Research Accomplishments.....	39
Reportable Outcomes.....	40
Conclusion.....	44
Appendix A.....	45
Appendix B.....	57

INTRODUCTION

The project entitled - Lightweight Portable Plasma Medical Device – Plasma Engineering Research Laboratory has made significant progress meeting the proposed milestones. The project has two objectives, in which the objective 1 is to develop a plasma research facility and establish a range of experimental plasma systems and diagnostics. The tasks under objective 1 were completed. The project's second objective is to develop a prototype of a portable plasma source for biomedical applications such as sterilization, infection treatment and cancer treatment. We have developed a test portable plasma source and tested on a range of bacteria and cancer cells and promising results were obtained. We have also designed and constructed another portable non-thermal atmospheric pressure plasma jet based on a dielectric barrier discharge configuration. The plasma and biological testing and characterization are in progress. The PI has established the Plasma Engineering Research Lab (PERL) with a state-of-the-art facilities and equipment obtained through this grant funding as well as several donations from the university and the community. The PI has mentored over 20 undergraduate students and 2 graduate students to perform various research projects. Several of these students have presented their work at various conferences and symposiums and few of those presentations has received best paper awards. The PI has mentored a visiting scientist and 4 postdoctoral research associates. The PI and the research team have published 5 journal articles and currently preparing 5 journal manuscripts which will be submitted in the upcoming weeks. The PERL has received a great visibility in the university campus as well as in the state. A no cost extension was requested and approved to continue and complete the tasks of second objective.

BODY

Table 1. The Project Objectives and Tasks

Task	Proposed Milestones	Base Line Plan Date	Status
Objective 1: Establish Plasma Engineering Research Lab			
1	Setup a direct current - atmospheric - resistive barrier cold plasma system	26 OCT 2011	Completed
2	Setup a 13.56 MHz radio frequency dielectric barrier plasma system	26 OCT 2011	Completed
3	Setup a 900 MHz/2.45 GHz wave plasma system	26 OCT 2011	Completed
4	Setup a laser induced breakdown plasma experimental system	26 OCT 2011	Completed
5	Implement plasma shadowgraphy diagnostics Setup	26 OCT 2011	Completed
6	Implement a two color laser interferometry diagnostics setup	26 OCT 2011	Completed
7	Implement a optical emission spectroscopy diagnostics setup	26 OCT 2011	Completed
Objective 2: Develop Portable Plasma Source			
8	Design phase: Design an optimized portable plasma source system	26 OCT 2012	Completed
9	Construction phase: Construct the portable plasma source based on the design analysis and utilizing the existing resources and knowledge gained from objective 1.	26 OCT 2012	Completed
10	Testing and characterization phase: Portable plasma source will be tested and characterized for its operating parameters and plasma parameters.	26 OCT 2012	In Progress
11	Biological testing: In-vitro biological testing.	26 OCT 2012	In Progress

I. OBJECTIVE 1: ESTABLISH PLASMA ENGINEERING RESEARCH LAB

1. Setup a direct current - atmospheric - resistive barrier cold plasma system

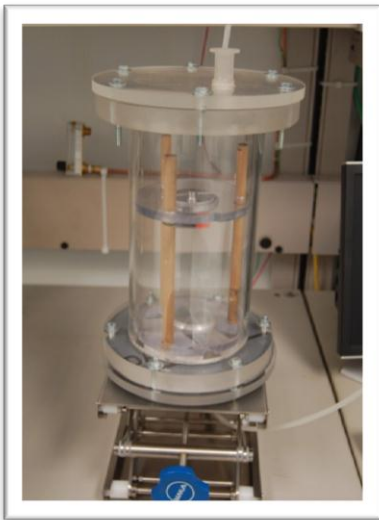
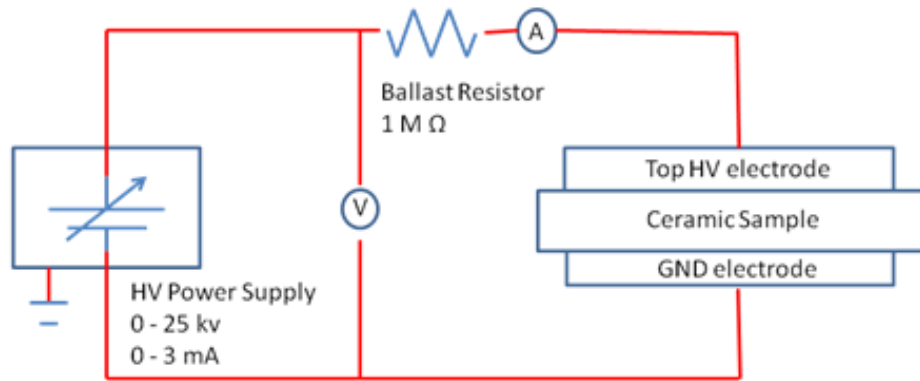


Figure 1. DC atmospheric pressure resistive barrier discharge

We have completed setting up the direct current atmospheric - resistive barrier cold plasma system. The DC power supply was acquired and atmospheric pressure plasma in air and helium has been experimented. A Mechanical Engineering Undergraduate Student is assisting on setting up the atmospheric Pressure resistive barrier discharge.

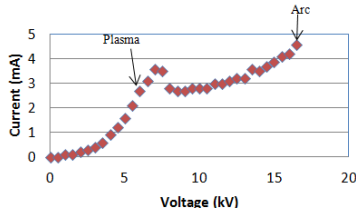


Fig.5- Moist Trial 1 of TAMUCC Stoneware

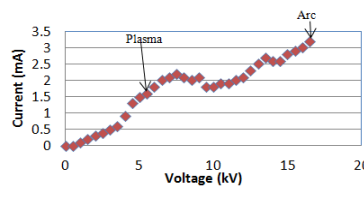


Fig. 6- Moist Trial 2 of TAMUCC Stoneware

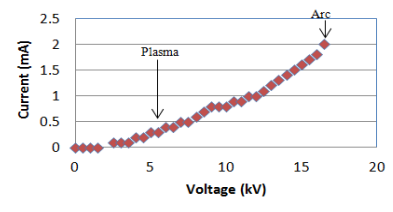


Fig. 7 - Moist Trial 3 of TAMUCC Stoneware

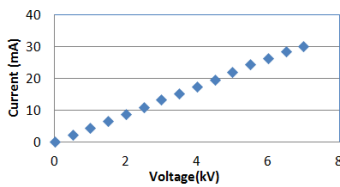


Fig8. - Moist Average of TAMUCC Stoneware

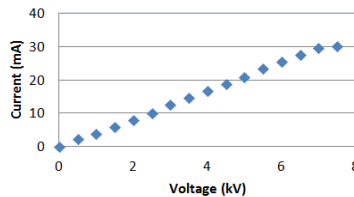


Fig9- Dry and Moist Average of TAMUCC Stoneware

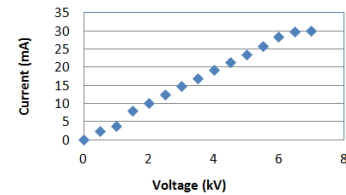


Fig.4- Average Dry Trial of TAMUCC Stoneware

Figure 2. The V-I characteristics of the resistive barrier DC plasma characteristics

The direct current resistive barrier discharge has been developed and tested for its voltage and current characteristics for different experimental conditions of the resistive barrier. The dryness and the moisture content of the resistive barrier has been varied and the VI characteristics and plasma parameters were diagnosed. The results are reported as technical report and presented in the key research accomplishments section.

2. Setup a 13.56 MHz radio frequency dielectric barrier plasma system



Figure 3. Setup a 13.56 MHz radio frequency dielectric barrier plasma system

We have completed the setup of a RF system that generates atmospheric pressure plasma at a low temperature. Currently a Hispanic Minority Mechanical Engineering Undergraduate student is assisting on setting up the experiment and collecting data. The data has been presented in a recent LSAMP conference and IEEE ICOPS conference.

Atmospheric pressure cold (non-thermal) plasmas have become increasingly prevalent within many research and industrial applications due to their range of reactive gas species produced that can be controlled and used in vast areas of application. In addition, the atmospheric plasma systems do not require expensive vacuum systems for their operation and generate a range of reactive ion species concentrations. This experimental research is being carried out to characterize and quantify the concentrations of the reactive ion species and other residual gases in order to theoretically extrapolate radial and axial distances. A set of gas flow rates were tested at fixed RF powers range from 60 W to 180 W. Through proportionally increasing oxygen gas flow rate and applied RF power the amount of reactive

ionized species are quantified and characterized. The experiment is also extended to various axial distances and the measured decay of reactive ion species which provides the required treatment distances based on the application treatment requirements.

The chemical characterization of the atmospheric pressure diffused plasma source was performed. The results confirm that the plasma source generates required amount of Nitrous Oxide gases that are the primary reaction agents to induce several healing mechanism in the human body.

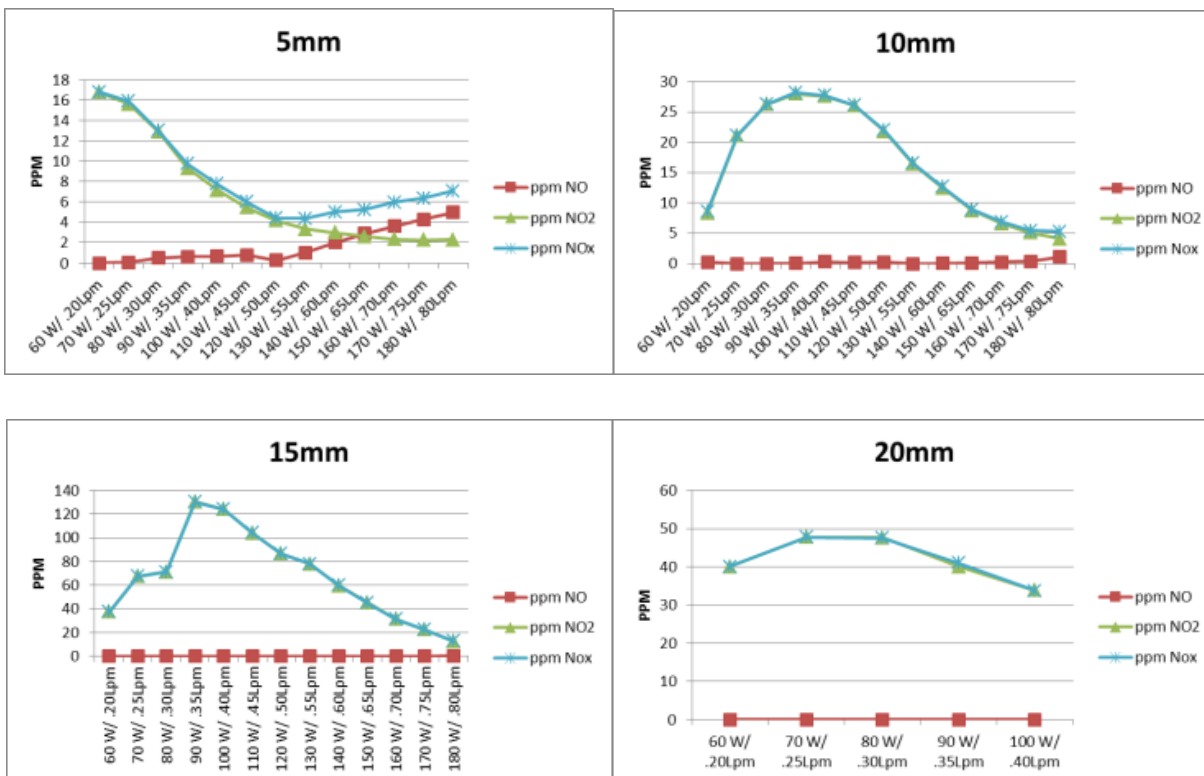


Figure 4. ppm at varying distances of Surfx® – Atomflo™ AH-250C - Testo-350 Diagnostics, Acquisition Software and Plasma Data Comparison

3. Setup a 900 MHz/2.45 GHz wave plasma system

The microwave plasma discharge systems are found be not aligned well with our research directions towards the medical and bio-medical related applications and therefore we have decided to acquire a small scale commercial system instead of developing a new system.

4. Setup a laser induced breakdown plasma experimental system

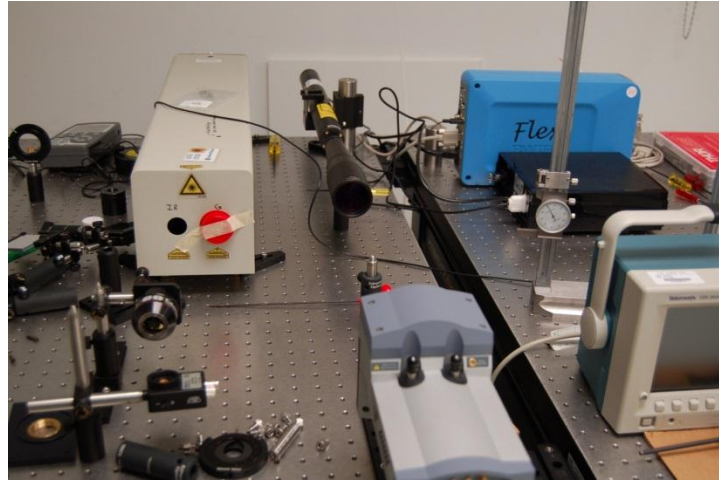
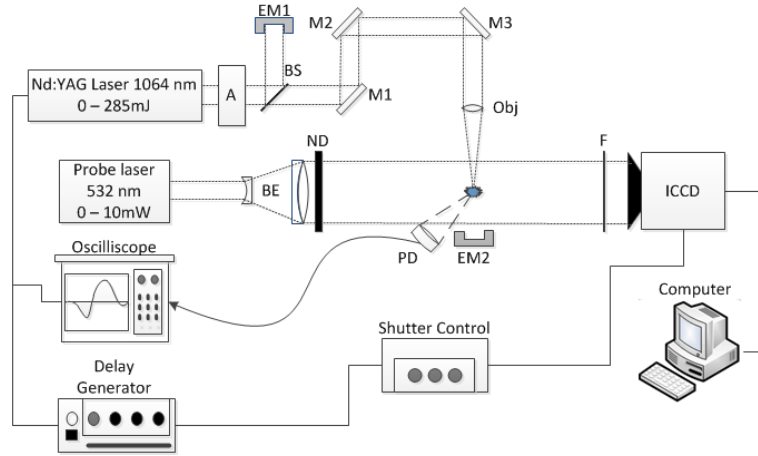


Figure 5. Setup a laser induced breakdown plasma experimental system

The picture of the experimental setup is shown in Fig. 5. In this experiment, a pulsed Nd:YAG laser (Spectra-Physics, Indi 40), with a 1st harmonic at $\lambda = 1064$ nm, 1.165 eV per photon and a 2nd harmonic at $\lambda = 532$ nm, 2.33 eV per photon is used. The laser output is a circular beam of 1-cm cross section diameter with Gaussian distributed beam intensity and 1.0 mrad beam divergence. The full-width at half maximum (FWHM) of the laser pulse is 6 ± 1 ns, with a 1-ns rise/fall time and a maximum available laser output energy of 450 mJ at 1-20 Hz rep rate. The laser outputs both 1st and 2nd harmonic laser beams simultaneously and in order to study the infrared laser induced plasma the 532 nm 2nd harmonic crystal generator was detuned and a dichromatic mirror separates any minimal 532 nm laser output from the 1064 nm pump laser. The laser output beam energy is controlled using a variable attenuator and each laser pulse is sampled through an IR beam sampler and the laser output energy is measured using laser

energy meter (Coherent, FieldMax II). In this experiment, all IR optical components are specially coated, with 98% transparency at 1064 nm. The IR beam is then reflected by a high damage threshold (20 J/cm²) IR coated kinematic mirror (TECHSPEC) in order to obtain a top-down configuration for the IR beam to enter the plasma chamber. The 1-cm-diameter IR beam is then passed through a 1064 nm transmission coated 3-cm-diameter Zinc Selenide window. The laser beam was focused by using a high-power handling (500 MW/cm²) objective lens mounted inside the plasma chamber. The objective lens (Thorlabs, LMH-5X-1064) has an effective focal length of 40-mm, with a 10-mm entrance aperture and a 0.13 NA. Due to its short focal length, the objective lens is mounted inside the plasma chamber using an adjustable length holder, so that the laser-induced plasma will be positioned at the cylindrical chamber air and visible through side windows for diagnostics. The space between the entrance IR window and the objective lens is maintained at the same pressure as that of the chamber pressure in order to avoid differential pressures acting on the objective lens. Great care was taken to position the objective lens together with the plasma chamber precisely in the line of sight with the IR laser beam. In addition, using the laser energy meter, it is found that the laser beam experiences a 5% loss as it passes through the coated IR optics, including the attenuator, beam sampler, mirrors and windows. The laser energy available immediately after the objective lens corresponding to a 300 ± 5 mJ laser output was measured by the Coherent FieldMax II energy meter to be 285 ± 5 mJ, corresponding to the measured incident laser energy on the focal spot, in agreement with the analytical estimate. A high-speed (<2-ns rise time) visible photodetector (Thorlabs, DET10A/M) mounted with collection optics is used to detect and observe the laser breakdown visible spark. The photodetector is connected to a high speed 2.5 GS/S oscilloscope to monitor the laser induced plasma emission. The plasma chamber was made from stainless steel and flushed several times before finally filling with dry air (< 10 ppm water) to the desired pressure ranging from 2000 Torr to 100 mTorr. Optical view ports on both sides of the cell are made of 3-cm-diameter by 5-mm-thick sapphire windows. The view ports enabled observation of the interior at right angles to the cell axis which is coincident with the direction of the laser beam, as well as for diagnosing the plasma. The chamber pressure was measured precisely by a pressure gauge with a pressure controller-readout (MKS Instruments, 910-11 and PDR 900-11). The gas flow through the chamber was regulated by a needle valve in the gas line and another valve in the pumping line. For one set of experiments on determining the effects of removing micro dust particles of diameters $\geq 0.1 \mu\text{m}$ on the breakdown threshold of dry air, we have inserted a filter capsule in the incoming gas line and cleaned residual dust on window and lens surfaces by means of an aerosol jet.

5. Implement plasma shadowgraphy diagnostics Setup

We have completed the laser focused plasma and the shadowgraphy diagnostics together. We have obtained very good results and he is working on two journal manuscripts based on the results.

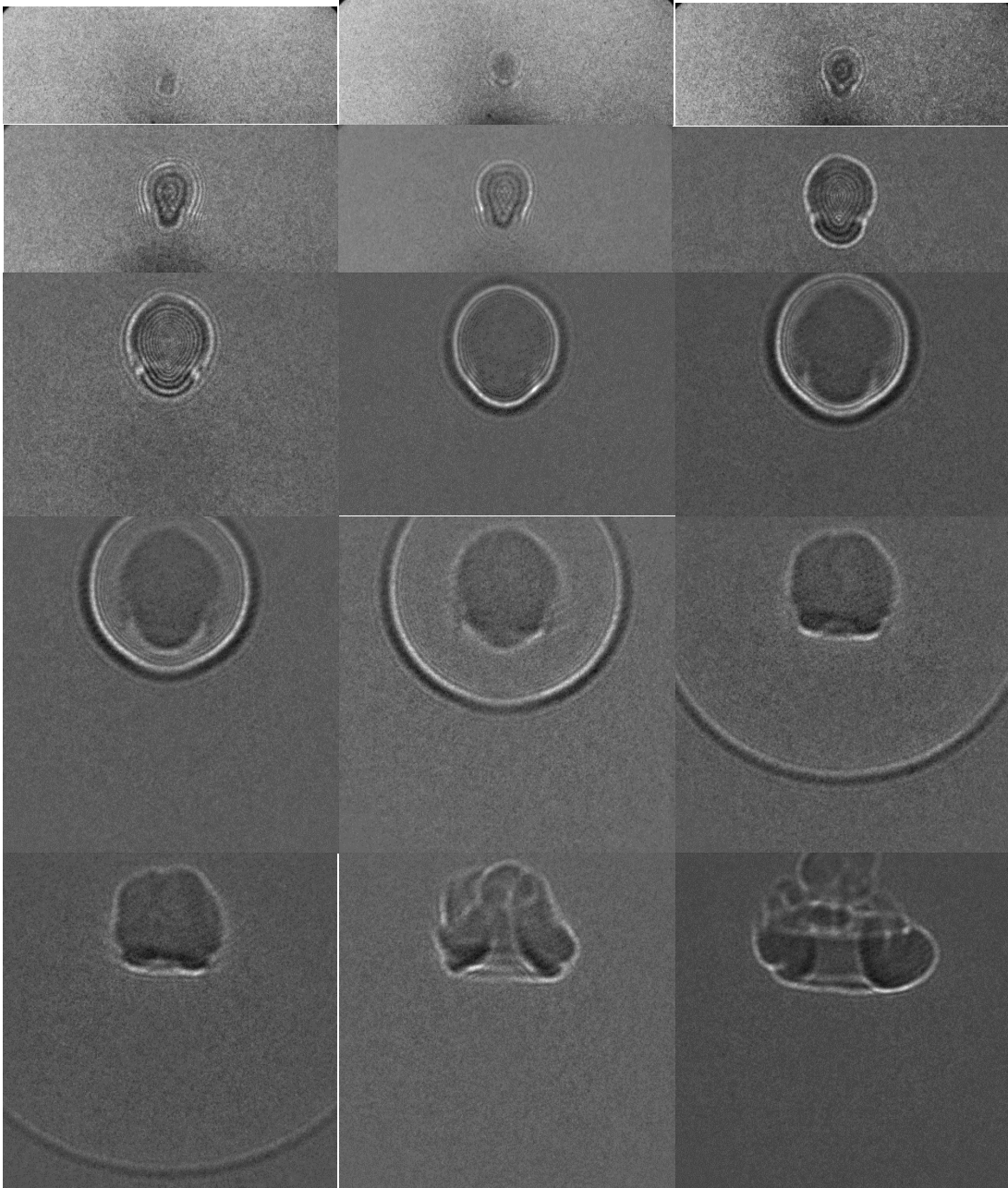


Figure 6. Shadowgrams of the laser induced plasma in air

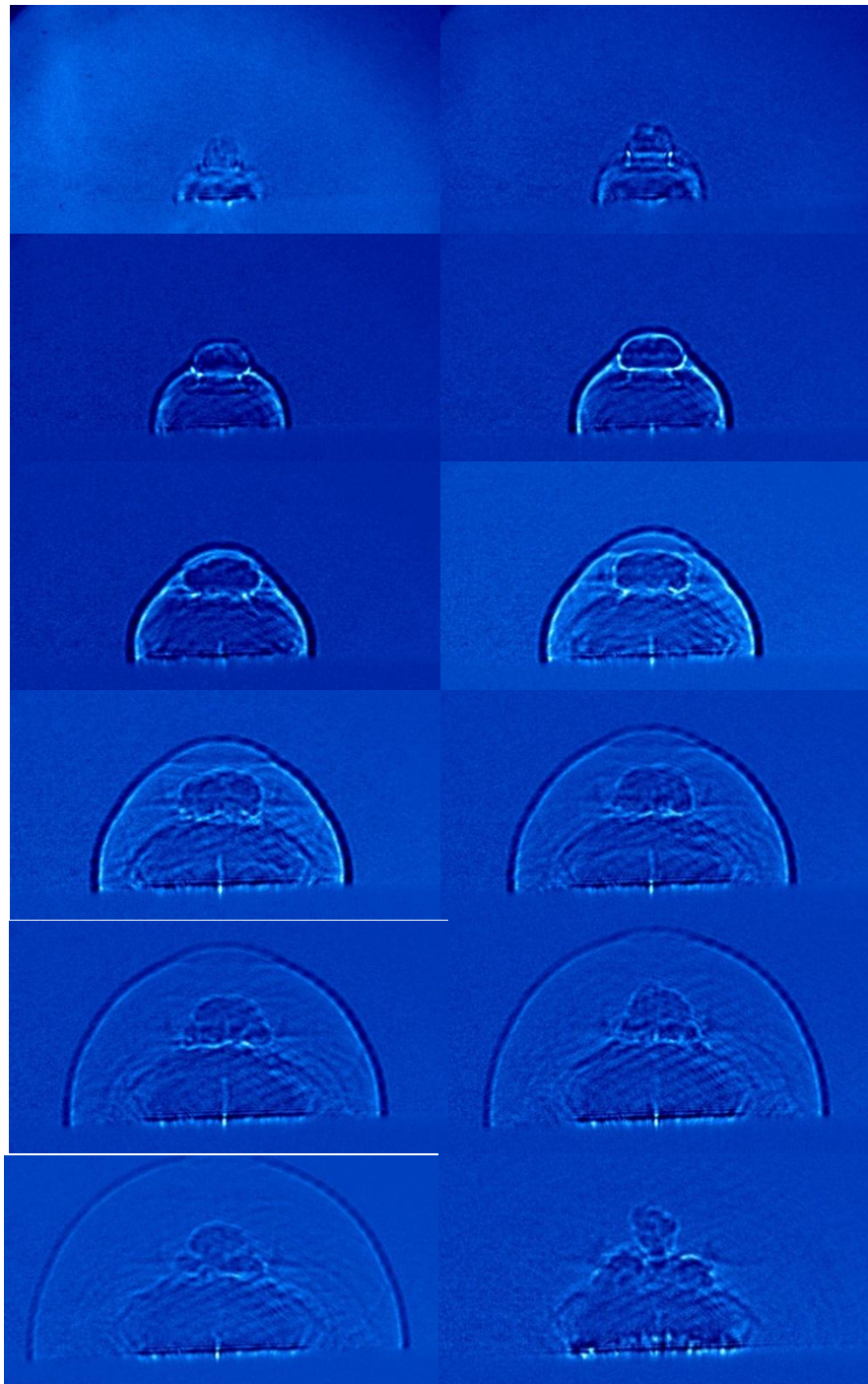


Figure 7. Shadowgrams of the laser induced plasma at air target interface

6. Implement a two color laser interferometry diagnostics setup

High resolution two-color laser interferometry diagnostics were realized using two different wavelengths to measure the electron density n_e of the laser induced plasma as well as the neutral gas density of the laser heated gas with spatial and temporal evolution. The interferometer works in the Mach–Zehnder configuration, in which the plasma is located in one of the arms of a two beam interferometer. The interferometer is configured to acquire an interference image of adjacent fringes of equal width when no plasma is formed. The changes in the optical index of the environment due to the presence of plasma and neutral gas profiles create a shift in the fringes that corresponds to the electron and neutral density profiles in the line of sight. These fringing patterns are captured by an intensified charged-coupled device ICCD ANDOR, DH 734 of 1024x1024 active pixels and a 30 x 30 μm^2 resolution camera with a minimum gate width of 10 ns connected to a computer. The plasma is illuminated by two 1 mm diameter probe lasers, a He–Ne red laser emitting at $\lambda = 632.8 \text{ nm}$ JDS Uniphase 1125P, and a high performance solid state green laser emitting at $\lambda = 532 \text{ nm}$ Edmund Optics, NT56–484 operated independently at 5 mW power levels. The probe laser beam sizes are expanded by a factor of 20 using an optical beam expander Edmund Optics, NT55–579 and a 20 mm aperture eliminates the edges of the expanded beam to improve the beam quality. The Gaussian wave front is split by a 50/50 beam splitter with one beam sent through the plasma chamber and the other used as a reference beam. Since the coherence length of the probe laser determined by the probe laser bandwidth of 0.05 nm is only 5.7 mm, both arms of the interferometer were adjusted to the same optical length of 61 cm within a few mm 5 mm offset. A mismatch of the two wave fronts by one coherence length causes a drop of the fringe contrast by a factor of $1/e$. The two view port windows on either side of the chamber are slightly tilted relative to the probe beam laser beam axis to avoid ghost images due to reflections. Optical interference filters with center wavelength at 532 or 632.82 nm are used in front of the ICCD to suppress the plasma self-luminescence. Both the test and the reference beams are aligned to overlap within 200 μm to assure the desired spatial resolution. The mirror for the reference beam is slightly tilted relative to the laser beam axis using a micropositioner. In this way a fringe pattern with the number of fringes proportional to the tilting angle is observed. A tilting of the mirror in the other plane rotates the fringe pattern. In the measurements, the null fringe pattern was arranged to show between eight and ten fringes over the 1.3 cm width field of view perpendicular to the observation axis. By using a digital delay generator the gating trigger pulse of the ICCD is precisely synchronized with the firing pulse of the excimer UV laser. These two pulses are compared by means of a 1 GHz sample rate oscilloscope LeCroy, WaveRunner 6100A. The gate width of the ICCD is varied by

using an electronic shutter controller with a typical gate width of 10 ns. Due to the high sensitivity of the ICCD, the milliwatt level cw powers of from the red and green lasers are sufficient to record images with a gate width of 10 ns.

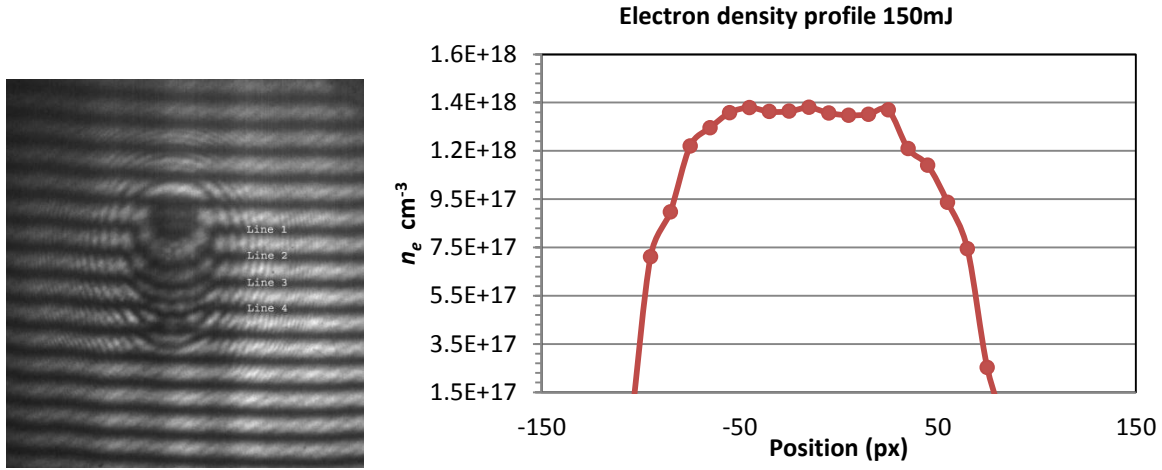


Figure 7A. Laser interferometry results

Laser interferometry results recently obtained in an identical configuration indicate line-integrated electron density values $\sim 10^{18} \text{ cm}^{-3}$ at $\sim 125 \text{ ns}$ into the blast expansion. The density was calculated using [(Thiyagarajan and Scharer 2008), (Weber and Fulghum 1997; Zhang, Lu et al. 2009)]:

$$\Delta = (2\lambda n_c)^{-1} \int n_e dl$$

$$n_e = \frac{(2\lambda n_c)\Delta}{l}$$

Where, Δ is the ratio of the fringe shift to the fringe spacing, λ is the wavelength of the probe laser, n_c is the critical density, n_e is the electron density which was assumed to be constant for this estimate, and the integral is over the path length. The image dimensions are 1.3cm x 1.3cm. This estimation is in agreement with the previously published work in this regime: including (Zhang, Lu et al. 2009).

7. Implement optical emission spectroscopy diagnostics setup

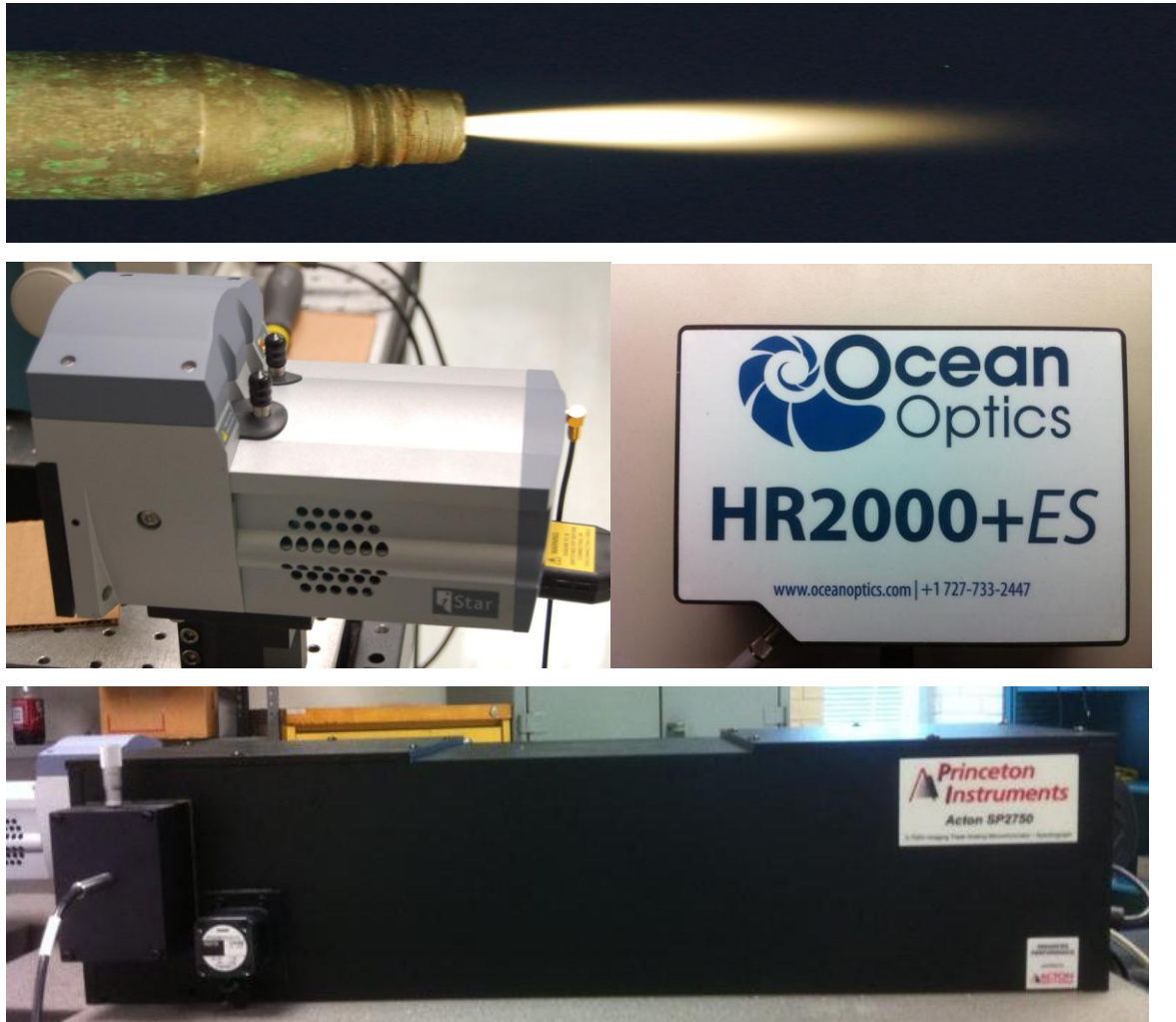


Figure 8. Optical emission spectroscopy diagnostics setup

The OES diagnostic setup is used as shown in Fig. 8 to measure the rotational T_{rot} and vibrational T_{vib} temperatures of the laser induced plasma. A high resolution narrow band 0.01 nm resolution monochromator Acton Research, model ARC-SP-2758 is used. The monochromator has a multiple grating option, which gives the flexibility of choosing the resolution and wavelength range. A holographic grating of 68_68 mm, 2400 grooves/mm, optimized for the entire visible wavelength range is used to acquire emission spectrum. The plasma emission is acquired by a collecting lens $f = 10$ and sent to a fast gating Andor iStar ICCD ANDOR, DH 734 through a high-quality 200–800 nm fiber-optic bundle. The Andor iStar ICCD

detector is integrated with an Acton SpectraPro 2750 spectrograph system. This system has a near-Lorentzian slit function with a halfmaximum width of 0.2 nm when the grating density is set to 1200 lines/mm. The UV excimer laser is synchronized with the gated ICCD in such a way that the spectral emissions from the laser induced plasma are acquired at different plasma lifetimes ranging from 45 ns to 100 micros with a gating time of $t_g=45$ ns for time windows t_{100} ns and $t_g=100$ ns for time windows t_{100} ns. The spectral emission signal strength of the laser induced plasma spark is very weak due to small plasma dimension and short gating times of 45–100 ns. In order to obtain good signal strength and spectral profile, 2000 laser shots are used at each acquisition time and the laser is operated at 1 Hz to maintain the same laser energy output.

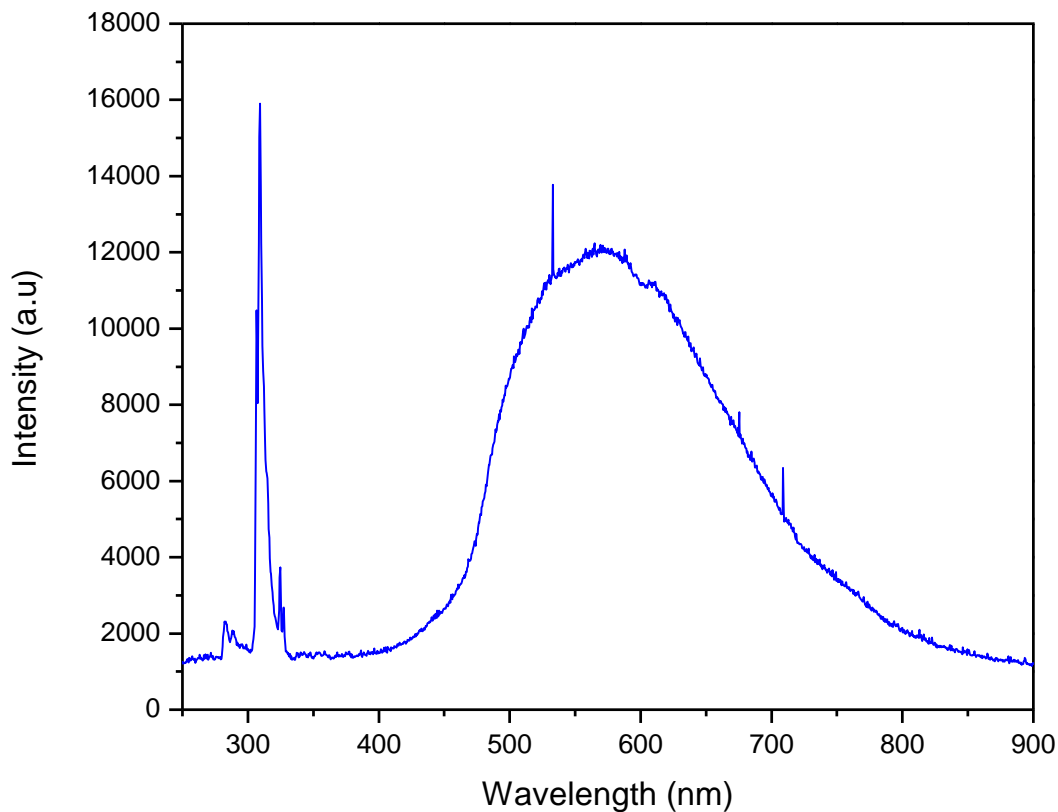


Figure 9. Optical emission spectrum of air plasma

II. OBJECTIVE 2: DEVELOP PORTABLE PLASMA SOURCE

Atmospheric pressure non-thermal resistive barrier plasma (RBP) jet was designed, constructed and characterized for plasma surface treatment procedures applied in biomedical applications. The RBP source can operate in both DC (battery) as well as in standard 60/50 Hz low frequency AC excitation, and to function effectively in both direct and indirect plasma exposure configurations depending on the type of treatment targets and applications. The design and construction aspects of the RBP source are presented including the electrode configuration, electrical, cooling and gas flow aspects. The RBP jet is tested and its characteristics such as the propagation velocity of the plasma jet, electrical properties, plasma gas temperature and nitric oxides concentration are characterized using optical laser plasma shadowgraphy, voltage-current characterization, optical emission spectroscopy and gas analyzer diagnostic measurements respectively. Using a laser shadowgraphy diagnostic we have measured the average propagation velocity of the plasma jet to be 150 - 200 m/s at 1 cm from the probe end. Discharge power is calculated from voltage-current characterization and plasma power is 26.33 W. An optical emission spectroscopy was applied and the gas temperature which is equivalent to the nitrogen rotational (Trot) temperatures was measured. After approximately 2 cm from the tip, along the axis the plasma emission drops and the high-temperature ceramic fiber-insulated-wire thermocouple probe was used to measure the temperatures of the gas flows along the downstream jet. The addition of a small portable external cooling unit has brought the temperatures of reactive oxygen species and other gases close to room temperature at the tip of the handheld plasma source unit. The concentrations of the reactive oxygen species at different spatial distances from the tip of the plasma jet were measured, at 5 cm distance from the electrode the nitric oxides level was measured to be in the range of 500-660 ppm and drops to ~100 ppm at 60 cm. The ppm values of nitric oxides after the cooling unit are observed to be of the same order of magnitude as compared to plasma jet. The portable RBP source was tested to be very effective for decontamination and disinfection of a wide range of foodborne and opportunistic nosocomial pathogens such as *Escherichia coli*, *Staphylococcus aureus*, *Pseudomonas aeruginosa* and *Bacillus cereus* and the preliminary results are presented. The effects of indirect exposure of the portable RBP source on monocytic leukemia cancer cells

(THP-1) were also tested and the results demonstrate that a preference for apoptosis in plasma treated THP-1 cells under particular plasma parameters and dosage levels. The tasks 8 and 9 under the objective 2 are completed as per the proposed milestones and the tasks 10 and 11 are in progress.

8. and 9. Design and Construction phase: Design and Construct the portable plasma source based on the design analysis and knowledge gained from objective 1.

The schematic block diagram of the portable resistive barrier plasma (RBP) source is shown in below. The RBP jet was designed and constructed for biomedical applications. The RBP jet was based on the principles of large volume non-thermal resistive barrier discharge (RBD) researched in the past by the PI Thiyagarajan et. al. The instrument was designed to be a light-weight portable handheld plasma source which is capable of operating in both direct and indirect plasma exposure modes. Direct exposure of plasma involves exposure of plasma directly on to a target treatment surface whereas the indirect plasma exposure involves exposure of only the ROS generated by the plasma instead of the plasma itself, thus eliminating the effect of any possible UV radiation produced by plasma in the case of direct plasma exposure.

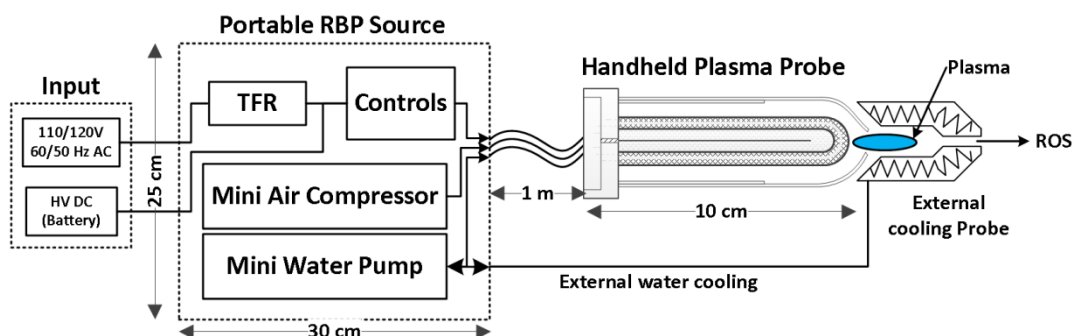


Figure 10. Design Schematic of the portable plasma source design

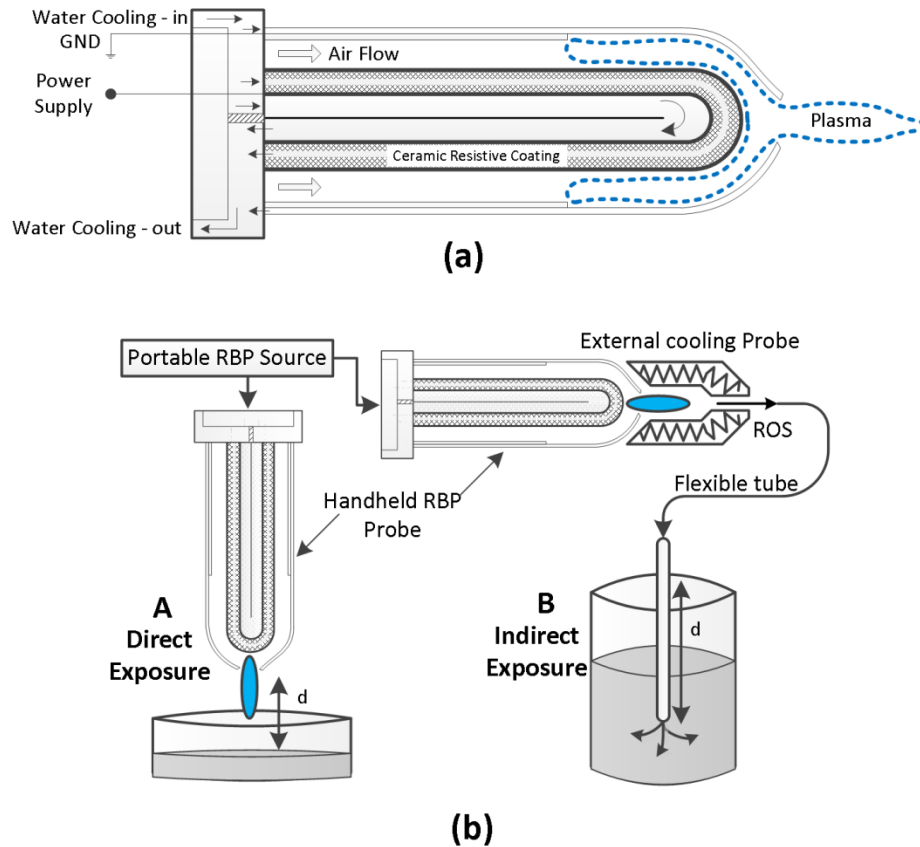


Figure 11. Direct and Indirect treatment methods

Since, the plasma instrument is principally a resistive barrier plasma source, it is capable of operating at both DC and low frequency AC, such as the standard operating voltages 120 V/60 Hz and 230 V/50 Hz which is stepped-up using a 6 kV, 30 mA (max) portable lightweight transformer housed in the power supply unit. The portable plasma source is primarily made up of two units namely the power supply control unit and the handheld plasma probe where the plasma jet is being generated. The handheld plasma probe unit is lightweight and maintained at room temperature through a cooling circuit and it is connected to the power supply unit through a flexible chord to facilitate the remote workability for medical practitioners and biomedical applications. The power supply unit was constructed in a portable form such that it can be easily carried over by operators, when needed. The power supply unit contains a mini 12 V DC water pump (Geo-Inline) for cooling the electrodes in the handheld plasma probe unit as well as the optional external cooling unit. The power supply unit also contains a mini 12 V DC air compressor weighing less than 3 lbs. to supply the forced air as an operating gas to the

handheld plasma probe unit. The power supply unit also houses transistor-transistor logic (TTL) and relay controls to select between AC and DC, and power levels and flow controls. The entire RBP source is constructed to fit within 12 × 10 × 10 inch³ portable metallic case and the entire power supply and RBS plasma source weighs ~20 lbs.

The schematic of the handheld plasma probe unit is shown, which consists of central deionized water cooled cylindrical electrode surrounded by deionized water cooled high density alumina ceramic resistive coating. The central electrode which is approximately 1 cm diameter and 10 cm long is surrounded by a double layer hollow ground electrode separated by an electrode gap space of 2 mm. The plasma source uses atmospheric pressure air as the operating gas, in which the air forced through the resistive barrier plasma source electrode gap space using a mini-compressor such that the plasma and ROS including nitric oxides at the tip of the handheld plasma source tip are controlled and maintained based on the plasma power and flow-rate. Plasma streamers are formed between the high-voltage resistive electrode and the ground electrode. A fraction of the forced air passing through the RBP source gets ionized and exits through a 2 mm pinhole type opening at the tip of the plasma source generating a stable plasma jet and continuous flow of ROS including nitric oxides. The plasma streamers formed in the cylindrical hollow electrode configuration are dynamic with respect to its location between the electrodes, which also assists in preventing localized heating and arc formation. The ceramic electrodes are water cooled through a mini-water pump.

For the indirect exposure method the concentrations of the nitric oxides are preserved by reducing the plasma temperature rapidly through a separate external small efficient cooling unit. For applications that require high temperature plasma, the additional cooling unit can be easily separated from the hand held plasma jet. The temperatures of selected ROS flow from the cooling unit tip were measured to be at room temperature which is ideal for treating heat sensitive materials and targets in the biomedical applications and medicine such as human skin treatment. The external cooling units are scalable and additional units can be added or removed in order to vary the exit temperature of selected ROS.

10. Testing and characterization phase: Portable plasma source will be tested and characterized for its operating parameters and plasma parameters.

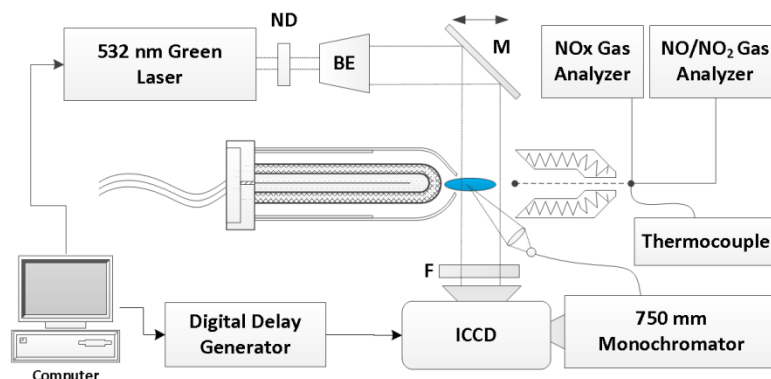


Figure 12. Schematic of Testing and characterization of portable plasma system

The characteristics of the resistive barrier plasma source such as the propagation velocity of the plasma jet, electrical characterization of the plasma jet, gas temperature and concentration of ROS including nitric oxides are characterized using diagnostics techniques namely optical laser plasma shadowgraphy, voltage current characterization, optical emission spectroscopy and gas analyzer techniques.

A high resolution 532 nm laser shadowgraphy diagnostic was setup as illustrated in Fig. 12, to measure the propagation velocity of the plasma jet. A computer-controlled 532 nm continuous-wave (CW) diode-pumped solid state probe laser outputs a 1 mm beam diameter TEM₀₀ laser beam with 0 – 10 mW adjustable power output that was expanded to 20 mm beam diameter using an anti-reflective (AR) coated 20X Galilean laser beam expander (Thorlabs, BE20M) with collimation adjustment. The expanded 532 nm laser beam axis was aligned to pass through the plasma jet and captured using an intensified charge coupled device (ICCD; Andor, iStar 734). The ICCD was computer controlled and capable of capturing high-resolution 1024 × 1024 pixel (13.6 × 13.6 mm) images with a minimum gating width of 2 ns and a maximum gain of 104. It was synchronized with a digital delay generator and shutter control. The delay timings were monitored and measured using a high speed digital oscilloscope. Optical interference filters with center wavelength at 532 ± 2 nm was used in front of the ICCD to suppress the plasma jet self-luminescence. The shadow of the laser induced plasma falls onto the ICCD sensor with a 1:1 ratio (1 pixel = 13.2 μm). The voltage applied to the high-voltage electrode is measured using a

high voltage probe (Tektronix P6015A) and the discharge current is measured using a current probe (Tektronix TCP202). The voltage–current waveforms are recorded using a 2 GHz digital oscilloscope (Tektronix TDS3034C). The optical emission spectroscopy diagnostic setup was used as shown in Fig. 12., to measure the plasma gas temperature rotational (T_{rot}) of the nitrogen in the plasma jet. A high resolution narrow band (0.01 nm resolution) monochromator (Acton Research, Model: SP-2750) was used. The monochromator has a multiple grating option, which gives the flexibility of choosing the resolution and wavelength range. A holographic grating of 68 x 68 mm, 2400 G/mm, optimized for the entire visible wavelength range was used to acquire emission spectrum. The plasma emission was acquired by a collecting lens ($f/10$) and sent to a fast gating Andor iStar ICCD (ANDOR, DH 734) through a high-quality (200-800 nm) fiber-optic bundle. The Andor iStar ICCD detector was integrated with an Acton SpectraPro 2750 spectrograph system. This system has a near-Lorentzian slit function with a half-maximum width of 0.2 nm when the grating density was set to 1200 lines/mm. A high-temperature ceramic fiber-insulated-wire thermocouple probe capable of measuring temperatures up to 1400 °C was used to measure the temperature of the downstream jet when plasma emission ends after approximately 2.5 cm.

The parts per million (ppm) concentration of the ROS including nitric oxides at different spatial distances from the tip of the plasma jet was measured using two gas sensors namely NOxCANg and Testo 350 M/XL gas analyzer as shown in Fig. 12. The NOxCANg is a versatile and highly integrable nitric oxides measurement diagnostics instrument which uses ceramic NO_x sensor to withstand high temperatures that was mounted in the probe tip and communicates the measured NO_x parameters from 0 to 5000 ppm to the Kvaser Leaf Light HS data bus and logs the data in the computer via its controller area network (CAN) bus port with a 150 ms response /refreshing time. The NOxCANg sensor was externally powered at 18V DC using Agilent E3631A Triple Output DC Power Supply. A data acquisition tool communicates with the NOxCANg sensor module through Kvaser Leaf Light HS data bus and logs the NO_x concentrations in ppm.

The non-thermal atmospheric pressure resistive barrier plasma (RBP) source was designed and constructed for surface treatment and biomedical applications. The RBP source was tested for its propagation velocity of the plasma jet, electrical diagnostics, plasma gas temperature and selected ROS concentrations such as nitric oxides that are primary characteristics needed for biomedical applications.

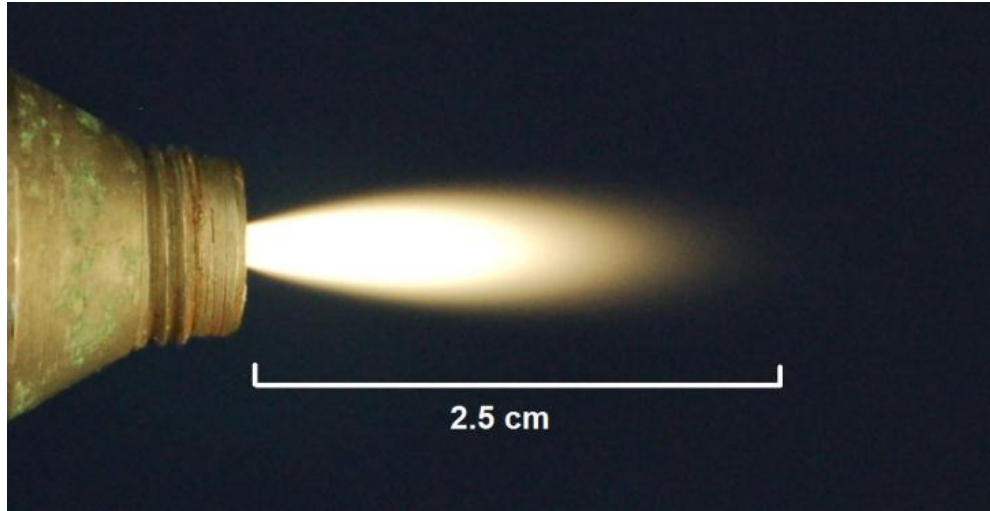


Fig. 13. Photograph of the RBP jet.

A photograph of the portable RBP jet is shown in the Fig. 13. The visible plasma jet spans approximately 2.5 cm from the exit tip and decays as it recombines and diffuses into the surrounding atmosphere.

The propagation velocity of the plasma jet is an important parameter in determining the treatment distances of surfaces to be treated in biomedical applications. We have developed a 532 nm laser shadowgraphy diagnostic technique to measure the propagation velocity of the portable resistive barrier plasma jet. The laser shadowgraphy technique also provided the flow dynamics of the plasma jet and neutral gases at elevated temperatures. In the laser plasma shadowgraphy technique, a synchronized CW 532 nm probe laser beam was expanded and sent through the test section where the plasma jet is located and its image falls directly onto the ICCD on the image plane. In a plasma, the refractive index is primarily a function of the electron density, which is the main plasma parameter determined by refractive-index measurements. Typical plasma diagnostics based on refractive effects include interferometry, Schlieren imaging, and shadowgraphy measurements. While the first technique gives a direct measure of the refractive index μ , the Schlieren image responds to the first spatial derivative of the index of refraction. The shadowgram however responds to the second spatial derivative or Laplacian. A shadowgraph measures lateral displacement of the light rays after passing through a medium such as plasma. An electromagnetic wave exerts a force on the charged constituents of the medium through which it propagates. This force accelerates the charge which, in turn, modifies the time-varying electromagnetic field. A solution of electromagnetic-wave propagation in plasma can

be obtained by solving the wave equation for a plane wave in the small amplitude approximation [58]. The refractive index of high-frequency electromagnetic wave propagation in unmagnetized plasma is:

$$\mu_e = \sqrt{1 - \frac{\omega_p^2}{\omega^2}} = \sqrt{1 - \frac{n_e}{n_c}} \quad (1)$$

where $\omega = 2\pi c/\lambda$ the frequency of the electromagnetic wave, $\omega_p = (n_e e^2 / \epsilon_0 m_e)^{1/2}$ is the electron plasma frequency, and $n_c = m_e \epsilon_0 \omega^2 e^{-2}$ is the cutoff electron density for which electromagnetic wave propagation is possible. If the refractive index in the test section μ is uniform, the screen will be essentially uniformly illuminated. If, however, the gradient of μ varies in space, as one may expect for high-temperature plasmas, i.e., when there is a significant second derivative of the refractive index, there will be variations in the illumination at the imaging screen. Regions where the second derivative of the refractive index is negative that will act like a converging lens.

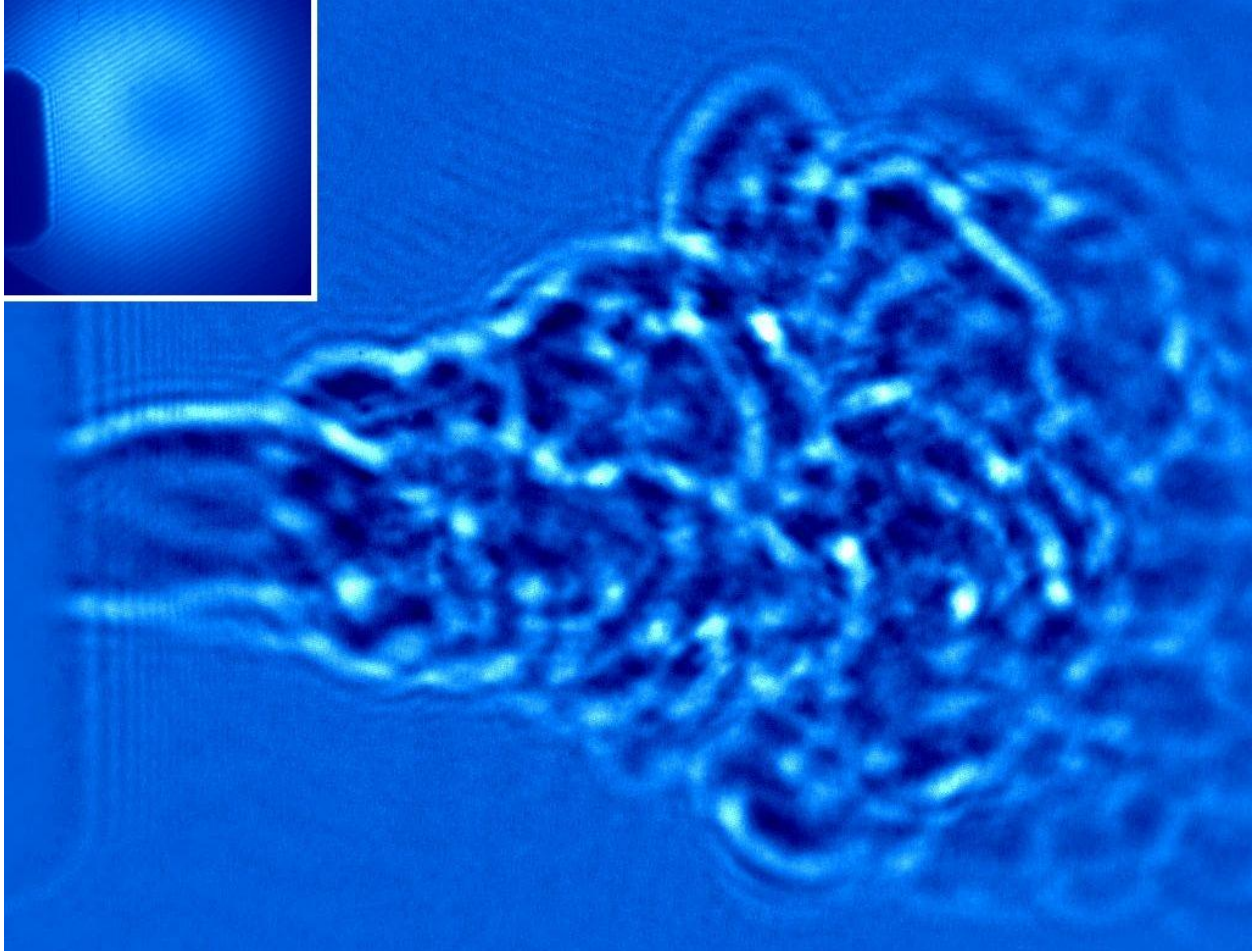


Fig. 14. Laser shadowgram of the plasma jet. Image size-1.25 x 1.75 cm. Sub-figure (top-left): laser shadowgram of gas flow-only and with power off (no plasma).

A laser shadowgram of the plasma jet obtained is shown in Fig. 14., by passing an expanded 532 nm probe laser beam through the plasma jet and capturing the transmitted laser beam on an image pane using a fast gated ICCD. Several shadowgrams were obtained at 100 ns gating time with a ICCD triggering delay time of 125 μ s, as indicated with an arrow in Figure 6. The same triggering signal is used to capture the voltage-current signals without the signal delay. By tracking the plasma eddies in the shadowgrams, we have measured the average propagation velocity of the plasma jet to be 150 - 200 m/s at 1 cm from the probe end. The laser shadowgraphy technique is based on the presence of significant second derivative of the refractive index, which can be caused by the presence of plasma as well as the neutral gas at elevated temperatures. Unlike Schlieren diagnostics that is based on the first derivative of the refractive index changes, the flow dynamics of the gas at near room temperatures are generally not captured through the laser shadowgraphy technique since it does not create enough second derivative refractive index changes in the laser beam path. Therefore the shadowgrams obtained through our laser shadowgraphy diagnostics can be caused by both the plasma jet and the heated neutral gas. It is further verified through turning on only the gas flow at room temperature and keeping the high-voltage off (plasma off), resulted in no observable shadowgrams in the ICCD, as shown in the sub-figure of Fig. 13. However, when we used a separate source of gas that is heated up to few hundred degrees C resulted in weak shadowgrams.

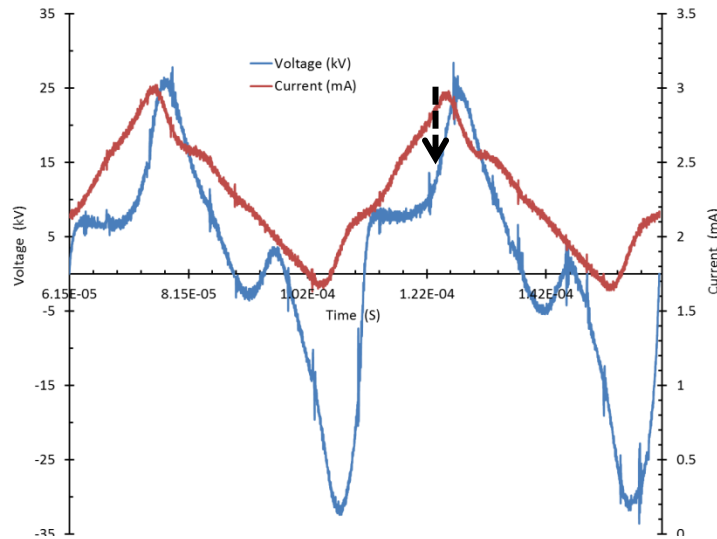


Fig 14. Voltage-Current waveform of the RB plasma jet in air. Discharge power is 26.33 W.

In the RBP jet, the discharge is initiated by applying a sufficient voltage between the electrodes by which the air between the electrodes breakdowns and results in a plasma jet sustained by applied voltage. Figure 14, shows the voltage-current waveform of the RBP jet. Both voltage and current

waveforms exhibit pulses of few microseconds long. The positive and negative half periods of the applied voltage are unsymmetrical due to the existence of only one resistance between the electrodes. The maximum voltage and current values are approximately 25 kV and 3 mA on the positive half period of the applied voltage, correspondingly. Using the voltage–current waveforms, the average power dissipated in the discharge is calculated by integrating the product of the discharge voltage and current over one cycle; according to the following equation (T = period of the discharge).

$$W = \frac{1}{T} \int_t^{t+T} I(t)V(t)dt \quad (2)$$

and the measured plasma power is 26.33 W.

Optical emission spectroscopy can be used to determine the plasma temperatures of the RBP jet with some assumptions. To determine the plasma rotational gas temperatures, local thermodynamic equilibrium (LTE) must be assumed. The local thermodynamic equilibrium is valid in the central region of the plasma jet but not at the larger outer radii. The ROS produced in the plasma are long lived active species that can propagate far beyond the plasma jet and in to the surrounding environment preferentially following the plasma jet direction. These long lived active species are important for biomedical applications and we have measured the NO_x concentration of ~900 ppm at 10 cm away from the plasma source exit nozzle. In this section the plasma temperature measurements using optical emission spectroscopy and the downstream neutral gas temperature measurements using thermocouple are presented.

The nitrogen rotational (T_{rot}) temperature which is equivalent to plasma gas temperature was measured using the N_2 C-B (2+) (N_2 second positive band system) rotational transitions in the range 364–383 nm, by matching them with a code simulated results from SPECAIR. This spectral range corresponds the $\Delta v = -2$ vibrational sequence of N_2 C-B (2+) band system and the best-fit SPECAIR spectrum can yield rotational temperatures (T_{rot}). SPECAIR is computer simulation software developed by Laux *et. al.* on the basis of the NonEquilibrium Air Radiation code (NEQAIR) by Park. SPECAIR performs the OES by determining the populations of the states of the radiative transitions using user-specified electronic, vibrational and rotational temperatures. The modeled transition rates are calculated based on tabulated data for the transitions. From the calculated transition probabilities and populations of radiating species, the line-by-line optical emission intensity was computed for the wavelengths of the transitions. The experimental spectra measured at different distances ranging from 0.2 cm to 2 cm and SPECAIR code matched spectrum are shown in Fig. 15.

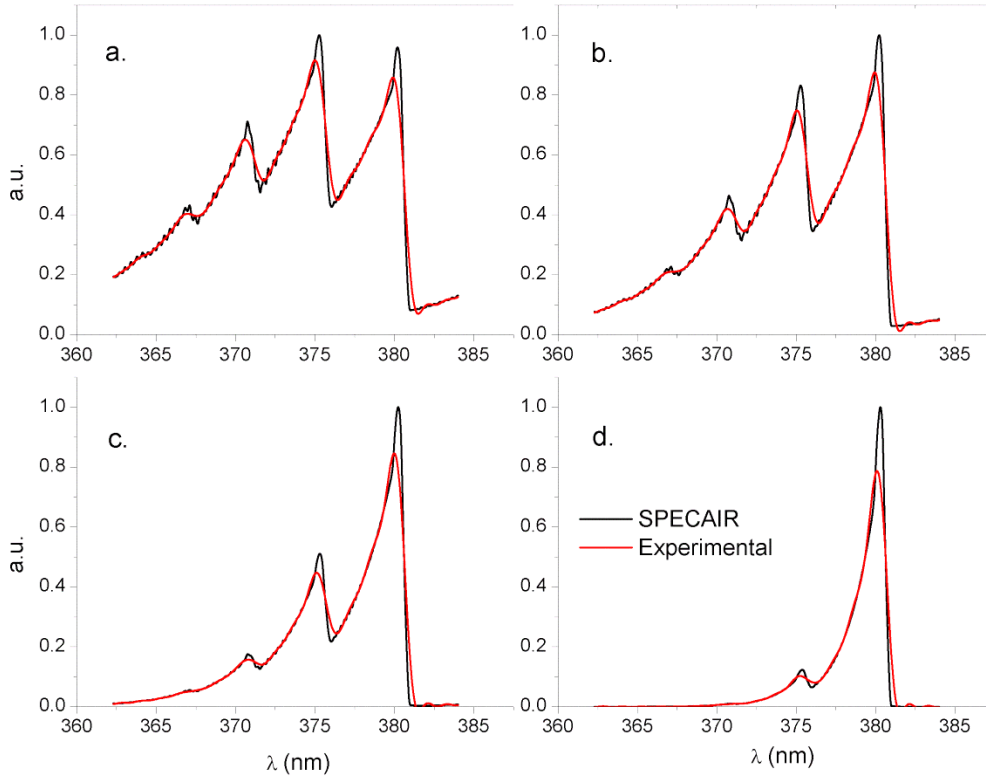


Fig. 15. Experimental and SPECAIR code simulated matching of emission spectra of RBP jet at different distances from exit. a. 0.2 cm – 3000 °C, b. 0.8 cm – 2000 °C, c. 1.5 cm – 1500 °C, d. 2 cm – 1000 °C.

The temperatures measured from the SPECAIR code matched spectrum resulted at temperatures as high as 3000 °C at 0.2 cm from the exit and decays to 2000 °C at 0.8 cm and continues to decay to 1500 °C at 1.5 cm and to 1000 °C at 2 cm. After approximately 2 cm from the exit nozzle tip along the axis, the plasma emission drops and therefore a high-temperature ceramic fiber-insulated-wire thermocouple probe was used to measure the temperatures of the neutral gas propagating in to the surrounding environment (downstream jet). The axial temperature decay of the plasma jet from the plasma source tip before entering the cooling unit or without the cooling unit is shown in Fig. 16., in which the data in solid circles (red) represent the optical emission spectroscopy results and the data in solid squares (black) represent the results from thermocouple measurements.

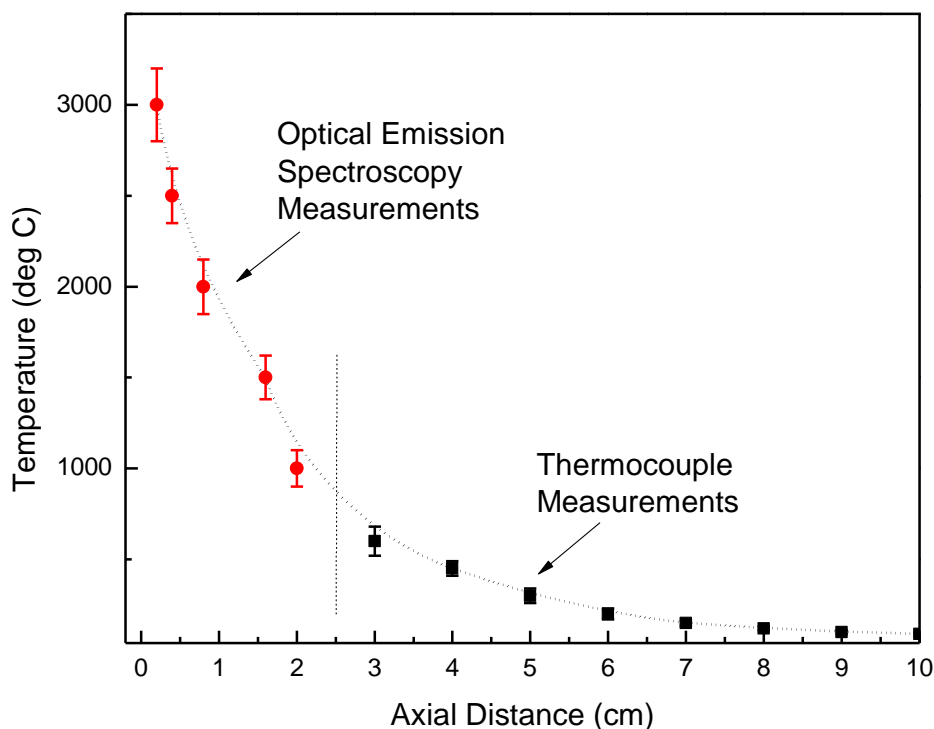


Fig. 16. The axial temperature decay of the plasma jet from the RBP source tip before entering the cooling unit.

The plasma temperature at the nozzle exit of the plasma source reaches around 3000 °C and the temperature drops rapidly to less than 100 °C at approximately 8 cm from the tip. The high gas temperature obtained from N₂ rotational temperature is due to excitation of N₂ to high rotational/vibrational levels and the excited N₂ species are generated in the plasma jet. However, plasma gas temperature drops rapidly towards the end of visible plasma jet. The temperature of the plasma plume at the exit reaches >2500 °C which is sufficient to generate nitric oxides. When the external cooling units were added the gas temperatures were brought close to room temperature at the tip of the handheld plasma source unit.

The concentration of the ROS produced by the plasma jet with and without the cooling unit are measured. The majority of the ions recombine before it exits through the cooling unit and at this stage several gas species and other parameters were monitored, including O_2 , O_3 , CO , CO_{low} , NO/NO_2 , NO_{low} , NO_x , $CO_{2(Infrared)}$, SO_2 , HC , H_2S , temperature, pressure, flow, velocity, efficiency, mass, etc. Based on the results we observed that nitric oxides are the predominant long lives species produced by the RBP source and some trace O_3 . The nitric oxide formation is a reversible plasma chemical reaction and it can be expressed as



The nitric oxides from the tip of the hand held plasma jet are measured using gas analyzers. The nitric oxide contains the active oxidation potential and reacting with oxygen in the environment as it exits the plasma source induces the formation of nitrogen dioxide at a smaller concentration. The decaying concentration of the nitric oxides from the plasma jet can be used as reference for the treatment distance between the target surface and the plasma source tip. The background NO_x concentration are measured using NO_xCANG module at various timings and at standard laboratory conditions well before the plasma source was operated and it was measured to be less than 0.5 ppm. The measurements are carried out at 20 data sets separated by 1 min with 1 second acquisition time at distances 5, 10, 20, 30, 60 and 100 cm from the tip. For consistency in the concentration measurements, three other sampling timings such as 10, 30 and 60 second are tested in addition to 1 second acquisition time. The NO_x concentrations of the plasma jet in ppm without the cooling unit are measured at various axial distances (in cm) from the tip and shown in Fig. 17.

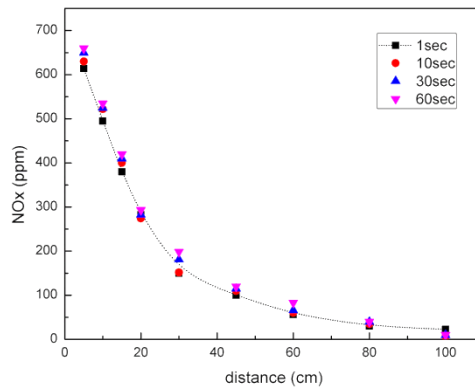
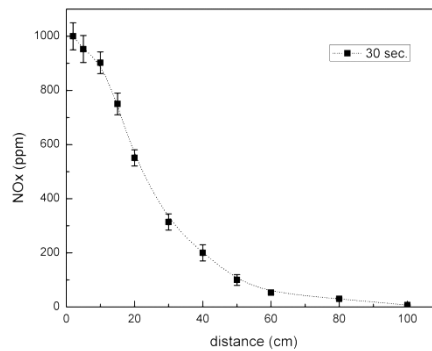


Fig. 17. The NO_x concentrations of the plasma jet from the RBP source in ppm without the cooling unit at various axial distances from the tip.

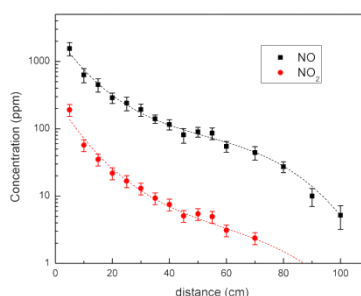
The results indicate the consistency of the plasma output characteristics and NO_x concentration levels for varied time averaged integration times and data sampling frequencies. The NO_x concentration peaks right at the electrode tip as expected and at 5 cm from the electrode, NO_x concentration was measured to be in the range of 500-660 ppm at different exposure times as listed in Fig. 17. The concentration drops to half of its initial value at ~20cm and it continues to drop to ~100 ppm at 60 cm and at 100 cm distance from the tip the concentration was very low (<10 ppm). The NO_x concentrations in ppm with the cooling unit added and measured at various axial distances (in cm) from the out tip of the cooling unit is shown in Figure below.



The NO_x concentrations in ppm with the cooling unit added to the RBP tip at various axial distances (in cm) from the out tip of the cooling unit.

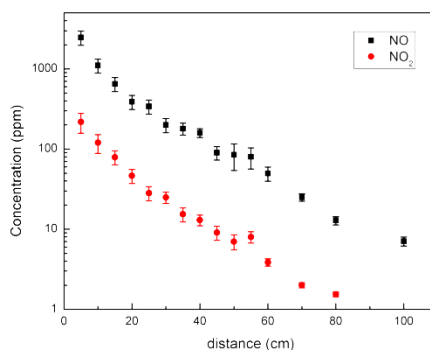
Based on the measurements it was observed that the NO_x concentration after the cooling unit was slightly higher (~950 ppm) compared to that of plasma jet (~615 ppm), this was due to the fact that plasma jet diffuses out after it exits from the handheld electrode whereas the probe diameter after the cooling unit is very small like a pinhole arrangement with 1 cm diameter opening leading to increased concentration.

NO_x is composed of two components such as the mono-nitrogen oxides or nitric oxides (NO) and nitrogen dioxide (NO_2). In order to measure the individual concentration levels of NO and NO_2 a different diagnostic tool was realized using a gas analyzer (Testo 350 M/XL) capable of identifying and characterizing over several molecular gases including NO and NO_2 . The Fig. below shows the concentrations of NO and NO_2 for the plasma jet without the cooling unit.



The concentrations of NO and NO₂ for the RBP jet without the external cooling unit.

The Fig. below shows the concentrations of NO and NO₂ from the probe with external cooling unit.

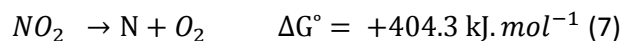


The concentrations of NO and NO₂ from the RBP probe with external cooling unit.

The concentration of NO₂ was much lesser compared to that of NO by an order of magnitude or higher. The ppm concentration of NO is at the preferred level for a wide range of standard biomedical treatment applications. The ppm concentration of NO₂ is below the OSHA safety standards. The formation of different active species produced in non-thermal air discharges involves complex plasma chemistries. At relatively high gas temperatures various nitrogen oxides (NO_x) are produced through N₂ and O₂ reactions [62, 63]. The production of NO_x species is mainly dependent on the oxygen (O₂) concentration in air plasmas. It has been shown that in air plasmas, a threshold value of 5% O₂ concentration is necessary for NO_x formation [62] mechanisms.



Based on the reactions 5 and 6, the NO₂ production (reaction 5) is more favorable than the NO production (reaction 6) in such plasma conditions.

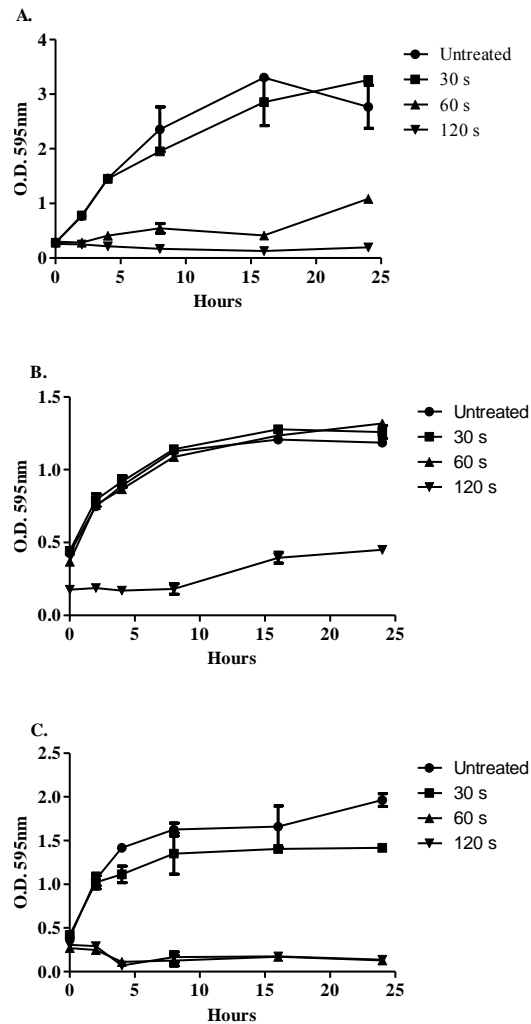


Furthermore, NO₂ decomposes into N + O₂ (reaction 7) and NO + O (reaction 8), in which the reaction 8 is more favorable than the reaction 7. Therefore it results in a higher NO concentration along the plasma jet compared to NO₂ as shown in Figures 11 and 12.

11. Biological testing: In-vitro biological testing.

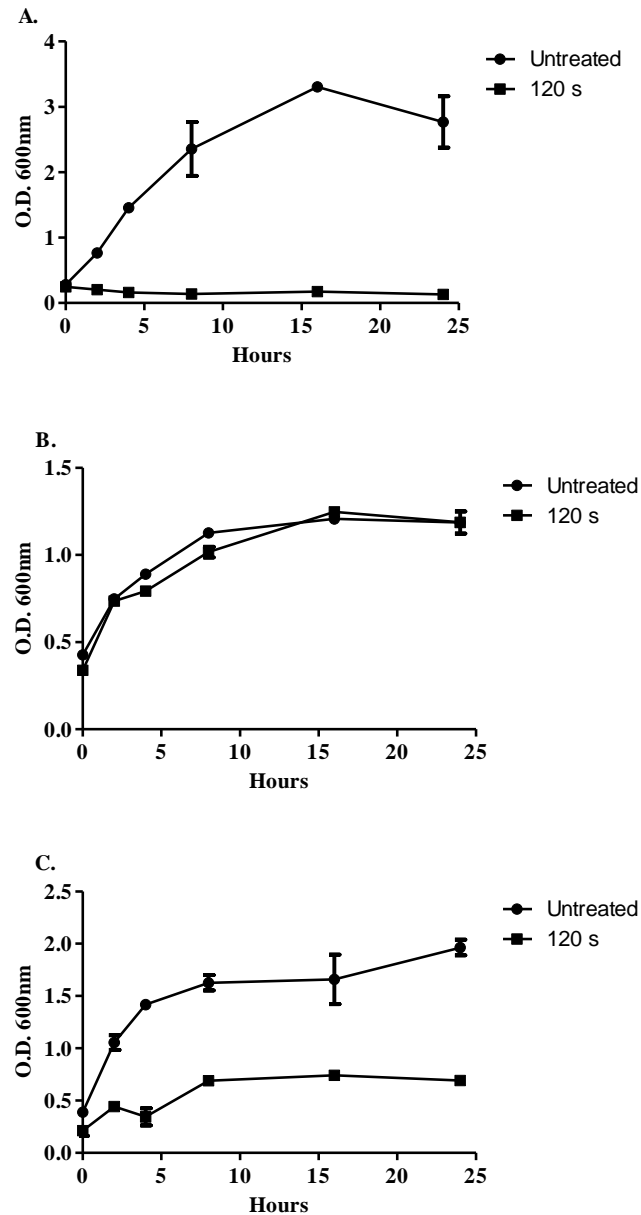
The effective sterilization of foodborne and opportunistic nosocomial pathogens is a major problem in food industry, biomedical and hospital applications, respectively. The resistive barrier plasma (RBP) jet was tested over a wide range of microbes for its decontamination and disinfection efficacy and we have found that the RBP source is very efficient in decontaminating wide range of infection and contamination causing bacteria. The direct and indirect exposure of the RBP jet (with the cooling unit) as a non-thermal sterilization method was tested on regrowth potential of post-partial-plasma-exposure of foodborne and nosocomial pathogens. Similarly the RBP jet was also tested on plasma efficiency at different bacterial concentrations for its effects on growth for pre and post plasma treated bacteria. In these tests, the ROS produced by the RBP source was applied to *Escherichia coli* ATCC 11775, *Bacillus cereus* ATCC 14579, *Staphylococcus aureus* ATCC 25923 and *Pseudomonas aeruginosa* ATCC 27853. An average of 30 CFU per 71 mm² was inoculated with the corresponding bacterium on a dry surface-agar plate, followed by the following exposure times 0, 30, 60, 120 and 180 seconds of plasma. 20 µl of *E. coli* 107 CFU/ml and *P. aeruginosa* 108 CFU/ml were treated with plasma for 0, 120, 240 and 360 seconds. The colonies that survived the plasma treatment and control colonies were transferred to tryptic soy broth (TSB) and their growth was observed for 24 hrs. Results have showed 100% and 96% of inactivation after 180s of treatment for *E. coli* and *S. aureus* respectively. A 100% of inactivation was observed for *B. cereus* and *P. aeruginosa* after 60s. *E. coli* and *P. aeruginosa* showed a log reduction of 3.4 and 3.9 orders respectively after

360s. The 24 hours re-growth results of direct exposure of plasma for 30, 60 and 120 seconds on *Escherichia coli* (ATCC 11775), *Neisseria meningitidis* (ATCC 700532) and *Staphylococcus aureus* MRSA (ATCC 259231) are shown in Fig. below.



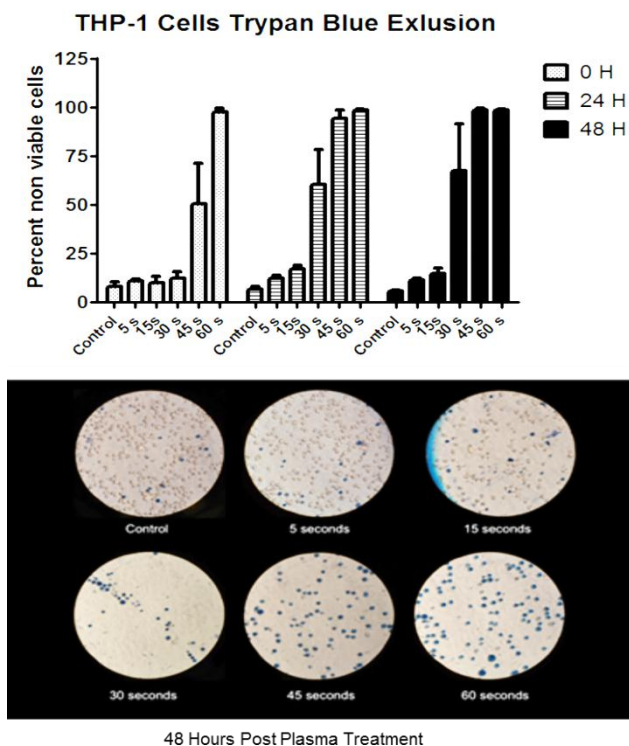
Density measurements over a 24 hour period of bacteria without direct plasma treatment (closed circles ●) or with direct treatment of plasma for 30 seconds (closed square ■), 60 seconds (closed up-pointing triangle ▲), or 120 seconds (down-pointing triangle ▼). A.) *Escherichia coli* (ATCC 11775). B.) *Neisseria meningitidis* (ATCC 700532). C.) *Staphylococcus aureus* (ATCC 259231).

The 24 hours re-growth results of indirect exposure of plasma 120 seconds on *Escherichia coli* (ATCC 11775), *Neisseria meningitidis* (ATCC 700532) and *Staphylococcus aureus* MRSA (ATCC 259231) are shown in Fig. below.



Density measurements over a 24 hour period of bacteria without indirect plasma treatment (closed circles ●) or with indirect treatment of plasma for 120 seconds (closed square ■). A.) *Escherichia coli* (ATCC 11775). B.) *Neisseria meningitidis* (ATCC 700532). C.) *Staphylococcus aureus* (ATCC 259231).

The growths of survived colonies were monitored and subjected to further treatment. The results indicate that the post treatment growth rates are similar to the pre-treatment growth rates. Therefore non-equilibrium plasma is effective in sterilizing bacteria at different concentrations with potential applications in the food industry and the medical field.

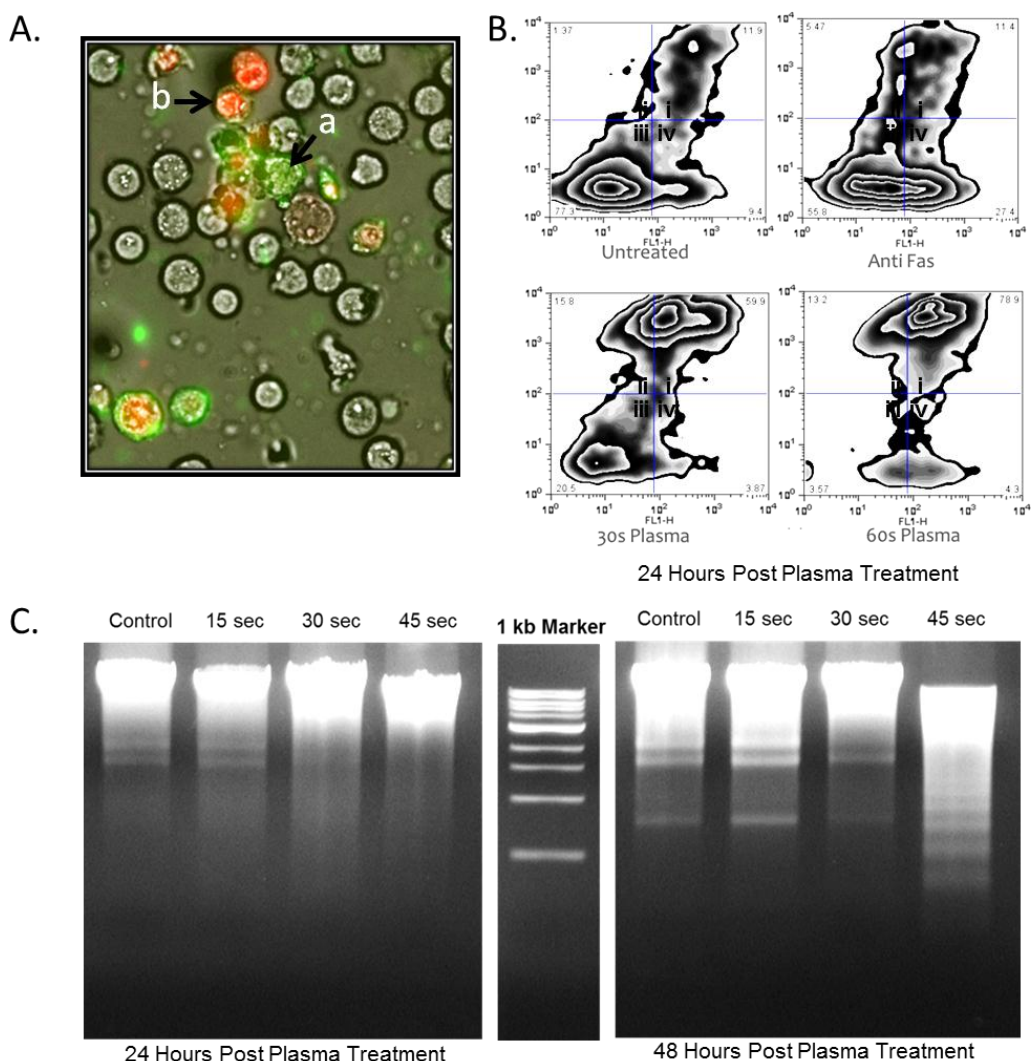


Viability of THP-1 cells after RBP treatment. (A) THP-1 cells 0 hours, 24h and 48h post plasma treatment of 0 seconds, 5s, 15s, 30s, 45s and 60s. Non viable cells are presented as the percent of treated cells that absorbed trypan blue dye as compared to control cells not treated by RBP. (B) Photograph of cells stained with typan blue dye 48h post plasma treatment.

The possibility of using the RBP jet for treating cancer cells was also tested, since the need for new and effective mechanisms to induce programmed cellular death (apoptosis) in cancerous cells is of great importance in cancer research. Application of direct as well as indirect exposure of plasma for cancer research is still in the exploratory stage and there remain several unanswered questions. We have tested the effects of indirect exposure of non-thermal air plasma on monocytic leukemia cancer cells (THP-1) and deciphering the mechanisms that modulate cellular induction of apoptosis. The phenotypes of interest were cells demonstrating

death morphologies of apoptosis or necrosis. This is important since cells undergoing necrosis can initiate an inflamed immune response that can be detrimental to a treated individual. The type of morphological cell death that occurred in THP-1 for various plasma treatment dosages (plasma power, flow and distance) was tested and the results are shown in Fig. above.

The results demonstrate that a preference for apoptosis in plasma treated THP-1 cells under particular plasma parameters and dosage levels. The THP-1 cells were identified as apoptotic utilizing a fluorescent dye conjugated with annexin V followed by identification of the cells through fluorescent microscopy and flow-cytometry diagnostics as shown in Fig. below.



Induction of apoptosis in THP-1 cells after RBP treatment. (A) Fluorescence microscopy of THP-1 cells stained with Annexin V FITC and propidium iodide. Cells undergoing apoptosis

stain with Annexin V and appear green (a), while cells without intact membrane due to necrosis appear red (b). (B) Flow cytometry detection of Annexin V and propidium iodide staining 24h post RBP treatment of 30s and 60s. Controls are untreated cells and anti-fas treated cells. Presented are the detection of stains from 10,000 events in which quadrants indicated (Q-I) propidium iodide stain, (Q-II) background, (Q-III) unstained, (Q-IV) annexin V. (C) DNA fragmentation assay of DAN from THP-1 cells 24h and 48h post RBP treatment of 0s, 15s, 30s and 45s. A 1kb ladder was used as a comparative indicator of the separation of DNA.

Further, DNA fragmentation assays, for late detection of apoptosis, correlated with are fluorescence data demonstrating patterns of apoptotic events. However, the data also revealed that higher plasma dosages presented with undesired necrotic morphologies in the THP-1 cells. The presented variabilities in the death morphologies by plasma treated THP-1 cells signify the need for further investigation on the cellular mechanisms induced by the indirect plasma exposure. Along with taking into account other death processes such as autophagy, a catabolic process involving the degradation of a cell's own components through the lysosomal machinery. The results obtained from this research indicate great potential for the use of our non-thermal resistive barrier based indirect plasma treatment method as an inexpensive and less invasive method for treating leukemia and other cancerous lesions.

KEY RESEARCH ACCOMPLISHMENTS

The project has met the project deadlines for majority of the proposed tasks under the Objective 1 and 2 during this period year. The status and remarks of the project milestones are given below.

Table 2. Status and remarks of the project milestones

Task	Proposed Milestones	Base Line Plan Date	Status/Remark
I. Objective 1: Establish Plasma Engineering Research Lab			
1	Setup a direct current - atmospheric - resistive barrier cold plasma system	26 OCT 2011	Completed
2	Setup a 13.56 MHz radio frequency dielectric barrier plasma system	26 OCT 2011	Completed
3	Setup a 900 MHz/2.45 GHz wave plasma system	26 OCT 2011	Completed
4	Setup a laser induced breakdown plasma experimental system	26 OCT 2011	Completed
5	Implement plasma shadowgraphy diagnostics Setup	26 OCT 2011	Completed
6	Implement a two color laser interferometry diagnostics setup	26 OCT 2011	Completed
7	Implement a optical emission spectroscopy diagnostics setup	26 OCT 2011	Completed
II. Objective 2: Develop Portable Plasma Source			
8	Design phase: Design an optimized portable plasma source system	26 OCT 2012	Completed
9	Construction phase: Construct the portable plasma source based on the design analysis and utilizing the existing resources and knowledge gained from objective 1.	26 OCT 2012	Completed
10	Testing and characterization phase: Portable plasma source will be tested and characterized for its operating parameters and plasma parameters.	26 OCT 2013	In Progress
11	Biological testing: In-vitro biological testing.	26 OCT 2013	In Progress

REPORTABLE OUTCOMES

A. MENTORING

The PI is dedicated to mentor students of diversity and underrepresented minority groups.

The PI has mentored the following scientists in the research

Dr. Zhen Ma

Dr. Kenneth Williamson

Dr. Abdollah Sarani

Xavier Gonzales

The PI has mentored the following Graduate Students

Heather Anderson

Anudeep Reddy Kandi

Jennifer Chancellor

The PI has mentored the following Undergraduate Students

Eduardo Valdez

Francisco Rodriguez

Bokang Yang

Thurman Walling

James Shames

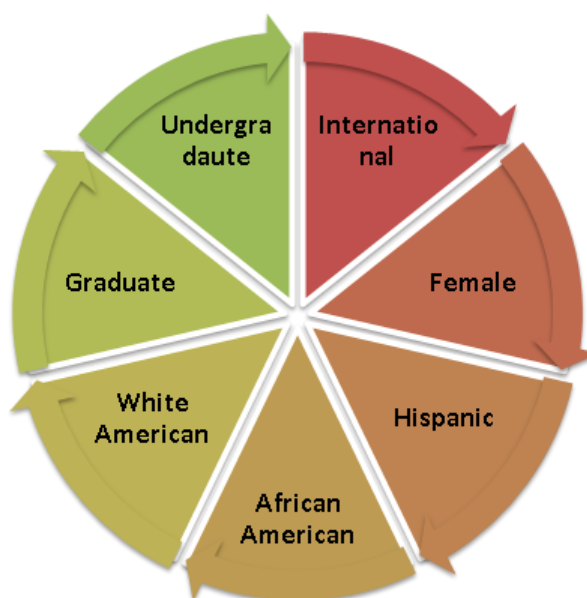
Isaac Colmenero

Kim Pham

Megan Norfolk

Jennifer Anderson

Amanda Whitmill



B. CONFERENCE PUBLICATIONS

1. Norfolk, M., Thiyagarajan, M., waldbeser, I., whitmill, A. (2011). Apoptosis and Autophagy in Cancer Cells Induced from Non-Thermal Ionized Plasma. San Jose, California: SACNAS National Conference.
2. Valdez, E., Thiyagarajan, M. (2011). Characterization of Diffused Atmospheric Pressure Cold Plasma System for Surface Modification. Corpus Christi, TX: Sigma Xi 11th Annual Undergraduate Research Symposium (Best Paper Award).
3. Vidal, G., Thiyagarajan, M., Pam, H. (2011). Cold Plasma Inactivation of E. coli and S. aureus on Solid Surfaces for Infection Treatment. San Jose, California: SACNAS National Conference.
4. Ausland, J., Thiyagarajan, M., Vidal, G. (2011). Deactivation of Escherichia coli using a Novel Cold Plasma Technology and its effect on the bacterial growth. Corpus Christi, TX: Sigma Xi 11th Annual Undergraduate Research Symposium.
5. Yang, B., Thiyagarajan, M. (2011). Electrical Conductivity Characterization of Novel TAMUCC Stoneware Ceramic at Various Experimental Conditions. Corpus Christi, TX: Sigma Xi 11th Annual Undergraduate Research Symposium.
6. Hes, J., Thiyagarajan, M., Branecky, C., Ramon, R. (2011). Electrical Conductivity Measurements and Analysis of Ceramic Materials at Various Moisture Conditions. Corpus Christi, TX: Sigma Xi 11th Annual Undergraduate Research Symposium.
7. Anderson, H., Thiyagarajan, M., Vidal, G., Pam, H. (2011). Non-Thermal Plasma Decontamination of E. Coli and S. Aureus – Research and Review. San Jose, California: SACNAS National Conference.
8. Ramon, R., Thiyagarajan, M. (2011). Portable Plasma Disinfection Conveyor System. Corpus Christi, TX: Sigma Xi 11th Annual Undergraduate Research Symposium.
9. Norfolk, M., Thiyagarajan, M. (2011). Pre-programmed Cell Death in Acute Monocytic Leukemia Cancer Cells Induced by Nonthermal Ionized Plasma. Corpus Christi, TX: Sigma Xi 11th Annual Undergraduate Research Symposium (Best Paper Award).
10. Valdez, E., Thiyagarajan, M. (2011). Reactive Gas Species Characterization of Diffused Atmospheric Pressure Cold Plasma System. San Jose, California: SACNAS National Conference.
11. Pam, H., Thiyagarajan, M., Vidal, G., Alison, D., Mott, J., Buck, G. (2011). Sterilization of Escherichia coli and Staphylococcus aureus Microorganism using a Novel Cold Plasma Technology. San Jose, California: SACNAS National Conference.
12. Pham, H., Thiyagarajan, M., Vidal, G., Buck, G., Mott, J. (2011). Sterilization of Staphylococcus aureus using a Novel Cold Plasma Technology and its effect on the bacterial growth. Corpus Christi, TX: Sigma Xi 11th Annual Undergraduate Research Symposium.

13. Rodriguez, F., Thiagarajan, M., Yang, B., Williamson, K. (2011). Surface Energy Modification using Atmospheric Pressure Cold Plasma System. Corpus Christi, TX: Sigma Xi 11th Annual Undergraduate Research Symposium.
14. Thiagarajan, M. (2011). Materials Engineering Course Design and Improvement for Effective Research Based Learning Environment. Corpus Christi, TX: TAMUCC 1st Faculty Symposium: Course Design for the Millennial Student.
15. Thiagarajan, M. (2011). Portable Plasma Biomedical Device for Cancer Treatment. Irvine, California: ASME Emerging Technologies - 6th Frontiers in Biomedical Devices Conference.
16. Thiagarajan, M. (2011). Portable Plasma Medical Device for Infection Treatment and Wound Healing. Irvine, California: ASME Emerging Technologies - 6th Frontiers in Biomedical Devices Conference.
17. Thiagarajan, M. (2011). Effects of Cold Plasma and Treatment of Leukemia Cancer Cells. Marseille, France: International Conference on Medical Physics and Biomedical Engineering.
18. Thiagarajan, M. (2011). Effects of Plasma Treatment on E. Coli, S. Aureus and N. Meningitidis Microbes. Marseille, France: International Conference on Medical Physics and Biomedical Engineering.
19. Thiagarajan, M. (2011). Characterization of Reactive Gas Species in Diffused Atmospheric Pressure Cold Plasma System. Paris, France: International Conference on Applied Chemistry and Chemical Engineering.
20. Thiagarajan, M., waldbeser, I. (2011). Effective Non-Thermal Plasma Induction of Apoptosis in Leukemia Cancer Cells. Chicago, IL: 38th IEEE International Conference on Plasma Science (ICOPS) and 24th Symposium on Fusion Engineering (SOFE).
21. Thiagarajan, M. (2011). Experimental Study of Shock Wave Discontinuities and Interactions with Laser Induced Plasmas. Chicago, IL: 38th IEEE International Conference on Plasma Science (ICOPS) and 24th Symposium on Fusion Engineering (SOFE).
22. Thiagarajan, M. (2011). High Power Pulsed Laser Induced Breakdown Plasma at Gas-Solid Interface. Chicago, IL: 18th IEEE International Pulsed Power Conference.
23. Thiagarajan, M. (2011). Plasma Treatment on E. Coli, S. Aureus, N. Meningitides for Food Industries. Paris, France: International Conference on Food Engineering and Biotechnology.
24. Thiagarajan, M., waldbeser, I. (2011). Portable Plasma Torch on E.Coli, S. Aureus, N. Meningitidis and other Clinical Isolates. Chicago, IL: 38th IEEE International Conference on Plasma Science (ICOPS) and 24th Symposium on Fusion Engineering (SOFE).
25. Thiagarajan, M., waldbeser, I. (2011). Treatment of Cancer Cells using a Pulsed Power Plasma Source. Chicago, IL: 18th IEEE International Pulsed Power Conference.

26. Thiyagarajan, M. (2011). Report on Portable Plasma Bio-Medical Device and Characterization. Omaha, Nebraska: Telemedicine and Advanced Technology Research Center - Midwest Technology Exchange Conference.
27. Whitmill, A., Thiyagarajan, M., waldbeser, I. (2011). Effects of Non-Thermal Ionized Plasma on THP-1 Acute Monocytic Leukemia Cells. Ithaca, NY: National Conference on Undergraduate Research (NCUR).
28. Whitmill, A., Thiyagarajan, M., waldbeser, I. (2011). Induction of Apoptosis in Leukemia Cells by Non-thermal Ionized Plasma. Prairie View, TX: 7th Annual LSAMP Conference (Best Paper Award).
29. Valdez, E., Thiyagarajan, M. (2011). Reactive Gas Species Characterization of Diffused Atmospheric Pressure Cold Plasma System. Prairie View, TX: 7th Annual LSAMP Conference.
30. Whitmill, A., Thiyagarajan, M., Waldbeser, L. (2011). Effects of Ionized Plasma on THP-1 Acute Monocytic Leukemia Cells. Corpus Christi, TX: 2011 Annual McNair Symposium.
31. Whitmill, A., Thiyagarajan, M., waldbeser, I. (2010). Effects of Ionized Plasma on Acute Monocytic Leukemia Cells. (pp. 74). Canyon, TX: 8th Annual Pathways Research Symposium.
32. Thiyagarajan, M., Hardeman, K., Waldbeser, L. S. (2010). Effects of Plasma Treatment on E. Coli, S. Aureus, N. Meningitidis and Other Clinical Isolates. (2010th ed., vol. 7, pp. 131). Anaheim, CA: 2010 SACNAS National Conference (Best Paper Award).
33. Walling, T., Thiyagarajan, M. (2010). Nitrogen Oxides and Light Wavelengths Produced by a Portable Plasma Device. (pp. 56). Canyon, TX: 8th Annual Pathways Research Symposium.
34. Thiyagarajan, M., Whitmill, A., waldbeser, I. (2010). Effects of Non-Thermal Ionized Plasma on Human Leukemia and Lymphoma Cells. (vol. 7, pp. 82). Anaheim, CA: 2010 SACNAS National Conference.
35. Whitmill, A., Thiyagarajan, M., waldbeser, I. (2010). Effects of Non-Thermal Ionized Plasma on Human Leukemia and Lymphoma Cells. (pp. 8). Texas: 10th Annual Research Symposium, South Texas Sigma Xi.
36. Walling, T., Thiyagarajan, M. (2010). Nitrogen Oxides and Light Wavelengths Produced by a Medical Treatment Device. (pp. 41). Texas: 10th Annual Research Symposium, South Texas Sigma Xi.

C. JOURNAL MANUSCRIPTS AND BOOKS PUBLISHED

1. M. Thiyagarajan et. al., Optical breakdown threshold investigation of 1064 nm laser induced air Plasmas, *Journal of Applied Physics*, 111, 073302 (2012); doi: 10.1063/1.3699368.
2. M. Thiyagarajan et. al., Experimental Investigation of 1064-nm IR Laser-Induced Air Plasma Using Optical Laser Shadowgraphy Diagnostics, *IEEE TRANSACTIONS ON PLASMA SCIENCE*, VOL. 40, NO. 10, OCTOBER 2012
3. Magesh Thiyagarajan. "Laser Induced Plasmas & Optical Diagnostics: Infrared & Ultraviolet Laser Breakdown Plasmas & Shadowgraphy, Interferometry, Optical Emission Spectroscopy Diagnostics." (LAP LAMBERT, 2011). ©. 268 pages, (ISBN: 978-3846548745). (2011).
4. Magesh Thiyagarajan. "Experimental Investigation of 193 nm Excimer Laser Induced Plasma in Air" (ProQuest, 2011). ©. 120 pages, (ISBN: 978-1243508751). (2011).
5. M. Thiyagarajan et. al., "THP-1 leukemia cancer treatment using a portable plasma device." *Health Technology and Informatics* vol. 173, no. 1 (2012).
6. M. Thiyagarajan et. al., "Portable plasma medical device for infection treatment." *Health Technology and Informatics* vol. 173, no. 1 (2012).
7. M. Thiyagarajan et. al., Characterization of Portable Resistive Barrier Plasma Jet and its Direct and Indirect Treatment for Antibiotic Resistant Bacteria and THP-1 Leukemia Cancer Cells, *IEEE Transactions on Plasma Science*, Volume: 40, Issue: 12, Part: 3

Conclusion

The PI and the research team have completed majority of the proposed tasks on or before the deadline and the tasks that are in progress will be completed in the upcoming year. The research outcomes are demonstrated. The research team has been taking initiatives for the future research work on animal testing and is aiming to request additional funding from funding agencies.

APPENDIX A – PI Resume

Dr. Magesh Thiyagarajan

Texas A&M University-Corpus Christi
Science & Technology, Computing Sciences

Office: Science and Technology ST222D, Office Phone: (361) 825-2144, Email: magesh@tamucc.edu

Education

PhD, University of Wisconsin - Madison, 2008.

MS, University of Tennessee - Knoxville, 2004.

BS, University of Madras - India, 2001.

Diploma in Computer Applications, TATA Infotech, India, 2000.

Licensures and Certifications

Disbursement of Funds, TAMUCC. (2010 - Present).

Biological Defense Safety Program and Technical Safety, TAMUCC. (2010 - Present).

CITI Collaborative Institutional Training Initiative - Responsible Conduct of Research, CITI. (2010 - Present).

TRIZ (Innovative way for new ideas). (2009 - Present).

Six-Sigma Green Belt Certification, General Electric Company (GE). (2008 - Present).

Intellectual Property for Technologists, General Electric Company (GE). (2008 - Present).

Hiring the Right People, General Electric Company (GE). (2008 - Present).

Entrepreneurial Business Program Certification, School of Business, University of Wisconsin-Madison. (2007 - Present).

Professional Employment

Assistant Professor of Engineering - Director of Plasma Engineering Research, Texas A&M University - Corpus Christi. (July 2009 - Present).

- Direct the Plasma Engineering and Science Research Projects

- Mentor interdisciplinary students to carry out research

- Lead the research on portable plasma based biomedical device for combat care application

- Lead the research on Bacterial deactivation mechanisms through cold plasma

- Lead the research on treatment of cancer cells through cold plasma

Lead Engineer, General Electric Company (GE). (March 2008 - June 2009).

- Key Lead on Plasma Medicine and Plasma Sterilization of Medical Devices.

- Task leader and key contributor for large scale waste gasification project.

- Extensive engineering, R&D and process control in optical data storage project.

- EIT – Electrical Impedance Tomography for brain and lung strokes.

- Technology, market research, fetched government proposals for a total of \$1.6 Million.

Research Fellow, University of Wisconsin – Madison, WI. (June 2004 - February 2008).

- Laser and RF Plasmas for Industrial and Military Applications

- The principal focus of my research is to design, implement, diagnose and characterize the laser induced plasmas for advanced industrial and military application.

- Proposed and written a research proposal and received a competitive grant of \$150,000.

Designed and built experimental setups to characterize high power 10 MW UV laser focused plasma in the presence of dielectric window materials for micro machining.
Collaborated with MIT and Texas Tech University research groups for optimized results.
Supervised and guided undergraduate and graduate research assistants.

Teaching Assistant, University of Wisconsin – Madison, WI. (August 2004 - June 2006).

Taught Electric Circuits Laboratory Course – for four semesters with class strength of 30.
Organized tutorials to clarify course material. Wrote instruction manual to help students use software and hardware in a better way. Class scored 7% higher in final than any of the professor's former classes.

Exceptional student feedback for all four semesters.

Received the Honorable mention for exceptional teaching performance during 2004 – 05.

Received the Best Teaching Assistant Award for the 2005 – 06 academic year.

Scientific Consultant, ASI Technology Corporation. (June 2003 - June 2004).

Designed and developed a novel plasma Stealth antenna prototype for military applications.

Scientific Consultant, Michael Grace Grant. (August 2002 - June 2004).

Developed a 25 kV High-Voltage experimental plasma ball lightning system

Research Assistant, University of Tennessee – Knoxville, TN. (August 2002 - May 2004).

Developed an effective biological plasma decontamination system- Patent Pending.

Presented research results to funding sources and fetched \$2 Million for further research.

Designed a commercial model of the plasma decontamination unit.

Project Coordinator, Engineering Enterprises. (August 2001 - June 2002).

Designed Analog and Digital IC circuit design using TTL and LSI chips.

Team Leader: Designed and implemented a Transistor Curve Tracer project.

Intern, General Electric Company – Alstom. (2001).

Professional Memberships

Louis Stokes Alliances for Minority Participation

McNair Scholars Program

American Society of Mechanical Engineers

Sigma Xi

Toastmasters International Club

MIT Entrepreneur Club

Eta Kappa Nu

Tau Beta Pi

Institute of Electrical and Electronics Engineers

Nuclear and Plasma Sciences Society

TEACHING

Teaching Experience

ENGR 2322, MATERIALS SCIENCE

ENTC 3410, MATERIAL SCIENCE

ENTC 4496, DIS: Design and Fabrication of Conveyor System with Variable Speeds

Non-Credit Instruction

Plasmas in the Engineering & Science Field, Presented to the Introduction to Engineering Class - Fall 2010. (October 2010).

Plasmas in the Engineering & Science Field. (October 2009).

Introduction to Plasma Science and Engineering, Freshman Seminar Series. (October 2009).

Teaching Awards and Honors

NSF Travel Award for ASEE Integrating Sustainability in Engineering Courses workshop, NSF. (2010).

Best Teaching Assistant Award, Dept. of Electrical Engineering, Univ. of Wisconsin Madison. (2005).

University of Madras Gold Medalist, University of Madras. (2001).

SCHOLARLY AND CREATIVE ACTIVITIES

Publications

Refereed

Conference Proceedings

Anderson, H., Thiyagarajan, M., waldbeser, I., Gonzalez, X., Norfolk, M., Whitmill, A. (2011). Apoptotic Behavior in THP-1 Acute Monocytic Leukemia Cancer Cells Induced by Nonthermal Plasma. College Station, TX: 9th Annual Pathways Research Conference.

Ausland, J., Thiyagarajan, M., Vidal, G. (2011). Deactivation of Escherichia coli using a Novel Cold Plasma Technology and its effect on the bacterial growth. College Station, TX: 9th Annual Pathways Research Conference.

Yang, B., Thiyagarajan, M. (2011). Electrical Conductivity Characterization of Novel TAMUCC Stoneware Ceramic at Various Experimental Conditions. College Station, TX: 9th Annual Pathways Research Conference.

Norfolk, M., Thiyagarajan, M., waldbeser, I., Gonzalez, X., Anderson, H., Whitmill, A. (2011). Nonthermal Ionized Plasma Induction of Pre-programmed Cell Death in Acute Monocytic Leukemia Cancer Cells. College Station, TX: 9th Annual Pathways Research Conference.

Kandi, A., Thiyagarajan, M., Williamson, K. (2011). Optical Characterization and Diagnostics of High Power 1064 nm Infrared Laser System. College Station, TX: 9th Annual Pathways Research Conference.

Pham, H., Thiyagarajan, M., Vidal, G., Buck, G., Mott, J. (2011). Sterilization of Staphylococcus aureus Microorganism using a Novel Cold Plasma Technology. College Station, TX: 9th Annual Pathways Research Conference.

Rodriguez, F., Thiyagarajan, M., Yang, B., Williamson, K. (2011). Surface Energy Modification using Atmospheric Pressure Cold Plasma System. College Station, TX: 9th Annual Pathways Research Conference.

Valdez, E., Thiyagarajan, M. (2011). Surface Modification using Diffused Atmospheric Pressure Cold Plasma System. College Station, TX: 9th Annual Pathways Research Conference.

- Norfolk, M., Thiyagarajan, M., waldbeser, I., whitmill, A. (2011). Apoptosis and Autophagy in Cancer Cells Induced from Non-Thermal Ionized Plasma. San Jose, California: SACNAS National Conference.
- Valdez, E., Thiyagarajan, M. (2011). Characterization of Diffused Atmospheric Pressure Cold Plasma System for Surface Modification. Corpus Christi, TX: Sigma Xi 11th Annual Undergraduate Research Symposium (Best Paper Award).
- Vidal, G., Thiyagarajan, M., Pam, H. (2011). Cold Plasma Inactivation of E. coli and S. aureus on Solid Surfaces for Infection Treatment. San Jose, California: SACNAS National Conference.
- Ausland, J., Thiyagarajan, M., Vidal, G. (2011). Deactivation of Escherichia coli using a Novel Cold Plasma Technology and its effect on the bacterial growth. Corpus Christi, TX: Sigma Xi 11th Annual Undergraduate Research Symposium.
- Yang, B., Thiyagarajan, M. (2011). Electrical Conductivity Characterization of Novel TAMUCC Stoneware Ceramic at Various Experimental Conditions. Corpus Christi, TX: Sigma Xi 11th Annual Undergraduate Research Symposium.
- Hes, J., Thiyagarajan, M., Branecky, C., Ramon, R. (2011). Electrical Conductivity Measurements and Analysis of Ceramic Materials at Various Moisture Conditions. Corpus Christi, TX: Sigma Xi 11th Annual Undergraduate Research Symposium.
- Anderson, H., Thiyagarajan, M., Vidal, G., Pam, H. (2011). Non-Thermal Plasma Decontamination of E. Coli and S. Aureus – Research and Review. San Jose, California: SACNAS National Conference.
- Ramon, R., Thiyagarajan, M. (2011). Portable Plasma Disinfection Conveyor System. Corpus Christi, TX: Sigma Xi 11th Annual Undergraduate Research Symposium.
- Norfolk, M., Thiyagarajan, M. (2011). Pre-programmed Cell Death in Acute Monocytic Leukemia Cancer Cells Induced by Nonthermal Ionized Plasma. Corpus Christi, TX: Sigma Xi 11th Annual Undergraduate Research Symposium (Best Paper Award).
- Valdez, E., Thiyagarajan, M. (2011). Reactive Gas Species Characterization of Diffused Atmospheric Pressure Cold Plasma System. San Jose, California: SACNAS National Conference.
- Pam, H., Thiyagarajan, M., Vidal, G., Alison, D., Mott, J., Buck, G. (2011). Sterilization of Escherichia coli and Staphylococcus aureus Microorganism using a Novel Cold Plasma Technology. San Jose, California: SACNAS National Conference.
- Pham, H., Thiyagarajan, M., Vidal, G., Buck, G., Mott, J. (2011). Sterilization of Staphylococcus aureus using a Novel Cold Plasma Technology and its effect on the bacterial growth. Corpus Christi, TX: Sigma Xi 11th Annual Undergraduate Research Symposium.
- Rodriguez, F., Thiyagarajan, M., Yang, B., Williamson, K. (2011). Surface Energy Modification using Atmospheric Pressure Cold Plasma System. Corpus Christi, TX: Sigma Xi 11th Annual Undergraduate Research Symposium.
- Thiyagarajan, M. (2011). Materials Engineering Course Design and Improvement for Effective Research Based Learning Environment. Corpus Christi, TX: TAMUCC 1st Faculty Symposium: Course Design for the Millennial Student.

Thiyagarajan, M. (2011). Portable Plasma Biomedical Device for Cancer Treatment. Irvine, California: ASME Emerging Technologies - 6th Frontiers in Biomedical Devices Conference.

Thiyagarajan, M. (2011). Portable Plasma Medical Device for Infection Treatment and Wound Healing. Irvine, California: ASME Emerging Technologies - 6th Frontiers in Biomedical Devices Conference.

Thiyagarajan, M. (2011). Effects of Cold Plasma and Treatment of Leukemia Cancer Cells. Marseille, France: International Conference on Medical Physics and Biomedical Engineering.

Thiyagarajan, M. (2011). Effects of Plasma Treatment on E. Coli, S. Aureus and N. Meningitidis Microbes. Marseille, France: International Conference on Medical Physics and Biomedical Engineering.

Thiyagarajan, M. (2011). Characterization of Reactive Gas Species in Diffused Atmospheric Pressure Cold Plasma System. Paris, France: International Conference on Applied Chemistry and Chemical Engineering.

Thiyagarajan, M., waldbeser, I. (2011). Effective Non-Thermal Plasma Induction of Apoptosis in Leukemia Cancer Cells. Chicago, IL: 38th IEEE International Conference on Plasma Science (ICOPS) and 24th Symposium on Fusion Engineering (SOFE).

Thiyagarajan, M. (2011). Experimental Study of Shock Wave Discontinuities and Interactions with Laser Induced Plasmas. Chicago, IL: 38th IEEE International Conference on Plasma Science (ICOPS) and 24th Symposium on Fusion Engineering (SOFE).

Thiyagarajan, M. (2011). High Power Pulsed Laser Induced Breakdown Plasma at Gas-Solid Interface. Chicago, IL: 18th IEEE International Pulsed Power Conference.

Thiyagarajan, M. (2011). Plasma Treatment on E. Coli, S. Aureus, N. Meningitides for Food Industries. Paris, France: International Conference on Food Engineering and Biotechnology.

Thiyagarajan, M., waldbeser, I. (2011). Portable Plasma Torch on E.Coli, S. Aureus, N. Meningitidis and other Clinical Isolates. Chicago, IL: 38th IEEE International Conference on Plasma Science (ICOPS) and 24th Symposium on Fusion Engineering (SOFE).

Thiyagarajan, M., waldbeser, I. (2011). Treatment of Cancer Cells using a Pulsed Power Plasma Source. Chicago, IL: 18th IEEE International Pulsed Power Conference.

Thiyagarajan, M. (2011). Report on Portable Plasma Bio-Medical Device and Characterization. Omaha, Nebraska: Telemedicine and Advanced Technology Research Center - Midwest Technology Exchange Conference.

Whitmill, A., Thiyagarajan, M., waldbeser, I. (2011). Effects of Non-Thermal Ionized Plasma on THP-1 Acute Monocytic Leukemia Cells. Ithaca, NY: National Conference on Undergraduate Research (NCUR).

Whitmill, A., Thiyagarajan, M., waldbeser, I. (2011). Induction of Apoptosis in Leukemia Cells by Non-thermal Ionized Plasma. Prairie View, TX: 7th Annual LSAMP Conference (Best Paper Award).

Valdez, E., Thiyagarajan, M. (2011). Reactive Gas Species Characterization of Diffused Atmospheric Pressure Cold Plasma System. Prairie View, TX: 7th Annual LSAMP Conference.

Whitmill, A., Thiyagarajan, M., Waldbeser, L. (2011). Effects of Ionized Plasma on THP-1 Acute Monocytic Leukemia Cells. Corpus Christi, TX: 2011 Annual McNair Symposium.

Whitmill, A., Thiyagarajan, M., waldbeser, I. (2010). Effects of Ionized Plasma on Acute Monocytic Leukemia Cells. (pp. 74). Canyon, TX: 8th Annual Pathways Research Symposium.

Thiyagarajan, M., Hardeman, K., Waldbeser, L. S. (2010). Effects of Plasma Treatment on E. Coli, S. Aureus, N. Meningitidis and Other Clinical Isolates. (2010th ed., vol. 7, pp. 131). Anaheim, CA: 2010 SACNAS National Conference (Best Paper Award).

Walling, T., Thiyagarajan, M. (2010). Nitrogen Oxides and Light Wavelengths Produced by a Portable Plasma Device. (pp. 56). Canyon, TX: 8th Annual Pathways Research Symposium.

Thiyagarajan, M., Whitmill, A., waldbeser, I. (2010). Effects of Non-Thermal Ionized Plasma on Human Leukemia and Lymphoma Cells. (vol. 7, pp. 82). Anaheim, CA: 2010 SACNAS National Conference.

Whitmill, A., Thiyagarajan, M., waldbeser, I. (2010). Effects of Non-Thermal Ionized Plasma on Human Leukemia and Lymphoma Cells. (pp. 8). Texas: 10th Annual Research Symposium, South Texas Sigma Xi.

Walling, T., Thiyagarajan, M. (2010). Nitrogen Oxides and Light Wavelengths Produced by a Medical Treatment Device. (pp. 41). Texas: 10th Annual Research Symposium, South Texas Sigma Xi.

Thiyagarajan, M., Whitmill, A., Waldbeser, L. S. (2010). Effects of Ionized Plasma on THP-1 Acute Monocytic Leukemia Cells. Davis, CA: 2010 National MCNAIR Conference.

Thiyagarajan, M., waldbeser, I. (2010). Plasma – NOX Induced Apoptosis on Various Cell Structures. (0730-9244 ed.). Norfolk, Virginia: 37th IEEE International Conference on Plasma Science.

Thiyagarajan, M., Scharer, J. (2007). Measurements of Air Breakdown and Scaling to Microwaves Using 193 nm Focused Laser Radiation. International Vacuum Electronics Conference, IEEE Proceedings of Vacuum Science.

Thiyagarajan, M., Scharer, J. (2007). Measurements of Air Breakdown Process Using 193 nm Focused Laser Radiation. Albuquerque, New Mexico: 34th International Conference on Plasma Science, IEEE Proceedings of Plasma Science.

Luo, S., Thiyagarajan, M., Scharer, J. (2007). Optimization and Diagnostics of High Pressure Air Plasmas. Albuquerque, New Mexico: 34th International Conference on Plasma Science, IEEE Proceedings of Plasma Science.

Thiyagarajan, M. (2006). Air Breakdown Process Using 193 nm Focused Laser Radiation. Madison, WI: Research Symposium - Univ. of Wisconsin Madison.

Luo, S., Thiyagarajan, M., Scharer, J. (2006). Diagnostics and Simulation of High pressure Argon and Nitrogen Plasma. Traverse City, Michigan: 33rd International Conference on Plasma Science, IEEE Proceedings of Plasma Science.

Thiyagarajan, M., Luo, S., Scharer, J. (2006). Optical Diagnostics of Laser Initiated, RF Sustained High Pressure Seeded Plasmas. Traverse City, Michigan: 33rd International Conference on Plasma Science, IEEE Proceedings of Plasma Science.

Alexeff, I., Thiyagarajan, M. (2005). Advances in Plasma Antenna Design. Monterey, California: 32nd International Conference on Plasma Science, IEEE Proceedings of Plasma Science.

Thiyagarajan, M., Alexeff, I. (2005). Atmospheric Pressure Resistive Barrier Cold Plasma for Biological Decontamination. Monterey, California: 32nd International Conference on Plasma Science, IEEE Proceedings of Plasma Science.

Scharer, J., Thiyagarajan, M., Luo, S. (2005). Efficient Creation of Laser Initiated, RF Sustained Atmospheric Pressure Range Plasmas. Monterey, California: 32nd International Conference on Plasma Science, IEEE Proceedings of Plasma Science.

Thiyagarajan, M., Scharer, J., Luo, S. (2005). Optical Emission Measurements of Laser Initiated, RF Sustained High Pressure Seeded Plasmas. Monterey, California: 32nd International Conference on Plasma Science, IEEE Proceedings of Plasma Science.

Thiyagarajan, M. (2005). Plasma Decontamination & Sterilization of Biological Agents. Tulsa, Oklahoma: SHPE National Conference.

Luo, S., Thiyagarajan, M., Scharer, J. (2005). RF Matching, Time Resolved Impedance, Power and Interferometer Measurements of Laser Initiated, RF Sustained Atmospheric Pressure Plasmas. Monterey, California: 32nd International Conference on Plasma Science, IEEE Proceedings of Plasma Science.

Thiyagarajan, M., Alexeff, I. (2004). Ambient Pressure Resistive Barrier Cold Plasma Discharge for Biological and Environmental Applications. Baltimore, Maryland: 31st International Conference on Plasma Science, IEEE Proceedings of Plasma Science.

Alexeff, I., Thiyagarajan, M. (2004). An Experimental Model of Ball Lightning. Baltimore, Maryland: 31st International Conference on Plasma Science, IEEE Proceedings of Plasma Science.

Thiyagarajan, M., Alexeff, I. (2004). Bio-Terrorism: Plasma Decontamination & Sterilization of Biological Warfare Agents. Knoxville, Tennessee: Sigma Xi Symposium.

Thiyagarajan, M., Akhtar, K., Scharer, J. (2004). Optical Emission Measurements of Laser Initiated, RF Sustained High Pressure Seeded Plasmas. Baltimore, Maryland: 31st International Conference on Plasma Science, IEEE Proceedings of Plasma Science.

Thiyagarajan, M., Alexeff, I. (2004). Plasma Stealth Antennas – A possible breakthrough in Stealth Technology. London, UK: Signature Management: Pursuit of Stealth conference.

Thiyagarajan, M., Alexeff, I. (2003). A Dual Mode – Steady State Atmospheric Pressure Nonthermal Resistive Barrier Plasma Discharge. San Francisco, California: 56th Gaseous Electronics Conference, American Physical Society.

Thiyagarajan, M., Alexeff, I., Paremswaran, S. (2003). Characteristics of the Steady-State Atmospheric Pressure DC Discharge. Seoul, South Korea: 30th International Conference on Plasma Science, IEEE Proceedings of Plasma Science.

Thiyagarajan, M., Alexeff, I., Parameswaran, S. (2003). Simple Model of an Experimental Ball Lightning. Seoul, South Korea: 30th International Conference on Plasma Science, IEEE Proceedings of Plasma Science.

Journal Articles

Thiyagarajan, M., Scharer, J. (2008). Experimental Investigation of 193 nm Laser Breakdown in Air. (5th ed., vol. 36, pp. 2512 – 2521). IEEE Transactions on Plasma Science.

Thiyagarajan, M., Scharer, J. (2008). Experimental Investigation of UV Laser Induced Plasma Density and Temperature Evolution in Air. (vol. 104, pp. 013303). Journal of Applied Physics.

Luo, S., Scharer, J., Thiyagarajan, M., Denning, M. (2006). Experimental study of laser initiated radiofrequency sustained high pressure plasmas. (6th ed., vol. 34). IEEE Transactions on Plasma Science.

Alexeff, I., Parameswaran, S., Thiyagarajan, M., Grace, M. (2005). An Observation of Synthetic Ball Lightning. (21st ed., vol. 33). IEEE Transactions on Plasma Science.

Thiyagarajan, M., Alexeff, I., Parameswaran, S., Beebe, S. (2005). Atmospheric Pressure Resistive Barrier Cold Plasma for Biological Decontamination. (21st ed., vol. 33). IEEE Transactions on Plasma Science.

Alexeff, I., Parameswaran, S., Thiyagarajan, M., Grace, M. (2004). An experimental study of ball lightning. (3rd ed., vol. 32). IEEE Transactions on Plasma Science.

Non-Refereed

Periodicals

Thiyagarajan, M., Walling, T., Chirinos, F., Chatham, G., Pekshev, A. (2010). Local firm eyes mass production - Technology speeds the healing process, can sterilize surfaces. Corpus Christi, TX: Caller Times. www.caller.com/news/2010/feb/22/plasma/

Research Reports

Thiyagarajan, M. (2010). Plasma Engineering and Science Research - TAMUCC. Engineering Research in Texas.

Thiyagarajan, M. (2010). Experimental Investigation of Air Plasma & Nitrogen Oxide Characteristics of Plasma. (vol. 2010). Texas: Texas Higher Education Coordinating Board.

Thiyagarajan, M., Walling, T., Elias, C. (2010). Report on Experimental Measurements of Spatially Resolved NOX Concentration from Plason Plasma Device. Plasma Technologies.

Presentations

Thiyagarajan, M. (Author & Presenter), Salazar, A. (Author), Gloria, J. (Author), Ramon, R. (Author), "Plasma Assisted Automatic Food Processing Unit," Coastal Bend Business Plan Competition, Coastal Bend Business Innovation Center, Corpus Christi. (December 2010).

Thiyagarajan, M. (Author & Presenter), "Sustainable Energy Research Program on Liquid Fuel Production through Innovative Plasma Processing of Low Ranking Coal," TAMUS - 2012 Federal Initiative Proposals, TAMUS, TAMUCC. (October 25, 2010).

Thiyagarajan, M. (Panelist), Pezold, F. L. (Panelist), Lyle, S. D. (Panelist), Lyle, C., Martin, G., Murphy, O., "SBIR/STTR Panel Discussion," SBIR/STTR Workshop, Coastal Bend Business Innovation Center, Texas A&M University Corpus Christi. (September 24, 2010).

Thiyagarajan, M., "Plasma Research at PERL TAMUCC," Office of Strategic Research Development Team visits the PERL lab, PERL, TAMUCC. (November 24, 2009).

Thiyagarajan, M., "Plasma Research at PERL, TAMUCC," TAMUS Chancellor Dr. Mike McKinney visits PERL Plasma Lab, PERL - TAMUCC. (November 5, 2009).

Thiyagarajan, M., "Plasma Research Overview at PERL," Lieutenant Governor David Dewhurst visits Plasma Lab, TAMUCC, PERL ST 221, TAMUCC. (October 20, 2009).

Thiyagarajan, M., "FI2011 - Plasma Research Proposal," TAMUS Feeral Initiative Team visits PERL Plasma Lab, TAMUCC, PERL, TAMUCC. (October 12, 2009).

Thiyagarajan, M., "Plasma Research at PERL TAMUCC," Drexel University - Technology Team visits Plasma PERL lab, PTI - TAMUCC, PERL TAMUCC. (September 24, 2009).

Contracts, Grants and Sponsored Research

Grant

Thiyagarajan, Magesh (Principal), "Fundamental Research on Electrochemical Effects of Using Non-thermal Non-equilibrium Microwave Plasmas on Low-rank Coal Particles," Sponsored by NSF-DOE, Federal, \$812,594.00.

Thiyagarajan, Magesh (Principal), "Plasma Assisted Microbial Decontamination for Food Product Processing Industries," Sponsored by Research Enhancement Grant, TAMUCC, Texas A&M University-Corpus Christi, \$3,775.00.

Thiyagarajan, Magesh (Principal), "Plasma Engineering Research," Sponsored by TAMUS - 2011 Federal Initiative, Federal, \$1,224,000.00.

Thiyagarajan, Magesh (Co-Principal), Chattam, Gary (Principal), "Universal Atmospheric Contaminant Scrubber for Submersibles," Sponsored by NAVY - Small Business Innovative Research (SBIR), Federal, \$100,000.00.

Thiyagarajan, Magesh (Principal), "Lightweight Portable Plasma Medical Device," Sponsored by DOD - USAMRAA, Federal, \$700,000.00. (September 2010 - September 2013).

Thiyagarajan, Magesh (Principal), "Cold Plasma & NO_x Induced Apoptosis Research on Various Human Cell Structures Aimed for Skin Cancer Treatment," Sponsored by Texas Research Development Fund (TRDF), State, \$25,000.00. (September 2010 - September 2012).

Thiyagarajan, Magesh (Principal), "Experimental Investigation of Air Plasma & Nitrogen Oxide (NO) Characteristics of Plasma Medical Manipulator Using Gas Chromatography and Optical Emission Spectroscopy," Sponsored by Texas Research Development Fund (TRDF), State, \$16,500.00. (December 2009 - September 2011).

Thiyagarajan, Magesh (Co-Principal), Waldbeser, Lillian S (Principal), "The Effect of Non-thermal Plasma on Human Leukemia and Lymphoma Cells," Sponsored by University Research Enhancement Grant, Texas A&M University-Corpus Christi, \$9,000.00. (September 2010 - August 2011).

Thiyagarajan, Magesh (Principal), Chen, Lea-Der (Co-Principal), Tintera, George Dunkin (Co-Principal), Balasubramanya, Mirley (Co-Principal), "Collaborative Research: Improving Student Reflection and Metacognitive Thinking: A Texas Collaborative for Faculty Development (IMRT)," Sponsored by NSF - TUES, Federal, \$64,706.00. (December 2010).

Thiyagarajan, Magesh (Principal), "Sustainable Energy Research Program on Liquid Fuel Production through Innovative Plasma Processing of Low-Ranking Coal," Sponsored by TAMUS - 2012 Federal Initiative, Federal, \$461,000.00. (October 2010 - December 2010).

Thiyagarajan, Magesh (Co-Principal), Um, Dugan (Principal), Karayaka, Hayrettin (Co-Principal), Simionescu, Petru-Aurelian (Co-Principal), "CNS - CISE - Research Experiences for Undergraduates Sites (Computer Sci. & Engg)," Sponsored by NSF - REU, Federal, \$328,665.00. (September 2010 - December 2010).

Thiyagarajan, Magesh (Principal), Tintera, George Dunkin (Co-Principal), Fernandez, John D (Co-Principal), Balasubramanya, Mirley (Co-Principal), "Collaborative Research: Improving Student Reflection and Metacognitive Thinking: A Texas Collaborative for Faculty Development," Sponsored by NSF – CCLI Phase 2, Federal, \$59,932.00. (February 2010 - December 2010).

Thiyagarajan, Magesh (Principal), "Atmospheric Pressure Cold Plasma Source for Teaching - Instructional and Research Applications related to Material Science," Sponsored by Higher Education Fund (HEF), State, \$25,000.00. (January 2010 - July 2010).

Thiyagarajan, Magesh (Principal), "Pre-proposal - Lightweight Portable Plasma Medical Device," Sponsored by DOD (USAMRMC), Federal, \$700,000.00. (2009).

Sponsored Research

Thiyagarajan, Magesh (Principal), "High Voltage Direct Current Large Volume Cold Plasma Source System – Plasma Engineering Research Lab," Texas A&M University-Corpus Christi, \$20,000.00. (August 2009 - September 2009).

Scholarly and Creative Awards and Honors

Outstanding Islander - Texas A&M University Corpus Christi, TAMUCC. (2011).
Best Research Paper Award - "Effects of Plasma Treatment on E. Coli, S. Aureus, N. Meningitidis and Other Clinical Isolates", National SACNAS Conference 2010. (2010).
Coastlines - TAMUCC Monthly Newsletter - Features Plasma Lab Research and Scholarly Activity, Texas A&M University Corpus Christi. (2010).
Campus News - TAMUCC - "Dr. Magesh Thiyagarajan Receives \$700,000 Department of Defense Research Grant for Plasma-Biomedical Engineering Research", Texas A&M University Corpus Christi. (2010).
Texas A&M University Corpus Christi - Facebook Page - Features DOD Research Grant Award for Plasma - Biomedical Engineering Research, TAMUCC. (2010).
The Islander Magazine - Spring 2010 - Dr. Magesh Thiyagarajan and the Plasma Engineering Research Lab is featured in the cover story - Page 14, Texas A&M University Corpus Christi. (2010).
Caller Times - News Paper Features a Cover Story on Research at Plasma Lab, Caller Times News Media. (2010).
QEM Travel Award for NSF-MRI Workshop, Quality Education for Minorities (QEM). (2010).
Who's Who in America - 2010, Marquis Who's Who. (2009).
The Islander Magazine - Fall 2009 - Featured Plasma Engineering Research Lab, TAMUCC. (2009).
Lt. Gov. David Dewhurst visits Plasma Research Lab, TAMUCC. (2009).
Vilas – Dissertator Fellowship Award, Univ. of Wisconsin - Madison. (2008).
Dissertator Travel Fellowship Award, Dept. of Electrical Engineering, Univ. of Wisconsin Madison. (2007).
Vilas – Dissertator Fellowship Award, Univ of Wisconsin - Madison. (2007).
Best Paper Award, SHPE - Society of Hispanic Professional Engineers. (2005).

IEEE - Graduate Fellowship Award, IEEE – NPSS (Institute of Electrical and Electronics Engineering). (2004).
The Citation Award for Professional Promise, University of Tennessee - Knoxville. (2004).
Best Project Award, University of Madras. (2001).

SERVICE

Department

Committee Member, Faculty Search Committee - Assistant Professor of Mechanical Engineering. (January 2011 - Present).
Committee Member, Faculty Search Committee - Associate Professor of Mechanical Engineering. (January 2011 - Present).
Committee Member, Engineering Technology ABET Re-Accreditation Review. (September 2009 - Present).
Attendee, Meeting, Industrial Advisory Board IAB. (October 2010).
Faculty Mentor, SACNAS Conference Booth - TAMUCC - Computing Sciences and Engineering Representative. (September 2010 - October 2010).
Committee Member, Engineering Education Program Coordinator II Search Committee. (August 2010 - September 2010).
Committee Member, Lab Coordinator II – Search Committee. (August 2010 - September 2010).
Committee Member, Engineering Labs and Machine Shop Reorganization. (May 2010 - September 2010).
Faculty Advisor, Brochure Design and Development for Mechanical Engineering and Engineering Technology (EET & MET) Programs. (November 2009 - April 2010).
Committee Member, Faculty Search Committee - Assistant Professor of Mechanical Engineering. (October 2009 - February 2010).
Committee Member, Engineering Technology Curriculum Review. (October 2009 - January 2010).
Committee Member, Faculty Search Committee - Associate Professor of Mechanical Engineering. (October 2009 - January 2010).

College

Faculty Advisor, ASME - Engineering Seminar Series. (October 2010 - Present).
Committee Member, Physics Faculty Search Committee. (September 2010 - Present).
Committee Member, S&T College Scholarship Committee. (August 2009 - Present).
Tour Guide Engineering Research Labs and Facilities, Associate Dean of Engineering Search. (February 2010).

University

Faculty Mentor, Louis Stokes Alliance for Minority Participation (LSAMP) Program. (August 2010 - Present).
Student Org Advisor (Professional Org), ASME-TAMUCC - American Society of Mechanical Engineers - TAMUCC Professional Engineering Chapter. (February 2010 - Present).
Faculty Mentor, McNair Scholars Program. (November 2009 - Present).
Committee Member, South Texas Engineering Alliance. (September 2009 - Present).
Committee Member, TAMUCC & Del Mar Community College Memorandum of Understanding (MOU) – Articulation Agreement for Mechanical Engineering. (July 2010 - January 2011).
Faculty Mentor, TAMUCC Booth - Austin Engineering Expo. (October 2010).
Program Organizer, 1st Coastal Bend Business Plan Competition - 2010. (January 2010 - March 2010).
Attendee, Meeting, CEO Breakfast - TAMUCC Student Research Representative. (March 2010).

Conference-Related, 7th Annual Texas A&M University System Pathways Student Research Symposium - Judge. (November 2009).
Guest Speaker, Community College STEM Conference - PERL Research Demonstration. (October 2009).
Committee Member, Texas A&M University System Engineering Program Meeting, Dallas, TX. (October 2009).

Professional

Committee Member, Del Mar College Engineering and Engineering Technology Advisory Committee. (February 2010 - Present).
Reviewer, Book, Statics and Strength of Materials, Mott, Pearson. (2010 - Present).
Reviewer, Grant Proposal, Coastal Bend Innovation Center. (2009 - Present).
Committee Member, TAMUCC Engineering Summer Camp Judge. (July 2010).
Reviewer, Journal Article, Journal of Optical Communications. (2009).
Committee Chair, General Electric - Newcomers Club. (2008 - 2009).
Reviewer, Conference Paper, 7th Annual TAMU System Pathways Symposium. (November 2009).
Officer, Vice President, IEEE - Madison WI Chapter. (2004 - 2005).

Public

Committee Member, Innovation Academy Mentors. (December 2010 - Present).
Collaborator, Plasma Technologies Inc - Community Entrepreneurial Technology Development and Validation. (July 2009 - Present).
Guest Speaker, Plasma Lab Tour - Victoria County Outreach program. (November 2010).
Guest Speaker, SBIR/STTR Workshop Panel - Coastal Bend Innovation Center. (September 2010).
Guest Speaker, Plasma Lab Tour for Innovation Academy Students. (August 2010).
Member, Coastal Bend Business Plan Competition. (January 2010 - March 2010).
Program Organizer, Coastal Bend Engineering Week Competition. (November 2009 - March 2010).
Committee Member, Science Fair Judge - School of Science and Technology Corpus Christi. (January 2010).
Guest Speaker, IDEA Public School - PERL Research Demonstration. (October 2009).

Service Awards and Honors

Semi-Finalist of the Coastal Bend Business Plan Competition, Coastal Bend Business Innovation Center. (2010).
American Society of Mechanical Engineers Membership Approved, TAMUCC. (2010).
Who's Who in America - 2011, Marquis. (2010).
Panelist - SBIR/STTR Workshop, Coastal Bend Business Innovation Center. (2010).
Best Business-Technology Plan - GE Growth Competition, General Electric Company (GE). (2008).
Best Business Plan Award - Plasma Devices, Burrill Business Plan Contest - Univ. of Wisconsin Madison. (2006).
Best Business Plan Award - Plasma Devices, Wisconsin Governor Business Plan Contest. (2006).

APPENDIX B – MANUSCRIPTS SUBMITTED

Optical breakdown threshold investigation of 1064 nm laser induced air plasmas

Journal of Applied Physics, 2012

We present the theoretical and experimental measurements and analysis of optical breakdown threshold for dry air by 1064 nm infrared laser radiation and the significance of the multiphoton and collisional cascade ionization process on the breakdown threshold measurements over pressures range from 10 Torr to 2.5 atmospheres. Theoretical estimates of the breakdown threshold laser intensities and electric fields are obtained using two distinct theories namely multiphoton and collisional cascade ionization theories. The theoretical estimates are validated by experimental measurements and analysis of laser induced breakdown process in dry air at a wavelength of 1064 nm by focusing 450-mJ max, 6 ns 75 MW max high-power 1064 nm IR laser radiation onto a 20- μm -radius spot size that produces laser power densities up to 3 – 6 TW/cm^2 , well above the threshold power flux for air ionization over the pressures of interest ranging from 10 Torr to 2.5 atm. The measured breakdown threshold laser intensities and electric fields are compared with classical and quantum theoretical ionization models as well as with 193 nm, shorter laser wavelength. A universal scaling analysis of the breakdown threshold measurement results provided a direct mechanism to compare breakdown threshold values over wide range of frequencies ranging from microwave to ultraviolet frequencies. Comparison of 1064 nm laser-induced effective field intensities for air breakdown measurements with data calculated based on the collisional cascade and multiphoton breakdown theories is used successfully to determine the collisional microwave scaled portion. The measured breakdown

threshold 1064-nm laser field intensities are then scaled to classical microwave breakdown theory after correcting for the multiphoton ionization process for different pressures.

^{a)}Electronic address: magesh@tamucc.edu

I. INTRODUCTION

Laser induced plasmas are of significant interests in a large domain of research and industrial applications in the field of science and technology.^{1,2} Laser-produced plasmas are widely used in laser ablation,³ micromachining,⁴ photochemistry,⁵ laser fusion,⁶ flow control,⁷⁻⁹ drag reduction in supersonic and hypersonic flows,^{10,11} ignition of combustion gases,¹² thrusters in space applications,¹³ and laser-initiated switching applications.¹⁴ This paper examines the air breakdown threshold by multiphoton and cascade ionization process at 1064 nm infrared (IR) wavelength laser radiation over a wide pressure ranges and the results are compared with previously published air breakdown threshold measurements carried out at microwave frequencies and at 193 nm ultraviolet (UV) wavelength.¹⁵

Laser-induced breakdown can be described as the formation of an ionized gas or plasma during or by the end of the laser pulse. The experimental condition that is usually used is the detection of a glow or flash in the focal region for 10%–50% of the laser firings.¹⁶ As described by Raizer,¹⁶ the photon-initiated electron cascading plasma process initiates when a pulsed laser beam is focused to a small volume, which produces a very sudden temperature rise in the medium at that point. If the electric field of the laser radiation in the focal region becomes greater than that of the binding electrons to their nuclei, it will trigger breakdown of the air molecules and produce ionization of the gas. Following the initial breakdown cascade effect takes place due to the increased plasma density and the medium becomes opaque to the laser

beam leads to further energy absorption. During the rising phase of the laser pulse, primary and secondary electrons are created by several mechanisms, such as, multiphoton ionization (MPI),¹⁷⁻¹⁹ free electrons in the air at room temperatures, and the inverse bremsstrahlung absorption or cascade ionization process, which corresponds to an ionizing collisional cascade (CC) evolution.^{20,21}

For the MPI process, a neutral atom absorbs enough laser photons within a quantum lifetime of the excited state¹⁸ [$\tau \approx h/\epsilon_\gamma = 3.5 \times 10^{-15}$ s (at 1064 nm)] to raise it from the ground state to the ionization level or above. When enough atoms are ionized, it can produce an observable flash.¹⁸ For a cascade ionization process, a few initial electrons in the breakdown region are required, which could be created by a process such as MPI of the gas species or the presence of dust or the creation of electrons at the ambient gas temperature. These electrons then gain energy by absorbing laser energy and undergoing elastic collisions with neutral atoms. After accumulating energy slightly higher than the ionization potential of the gas, the electron may ionize an atom by inelastic collisions producing two electrons of low energy; these are then available for the process to be repeated.²¹

These two ionization mechanisms, Multiphoton ionization and Collisional Cascade ionization, differ fundamentally and are described by different theories that are necessary to understand the experiments at 1064 nm with higher laser energies otherwise stated higher photon flux in comparison with previously reported 193 nm UV laser breakdown experiments.¹⁵ In the previous 193 nm UV laser breakdown threshold study, a 180-mJ, 20 ± 2 ns, 10 MW UV laser beam with a photon flux of 1.75×10^{17} photons per pulse was focused to a 30- μ m spot size to create optical breakdown.¹⁵ In this paper, we report measurements and analysis of 1064 nm IR laser breakdown threshold experiments in which a 450-mJ, 6-ns laser beam with a photon flux of

$1.3 - 2.4 \times 10^{18}$ photons per pulse was focused to a $20\text{-}\mu\text{m}$ spot size to create optical breakdown. It was reported that the photon energy of the 193 nm laser is 6.42 eV suggesting approximately 3 photons to be absorbed within the photon excitation life time of 6.5×10^{-16} seconds for ionization of air with an ionization energy of 15.6 eV further illustrating the significance of multiphoton ionization at the 193 nm UV laser radiation.¹⁵ Similar theory is extended to the 1064 nm, in which the photon energy of the 1064 nm laser is 1.165 eV suggesting approximately 14 photons to be absorbed within the photon excitation life time of 3.5×10^{-15} seconds for ionization of air. It shows that, for the multiphoton ionization of air at 1064 nm it requires approximately 5 times more ($5\times$) photons than at 193 nm, however the photon excitation life time is 6 times longer ($6\times$) at 1064 nm than at 193 nm suggesting a potential contribution of multiphoton ionization even at 1064 nm in addition to the cascade collisional ionization process at varied pressures especially at low collision or collision less pressures. In general, the cascade theory best describes the breakdown at high pressures (>100 torr) and long laser pulse lengths (>10 ns). On the other hand, the MPI theory alone should best describe the breakdown at lower pressures, in the millitorr regime where the electrons are more collision less, and for shorter pulse lengths (<1 ns) where the cascade process cannot develop.²¹

We report measurements and analysis of air breakdown processes, in this paper, by focusing a 1064 nm 250-450-mJ, 6 ns, 42 – 75 MW high-power IR laser radiation onto a $20\text{-}\mu\text{m}$ -radius spot size ($r = f\alpha/2$, where $f = 4$ cm is the focal length and $\alpha = 1$ mrad is our laser beam divergence) that produces laser power densities up to $3 - 6 \text{ TW/cm}^2$, well above the CC threshold power flux for air ionization at this wavelength that is 10^{10} W/cm^2 .²² The breakdown threshold is measured and compared utilizing classical²³ and quantum theoretical ionization models.^{17,18} The measurements and analysis of the 1064 nm infrared laser induced optical

breakdown results extended to photon energies (eV), multiphoton ionization threshold intensities (W/cm^2) for corresponding photon excitation lifetimes (seconds), collisional cascade laser breakdown threshold intensities (W/cm^2), breakdown electric field and effective electric field and compared with 193 nm ultraviolet laser radiation. In addition, our investigation of the breakdown threshold field intensities for air using 1064 nm laser radiation is extended to correlate the corresponding threshold field requirements by using high-power microwave radiation by means of “universal plot”.^{23,24} A universal scaling analysis of these results allows one to predict aspects of high-power microwave air breakdown based on measured laser breakdown observations. The high-power microwave breakdown threshold has been investigated experimentally and computationally.

The theoretical air breakdown threshold estimation for 1064 nm at 760 Torr in comparison with 193 nm are presented in Section II, the experimental and diagnostics setup are presented in Section III, experimental results are discussed in Section IV, and a summary is presented in Section V.

II. THEORETICAL AIR BREAKDOWN THRESHOLD ESTIMATION

A. Multiphoton ionization

The breakdown threshold based on the quantum MPI processes is derived by Nelson.^{17,25} In MPI, a neutral atom absorbs enough laser photons within the quantum excitation lifetime to raise it from the ground state to the ionization level or above. If enough atoms are ionized, it may produce a visible flash.²¹ The interaction laser intensity threshold I_0 is written in terms of flux density as

$$I_0 = h\nu c N_0, \quad (1)$$

with $N_0 = 2(2\pi)^3 \times 137 \times (1/\lambda)^3$. Therefore, the breakdown threshold laser intensity can be defined as

$$I_{B(\text{MPI})} = S I_0, \quad (2)$$

where S is the MPI coefficient, which is the ratio of ionization potential, U_i , of the gas (15.6 eV for air)^{23,24,26} to the photon energy, ε_γ , of the laser beam ($\varepsilon_\gamma = 1.24/\lambda$ (eV), where λ is the vacuum wavelength in micrometers). With $\varepsilon_\gamma = 1.165$ -eV photon energy for the 1064 nm laser radiation, it requires approximately $S = 14$ photons to be absorbed within the quantum excitation lifetime $\tau \approx h/\varepsilon_\gamma = 3.5 \times 10^{-15}$ s in order to ionize the air molecules. Thus, the breakdown laser intensity threshold value for 760-torr air at 1064 nm laser radiation is $I_{B(\text{MPI})} = 4.42 \times 10^9$ W/cm². The corresponding rms breakdown electric field is obtained from¹⁶

$$E_{B(\text{MPI})} = 1.94 \times 10^4 \sqrt{I_{B(\text{MPI})}} \quad \text{m}, \quad (3)$$

where $I_{B(\text{MPI})}$ is expressed in MW/cm² and we obtain $E_{B(\text{MPI})} = 1.3 \times 10^6$ V/cm.

Similarly, it was reported that the multiphoton ionization theory was applied to 193 nm laser radiation in which a 6.42-eV photon energy requires $S = 3$ photons to be absorbed within the quantum excitation lifetime $\tau \approx h/\varepsilon_\gamma = 6.5 \times 10^{-16}$ s in order to ionize the air molecules and the estimated laser intensity threshold value for 760-Torr air at 193 nm laser radiation was reported as $I_{B(\text{MPI})} = 8.73 \times 10^{11}$ W/cm²,¹⁵ which is approximately two orders of magnitude higher compared to that of 1064 nm. The corresponding rms breakdown electric field at 193 nm was reported as $E_{B(\text{MPI})} = 18 \times 10^6$ V/cm,¹⁵ which is an order of magnitude higher compared to that of 1064 nm estimates. It is evident that, it requires lesser laser intensity at the focal volume

for a 1064 nm laser compared to a 193 nm laser in order for an optical breakdown formation as the breakdown threshold intensity I_B is inversely proportional to the cube of the laser wavelength for the multiphoton ionization process.

B. Collisional cascade ionization

The theory of Collisional Cascade (CC) ionization phenomena in air was reviewed by Kroll and Watson,¹⁸ based on the data obtained by MacDonald.²³ In the cascade ionization process, a few initial free electrons are assumed to be present in the focal region, and these electrons then gain energy by absorbing laser energy upon elastic collisions with neutral atoms. After a cascade that accumulates energy slightly higher than the ionization potential of the gas, the electron may ionize an atom by inelastic collisions producing two electrons of low energy; these are then subjected to the collisional process and are repeated. If enough atoms are ionized within the laser pulse period, breakdown is observed as a bright spark.¹⁸ Based on this theory, the threshold power flux for breakdown is given by¹⁸

$$I_{B(CC)} = 1.44 \times 10^6 (p^2 + 2.2 \times 10^5 \lambda^{-2}) \text{ W/cm}^2, \quad (4)$$

where p is the pressure in atmospheric pressure units and λ is the radiation wavelength in micrometers. Although this theory is primarily based on observations at microwave frequencies, and as well as pressures below atmospheric conditions, it can also be scaled to 1064 nm-wavelength laser frequencies.²⁴ Assuming that there are no dust particles ($r \sim 1\text{--}2 \mu\text{m}$) nor significant water vapor in the air the cascade ionization theory predicts a breakdown flux intensity threshold value for 1064 nm wavelength of $I_{B(CC)} = 2.8 \times 10^{11} \text{ W/cm}^2$ corresponding to $E_{B(CC)} = 10.3 \times 10^6 \text{ V/cm}$.

Similarly the collisional cascade microwave breakdown theory was also extended to previously published 193 nm laser breakdown of air at 760 Torr and the estimated breakdown flux intensity threshold value was reported to be of $I_{B(CC)} = 8.5 \times 10^{12} \text{ W/cm}^2$ corresponding to $E_{B(CC)} = 56 \times 10^6 \text{ V/cm}$, at 760 Torr air and assuming that there are no dust particles ($r \sim 1\text{--}2 \mu\text{m}$) nor significant water vapor in the air.¹⁵ These breakdown threshold estimates at 193 nm is approximately one order of magnitude higher compared to that of 1064 nm. It is evident that, it requires lesser laser intensity at the focal volume for a 1064 nm laser compared to a 193 nm laser in order an optical breakdown formation as the breakdown threshold intensity I_B is inversely proportional to the square of the laser wavelength for the collisional cascade ionization.

Based on the breakdown threshold electric field estimates, it can be inferred that for an optical breakdown of air at 760 Torr using 193 nm laser radiation the multiphoton ionization process contributes to approximately 25% of the total breakdown threshold and the remaining 75% is contributed by the collisional cascade ionization process whereas by using the 1064 nm laser radiation the multiphoton ionization process contributes to approximately 10% of the total breakdown threshold and the remaining 90% is contributed by the collisional cascade ionization process. These MPI contributions at 1064 nm can be further higher at lower pressures where collisions are low, which is of interest in this paper.

The Fig. 1. illustrates the comparison of the breakdown threshold estimates of the 1064 nm and 193 nm laser radiations based on the collisional cascade microwave breakdown theory for a wide range of pressures in a universal plot of effective electric field plotted as a function of pressure normalized by diffusion lengths. In this case, the estimated values for 193 nm is obtained with a diffusion length of $12 \mu\text{m}$ ¹⁵ and for 1064 nm the experimental diffusion length is of $8 \mu\text{m}$. The solid line in Fig. 1. is the classical microwave breakdown theory for 2.8 GHz with

a diffusion length of 0.2 cm^{23} and the region of interest and study for this paper is highlighted in the graph representing the pressure regime of interest, ranging from 10 Torr to 2000 Torr (~ 2.5 atmospheres). It can be observed that the trend of breakdown threshold as a function of pressure for 1064 and 193 nm for dry air are similar for vacuum pressures and up to 100-125 atmospheres, and beyond which the significant differences in the trend can be observed.

III. EXPERIMENTAL SETUP

The schematic diagram of the experimental setup is shown in Fig. 2. In this experiment, a pulsed Nd:YAG laser (Spectra-Physics, Indi 40), with a 1st harmonic at $\lambda = 1064 \text{ nm}$, 1.165 eV per photon and a 2nd harmonic at $\lambda = 532 \text{ nm}$, 2.33 eV per photon is used. The laser output is a circular beam of 1-cm cross section diameter with Gaussian distributed beam intensity and 1.0 mrad beam divergence. The full-width at half maximum (FWHM) of the laser pulse is $6 \pm 1 \text{ ns}$, with a 1-ns rise/fall time and a maximum available laser output energy of 450 mJ at 1-20 Hz rep rate. The laser outputs both 1st and 2nd harmonic laser beams simultaneously and in order to study the infrared laser induced plasma the 532 nm 2nd harmonic crystal generator was detuned and a dichromatic mirror separates any minimal 532 nm laser output from the 1064 nm pump laser. The laser output beam energy is controlled using a variable attenuator and each laser pulse is sampled through an IR beam sampler and the laser output energy is measured using laser energy meter (Coherent, FieldMax II). In this experiment, all IR optical components are specially coated, with 98% transparency at 1064 nm. The IR beam is then reflected by a high damage threshold (20 J/cm^2) IR coated kinematic mirror (TECHSPEC) in order to obtain a top-down configuration for the IR beam to enter the plasma chamber. The 1-cm-diameter IR beam is then

passed through a 1064 nm transmission coated 3-cm-diameter Zinc Selenide window. The laser beam was focused by using a high-power handling (500 MW/cm^2) objective lens mounted inside the plasma chamber. The objective lens (Thorlabs, LMH-5X-1064) has an effective focal length of 40-mm, with a 10-mm entrance aperture and a 0.13 NA. Due to its short focal length, the objective lens is mounted inside the plasma chamber using an adjustable length holder, so that the laser-induced plasma will be positioned at the cylindrical chamber air and visible through side windows for diagnostics. The space between the entrance IR window and the objective lens is maintained at the same pressure as that of the chamber pressure in order to avoid differential pressures acting on the objective lens. Great care was taken to position the objective lens together with the plasma chamber precisely in the line of sight with the IR laser beam. In addition, using the laser energy meter, it is found that the laser beam experiences a 5% loss as it passes through the coated IR optics, including the attenuator, beam sampler, mirrors and windows. The laser energy available immediately after the objective lens corresponding to a $300 \pm 5 \text{ mJ}$ laser output was measured by the Coherent FieldMax II energy meter to be $285 \pm 5 \text{ mJ}$, corresponding to the measured incident laser energy on the focal spot, in agreement with the analytical estimate. A high-speed ($< 2\text{-ns}$ rise time) visible photodetector (Thorlabs, DET10A/M) mounted with collection optics is used to detect and observe the laser breakdown visible spark. The photodetector is connected to a high speed 2.5 GS/S oscilloscope to monitor the laser induced plasma emission. The plasma chamber was made from stainless steel and flushed several times before finally filling with dry air ($< 10 \text{ ppm}$ water) to the desired pressure ranging from 2000 Torr to 100 mTorr. Optical view ports on both sides of the cell are made of 3-cm-diameter by 5-mm-thick sapphire windows. The view ports enabled observation of the interior at right angles to the cell axis which is coincident with the direction of the laser beam, as well as for

diagnosing the plasma. The chamber pressure was measured precisely by a pressure gauge with a pressure controller–readout (MKS Instruments, 910-11 and PDR 900-11). The gas flow through the chamber was regulated by a needle valve in the gas line and another valve in the pumping line. For one set of experiments on determining the effects of removing micro dust particles of diameters $\geq 0.1 \mu\text{m}$ on the breakdown threshold of dry air, we have inserted a filter capsule in the incoming gas line and cleaned residual dust on window and lens surfaces by means of an aerosol jet. The filter houses a dual-pleated polytetrafluoroethylene (PTFE) filtering element with $\leq 0.1\text{-}\mu\text{m}$ pore size.

IV. EXPERIMENTAL MEASUREMENTS, RESULTS, AND DISCUSSION

In general the breakdown threshold is defined as the minimum laser energies or intensities at which 10-50% of the laser pulses resulted in a visible optical breakdown.²⁴ Similarly, in this experimental study, the breakdown threshold is defined as the minimum laser intensity at which the air breakdown with a visible spark is observed for 50% of the laser pulses. The occurrence of breakdown was detected by observing a visible spark at a right angle to the laser beam direction using a high-speed (<2-ns rise time) visible photodetector (Thorlabs, DET10A/M) while gradually increasing the intensity for each laser pulse. The measurements were made in dry air (< 10-ppm water) at room temperature. The primary measurement is the incoming laser energy with the corresponding intensity at the focal spot and is then calculated. In this paper, the focal length f of the objective lens used is 4.0 cm, and the diameter d of the unfocused laser beam used is 1.0 cm, with a laser beam divergence α of 1.0 mrad. Following standard optical focal theory, the minimum focal volume is assumed to be cylindrical²⁴ with a

corresponding radius of $r_0 = f\alpha/2 = 20 \mu\text{m}$ and an axial length (depth of focus) of $l_0 = 0.414 (\alpha/d)f^2 = 66 \mu\text{m}$. The characteristic diffusion length is obtained by^{23,24,27}

$$\left(\frac{1}{\Lambda}\right)^2 = \left(\frac{\pi}{l_0}\right)^2 + \left(\frac{2.405}{r_0}\right)^2, \quad (5)$$

which yields a value of $\Lambda = 8 \mu\text{m}$. This value for plasma diffusion length is close to the $2r_0/6 - (\mu\text{m})$ value used in previous longer wavelength (10.6- μm) air breakdown laser experiments.²⁸ Another aspect when comparing the pulsed 1064 nm laser breakdown data to the steady-state continuous wave (CW) microwave breakdown case is that, although the laser energy is pulsed (6 ns), there are many oscillations (1.7×10^6 cycles) in the electric field within a single pulse. The threshold breakdown in air using a focused laser radiation is independent of pulse length and can be treated as if in steady state if the number of cycles contained within the pulse is more than 10^6 .²⁴ The breakdown threshold laser intensity at the focal minimum is determined by

$$I_B = \frac{1}{\pi} \left(\frac{W_B}{r_0^2 \tau_p} \right), \quad (6)$$

where W_B is the minimum laser pulse energy at which the breakdown is observed, r_0 is the focal spot radius, and τ_p is the FWHM of the laser pulse. In our experiment, we have measured the breakdown threshold for air at pressures ranging from 10 to 2000 torr (~ 2.5 atm). Fig. 3. shows the measured breakdown threshold energies W_B (mJ) and from which the derived breakdown threshold laser intensities I_B (W/cm^2) for different pressures. The 1064 nm I_B value for dry air at 760 Torr was measured to be $2 \times 10^{11} \text{ W}/\text{cm}^2$, which is close to the theoretical estimates. It is evident that at laser frequencies, higher energies are required at low collisional pressures than at higher collisional pressures. From I_B , the breakdown threshold electric field E_B is determined using $E_B = 1.94 \times 10^4 \sqrt{I_B}$ with I_B is in MW/cm^2 . In Fig. 4., the solid squares show the measured

breakdown electric field in air for various pressures. The E_B value for dry air at 760 torr was measured to be 8.8×10^6 V/cm, which is close to the theoretical estimates, and it is observed that E_B decreases for pressures ranging from 10 torr to 2.5 atm, which is expected in our regime where the laser frequency ω is much higher than the electron collision frequency ν_c ($\omega \gg \nu_c$). It indicates that for such high-frequency wave fields, there are many oscillations of the electric field per collision. It is therefore convenient to make use of the concept of effective electric field for energy transfer. The effective electric field appears in the form^{23,24}

$$E_{\text{eff}} = E_B \left(\frac{\nu_c^2}{\nu_c^2 + \omega^2} \right)^{1/2}. \quad (7)$$

The effective electric field represents the effectiveness of the electric field in coupling its energy to the electron with the field multiplied by the factor $(\nu_c^2/(\nu_c^2 + \omega^2))^{1/2}$. For our experimental conditions, $\omega/\nu_c \gg 1$, and thus

$$E_{\text{eff}} \approx E_B \left(\frac{\nu_c}{\omega} \right). \quad (8)$$

The electron collision frequency is determined by $\nu_c = \beta \times 10^9 p$, where p is in torr.^{23,24,26} The parameter β depends on the gas used, with a value of 5.33 for air data. The effective electric field E_{eff} is shown in Fig. 4. (solid circles) as a function of pressures ranging from 10 torr to 2.5 atm, and it is observed to increase within the pressure range, which means that the effectiveness of energy coupling through electron collisions is higher above atmospheric pressures when compared to partial vacuum conditions.

It has been observed by Stricker²⁴ that, at 1.064- μm laser wavelengths, for gas pressures above few hundred Torr and for pulse lengths in the 10^{-9} -s range, gas breakdown is best described by the cascade ionization processes.²¹ However, at lower pressures the 1064 nm laser wavelength

laser radiation can also play a role through multiphoton ionization. Using the concept of effective electric field, the comparison of 1.06- μm laser-induced breakdown data for air with scaled calculations based on the CC theory was done effectively when compared with microwave data and shows good agreement.²⁴ The laser-induced breakdown data are effectively compared with the microwave data using a universal plot that has $E_{\text{eff}}\Lambda$ as the ordinate plotted as a function of $p\Lambda$. The 2-D universal plot represents all four laser breakdown parameters including pressure, frequency, diffusion length, and electric field.

The experimental values of $E_{\text{eff}}\Lambda$ obtained from our measured dry-air breakdown data without any gas filters are compared with typical microwave CW data for air is shown in Fig. 5. The solid curve shows the typical microwave CW data at 2.8 GHz with 0.2 cm diffusion length and the dashed curve shows the classical cascade breakdown theory [equation (4)] extended to 1064 nm laser radiation wavelength. According to this theoretical result, the breakdown threshold for air at 1064 nm-wavelength radiation converges with the microwave breakdown data at above atmospheric pressures and deviates significantly for very low pressures. However, for low pressures, the medium becomes less collisional, and the MPI process will dominate over the collisional breakdown process, although the MPI process is a weak function of pressure $p^{-1/3}$.²⁷ In Fig. 5, the triangles show the measured breakdown data for air from 10 torr to 2 atm. In order to compare it with the collisional microwave breakdown, the 1064 nm laser-induced breakdown data, where MPI processes play a role at lower pressures, a correction for the MPI process as a function of pressure is necessary. From the measured breakdown data, the portion of MPI effects as a function of pressure $p^{-1/3}$ is eliminated by correcting with a multiplicative factor $E_B \times [(E_{B(CC)}(p) + E_{B(MPI)}(p))/E_{B(CC)}(p)]$, where the terms are given by Eqs. (3) and (4) as a function of pressure, and the results are shown by circles in Fig. 5. The corrected CC data shift to

a much higher value at lower pressures where the MPI process is significant compared to that in higher pressures where collisional processes dominate. This means that a higher electric field is required in order to obtain breakdown at lower pressures without the influence of MPI processes. The breakdown threshold values were then multiplied by a scaling factor of 2.1 in order to scale with the microwave breakdown plot to examine the overall trend of the data as pressure is varied. The scaled data are shown by squares in Fig. 5. Similar scaling values were used in 1.06- μm laser breakdown experiment at above atmospheric pressures (1 – 50 atm) in order to compare the scaled results with microwave breakdown data. In which the multiphoton ionization process was ignored due to the high collisional pressures and dominating collisional cascade ionization process. In our case sub-atmospheric pressures are studied and the 2.1 scaling factor can also be due to the fact that larger spatial wavelength averages of the microwave breakdown data are on the order of several centimeters, whereas the localized laser focus diameter is 20 μm . Another possibility for the factor is the presence of microscopic dust particles on the order of several micrometers in size, which has been shown to reduce breakdown for shorter laser wavelengths but does not influence the longer wavelength microwave breakdown.²⁸ In order to investigate the effect of dust on the breakdown threshold, consequently, on the scaling factor, we have carried out a set of similar breakdown threshold measurements with a 0.1- μm dual-pleated PTFE filter inserted in the incoming gas pipeline. In laboratory air, the average size of dust particles is about 1–2- μm diameter,²⁸ and therefore, filtering dust particles of 0.1 μm or larger diameter will rid our system of them if present. The result of the breakdown threshold measurements as a function of pressure range from 10 torr to 2.5 atm is shown in Fig. 6. With the filter present, the minimum pressure at which the breakdown was observed is 15 torr, whereas without the filter, the minimum breakdown pressure is 10 torr. As expected, the breakdown threshold for dry air as a

function of pressure increases somewhat at lower pressures with the 0.1- μm filter. After correcting for the MPI process from the measured breakdown threshold values (triangles) that are then given by circles, we then multiply the result by a scaling factor of 1.74 in order to fit the measured data with the microwave breakdown curve, as shown in solid squares. It is evident that the presence of dust particles does play a role in the breakdown threshold values at lower pressures, as observed in our case. The scaling factor can also be attributed to the wide differences in frequencies between the microwave and laser frequencies. The resulting IR laser pressure scaling agrees well with the average microwave curve. In our experiment, the overall pressure variation of the scaled data is in good agreement with the classical microwave breakdown results. It should also be noted that the microwave cascade curve is an average and subject to a range variation about the plotted values. The important aspect is that the pressure scaling of laser and microwave cases is similar over a wide range of pressures, as well as at lower pressures where a correction of the MPI process is necessary.

The measured 1064 nm optical breakdown threshold electric fields and corresponding effective electric fields for pressures range from 10 Torr to 2.5 atm is compared with the 193 nm laser breakdown measurements in Fig. 7. It can be observed that the breakdown electric field required for air breakdown in the pressure regime of interest at 1064 nm is approximately an order of magnitude less than that of at 193 nm. The effective electric fields for both laser wavelengths appear very close suggesting that for the same amount of effective coupling of the laser energy on to medium (gas) it requires less amount of laser intensity when an infrared 1064 nm laser radiation is used compare to an ultraviolet 193 nm laser radiation.

V. SUMMARY

The theoretical estimates of the 1064 nm air breakdown threshold laser intensities and breakdown electric fields are obtained using multiphoton ionization and collisional cascade ionization theories at 760 Torr and at other pressures and compared with breakdown threshold estimates for 193 nm laser radiation. Based on the multiphoton ionization theory the estimated breakdown threshold for 1064 nm laser intensity at 760 Torr is $I_{B(MPI)} = 4.42 \times 10^9 \text{ W/cm}^2$ and the estimated breakdown threshold electric field is $E_{B(MPI)} = 1.3 \times 10^6 \text{ V/cm}$. Based on the estimates it is observed that the breakdown threshold estimates for 1064 nm is one or two orders of magnitude lower in comparison with breakdown threshold estimates for 193 nm. This observation of low breakdown threshold at 1064 nm is explained through several aspects, including the longer photon excitation lifetimes to absorb the required number of photons, inverse proportional relationship between the breakdown threshold intensities and electric fields with laser wavelength powers. It is estimated that, for the 1064 nm laser breakdown at 760 Torr, multiphoton ionization process contributes to ~10% and collisional cascade ionization process contributes to the remaining ~90% of the total ionization mechanism.

The theoretical breakdown threshold estimates are validated by 1064 nm experimental laser breakdown threshold measurements. A 250-450-mJ, 6 ns, 42 – 75 MW high-power 1064 nm Nd:YAG laser with 1 cm beam diameter and 1.0 mrad beam divergence is focused onto a 20- μm -radius spot size in dry-air using an objective lens for pressures ranging from 10 torr to 2.5 atm, where multi-photon and CC processes are significant, have been carried out. The breakdown threshold laser energies for various pressures are measured and from which the corresponding laser breakdown threshold intensities, breakdown electric fields and effective electric fields are obtained. The measured breakdown threshold field intensities are scaled to the classical

microwave theory by correcting for MPI processes at various pressures. The MPI processes were observed to be dominant at pressures below 100 torr where the plasma is less collisional, whereas the cascade ionization process dominates for pressures above 100 torr up to 2.5 atm. Based on the breakdown measurements and comparing with the classical and quantum theories, 88% of the total ionization mechanism is carried out by the cascade ionization process, and 12% of the ionization process is carried out by the MPI process at $p = 760$ torr. The MPI-corrected measured breakdown threshold data were scaled and fitted the CC microwave breakdown measurement pressure variation well. A scaling factor of 2.1 is used to scale the 1064 nm breakdown threshold data after correcting multiphoton ionization process on to the classical microwave breakdown theory. The effect of the presence of sub-micron particles on the breakdown threshold was carried out with 0.1- μm filtered air and the measurements show that slightly higher breakdown field is required especially at lower pressures and in close agreement with microwave measurements when scaled with a scaling factor of 1.74, indicating that small sub-micron dust particles can reduce breakdown threshold at laser wavelengths.

ACKNOWLEDGEMENTS

This work was partially supported by the College of Science and Engineering at the Texas A&M University-Corpus Christi, Texas Research and Development Fund (TRDF) and the Department of Defense (DOD)/Army grant (W81XWH-10-1-0923) administered by the U.S. Army Medical Research & Materiel Command (USAMRMC) and the Telemedicine & Advanced Technology Research Center (TATRC), at Fort Detrick, MD. The authors would like to thank Uma Magesh and Kenneth Williamson for assistance.

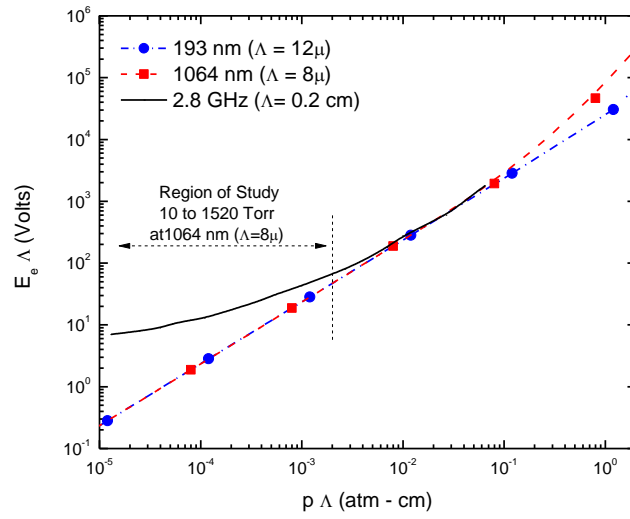


FIG. 1. Universal plot of microwave breakdown theory at 2.8 GHz with $\Lambda = 0.2$ cm (solid line) extended to laser breakdown at $\lambda = 1064$ nm with $\Lambda = 8$ microns (square, dash) and $\lambda = 193$ nm with $\Lambda = 12$ microns (circles, dash-dot-dash).

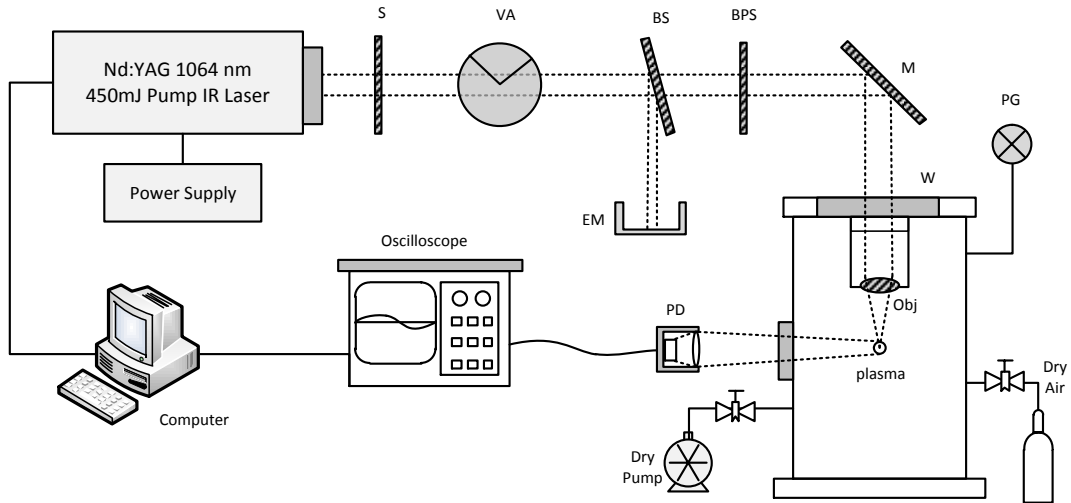


FIG. 2. Schematic of the experimental and diagnostic setup of 1064 nm laser-induced air plasma. S – Shutter. VA – Variable Attenuator. BS – Beam Sampler. EM – Energy Meter. BPS – Beam Profile Sampler. M – Mirror. W – Window. PG – Pressure Gauge. Obj – Objective Lens. PD – Photo Detector.

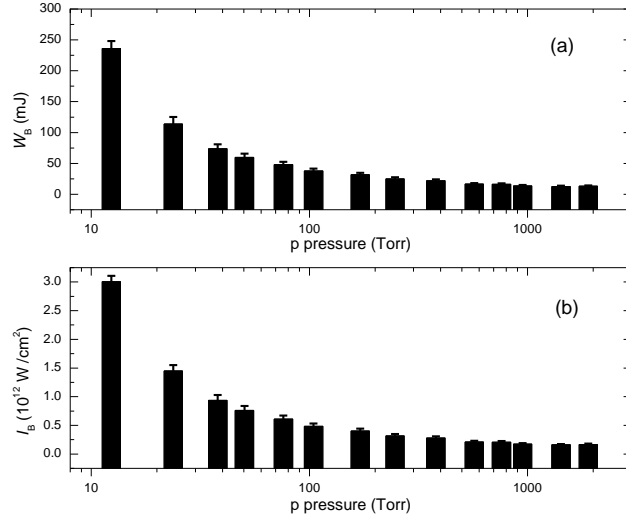


FIG. 3. Breakdown threshold measurement results. (a). Measured 1064 nm air breakdown threshold laser energies as a function of pressure. (b). Breakdown threshold 1064 nm laser power intensities at the focal volume derived from breakdown threshold laser energy as a function of pressure.

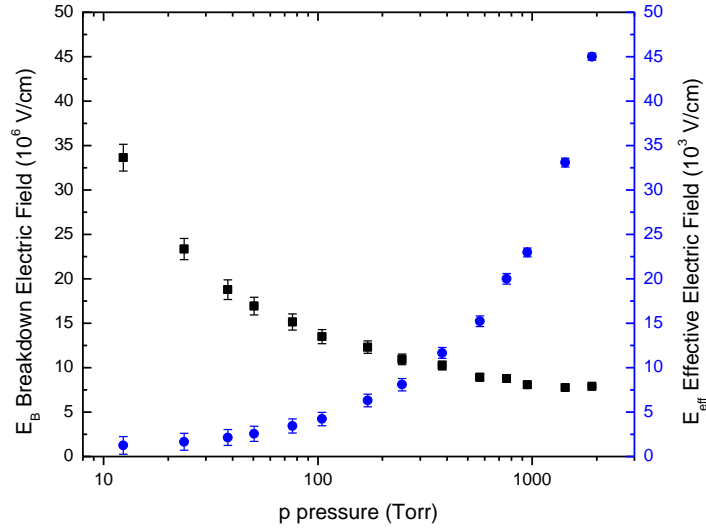


FIG. 4. Measured breakdown threshold electric field E_B and effective electric field E_{eff} plotted as a function of pressure p in Torr.

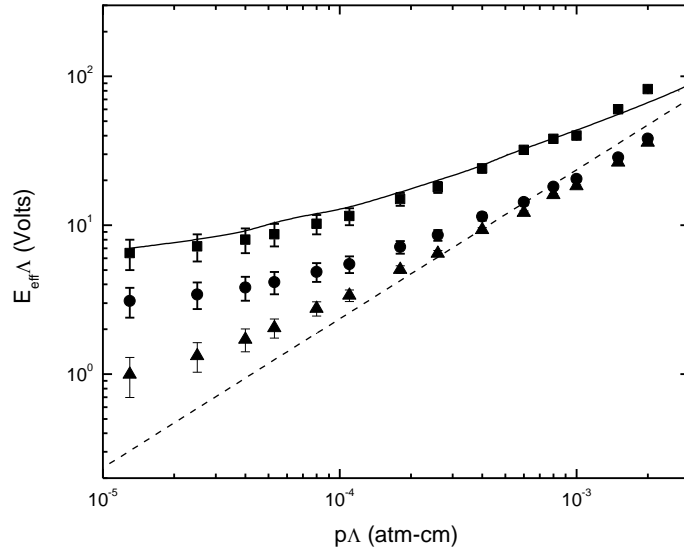


FIG. 5. Universal plot of (triangles) experimental 1064-nm laser breakdown threshold fields in dry air (without gas filter) compared with (solid line) microwave theory. (Dotted line) Microwave theory extended to $\lambda = 1064$ nm. (Circles) MPI-corrected breakdown threshold data. (Squares) Data in circles scaled by a factor of 2.1.

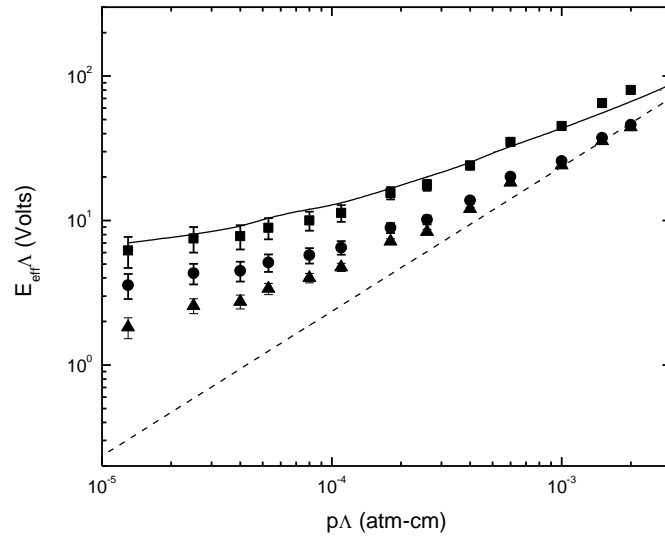


FIG. 6. Universal plot of (triangles) experimental 1064-nm laser breakdown threshold fields in dry air (with 0.1- μm filter) compared with (solid line) microwave theory. (Dotted line) Microwave theory extended to $\lambda = 1064$ nm. (Circles) MPI-corrected breakdown threshold data. (Squares) Data in circles scaled by a factor of 1.74.

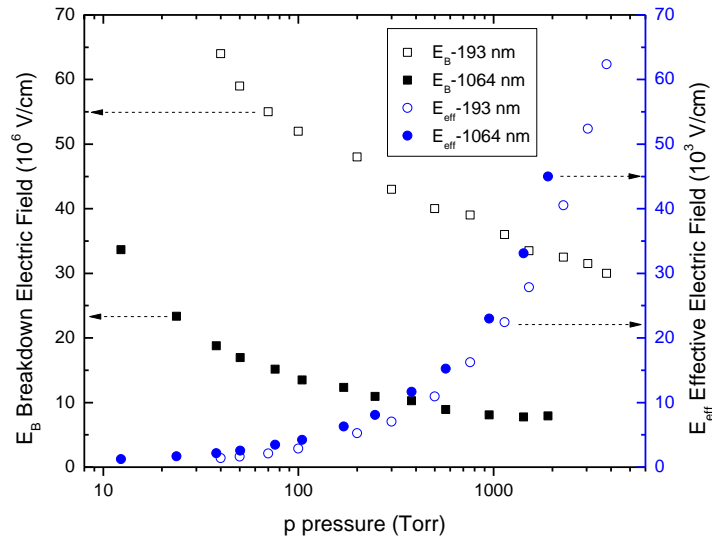


FIG. 7. Measured 1064 nm laser air breakdown threshold electric fields (solid squares) and effective electric fields (solid circles) in comparison with measures 193 nm laser air breakdown threshold electric fields (line squares) and effective electric fields (line circles).

REFERENCES

- 1 C. Phipps, Laser Ablation and Its Applications, 1 ed. (Springer-Verlag, NEW York, 2006).
- 2 C. A. David, Lasers-Induced Plasmas and Applications (CRC Press, Boca Raton, FL, 1989).
- 3 A. N. Panchenko, M. A. Shulepov, A. E. Tel'Minov, L. A. Zakharov, A. A. Paletsky, and N. M. Bulgakova, Journal of Physics D: Applied Physics 44 (2011).
- 4 T. T. Mon, K. F. Muhammad, A. H. Ahmad, and Z. Mohid, in Experimental micromachining of silicon with Nd-YAG laser, Malaysia, 2011 (Trans Tech Publications), p. 244.
- 5 P. G. Ashmore, Photochemistry and reaction kinetics (Cambridge Univ. Press, London, 1967).
- 6 P. U. Andersson and L. Holmlid, Journal of Fusion Energy, 1 (2011).
- 7 R. G. Adelgren, G. S. Elliott, and J. B. Crawford, AIAA Journal 43, 776 (2005).
- 8 R. G. Adelgren, H. Yan, G. S. Elliott, D. D. Knight, T. J. Beutner, and A. A. Zheltovodov, AIAA Journal 43, 256 (2005).
- 9 D. W. Riggins and H. F. Nelson, AIAA Journal 38, 723 (2000).

- 10 L. N. Myrabo, Y. P. Raizer, M. N. Shneider, and R. Bracken, *High Temperature* 42, 901 (2004).
- 11 D. Riggins, H. F. Nelson, and E. Johnson, *AIAA Journal* 37, 460 (1999).
- 12 T. X. Phuoc, *Optics Communications* 175, 419 (2000).
- 13 K. Toyoda, K. Komurasaki, and Y. Arakawa, *Vacuum* 65, 383 (2002).
- 14 B. Dromey, S. Kar, M. Zepf, and P. Foster, *Review of Scientific Instruments* 75, 645 (2004).
- 15 M. Thiagarajan and J. E. Scharer, *IEEE Transactions on Plasma Science* 36, 2512 (2008).
- 16 Y. P. Raizer, *Gas Discharge Physics* (Springer-Verlag, Berlin, Germany, 1991).
- 17 M. P. Nelson, *C. R. Acad. Sci. Paris* (1964).
- 18 N. Kroll and K. M. Watson, *Physical Review A* 5, 1883 (1972).
- 19 I. P. Shkarofsky, *RCA Review* 35, 48 (1974).
- 20 G. Bekefi, *Principles of Laser Plasmas* (Wiley, New York, 1976).
- 21 C. H. Chan, C. D. Moody, and W. B. McKnight, *Journal of Applied Physics* 44, 1179 (1973).
- 22 P. F. Browne, *Proceedings of the Physical Society of London* 86, 1323 (1965).
- 23 A. D. MacDonald, *Microwave Breakdown in Gases* (Wiley, New York, 1966).
- 24 J. Stricker and J. G. Parker, *Journal of Applied Physics* 53, 851 (1982).
- 25 S. Soubacq, P. Pignolet, E. Schall, and J. Batina, *Journal of Physics D-Applied Physics* 37, 2686 (2004).
- 26 U. Jordan, D. Anderson, L. Lapierre, M. Lisak, T. Olsson, J. Puech, V. E. Semenov, J. Sombrin, and R. Tomala, *IEEE Transactions on Plasma Science* 34, 421 (2006).
- 27 R. Tambay and R. K. Thareja, *Journal of Applied Physics* 70, 2890 (1991).
- 28 D. E. Lencioni and L. C. Pettingill, *Journal of Applied Physics* 48, 1848 (1977).

Characterization of Portable Resistive Barrier Plasma Jet and its Direct and Indirect Treatment for Antibiotic Resistant Bacteria and THP-1 Leukemia Cancer Cells

Magesh Thiyagarajan, *Member, IEEE*, Abdollah Sarani and Xavier Gonzalez

Plasma Engineering Research Lab

College of Science and Engineering

Texas A&M University – Corpus Christi

6300 Ocean Drive, Unit 5797, ST 222D

Corpus Christi, Texas 78412, USA

e-mail: magesh@tamucc.edu

Abstract

Atmospheric pressure non-thermal resistive barrier plasma (RBP) jet was designed, constructed and characterized for plasma surface treatment procedures applied in biomedical applications. The RBP source can operate in both DC (battery) as well as in standard 60/50 Hz low frequency AC excitation, and to function effectively in both direct and indirect plasma exposure configurations depending on the type of treatment targets and applications. The design and construction aspects of the RBP source are presented including the electrode configuration, electrical, cooling and gas flow aspects. The RBP jet is tested and its characteristics such as the propagation velocity of the plasma jet, electrical properties, plasma gas temperature and nitric oxides concentration are characterized using optical laser plasma shadowgraphy, voltage-current characterization, optical emission spectroscopy and gas analyzer diagnostic measurements respectively. Using a laser shadowgraphy diagnostic we have measured the average propagation velocity of the plasma jet to be 150 - 200 m/s at 1 cm from the probe end. Discharge power is calculated from voltage-current characterization and plasma power is 26.33 W. An optical emission spectroscopy was applied and the gas temperature which is equivalent to the nitrogen rotational (T_{rot}) temperatures was measured. After approximately 2 cm from the tip, along the axis the plasma emission drops and the high-temperature ceramic fiber-insulated-wire thermocouple probe was used to measure the temperatures of the gas flows along the downstream jet. The addition of a small portable external cooling unit has brought the temperatures of reactive oxygen species and other gases close to room temperature at the tip of the handheld plasma source unit. The concentrations of the reactive oxygen species at different spatial distances from the tip of the plasma jet were measured, at 5 cm distance from the electrode the nitric oxides level was measured to be in the range of 500-660 ppm and drops to

~100 ppm at 60 cm. The ppm values of nitric oxides after the cooling unit are observed to be of the same order of magnitude as compared to plasma jet. The portable RBP source was tested to be very effective for decontamination and disinfection of a wide range of foodborne and opportunistic nosocomial pathogens such as *Escherichia coli*, *Staphylococcus aureus*, *Pseudomonas aeruginosa* and *Bacillus cereus* and the preliminary results are presented. The effects of indirect exposure of the portable RBP source on monocytic leukemia cancer cells (THP-1) were also tested and the results demonstrate that a preference for apoptosis in plasma treated THP-1 cells under particular plasma parameters and dosage levels.

Index Terms – Plasma jet, resistive barrier plasma, atmospheric pressure plasma, air plasma, biomedical, medicine, bacteria, cancer

1. Introduction

Non-equilibrium or non-thermal plasmas are characterized by a large difference between the plasma electron temperature and the plasma gas temperature (ions and neutrals). In such non-thermal plasmas, the electron temperature ranging from few electron volts (eV) to more than 20 eV while the gas temperature is much lower than that of electrons. Non-equilibrium plasmas are typically sustained by applying a substantial applied voltage to the gas between the electrodes. Moreover, the atmospheric pressure non-equilibrium discharges have received more attention recently due to its potential for a wide range of applications. Non-equilibrium, atmospheric pressure plasmas are increasingly being used in various novel applications such as surface modification of the polymeric substrates [1], environmental processing [2], light sources [3], biomedical applications [4], and in microelectronic devices [5]. The most common ways for generating atmospheric pressure non-equilibrium plasma based on different electrode configuration and mechanism of plasma formation include; atmospheric pressure glow discharge plasmas [6], DC/AC corona [7-9], dielectric barrier discharge (from low frequency to several megahertz) [10], floating barrier discharges [11], inductively coupled plasma torches [12, 13], plasma pencil [14], plasma needles [15-19], resistive barrier discharge [20, 21], atmospheric pressure plasma jets (from dc to few gigahertz) [22] and microwave driven discharges in the gigahertz range [23]. In this work, a non-equilibrium resistive barrier air plasma jet is generated under the atmospheric pressure using high voltage power generator. The plasma plume can be extended up to several centimeters long in the surrounding air. The plasma jet is generated with air as inlet gas and its plume length depends on applied voltage, gas flow rate and dissipated discharge power.

The applications of non-equilibrium gas discharge plasmas in medical, hospital, environmental, consumer and industrial applications, and in particular the food processing, air filtration, microbial decontamination and sterilization in liquids and solid surfaces, and treatment of living tissues are continued to grow [24-39]. The non-equilibrium plasmas pose a potential alternative to conventional sterilization techniques that are being used currently. In particular, non-equilibrium plasma based treatment and sterilization is found to be very attractive in biomedical applications due to the heat sensitive nature of the medical targets, devices and supplies [40-50]. The non-equilibrium plasmas have several benefits such as: low temperature of operation with increased efficacy than high temperature autoclaving technique; surface treatments and inactivation at low penetration depths without altering the bulk properties of materials; efficient treatments without the need for toxic chemical gases such as ethylene oxide gas (EOG) or chemical liquid agents such as peroxyacetic acid which is harmful to living tissue and potential breathing health hazards, furthermore the requirement for large water consumption for a post-chemical treatment rinsing process; lack of radiation emissions such as in the case of ion-beam and x-ray techniques; cost effective and ability to be incorporated into the existing inline processing and applications. The reactive oxygen species (ROS) produced by non-equilibrium plasmas have high oxidation abilities and ability to induce several biochemical reactions that are effective in medicine and biomedical applications, yet the byproducts produced by the non-equilibrium plasma and radical reactions are virtually harmless to the surrounding environment [43-45, 49].

The non-equilibrium plasma treatment can also play a significant role in industrial applications related to the medical products and supplies [25, 33, 35, 49]. At present, the manufacturing processes of sterile medical products and supplies employs conventional moist

based heat treatments as a method of sterilization. Conversely, this technique pose a great challenge due to the fact that, not all products especially the majority of medical products and supplies can endure thermal load, moisture, radiation and toxic chemical gases and liquids. In medical industry, for terminal sterilization applications and heat sensitive materials toxic chemicals such as ethylene oxide is used at present due to its penetrative properties. However this technique also poses health risks related to breathing hazards and skin hazards for operators. Another non-thermal or low temperature treatment technique used at present is by the use of radiation, such as e-beam, ion-beam, x-ray and gamma radiation methods that are mostly employed at off-site facilities due to the high capital and operational costs required, which can add further cost related to transportation expenses. Although these techniques has high depth of penetration ability on target materials to be treated, it can ultimately alter the product characteristics due to high beam energy especially in medical devices and supplies where a wide range of polymer materials are employed, which can degrade due to radiation exposure [43, 45, 49, 50].

Based on the above mentioned challenges and drawbacks of the current technologies employed in sterilization and decontamination related applications in biomedical industry as well in the industrial and manufacturing application of medical devices and supplies, the non-equilibrium plasma methodology found to be very attractive and superior. Therefore the non-thermal plasma technology can be considered as a novel method to safely and effectively sterilize products in a variety of medical and manufacturing applications. Realizing this opportunity, several companies and research groups are in the process of developing range of non-thermal plasma sources due to its competitive advantage for sterilization aspects of wide range of processes and products including processing and preservation of food items such as

vegetables, fruits and packaged foods, medical devices and supplies such as vials, syringes and catheters, and terminal sterilization of disposal products etc. [25-50]. Atmospheric pressure plasmas are of great interest compared to low pressure (vacuum) plasmas for industrial surface processing and treatment applications since these applications demand continuous flow of operations in the processing lines and cannot afford a vacuum plasma treatment batch processes. Several types of atmospheric pressure plasma sources have been developed and evaluated for wide range of applications including microbial inactivation, surface modification of materials and living cells and tissues as well as deposition of films and coatings. In addition to the interest and benefit of atmospheric pressure plasmas, the type of gases used for its operation is also of interest, particularly the readily available atmospheric pressure air or otherwise referred as laboratory air is preferred, instead of the need for a separate supply of gases, such as the frequently used gases like helium and argon. In most of the cases of atmospheric pressure air plasmas, the plasma source is bulky and heavy in order to produce considerable plasma volume exiting the excitation electrodes for surface treatment applications or in some cases with smaller power supplies, the plasma is very thin and contained between the electrodes limiting its surface treatment and processing for biomedical applications. Considering the emerging applications in the medical and biomedical fields, portability and light-weight aspect of the plasma source is very important. Similarly, certain biomedical applications can be sensitive to the direct application of plasma and the UV radiation produced by the plasma. Therefore, a need for an indirect plasma exposure also arises for certain applications. In this paper, the authors are presenting the design, construction and characterization results of light-weight portable resistive barrier plasma (RBP) source that can operate in either DC or low frequency 50/60 Hz AC power as well as in either direct or indirect plasma treatment modes. The characteristics of the portable

RBP source such as the propagation velocity of the plasma jet, plasma temperature and nitric oxide concentration are characterized using four diagnostics namely plasma shadowgraphy, voltage-current characterization, optical emission spectroscopy (OES) and gas analyzer measurements and the results are presented. Due to the nature of the article focusing on the design, construction and testing of the portable RBP source, the results relating to the biomedical applications are only presented briefly in this article.

2. Experimental and Diagnostic Design and Construction

2.1. Resistive Barrier Plasma Source

The schematic block diagram of the portable resistive barrier plasma (RBP) source is shown in Fig. 1. The RBP jet was designed and constructed for biomedical applications. The RBP jet was based on the principles of large volume non-thermal resistive barrier discharge (RBD) researched in the past by the author Thiagarajan *et. al.* [20, 51, 52]. The instrument was designed to be a light-weight portable handheld plasma source which is capable of operating in both direct and indirect plasma exposure modes. Direct exposure of plasma involves exposure of plasma directly on to a target treatment surface whereas the indirect plasma exposure involves exposure of only the ROS generated by the plasma instead of the plasma itself, thus eliminating the effect of any possible UV radiation produced by plasma in the case of direct plasma exposure.

Since, the plasma instrument is principally a resistive barrier plasma source, it is capable of operating at both DC and low frequency AC, such as the standard operating voltages 120 V/60 Hz and 230 V/50 Hz which is stepped-up using a 6 kV, 30 mA (max) portable lightweight transformer housed in the power supply unit. The portable plasma source is primarily made up of two units namely the power supply control unit and the handheld plasma probe where the plasma

jet is being generated. The handheld plasma probe unit is lightweight and maintained at room temperature through a cooling circuit and it is connected to the power supply unit through a flexible chord to facilitate the remote workability for medical practitioners and biomedical applications. The power supply unit was constructed in a portable form such that it can be easily carried over by operators, when needed. The power supply unit contains a mini 12 V DC water pump (Geo-Inline) for cooling the electrodes in the handheld plasma probe unit as well as the optional external cooling unit. The power supply unit also contains a mini 12 V DC air compressor weighing less than 3 lbs. to supply the forced air as an operating gas to the handheld plasma probe unit. The power supply unit also houses transistor-transistor logic (TTL) and relay controls to select between AC and DC, and power levels and flow controls. The entire RBP source is constructed to fit within $12 \times 10 \times 10 \text{ inch}^3$ portable metallic case and the entire power supply and RBS plasma source weighs ~20 lbs.

The schematic of the handheld plasma probe unit is shown in Fig. 2. a, which consists of central deionized water cooled cylindrical electrode surrounded by deionized water cooled high density alumina ceramic resistive coating. The central electrode which is approximately 1 cm diameter and 10 cm long is surrounded by a double layer hollow ground electrode separated by an electrode gap space of 2 mm. The plasma source uses atmospheric pressure air as the operating gas, in which the air forced through the resistive barrier plasma source electrode gap space using a mini-compressor such that the plasma and ROS including nitric oxides at the tip of the handheld plasma source tip are controlled and maintained based on the plasma power and flow-rate. Plasma streamers are formed between the high-voltage resistive electrode and the ground electrode. A fraction of the forced air passing through the RBP source gets ionized and exits through a 2 mm pinhole type opening at the tip of the plasma source generating a stable

plasma jet and continuous flow of ROS including nitric oxides. The plasma streamers formed in the cylindrical hollow electrode configuration are dynamic with respect to its location between the electrodes, which also assists in preventing localized heating and arc formation. The ceramic electrodes are water cooled through a mini-water pump.

The direct and indirect exposure of RBP is shown in Fig 2. b. For the indirect exposure method the concentrations of the nitric oxides are preserved by reducing the plasma temperature rapidly through a separate external small efficient cooling unit. For applications that require high temperature plasma, the additional cooling unit can be easily separated from the hand held plasma jet. The temperatures of selected ROS flow from the cooling unit tip were measured to be at room temperature which is ideal for treating heat sensitive materials and targets in the biomedical applications and medicine such as human skin treatment. The external cooling units are scalable and additional units can be added or removed in order to vary the exit temperature of selected ROS.

2.2. Diagnostics Setup

The characteristics of the resistive barrier plasma source such as the propagation velocity of the plasma jet, electrical characterization of the plasma jet, gas temperature and concentration of ROS including nitric oxides are characterized using diagnostics techniques namely optical laser plasma shadowgraphy, voltage current characterization, optical emission spectroscopy and gas analyzer techniques.

A high resolution 532 nm laser shadowgraphy diagnostic [53, 54] was setup as illustrated in Fig. 3, to measure the propagation velocity of the plasma jet. A computer-controlled 532 nm continuous-wave (CW) diode-pumped solid state probe laser outputs a 1 mm beam diameter

TEM_{00} laser beam with 0 – 10 mW adjustable power output that was expanded to 20 mm beam diameter using an anti-reflective (AR) coated 20X Galilean laser beam expander (Thorlabs, BE20M) with collimation adjustment. The expanded 532 nm laser beam axis was aligned to pass through the plasma jet and captured using an intensified charge coupled device (ICCD; Andor, iStar 734). The ICCD was computer controlled and capable of capturing high-resolution 1024×1024 pixel (13.6 x 13.6 mm) images with a minimum gating width of 2 ns and a maximum gain of 10^4 . It was synchronized with a digital delay generator and shutter control. The delay timings were monitored and measured using a high speed digital oscilloscope. Optical interference filters with center wavelength at 532 ± 2 nm was used in front of the ICCD to suppress the plasma jet self-luminescence. The shadow of the laser induced plasma falls onto the ICCD sensor with a 1:1 ratio (1 pixel = $13.2 \mu\text{m}$). The voltage applied to the high-voltage electrode is measured using a high voltage probe (Tektronix P6015A) and the discharge current is measured using a current probe (Tektronix TCP202). The voltage–current waveforms are recorded using a 2 GHz digital oscilloscope (Tektronix TDS3034C). The optical emission spectroscopy diagnostic setup [53, 54] was used as shown in Fig. 3., to measure the plasma gas temperature rotational (T_{rot}) of the nitrogen in the plasma jet. A high resolution narrow band (0.01 nm resolution) monochromator (Acton Research, Model: SP-2750) was used. The monochromator has a multiple grating option, which gives the flexibility of choosing the resolution and wavelength range. A holographic grating of 68 x 68 mm, 2400 G/mm, optimized for the entire visible wavelength range was used to acquire emission spectrum. The plasma emission was acquired by a collecting lens (f/10) and sent to a fast gating Andor iStar ICCD (ANDOR, DH 734) through a high-quality (200-800 nm) fiber-optic bundle. The Andor iStar ICCD detector was integrated with an Acton SpectraPro 2750 spectrograph system. This system has a near-Lorentzian slit function with a half-maximum

width of 0.2 nm when the grating density was set to 1200 lines/mm. A high-temperature ceramic fiber-insulated-wire thermocouple probe capable of measuring temperatures up to 1400 °C was used to measure the temperature of the downstream jet when plasma emission ends after approximately 2.5 cm.

The parts per million (ppm) concentration of the ROS including nitric oxides at different spatial distances from the tip of the plasma jet was measured using two gas sensors namely NO_xCANg and Testo 350 M/XL gas analyzer as shown in Fig. 3. The NO_xCANg is a versatile and highly integrable nitric oxides measurement diagnostics instrument which uses ceramic NO_x sensor to withstand high temperatures that was mounted in the probe tip and communicates the measured NO_x parameters from 0 to 5000 ppm to the Kvaser Leaf Light HS data bus and logs the data in the computer via its controller area network (CAN) bus port with a 150 ms response /refreshing time. The NO_xCANg sensor was externally powered at 18V DC using Agilent E3631A Triple Output DC Power Supply. A data acquisition tool communicates with the NO_xCANg sensor module through Kvaser Leaf Light HS data bus and logs the NO_x concentrations in ppm.

3. Results and Discussion

The non-thermal atmospheric pressure resistive barrier plasma (RBP) source was designed and constructed for surface treatment and biomedical applications. The RBP source was tested for its propagation velocity of the plasma jet, electrical diagnostics, plasma gas temperature and selected ROS concentrations such as nitric oxides that are primary characteristics needed for biomedical applications. A photograph of the portable RBP jet is

shown in the Fig. 4. The visible plasma jet spans approximately 2.5 cm from the exit tip and decays as it recombines and diffuses into the surrounding atmosphere.

The propagation velocity of the plasma jet is an important parameter in determining the treatment distances of surfaces to be treated in biomedical applications. We have developed a 532 nm laser shadowgraphy diagnostic technique to measure the propagation velocity of the portable resistive barrier plasma jet. The laser shadowgraphy technique also provided the flow dynamics of the plasma jet and neutral gases at elevated temperatures. In the laser plasma shadowgraphy technique, a synchronized CW 532 nm probe laser beam was expanded and sent through the test section where the plasma jet is located and its image falls directly onto the ICCD on the image plane. In a plasma, the refractive index is primarily a function of the electron density, which is the main plasma parameter determined by refractive-index measurements. Typical plasma diagnostics based on refractive effects include interferometry, Schlieren imaging, and shadowgraphy measurements [55]. While the first technique gives a direct measure of the refractive index μ , the Schlieren image responds to the first spatial derivative of the index of refraction. The shadowgram however responds to the second spatial derivative or Laplacian [56]. A shadowgraph measures lateral displacement of the light rays after passing through a medium such as plasma. An electromagnetic wave exerts a force on the charged constituents of the medium through which it propagates. This force accelerates the charge which, in turn, modifies the time-varying electromagnetic field [57]. A solution of electromagnetic-wave propagation in plasma can be obtained by solving the wave equation for a plane wave in the small amplitude approximation [58]. The refractive index of high-frequency electromagnetic wave propagation in unmagnetized plasma is:

$$\mu_e = \sqrt{1 - \frac{\omega_p^2}{\omega^2}} = \sqrt{1 - \frac{n_e}{n_c}} \quad (1)$$

where $\omega = 2\pi c/\lambda$ the frequency of the electromagnetic wave, $\omega_p = (n_e e^2 / \epsilon_0 m_e)^{1/2}$ is the electron plasma frequency, and $n_c = m_e \epsilon_0 \omega^2 e^{-2}$ is the cutoff electron density for which electromagnetic wave propagation is possible. If the refractive index in the test section μ is uniform, the screen will be essentially uniformly illuminated. If, however, the gradient of μ varies in space, as one may expect for high-temperature plasmas, i.e., when there is a significant second derivative of the refractive index, there will be variations in the illumination at the imaging screen. Regions where the second derivative of the refractive index is negative that will act like a converging lens. A laser shadowgram of the plasma jet obtained is shown in Fig. 5., by passing an expanded 532 nm probe laser beam through the plasma jet and capturing the transmitted laser beam on an image pane using a fast gated ICCD. Several shadowgrams were obtained at 100 ns gating time with a ICCD triggering delay time of 125 μ s, as indicated with an arrow in Figure 6. The same triggering signal is used to capture the voltage-current signals without the signal delay. By tracking the plasma eddies in the shadowgrams, we have measured the average propagation velocity of the plasma jet to be 150 - 200 m/s at 1 cm from the probe end. The laser shadowgraphy technique is based on the presence of significant second derivative of the refractive index, which can be caused by the presence of plasma as well as the neutral gas at elevated temperatures. Unlike Schlieren diagnostics that is based on the first derivative of the refractive index changes, the flow dynamics of the gas at near room temperatures are generally not captured through the laser shadowgraphy technique since it does not create enough second derivative refractive index changes in the laser beam path. Therefore the shadowgrams obtained through our laser shadowgraphy diagnostics can be caused by both the plasma jet and the heated neutral gas. It is further verified through turning on only the gas flow at room temperature and keeping the high-voltage off (plasma off), resulted in no observable shadowgrams in the ICCD,

as shown in the sub-figure of Fig. 5. However, when we used a separate source of gas that is heated up to few hundred degrees C resulted in weak shadowgrams.

In the RBP jet, the discharge is initiated by applying a sufficient voltage between the electrodes by which the air between the electrodes breakdowns and results in a plasma jet sustained by applied voltage. Figure 6, shows the voltage-current waveform of the RBP jet. Both voltage and current waveforms exhibit pulses of few microseconds long. The positive and negative half periods of the applied voltage are unsymmetrical due to the existence of only one resistance between the electrodes. The maximum voltage and current values are approximately 25 kV and 3 mA on the positive half period of the applied voltage, correspondingly. Using the voltage–current waveforms, the average power dissipated in the discharge is calculated by integrating the product of the discharge voltage and current over one cycle; according to the following equation (T = period of the discharge) [59].

$$W = \frac{1}{T} \int_t^{t+T} I(t)V(t)dt \quad (2)$$

and the measured plasma power is 26.33 W.

Optical emission spectroscopy can be used to determine the plasma temperatures of the RBP jet with some assumptions. To determine the plasma rotational gas temperatures, local thermodynamic equilibrium (LTE) must be assumed. The local thermodynamic equilibrium is valid in the central region of the plasma jet but not at the larger outer radii [60]. The ROS produced in the plasma are long lived active species that can propagate far beyond the plasma jet and in to the surrounding environment preferentially following the plasma jet direction. These long lived active species are important for biomedical applications and we have measured the NO_x concentration of ~900 ppm at 10 cm away from the plasma source exit nozzle. In this

section the plasma temperature measurements using optical emission spectroscopy and the downstream neutral gas temperature measurements using thermocouple are presented.

The nitrogen rotational (T_{rot}) temperature which is equivalent to plasma gas temperature was measured using the N₂ C-B (2+) (N₂ second positive band system) rotational transitions in the range 364-383 nm, by matching them with a code simulated results from SPECAIR. This spectral range corresponds the $\Delta v = -2$ vibrational sequence of N₂ C-B (2+) band system and the best-fit SPECAIR spectrum can yield rotational temperatures (T_{rot}). SPECAIR is computer simulation software developed by Laux *et. al.* [61] on the basis of the NonEquilibrium Air Radiation code (NEQAIR) by Park. SPECAIR performs the OES by determining the populations of the states of the radiative transitions using user-specified electronic, vibrational and rotational temperatures. The modeled transition rates are calculated based on tabulated data for the transitions. From the calculated transition probabilities and populations of radiating species, the line-by-line optical emission intensity was computed for the wavelengths of the transitions. The experimental spectra measured at different distances ranging from 0.2 cm to 2 cm and SPECAIR code matched spectrum are shown in Fig. 7. The temperatures measured from the SPECAIR code matched spectrum resulted at temperatures as high as 3000 °C at 0.2 cm from the exit and decays to 2000 °C at 0.8 cm and continues to decay to 1500 °C at 1.5 cm and to 1000 °C at 2 cm. After approximately 2 cm from the exit nozzle tip along the axis, the plasma emission drops and therefore a high-temperature ceramic fiber-insulated-wire thermocouple probe was used to measure the temperatures of the neutral gas propagating in to the surrounding environment (downstream jet). The axial temperature decay of the plasma jet from the plasma source tip before entering the cooling unit or without the cooling unit is shown in Fig. 8., in which the data in solid circles (red) represent the optical emission spectroscopy results and the data in solid

squares (black) represent the results from thermocouple measurements. The plasma temperature at the nozzle exit of the plasma source reaches around 3000 °C and the temperature drops rapidly to less than 100 °C at approximately 8 cm from the tip. The high gas temperature obtained from N₂ rotational temperature is due to excitation of N₂ to high rotational/vibrational levels and the excited N₂ species are generated in the plasma jet. However, plasma gas temperature drops rapidly towards the end of visible plasma jet. The temperature of the plasma plume at the exit reaches >2500 °C which is sufficient to generate nitric oxides. When the external cooling units were added the gas temperatures were brought close to room temperature at the tip of the handheld plasma source unit.

The concentration of the ROS produced by the plasma jet with and without the cooling unit are measured. The majority of the ions recombine before it exits through the cooling unit and at this stage several gas species and other parameters were monitored, including O₂, O₃, CO, CO_{low}, NO/NO₂, NO_{low}, NO_x, CO_{2(Infrared)}, SO₂, HC, H₂S, temperature, pressure, flow, velocity, efficiency, mass, etc. Based on the results we observed that nitric oxides are the predominant long lives species produced by the RBP source and some trace O₃. The nitric oxide formation is a reversible plasma chemical reaction and it can be expressed as

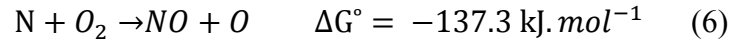
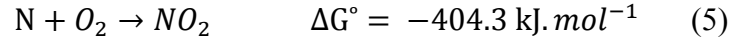
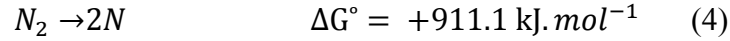


The nitric oxides from the tip of the hand held plasma jet are measured using gas analyzers. The nitric oxide contains the active oxidation potential and reacting with oxygen in the environment as it exits the plasma source induces the formation of nitrogen dioxide at a smaller concentration. The decaying concentration of the nitric oxides from the plasma jet can be used as reference for the treatment distance between the target surface and the plasma source tip. The background NO_x concentration are measured using NO_xCANg module at various timings and at standard

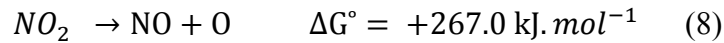
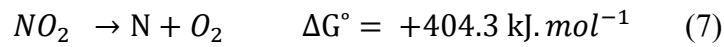
laboratory conditions well before the plasma source was operated and it was measured to be less than 0.5 ppm. The measurements are carried out at 20 data sets separated by 1 min with 1 second acquisition time at distances 5, 10, 20, 30, 60 and 100 cm from the tip. For consistency in the concentration measurements, three other sampling timings such as 10, 30 and 60 second are tested in addition to 1 second acquisition time. The NO_x concentrations of the plasma jet in ppm without the cooling unit are measured at various axial distances (in cm) from the tip and shown in Fig. 9. The results indicate the consistency of the plasma output characteristics and NO_x concentration levels for varied time averaged integration times and data sampling frequencies. The NO_x concentration peaks right at the electrode tip as expected and at 5 cm from the electrode, NO_x concentration was measured to be in the range of 500-660 ppm at different exposure times as listed in Fig. 9. The concentration drops to half of its initial value at ~20cm and it continues to drop to ~100 ppm at 60 cm and at 100 cm distance from the tip the concentration was very low (<10 ppm). The NO_x concentrations in ppm with the cooling unit added and measured at various axial distances (in cm) from the out tip of the cooling unit is shown in Fig. 10. Based on the measurements it was observed that the NO_x concentration after the cooling unit was slightly higher (~950 ppm) compared to that of plasma jet (~615 ppm), this was due to the fact that plasma jet diffuses out after it exits from the handheld electrode whereas the probe diameter after the cooling unit is very small like a pinhole arrangement with 1 cm diameter opening leading to increased concentration.

NO_x is composed of two components such as the mono-nitrogen oxides or nitric oxides (NO) and nitrogen dioxide (NO_2). In order to measure the individual concentration levels of NO and NO_2 a different diagnostic tool was realized using a gas analyzer (Testo 350 M/XL) capable of identifying and characterizing over several molecular gases including NO and NO_2 . The Fig.

11., shows the concentrations of NO and NO₂ for the plasma jet without the cooling unit and the Fig. 12., shows the concentrations of NO and NO₂ from the probe with external cooling unit. The concentration of NO₂ was much lesser compared to that of NO by an order of magnitude or higher. The ppm concentration of NO is at the preferred level for a wide range of standard biomedical treatment applications. The ppm concentration of NO₂ is below the OSHA safety standards. The formation of different active species produced in non-thermal air discharges involves complex plasma chemistries. At relatively high gas temperatures various nitrogen oxides (NO_x) are produced through N₂ and O₂ reactions [62, 63]. The production of NO_x species is mainly dependent on the oxygen (O₂) concentration in air plasmas. It has been shown that in air plasmas, a threshold value of 5% O₂ concentration is necessary for NO_x formation [62] mechanisms.



Based on the reactions 5 and 6, the NO₂ production (reaction 5) is more favorable than the NO production (reaction 6) in such plasma conditions.



Furthermore, NO₂ decomposes into N + O₂ (reaction 7) and NO + O (reaction 8), in which the reaction 8 is more favorable than the reaction 7. Therefore it results in a higher NO concentration along the plasma jet compared to NO₂ as shown in Figures 11 and 12.

The effective sterilization of foodborne and opportunistic nosocomial pathogens is a major problem in food industry, biomedical and hospital applications, respectively. The resistive

barrier plasma (RBP) jet was tested over a wide range of microbes for its decontamination and disinfection efficacy and we have found that the RBP source is very efficient in decontaminating wide range of infection and contamination causing bacteria [64-67]. The direct and indirect exposure of the RBP jet (with the cooling unit) as a non-thermal sterilization method was tested on regrowth potential of post-partial-plasma-exposure of foodborne and nosocomial pathogens. Similarly the RBP jet was also tested on plasma efficiency at different bacterial concentrations for its effects on growth for pre and post plasma treated bacteria. In these tests, the ROS produced by the RBP source was applied to *Escherichia coli* ATCC 11775, *Bacillus cereus* ATCC 14579, *Staphylococcus aureus* ATCC 25923 and *Pseudomonas aeruginosa* ATCC 27853. An average of 30 CFU per 71 mm² was inoculated with the corresponding bacterium on a dry surface-agar plate, followed by the following exposure times 0, 30, 60, 120 and 180 seconds of plasma. 20 µl of *E. coli* 10⁷ CFU/ml and *P. aeruginosa* 108 CFU/ml were treated with plasma for 0, 120, 240 and 360 seconds. The colonies that survived the plasma treatment and control colonies were transferred to tryptic soy broth (TSB) and their growth was observed for 24 hrs. Results have showed 100% and 96% of inactivation after 180s of treatment for *E. coli* and *S. aureus* respectively. A 100% of inactivation was observed for *B. cereus* and *P. aeruginosa* after 60s. *E. coli* and *P. aeruginosa* showed a log reduction of 3.4 and 3.9 orders respectively after 360s. The 24 hours re-growth results of direct exposure of plasma for 30, 60 and 120 seconds on *Escherichia coli* (ATCC 11775), *Neisseria meningitidis* (ATCC 700532) and *Staphylococcus aureus* MRSA (ATCC 259231) are shown in Fig. 13. The 24 hours re-growth results of indirect exposure of plasma 120 seconds on *Escherichia coli* (ATCC 11775), *Neisseria meningitidis* (ATCC 700532) and *Staphylococcus aureus* MRSA (ATCC 259231) are shown in Fig. 14. The growths of survived colonies were monitored and subjected to further treatment. The results

indicate that the post treatment growth rates are similar to the pre-treatment growth rates. Therefore non-equilibrium plasma is effective in sterilizing bacteria at different concentrations with potential applications in the food industry and the medical field.

The possibility of using the RBP jet for treating cancer cells was also tested, since the need for new and effective mechanisms to induce programmed cellular death (apoptosis) in cancerous cells is of great importance in cancer research. Application of direct as well as indirect exposure of plasma for cancer research is still in the exploratory stage and there remain several unanswered questions. We have tested the effects of indirect exposure of non-thermal air plasma on monocytic leukemia cancer cells (THP-1) and deciphering the mechanisms that modulate cellular induction of apoptosis [68-72]. The phenotypes of interest were cells demonstrating death morphologies of apoptosis or necrosis. This is important since cells undergoing necrosis can initiate an inflamed immune response that can be detrimental to a treated individual. The type of morphological cell death that occurred in THP-1 for various plasma treatment dosages (plasma power, flow and distance) was tested and the results are shown in Fig. 15. The results demonstrate that a preference for apoptosis in plasma treated THP-1 cells under particular plasma parameters and dosage levels. The THP-1 cells were identified as apoptotic utilizing a fluorescent dye conjugated with annexin V followed by identification of the cells through fluorescent microscopy and flow-cytometry diagnostics as shown in Fig. 16. Further, DNA fragmentation assays, for late detection of apoptosis, correlated with are fluorescence data demonstrating patterns of apoptotic events. However, the data also revealed that higher plasma dosages presented with undesired necrotic morphologies in the THP-1 cells. The presented variabilities in the death morphologies by plasma treated THP-1 cells signify the need for further investigation on the cellular mechanisms induced by the indirect plasma exposure. Along with

taking into account other death processes such as autophagy, a catabolic process involving the degradation of a cell's own components through the lysosomal machinery. The results obtained from this research indicate great potential for the use of our non-thermal resistive barrier based indirect plasma treatment method as an inexpensive and less invasive method for treating leukemia and other cancerous lesions.

Conclusion

The resistive barrier plasma (RBP) jet was designed and constructed for both direct and indirect plasma treatment to be very suitable for biomedical applications. The RBP source can be operated at both DC and standard low frequency AC, and also able to function effectively in both direct and indirect plasma exposure configurations based on the type of treatment targets and applications. The characteristics of the RBP jet such as the propagation velocity of the plasma jet, electrical properties and discharge power, plasma gas temperature and nitric oxide concentration were characterized using plasma shadowgraphy, voltage-current characterization, optical emission spectroscopy and gas analyzer measurements. A high resolution 532 nm laser shadowgraphy diagnostic showed the average propagation velocity of the plasma jet to be 150 - 200 m/s at 1 cm from the probe end. Plasma power is obtained from voltage-current waveforms and found to be 26.33 W. A high resolution narrow band optical emission spectroscopy diagnostic from the N₂ C-B (2+) (N₂ second positive band system) rotational transitions in the range 364-383 nm showed the gas temperature equivalent to the rotational (T_{rot}) temperature to be as 3000 °C at 0.2 cm from the exit and decays to 2000 °C at 0.8 cm and continues to decay to 1500 °C at 1.5 cm and to 1000 °C at 2 cm and the temperature falls down to room temperature with the addition of external cooling unit. The parts per million (ppm) concentration of the nitric oxide (NO) at different spatial distances from the tip of the plasma jet were measured to be in the range of 500-660 ppm at 5 cm distance from the electrode and drops to ~100 ppm at 60 cm. The RBP jet was tested to be very effective for decontamination and disinfection of a wide range of foodborne and opportunistic nosocomial pathogens *Escherichia coli*, *Bacillus cereus*, *Staphylococcus aureus* and *Pseudomonas aeruginosa*. The indirect exposure of the RBP jet on monocytic leukemia cancer cells (THP-1) was found to be effective and the results demonstrate

that a preference for apoptosis in plasma treated THP-1 cells under particular plasma parameters and dosage levels.

Acknowledgments

This work was supported in part by the College of Science and Engineering, School of Engineering and Computing Sciences at the Texas A&M University-Corpus Christi, Texas Research and Development Fund (TRDF) and the Department of Defense (DOD) /Army grant (W81XWH-10-1-0923) administered by the U.S. Army Medical Research & Materiel Command (USAMRMC) and the Telemedicine & Advanced Technology Research Center (TATRC), at Fort Detrick, MD. The authors would like to thank Keisha Hardeman, Dr. Lillian Waldbeser and Amanda Whitmill for their in part contributions.

List of Figure Captions

Fig. 1. The schematic block diagram of the resistive barrier plasma (RBP) jet. TRF: Transformer, ROS: Reactive Oxygen Species.

Fig. 2. (a) The schematic of the handheld RBP probe unit, (b) Plasma/ROS exposure experimental configuration (A. Direct plasma exposure, B. Indirect plasma exposure).

Fig. 3. Schematic of laser shadowgraphy, optical emission spectroscopy and gas analyzer diagnostics used to characterize the RBP. ND-neutral density filter, BE-beam expander, M-mirror, F-filter.

Fig. 4. Photograph of the RBP jet.

Fig. 5. Laser shadowgram of the plasma jet. Image size-1.25 x 1.75 cm. Sub-figure (top-left): laser shadowgram of gas flow-only and with power off (no plasma).

Fig 6. Voltage-Current waveform of the RB plasma jet in air. Discharge power is 26.33 W.

Fig. 7. Experimental and SPECAIR code simulated matching of emission spectra of RBP jet at different axial distances from exit. a. 0.2 cm – 3000 °C, b. 0.8 cm – 2000 °C, c. 1.5 cm – 1500 °C, d. 2 cm – 1000 °C.

Fig. 8. The axial temperature decay of the plasma jet from the RBP source tip before entering the cooling unit.

Fig. 9. The NO_x concentrations of the plasma jet from the RBP source in ppm without the cooling unit at various axial distances from the tip.

Fig. 10. The NO_x concentrations in ppm with the cooling unit added to the RBP tip at various axial distances (in cm) from the out tip of the cooling unit.

Fig. 11. The concentrations of NO and NO₂ for the RBP jet without the external cooling unit.

Fig. 12. The concentrations of NO and NO₂ from the RBP probe with external cooling unit.

Fig. 13. Density measurements over a 24 hour period of bacteria without direct plasma treatment (closed circles ●) or with direct treatment of plasma for 30 seconds (closed square ■), 60 seconds (closed up-pointing triangle ▲), or 120 seconds (down-pointing triangle ▼). A.) *Escherichia coli* (ATCC 11775). B.) *Neisseria meningitidis* (ATCC 700532). C.) *Staphylococcus aureus* (ATCC 259231).

Fig. 14. Density measurements over a 24 hour period of bacteria without indirect plasma treatment (closed circles ●) or with indirect treatment of plasma for 120 seconds (closed square ■). A.) *Escherichia coli* (ATCC 11775). B.) *Neisseria meningitidis* (ATCC 700532). C.) *Staphylococcus aureus* (ATCC 259231).

Fig. 15. Viability of THP-1 cells after RBP treatment. (A) THP-1 cells 0 hours, 24h and 48h post plasma treatment of 0 seconds, 5s, 15s, 30s, 45s and 60s. Non viable cells are presented as the percent of treated cells that absorbed trypan blue dye as compared to control cells not treated by RBP. (B) Photograph of cells stained with trypan blue dye 48h post plasma treatment.

Fig. 16. Induction of apoptosis in THP-1 cells after RBP treatment. (A) Fluorescence microscopy of THP-1 cells stained with Annexin V FITC and propidium iodide. Cells undergoing apoptosis stain with Annexin V and appear green (a), while cells without intact membrane due to necrosis appear red (b). (B) Flow cytometry detection of Annexin V and propidium iodide staining 24h post RBP treatment of 30s and 60s. Controls are untreated cells and anti-fas treated cells. Presented are the detection of stains from 10,000 events in which quadrants indicated (Q-I) propidium iodide stain, (Q-II) background, (Q-III) unstained, (Q-IV) annexin V. (C) DNA fragmentation assay of DAN from THP-1 cells 24h and 48h post

RBP treatment of 0s, 15s, 30s and 45s. A 1kb ladder was used as a comparative indicator of the separation of DNA.

Figures

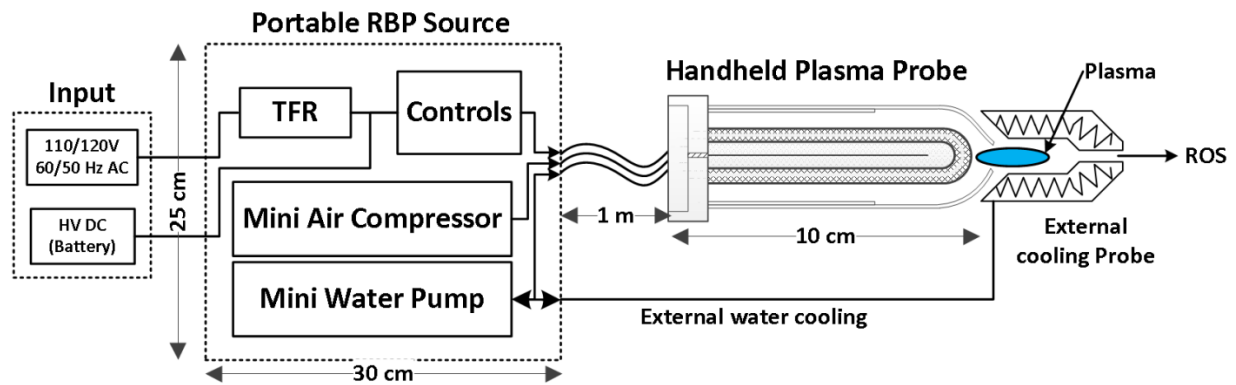


Fig. 1. The schematic block diagram of the resistive barrier plasma (RBP) jet. TRF: Transformer, ROS: Reactive Oxygen Species.

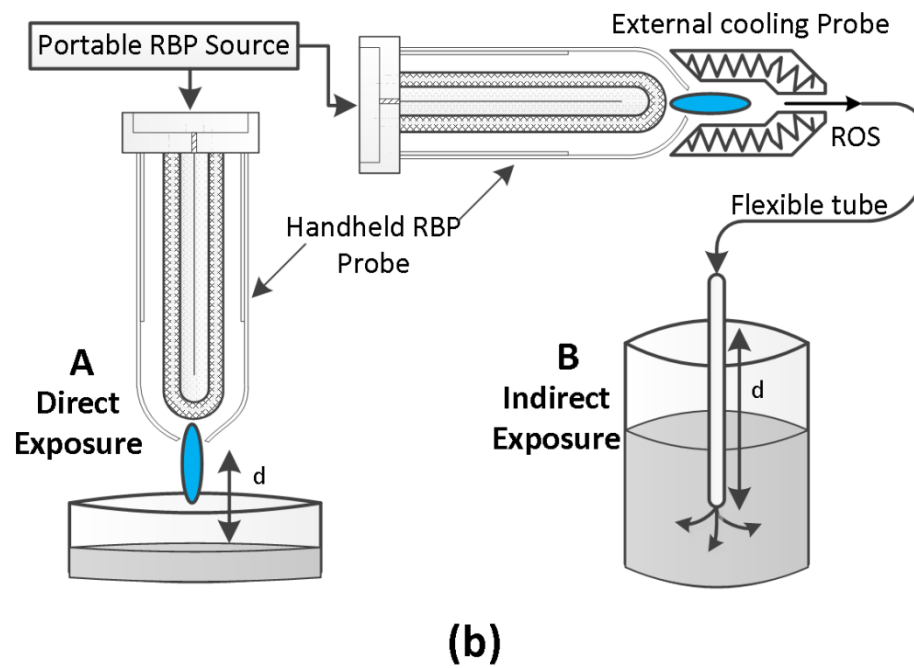
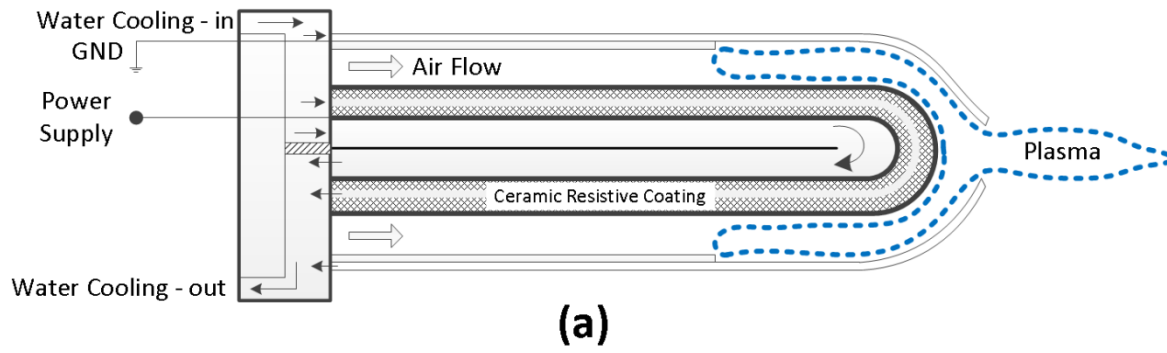


Fig. 2. (a) The schematic of the handheld RBP probe unit, (b) Plasma/ROS exposure experimental configuration (A. Direct plasma exposure, B. Indirect plasma exposure).

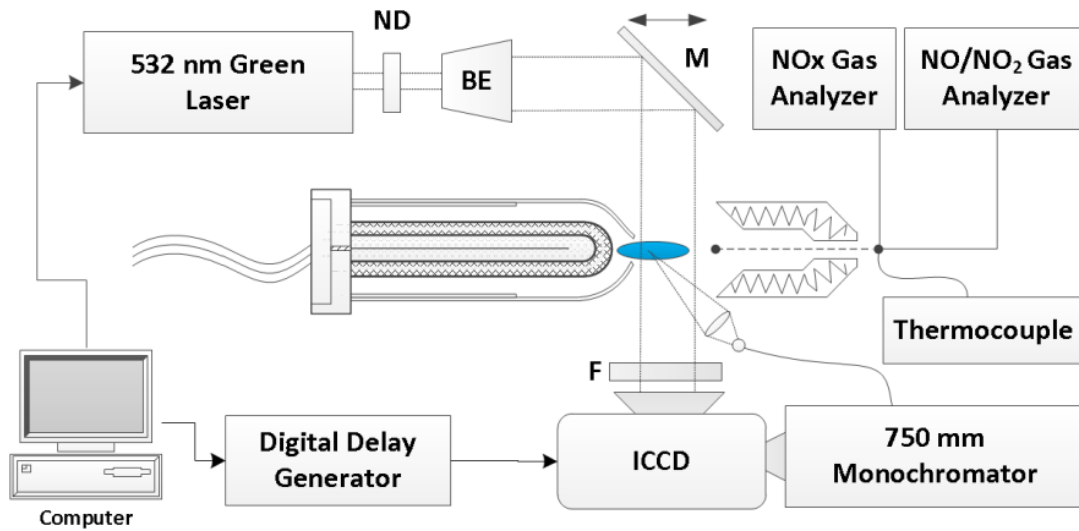


Fig. 3. Schematic of laser shadowgraphy, optical emission spectroscopy and gas analyzer diagnostics used to characterize the RBP. ND-neutral density filter, BE-beam expander, M-mirror, F-filter.

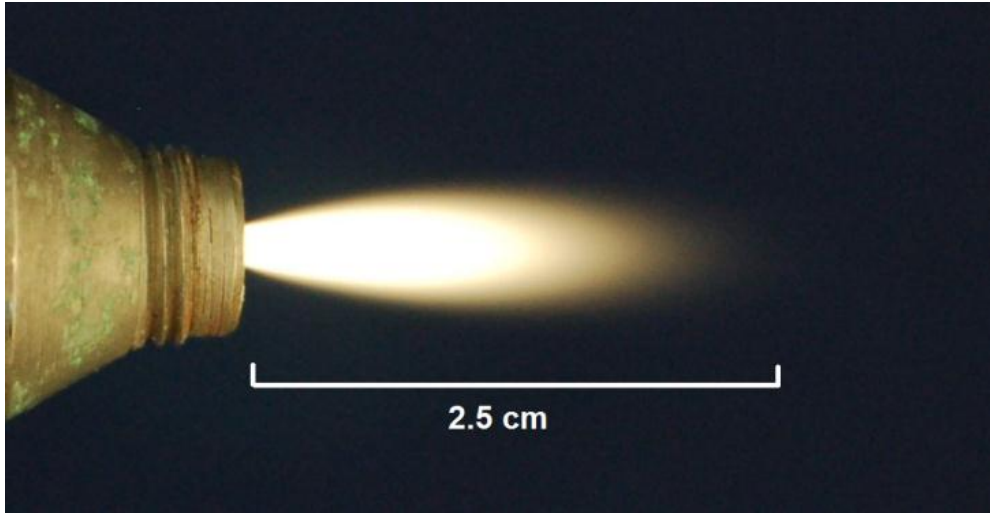


Fig. 4. Photograph of the RBP jet.

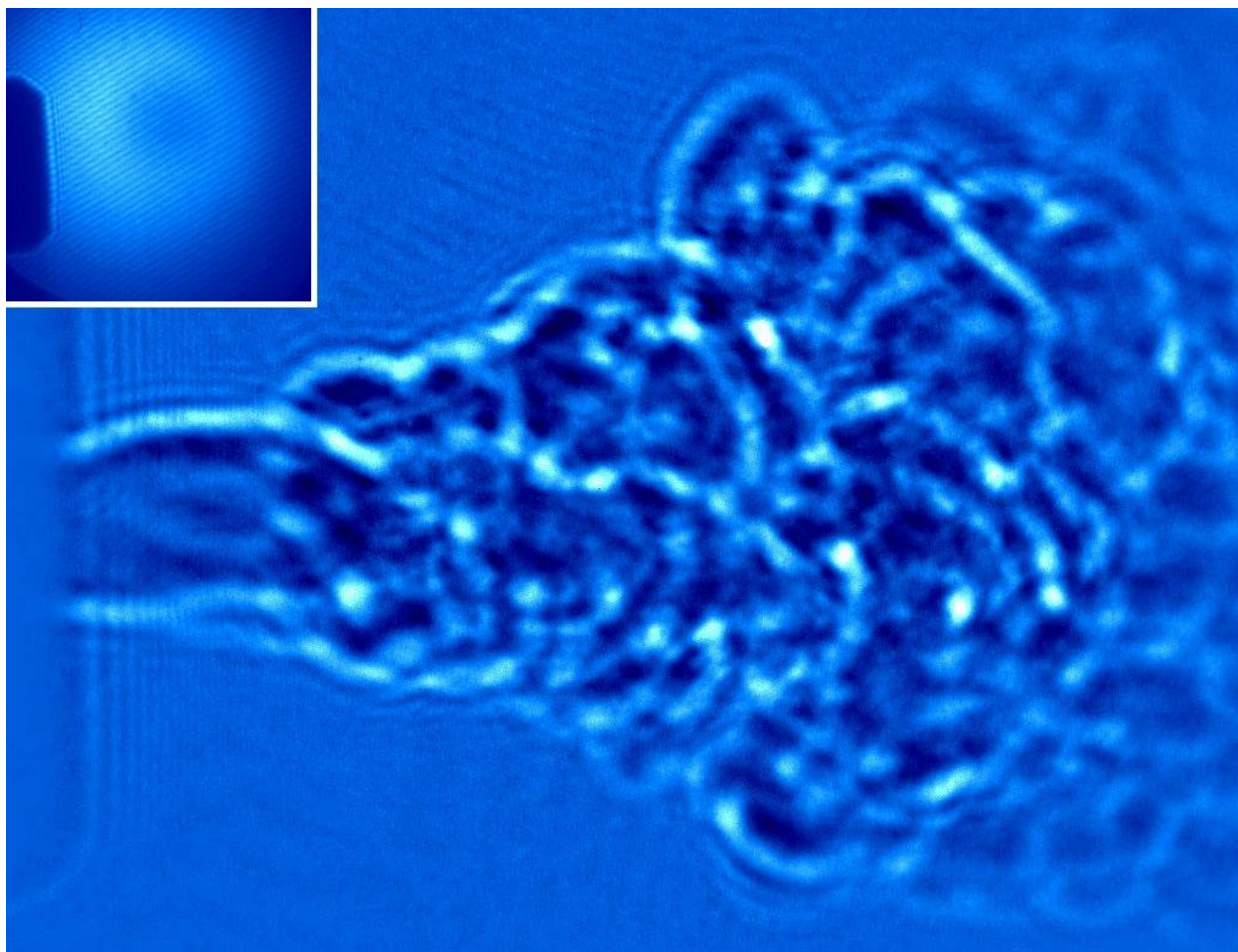


Fig. 5. Laser shadowgram of the plasma jet. Image size-1.25 x 1.75 cm. Sub-figure (top-left):
laser shadowgram of gas flow-only and with power off (no plasma).

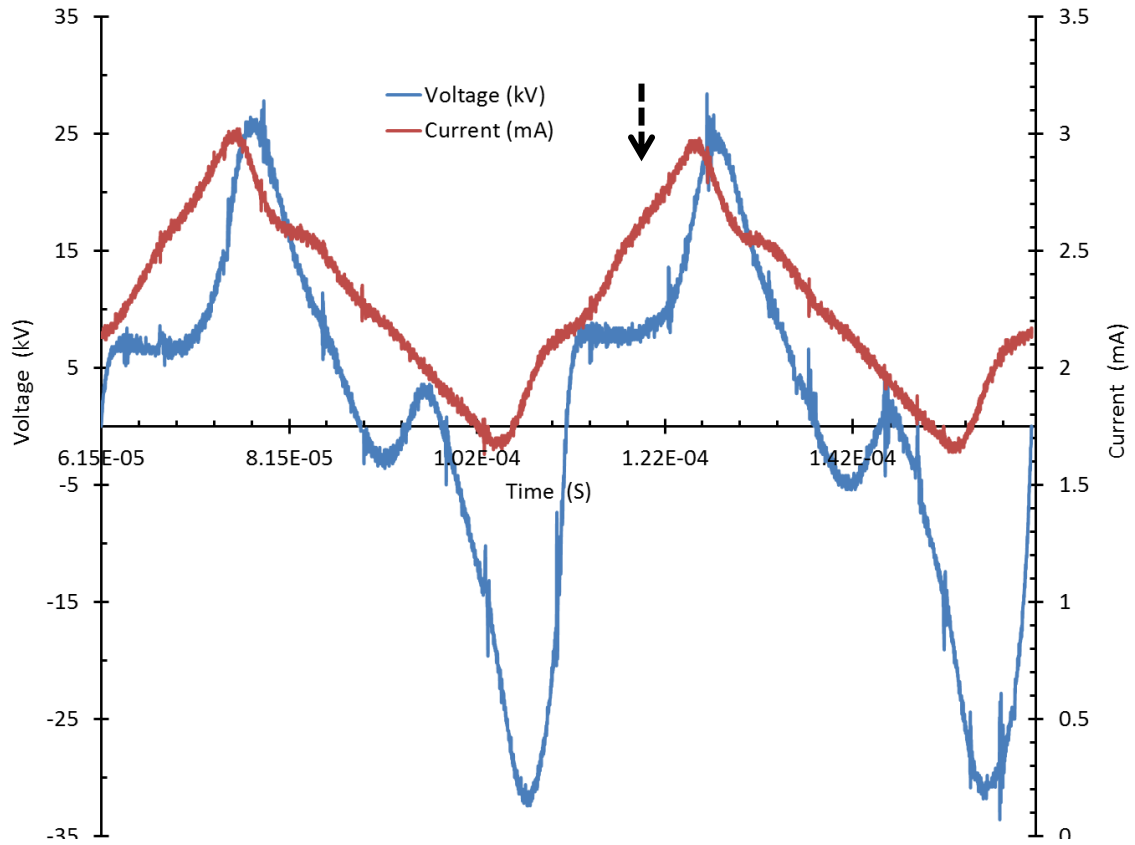


Fig 6. Voltage-Current waveform of the RB plasma jet in air. Discharge power is 26.33 W.

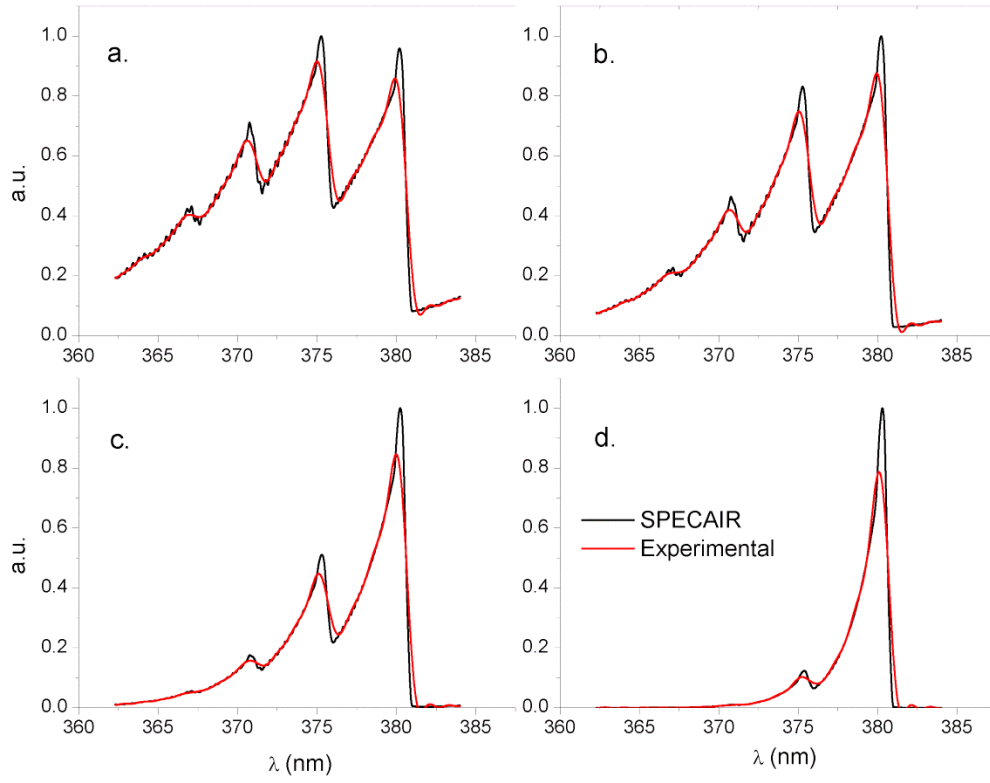


Fig. 7. Experimental and SPECAIR code simulated matching of emission spectra of RBP jet at different axial distances from exit. a. 0.2 cm – 3000 °C, b. 0.8 cm – 2000 °C, c. 1.5 cm – 1500 °C, d. 2 cm – 1000 °C.

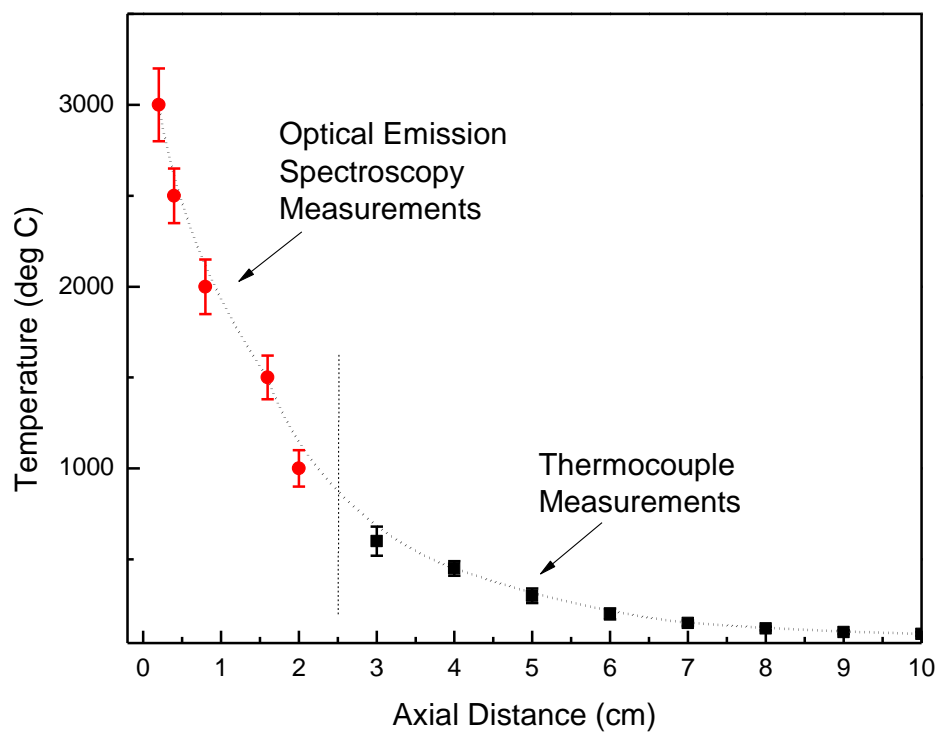


Fig. 8. The axial temperature decay of the plasma jet from the RBP source tip before entering the cooling unit.

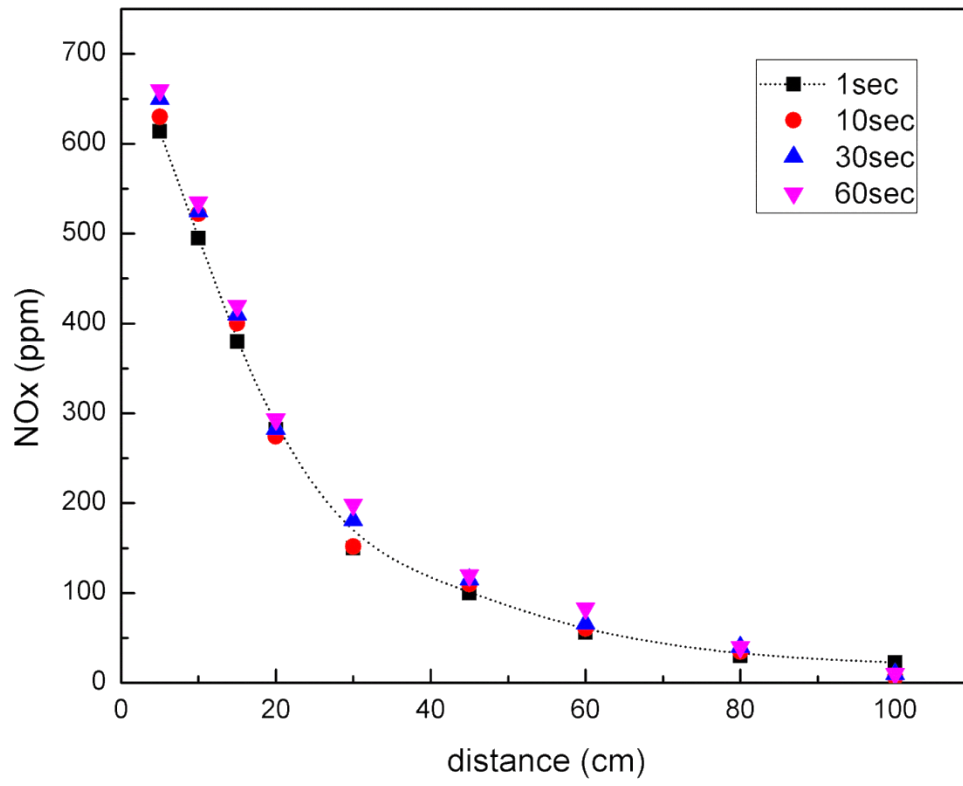


Fig. 9. The NO_x concentrations of the plasma jet from the RBP source in ppm without the cooling unit at various axial distances from the tip.

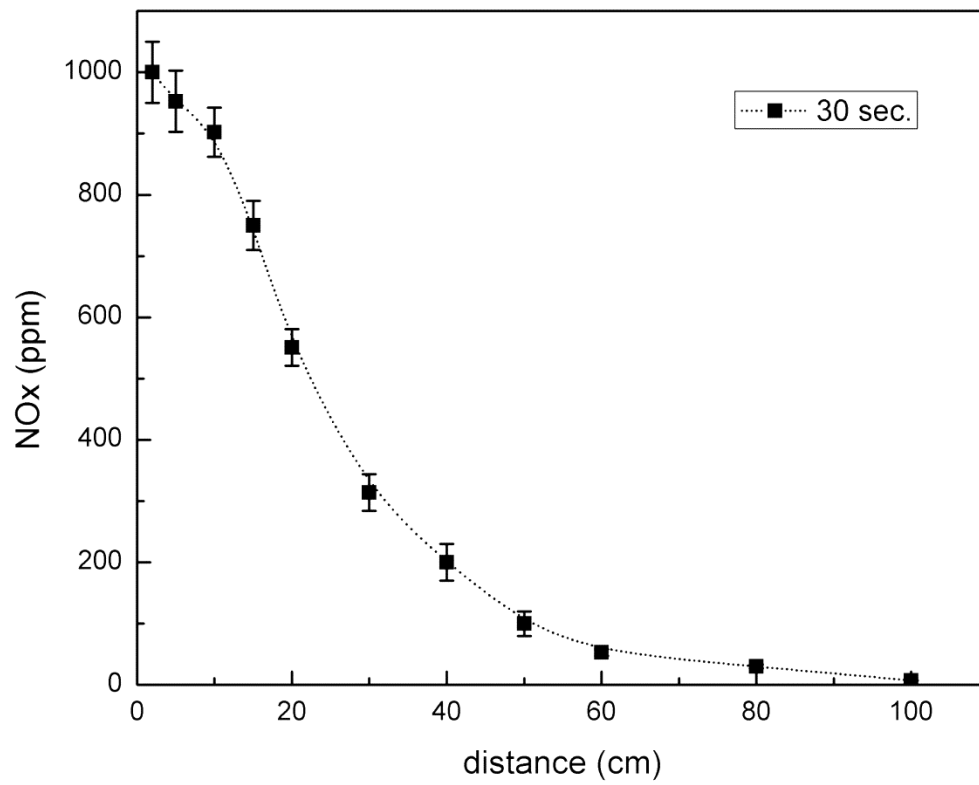


Fig. 10. The NO_x concentrations in ppm with the cooling unit added to the RBP tip at various axial distances (in cm) from the out tip of the cooling unit.

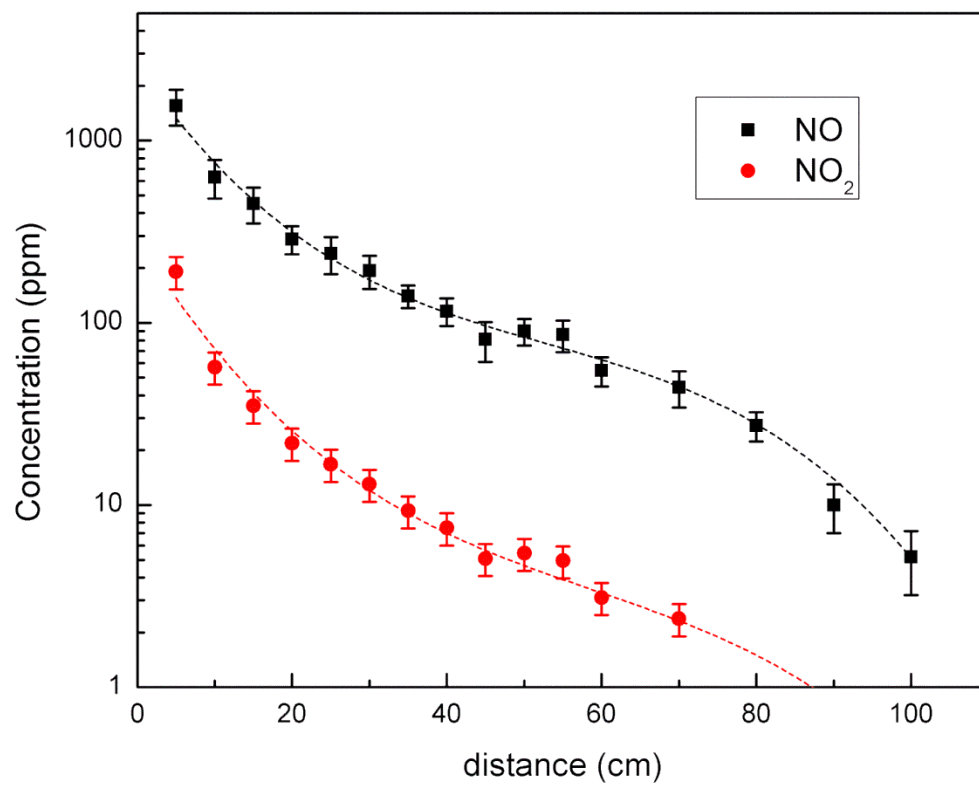


Fig. 11. The concentrations of NO and NO₂ for the RBP jet without the external cooling unit.

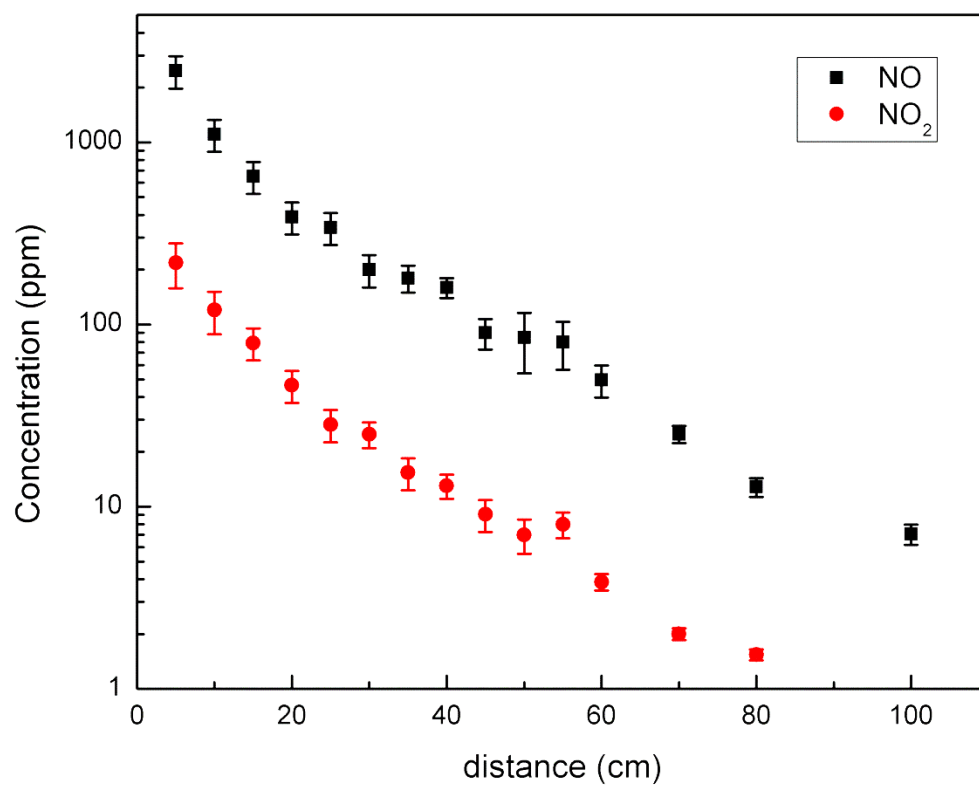


Fig. 12. The concentrations of NO and NO₂ from the RBP probe with external cooling unit.

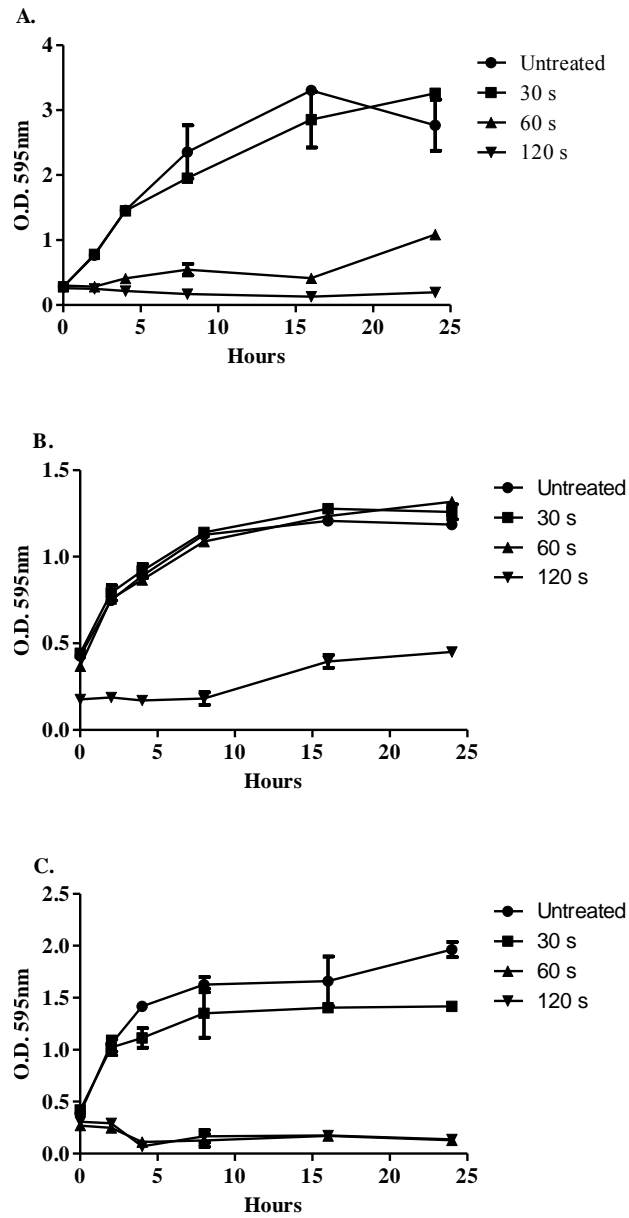


Fig. 13. Density measurements over a 24 hour period of bacteria without direct plasma treatment (closed circles ●) or with direct treatment of plasma for 30 seconds (closed square ■), 60 seconds (closed up-pointing triangle ▲), or 120 seconds (down-pointing triangle ▼). A.) *Escherichia coli* (ATCC 11775). B.) *Neisseria meningitidis* (ATCC 700532). C.) *Staphylococcus aureus* (ATCC 259231).

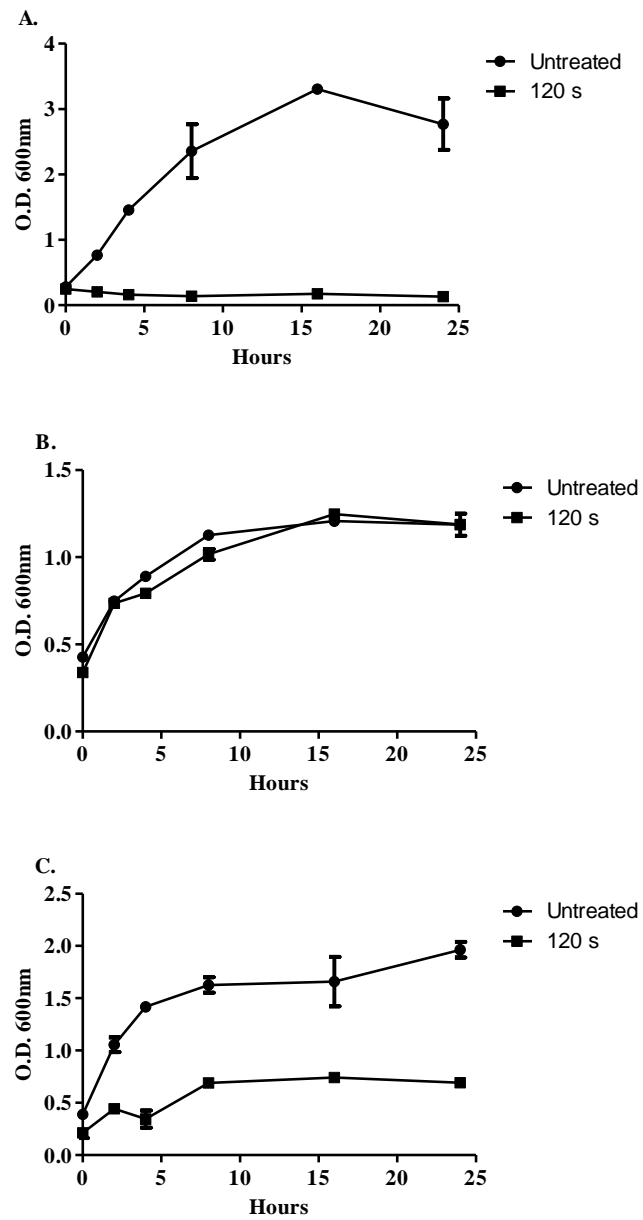


Fig. 14. Density measurements over a 24 hour period of bacteria without indirect plasma treatment (filled circles ●) or with indirect treatment of plasma for 120 seconds (filled square ■). A.) *Escherichia coli* (ATCC 11775). B.) *Neisseria meningitidis* (ATCC 700532). C.) *Staphylococcus aureus* (ATCC 259231).

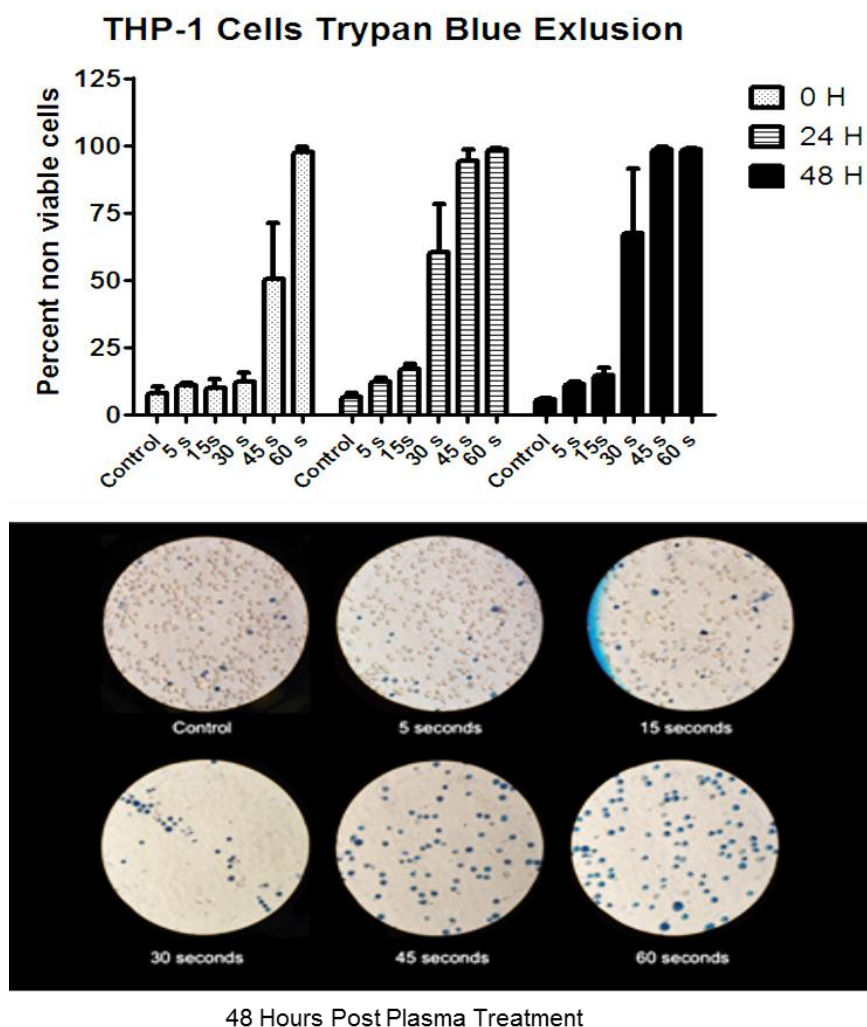


Fig. 15. Viability of THP-1 cells after RBP treatment. (A) THP-1 cells 0 hours, 24h and 48h post plasma treatment of 0 seconds, 5s, 15s, 30s, 45s and 60s. Non viable cells are presented as the percent of treated cells that absorbed trypan blue dye as compared to control cells not treated by RBP. (B) Photograph of cells stained with typan blue dye 48h post plasma treatment.

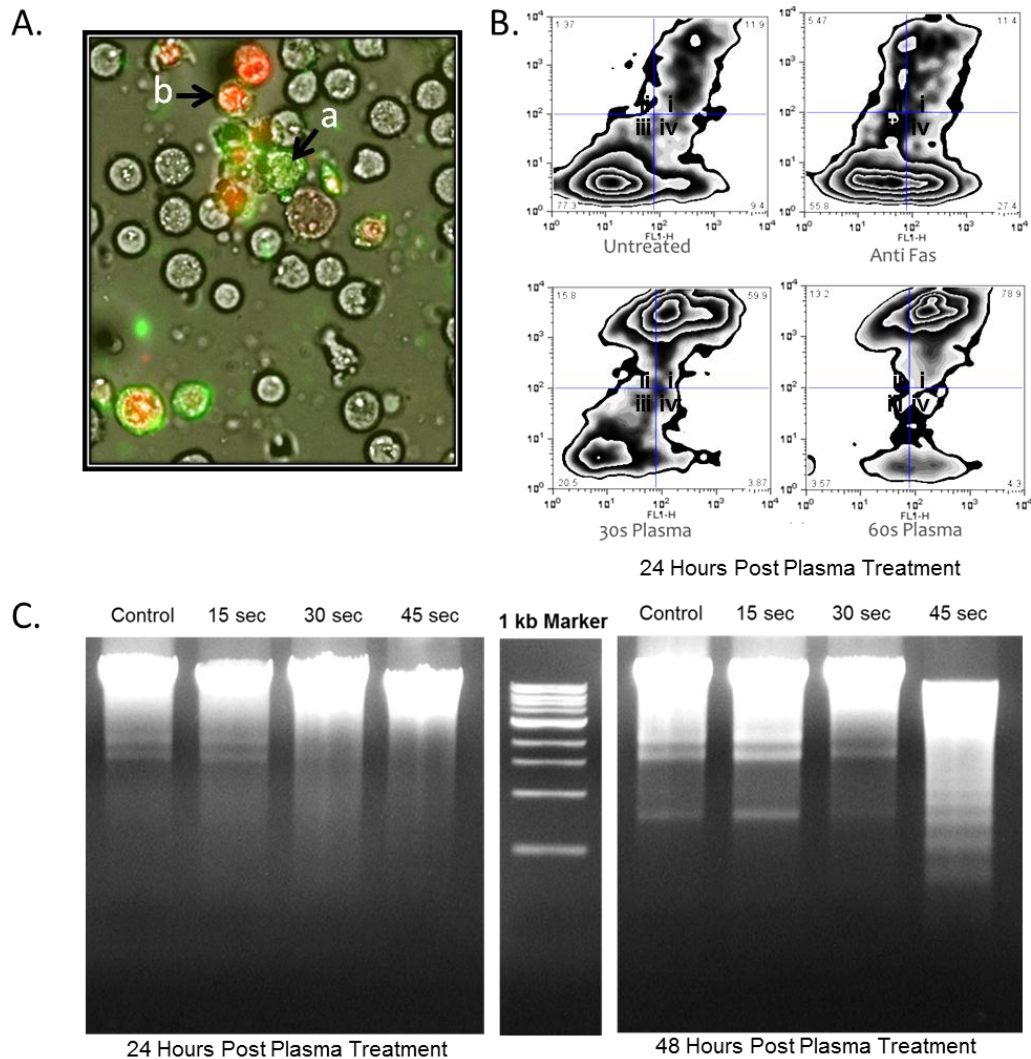


Fig. 16. Induction of apoptosis in THP-1 cells after RBP treatment. (A) Fluorescence microscopy of THP-1 cells stained with Annexin V FITC and propidium iodide. Cells undergoing apoptosis stain with Annexin V and appear green (a), while cells without intact membrane due to necrosis appear red (b). (B) Flow cytometry detection of Annexin V and propidium iodide staining 24h post RBP treatment of 30s and 60s. Controls are untreated cells and anti-fas treated cells. Presented are the detection of stains from 10,000 events in which quadrants indicated (Q-I) propidium iodide stain, (Q-II) background, (Q-III) unstained, (Q-IV) annexin V. (C) DNA fragmentation assay of DAN from THP-1 cells 24h and 48h post RBP treatment of 0s, 15s, 30s and 45s. A 1kb ladder was used as a comparative indicator of the separation of DNA.

References

- [1] Y. Akishev, *et al.*, "Novel AC and DC non-thermal plasma sources for cold surface treatment of polymer films and fabrics at atmospheric pressure," *Plasmas and Polymers*, vol. 7, pp. 261-289, Sep 2002.
- [2] K. Hensel, *et al.*, "Dc microdischarges inside porous ceramics," *Ieee Transactions on Plasma Science*, vol. 33, pp. 574-575, Apr 2005.
- [3] T. I. Lee, *et al.*, "Dielectric barrier hollow cathode discharge and its enhanced performance for light source," *Applied Physics Letters*, vol. 87, Dec 26 2005.
- [4] G. Fridman, *et al.*, "Applied plasma medicine," *Plasma Processes and Polymers*, vol. 5, pp. 503-533, 2008.
- [5] R. M. Sankaran and K. P. Giapis, "Maskless etching of silicon using patterned microdischarges," *Applied Physics Letters*, vol. 79, pp. 593-595, Jul 30 2001.
- [6] R. Ben Gadri, *et al.*, "Sterilization and plasma processing of room temperature surfaces with a one atmosphere uniform glow discharge plasma (OAUGDP)," *Surface & Coatings Technology*, vol. 131, pp. 528-542, Sep 1 2000.
- [7] L. B. Loeb, "Recent developments in analysis of the mechanisms of positive and negative coronas in air," *Journal of Applied Physics*, vol. 19, pp. 882-897, 1948.
- [8] C. M. Nunez, *et al.*, "Corona destruction – an innovative control technology for VOCs and air toxins," *Journal of the Air & Waste Management Association*, vol. 43, pp. 242-247, Feb 1993.
- [9] J. M. Strobel, *et al.*, "Aging of air- orona treated polypropylene film", " *Journal of Adhesion Science and Technology*, vol. 5, pp. 119-130, 1991.
- [10] A. Indarto, "A review of direct methane conversion to methano by dielectric barrier discharge," *Ieee Transactions on Dielectrics and Electrical Insulation*, vol. 15, pp. 1038-1043, Aug 2008.
- [11] G. Fridman, *et al.*, "Blood coagulation and living tissue sterilization by floating-electrode dielectric barrier discharge in air," *Plasma Chemistry and Plasma Processing*, vol. 26, pp. 425-442, Aug 2006.
- [12] N. Kovacic, *et al.*, "Diagnostics in an air inductively coupled plasma," *Spectrochimica Acta Part B-Atomic Spectroscopy*, vol. 40, pp. 943-957, 1985.
- [13] K. Akhtar, *et al.*, "Radio-frequency sustainment of laser initiated, high-pressure air constituent plasmas," in *Radio Frequency Power in Plasmas*. vol. 694, C. B. Forest, Ed., ed, 2003, pp. 411-414.
- [14] M. Laroussi, *et al.*, "Inactivation of bacteria by the plasma pencil," *Plasma Processes and Polymers*, vol. 3, pp. 470-473, Aug 2006.
- [15] E. Stoffels, *et al.*, "Plasma needle: a non-destructive atmospheric plasma source for fine surface treatment of (bio)materials," *Plasma Sources Science & Technology*, vol. 11, pp. 383-388, Nov 2002.
- [16] Y. Sakiyama and D. B. Graves, "Corona-glow transition in the atmospheric pressure RF-excited plasma needle," *Journal of Physics D-Applied Physics*, vol. 39, pp. 3644-3652, Aug 2006.
- [17] E. Stoffels, *et al.*, "A plasma needle generates nitric oxide," *Plasma Sources Science & Technology*, vol. 15, pp. 501-506, Aug 2006.
- [18] X. Lu, *et al.*, "A simple atmospheric pressure room-temperature air plasma needle device for biomedical applications," *Applied Physics Letters*, vol. 95, Nov 2009.

- [19] X. C. Li, *et al.*, "A plasma needle for generating homogeneous discharge in atmospheric pressure air," *Physics of Plasmas*, vol. 17, Sep 2010.
- [20] M. Thiagarajan, *et al.*, "Atmospheric pressure resistive barrier cold plasma for biological decontamination," *IEEE Transactions on Plasma Science*, vol. 33, pp. 322-323, Apr 2005.
- [21] M. Laroussi, *et al.*, "The resistive barrier discharge," *Ieee Transactions on Plasma Science*, vol. 30, pp. 158-159, Feb 2002.
- [22] A. Sarani, *et al.*, "Atmospheric pressure plasma jet in Ar and Ar/H₂O mixtures: Optical emission spectroscopy and temperature measurements," *Physics of Plasmas*, vol. 17, Jun 2010.
- [23] C. M. Ferreira, *et al.*, "Air-water microwave plasma torch as a NO source for biomedical applications," *Chemical Physics*, vol. 398, pp. 248-254, Apr 4 2012.
- [24] M. Mekki, *et al.*, "Optimization of Plasma Treatment, Manipulative Variables and Coating Composition for the Controlled Filling and Coating of a Microstructured Reservoir Stent," *Journal of Medical Devices*, vol. 3, p. 011005, 2009.
- [25] M. Laroussi, "Nonthermal decontamination of biological media by atmospheric-pressure plasmas: Review, analysis, and prospects," *Ieee Transactions on Plasma Science*, vol. 30, pp. 1409-1415, Aug 2002.
- [26] A. Schutze, *et al.*, "The atmospheric-pressure plasma jet: A review and comparison to other plasma sources," *Ieee Transactions on Plasma Science*, vol. 26, pp. 1685-1694, Dec 1998.
- [27] T. Oda, "Non-thermal plasma processing for environmental protection: decomposition of dilute VOCs in air," *Journal of Electrostatics*, vol. 57, pp. 293-311, Mar 2003.
- [28] H. H. Kim, "Nonthermal plasma processing for air-pollution control: A historical review, current issues, and future prospects," *Plasma Processes and Polymers*, vol. 1, pp. 91-110, Sep 2004.
- [29] L. F. Gaunt, *et al.*, "Bactericidal action of the reactive species produced by gas-discharge nonthermal plasma at atmospheric pressure: A review," *Ieee Transactions on Plasma Science*, vol. 34, pp. 1257-1269, Aug 2006.
- [30] S. Perni, *et al.*, "Cold atmospheric plasma disinfection of cut fruit surfaces contaminated with migrating microorganisms," *Journal of Food Protection*, vol. 71, pp. 1619-1625, Aug 2008.
- [31] H. L. Chen, *et al.*, "Removal of Volatile Organic Compounds by Single-Stage and Two-Stage Plasma Catalysis Systems: A Review of the Performance Enhancement Mechanisms, Current Status, and Suitable Applications," *Environmental Science & Technology*, vol. 43, pp. 2216-2227, Apr 2009.
- [32] T. Desmet, *et al.*, "Nonthermal Plasma Technology as a Versatile Strategy for Polymeric Biomaterials Surface Modification: A Review," *Biomacromolecules*, vol. 10, pp. 2351-2378, Sep 2009.
- [33] H. D. Stryczewska and A. Lekawa, "Applications of nonthermal plasma in biotechnologies," *Przegląd Elektrotechniczny*, vol. 85, pp. 83-86, 2009.
- [34] B. F. Yu, *et al.*, "Review of research on air-conditioning systems and indoor air quality control for human health," *International Journal of Refrigeration-Revue Internationale Du Froid*, vol. 32, pp. 3-20, Jan 2009.
- [35] S. Cheruthazhekatt, *et al.*, "Gas plasmas and plasma modified materials in medicine," *Journal of Applied Biomedicine*, vol. 8, pp. 55-66, Jun 2010.

- [36] K. Skalska, *et al.*, "Trends in NO(x) abatement: A review," *Science of the Total Environment*, vol. 408, pp. 3976-3989, Sep 2010.
- [37] J. Heinlin, *et al.*, "Plasma applications in medicine with a special focus on dermatology," *Journal of the European Academy of Dermatology and Venereology*, vol. 25, pp. 1-11, Jan 2011.
- [38] N. N. Misra, *et al.*, "Nonthermal Plasma Inactivation of Food-Borne Pathogens," *Food Engineering Reviews*, vol. 3, pp. 159-170, Dec 2011.
- [39] D. Knorr, *et al.*, "Emerging Technologies in Food Processing," in *Annual Review of Food Science and Technology*, Vol 2. vol. 2, M. P. Doyle and T. R. Klaenhammer, Eds., ed, 2011, pp. 203-235.
- [40] S. Moreau, *et al.*, "Using the flowing afterglow of a plasma to inactivate *Bacillus subtilis* spores: Influence of the operating conditions," *Journal of Applied Physics*, vol. 88, pp. 1166-1174, 2000.
- [41] G. E. Van Poucke, *et al.*, "Target controlled infusions: targeting the effect site while limiting peak plasma concentration," *Biomedical Engineering, IEEE Transactions on*, vol. 51, pp. 1869-1875, 2004.
- [42] L. F. Gaunt, *et al.*, "Bactericidal Action of the Reactive Species Produced by Gas-Discharge Nonthermal Plasma at Atmospheric Pressure: A Review," *Plasma Science, IEEE Transactions on*, vol. 34, pp. 1257-1269, 2006.
- [43] N. Hayashi, *et al.*, "Sterilization of Medical Equipment Using Oxygen Radicals Produced by Water Vapor RF Plasma," *Plasma Science, IEEE Transactions on*, vol. 36, pp. 1302-1303, 2008.
- [44] J. F. Kolb, *et al.*, "Cold atmospheric pressure air plasma jet for medical applications," *Applied Physics Letters*, vol. 92, pp. 241501-241501-3, 2008.
- [45] P. K. Chu, *et al.*, "Special Issue on Plasma-Based Surface Modification and Treatment Technologies," *Plasma Science, IEEE Transactions on*, vol. 37, pp. 1121-1122, 2009.
- [46] E. Karakas, *et al.*, "Destruction of synuclein based amyloid fibrils by a low temperature plasma jet," *Applied Physics Letters*, vol. 97, pp. 143702-143702-3, 2010.
- [47] R. Bussiahn, *et al.*, "The hairline plasma: An intermittent negative dc-corona discharge at atmospheric pressure for plasma medical applications," *Applied Physics Letters*, vol. 96, pp. 143701-143701-3, 2010.
- [48] Y. Xu, *et al.*, "On the Mechanism of Plasma Inducing Cell Apoptosis," *Plasma Science, IEEE Transactions on*, vol. 38, pp. 2451-2457, 2010.
- [49] O. Yardimci and P. Setlow, "Plasma Sterilization: Opportunities and Microbial Assessment Strategies in Medical Device Manufacturing," *Plasma Science, IEEE Transactions on*, vol. 38, pp. 973-981, 2010.
- [50] V. S. Johnson, *et al.*, "A Cold Atmospheric-Pressure Helium Plasma Generated in Flexible Tubing," *Plasma Science, IEEE Transactions on*, vol. 39, pp. 2360-2361, 2011.
- [51] M. Thiagarajan and I. Alexeff, "A Dual Mode – Steady State Atmospheric Pressure Nonthermal Resistive Barrier Plasma Discharge," in *Gaseous Electronics Conference, American Physical Society*, San Francisco, California, 2003.
- [52] M. Thiagarajan, *et al.*, "Ambient pressure resistive barrier cold plasma discharge for biological and environmental applications," in *IEEE Conference Record - Abstracts: The 31st IEEE International Conference on Plasma Science, ICOPS2004, June 28, 2004 - July 1, 2004*, Baltimore, MD, United states, 2004, p. 197.

- [53] M. Thiagarajan and J. E. Scharer, "Experimental Investigation of 193-nm Laser Breakdown in Air," *Ieee Transactions on Plasma Science*, vol. 36, pp. 2512-2521, Oct 2008.
- [54] M. Thiagarajan and J. Scharer, "Experimental investigation of ultraviolet laser induced plasma density and temperature evolution in air," *Journal of Applied Physics*, vol. 104, Jul 1 2008.
- [55] M. Villagran-Muniz, *et al.*, "Shadowgraphy and interferometry using a CW laser and a CCD of a laser-induced plasma in atmospheric air," *Ieee Transactions on Plasma Science*, vol. 29, pp. 613-616, Aug 2001.
- [56] G. S. Settles, *Schlieren and shadowgraph techniques: visualizing phenomena in transparent media*: Springer, 2001.
- [57] H. Hutchinson, *Principles of Plasma Diagnostics*: Cambridge University Press, 2002.
- [58] C. H. Chan, *et al.*, "Significant loss mechanisms in gas breakdown at 10.6 μ ," *Journal of Applied Physics*, vol. 44, pp. 1179-1188, 1973 1973.
- [59] F. Massines and G. Gouda, "A comparison of polypropylene-surface treatment by filamentary, homogeneous and glow discharges in helium at atmospheric pressure," *Journal of Physics D-Applied Physics*, vol. 31, pp. 3411-3420, Dec 21 1998.
- [60] S. C. Snyder, *et al.*, "Determination of Gas-Temperature and Velocity Profiles in an Argon Thermal-Plasma Jet by Laser-Light Scattering," *Physical Review E*, vol. 47, pp. 1996-2005, Mar 1993.
- [61] C. O. Laux, *et al.*, "Optical diagnostics of atmospheric pressure air plasmas," *Plasma Sources Science & Technology*, vol. 12, pp. 125-138, May 2003.
- [62] S. Futamura, *et al.*, "Behavior of N-2 and nitrogen oxides in nonthermal plasma chemical processing of hazardous air pollutants," *Ieee Transactions on Industry Applications*, vol. 36, pp. 1507-1514, Nov-Dec 2000.
- [63] S. Futamura, *et al.*, "The dependence of nonthermal plasma behavior of VOCs on their chemical structures," *Journal of Electrostatics*, vol. 42, pp. 51-62, Oct 1997.
- [64] M. Thiagarajan and L. Waldbeser, "Portable Plasma Medical Device for Infection Treatment," *Health Technology and Informatics*, vol. 173, 2012.
- [65] M. Thiagarajan, "Portable Plasma Medical Device for Infection Treatment and Wound Healing," presented at the ASME Emerging Technologies - 6th Frontiers in Biomedical Devices Conference, Irvine, California, 2011.
- [66] M. Thiagarajan and L. S. Waldbeser, "Portable Plasma Torch on E.Coli, S. Aureus, N. Meningitidis and other Clinical Isolates," in *38th IEEE International Conference on Plasma Science (ICOPS) and 24th Symposium on Fusion Engineering (SOFE)*, Chicago, IL, 2011.
- [67] G. Vidal, *et al.*, "Cold Plasma Inactivation of E. coli and S. aureus on Solid Surfaces for Infection Treatment," presented at the SACNAS National Conference, San Jose, California, 2011.
- [68] M. Thiagarajan, *et al.*, "THP-1 Leukemia Cancer Treatment Using a Portable Plasma Device," *Health Technology and Informatics*, vol. 173, 2012.
- [69] M. Thiagarajan, *et al.*, "Treatment of Cancer Cells using a Pulsed Power Plasma Source," in *18th IEEE International Pulsed Power Conference*, Chicago, IL, 2011.
- [70] M. Thiagarajan, *et al.*, "Effective Non-Thermal Plasma Induction of Apoptosis in Leukemia Cancer Cells," in *38th IEEE International Conference on Plasma Science (ICOPS) and 24th Symposium on Fusion Engineering (SOFE)*, Chicago, IL, 2011.

- [71] M. Thiyagarajan, "Portable Plasma Biomedical Device for Cancer Treatment," presented at the ASME Emerging Technologies - 6th Frontiers in Biomedical Devices Conference, Irvine, California, 2011.
- [72] M. Thiyagarajan, "Effects of Cold Plasma and Treatment of Leukemia Cancer Cells," presented at the International Conference on Medical Physics and Biomedical Engineering, Marseille, France, 2011.

Magesh Thiagarajan received the B.S. degree from the University of Madras, Chennai, India, the M.S. degree from the University of Tennessee, Knoxville, and the Ph.D. degree (work completed December 2007) from the University of Wisconsin-Madison, Madison, in 2008.

He is the Director of the Plasma Engineering Research Laboratory and an Assistant Professor of engineering at the Texas A&M University, Corpus Christi. Prior to that, he was a Lead Engineer with the Global Research Center, General Electric Company, Albany, NY. He has published two books on laser-induced plasmas and its optical diagnostics. His current research is focused on nonthermal plasma jets; and its applications in materials processing, microbial deactivation, and cancer treatment; laser plasmas in gases, liquids, and at phase boundaries; laser shadowgraphy; laser interferometry; optical emission spectroscopy.

Dr. Thiagarajan is a recipient of the UTK Citation Award for professional promise, the IEEE Fellowship Award, the University of Madras Gold Medalist Award, and Wisconsin Governor's and Texas Coastal Bend Best Technology Business Awards. He is a member of IEEE, ASME, Tau Beta Pi, Eta Kappa Nu and he holds a green belt in Six-Sigma.

Abdollah Sarani received the B.Sc. degree from the University of Sistan and Balouchestan, Zahedan, Iran, the M.Sc. degree from the National University of Iran (Shahid Beheshti University), Tehran, Iran, and the Ph.D. degree from the University of Ghent, Ghent, Belgium, in 2012.

Currently, he is a Postdoctoral Research Associate with the Plasma Engineering Research Laboratory, Texas A&M University, Corpus Christi. He is a recipient of the IAP program scholarship for Plasma Surface Interactions, and master's thesis award of excellence. He is a member of the International Plasma Chemistry Society.

Xavier Gonzalez received the B.S. degree from the Texas A&M University, Corpus Christi, the M.S. degree from the Texas A&M University Health Science Center, College Station, and he is expected to receive the Ph.D. degree from the Universidad Nacional Autónoma de México (UNAM), Mexico City, México, in 2013.

Currently, he is a Research Associate with the Plasma Engineering Research Laboratory, Texas A&M University, Corpus Christi. He is a recipient of the CONACyT scholarship, the NIH Predoctoral Fellowship, the NIH Bridge Grant and the NIH Fogarty International Scholars Awards.

Experimental Investigation of 1064 nm IR Laser Induced Air Plasma Using Optical Laser
Shadowgraphy Diagnostics

Magesh Thiagarajan, Kenneth Williamson, Anudeep Reddy Kandi

Plasma Engineering Research Lab (PERL), College of Science and Engineering,

Texas A&M University-Corpus Christi, Texas 78412, USA

Abstract

Experimental measurements and analysis of pulsed 1064 nm Nd:YAG laser-induced air breakdown plasma at 760 Torr has been carried out using high speed and high resolution laser shadowgraphy and optical diagnostics. Three different experimental laser energies and pulse widths such as 170 mJ at 8 ns, 130 mJ at 7 ns and 65 mJ at 12 ns are studied. The laser pulses were focused down to a $\sim 7 \mu\text{m}$ spot size in air and the resulting laser flux densities range from 4-14 TW/cm^2 . A 532 nm laser shadowgraphy coupled with high speed and high resolution image capturing diagnostics has been established to investigate spatio-temporal evolution and hydrodynamic behavior of the 1064 nm laser induced plasma and neutral density shock during the formation, expansion and collapsing stages. The observed plasma formations were aspherical due to absorption translation during the initial laser-energy coupling. The aspherical feature seeded the hydrodynamic instability leading to the ultimate destabilization of the hot gaseous core after approximately 10 μs . The active plasma lifetime through plasma self-luminescence measurements indicate variations from 200 – 500 ns for the three laser pulses. Shock propagation velocity and plasma volume for three laser pulse series indicate similarly shaped profiles at different expansion velocities. Early plasma expansion velocities of 20 km/s were measured and using Hugoniot relations the neutral shock pressures and temperatures were inferred and the results at the early plasma expansion stage were found to be over 1000 atmospheres and 4 eV.

Keywords/Index Terms—Air breakdown, air plasma, laser plasma, laser induced plasma, laser shadowgraphy, laser plasma hydrodynamics, plasma and shock discontinuities, plasma

I. Introduction

There is a great deal of research and industrial interest in laser induced plasmas and the range of applications involving plasmas produced by lasers spans a large domain within science and technology. The laser induced plasmas are widely used in laser ablation [1], micromachining [2], photochemistry [3], laser fusion [4], flow control [5-7], drag reduction in supersonic and hypersonic flows [8, 9], ignition of combustion gases [10], thrusters in space applications [11], and laser-initiated switching applications [12]. The formation of laser-induced optical breakdown studies in a gas has been summarized by Raizer [13]. Due to continued development of laser technology there has been steady interest in the laser induced breakdown plasmas. The development of optical diagnostics such as nanosecond range fast gating high resolution digital imaging can be used as a significant diagnostic tool to investigate the rapidly varying electrohydrodynamic behavior of the laser induced plasmas.

Laser energy initiates plasma formation within a transparent medium when the maximum local electric field strength exceeds the electron binding potential [14]. Intense, localized electric fields of sufficient strength to ionize the medium can be produced by focusing laser energy. The initial ionization greatly reduces the transparency of the medium allowing for the majority of the laser energy to be absorbed or reflected by the medium during the creation of laser-induced plasma. The sudden formation of hot, dense plasma at the laser focal point consequently launches a detonation shock wave. The velocity of the shock front is directly related to the initial parameters of the plasma. Thus, using Hugoniot relations, the shock front position and velocity may be utilized as diagnostic tools for the study of laser-induced plasma [14].

The initial breakdown is a photon-initiated electron ionization process with two competing physical mechanisms: multiphoton ionization also named as quantum resonant multi-photon

ionization (REMPI) [15-21] and ionizing collisional cascade or inverse bremsstrahlung absorption [22, 23]. For the MPI process, a neutral atom absorbs enough laser photons within a quantum lifetime of the excited state [15] [$\tau \approx \hbar/\varepsilon_\gamma = 3.5 \times 10^{-15}$ s (at 1064 nm)] to raise it from the ground state to the ionization level or above. When enough atoms are ionized, it can produce an observable flash [15]. The ionizing collisional cascade (CC) process occurs due to the acceleration of existing free electrons, either from the MPI process or naturally occurring, by the intense electric field supplied by the focused laser energy. Electrons accelerated to an energy higher than the ionization potential of the medium may ionize an atom by inelastic collisions producing two electrons of lower energy, which are then available for the process to be repeated [23]. The evolution of the laser-induced plasma system can be described by four progressive steps [24]: initial release of electrons by the MPI effect [24]; ionization of the gas in the focal region by CC ionization; absorption and partial reflection of laser energy by the plasma; and formation and propagation of a detonation shock wave into the surrounding gas during the relaxation of the focal region plasma.

Based on the multiphoton ionization theory [15-21], the breakdown threshold laser intensity defined as $I_{B(\text{MPI})} = SI_0$, where S is the MPI coefficient, which is the ratio of ionization potential U_i of the gas (15.6 eV for air) [25-27] to the photon energy ε_γ of the laser beam ($\varepsilon_\gamma = 1.24/\lambda$ (eV), where λ is the vacuum wavelength in micrometers). With $\varepsilon_\gamma = 1.165$ eV photon energy for the 1064 nm laser radiation, it requires approximately $S = 14$ photons to be absorbed within the quantum excitation lifetime $\tau \approx \hbar/\varepsilon_\gamma = 3.5 \times 10^{-15}$ s in order to ionize the air molecules. Thus, the breakdown threshold laser intensity value for 760 Torr air at 1064 nm laser radiation is $I_{B(\text{MPI})} = 4.42 \times 10^9$ W/cm² [28]. The corresponding rms breakdown electric field is

obtained from [13] $E_{B(MPI)} = 1.94 \times 10^4 \sqrt{I_{B(MPI)}}$ m, where $I_{B(MPI)}$ is expressed in MW/cm² and we obtain $E_{B(MPI)} = 1.3 \times 10^6$ V/cm [28].

Based on the collisional cascade theory, the threshold power flux for breakdown is given by [15]: $I_{B(CC)} = 1.44 \times 10^6 (p^2 + 2.2 \times 10^5 \lambda^{-2})$ W/cm², where p is the pressure in atmospheric pressure units and λ is the radiation wavelength in micrometers. Although this theory is primarily based on observations at microwave frequencies, and as well as pressures below atmospheric conditions, it can also be scaled to 1064 nm wavelength laser frequencies [26]. The cascade ionization theory predicts a breakdown flux intensity threshold value for 760 Torr air at 1064 nm wavelength as $I_{B(CC)} = 2.8 \times 10^{11}$ W/cm² corresponding to $E_{B(CC)} = 10.3 \times 10^6$ V/cm. These estimates suggesting the presence of multiphoton ionization at 1064 nm laser ionization of air at 760 Torr. The authors have presented a detailed theoretical and experimental work on this topic elsewhere [28].

Recent advances in diagnostic methodology, numerical modeling, and analytical techniques allow for more detailed investigation of the laser-induced plasma system. High speed shutters and intensified charge coupled devices provide the temporal resolution needed for advanced shadowgraphy, Schlieren, and interferometry imaging systems [29]. Three dimensional gas and electron density maps were attained through Abel transformed interferometry [30]. In this paper we have utilized a fast gating intensified charge coupled device to capture the spatio-temporal electro-hydrodynamics of the 1064 nm infrared laser induced plasma in air using a 532 nm optical probe laser shadowgraphy diagnostics in high spatial and temporal resolution. The laser beam was focused downwards as a part of our future work on laser plasmas in liquids.

II. Shadowgraphy Diagnostics

In a plasma, the refractive index is primarily a function of the electron density, which is the main plasma parameter determined by refractive-index measurements. Typical plasma diagnostics based on refractive effects include interferometry, Schlieren imaging, and shadowgraphy measurements [29]. While the first technique gives a direct measure of the refractive index μ , the Schlieren image responds to the first spatial derivative of the index of refraction. The shadowgram however responds to the second spatial derivative or Laplacian [31]. In these experiments, the shadowgraphy technique is applied for visualizing the laser-induced plasma and laser-heated gas dynamic processes. A shadowgraph measures lateral displacement of the light rays after passing through a medium such as plasma. An electromagnetic wave exerts a force on the charged constituents of the medium through which it propagates. This force accelerates the charge which, in turn, modifies the time-varying electromagnetic field [32]. A solution of electromagnetic-wave propagation in plasma can be obtained by solving the wave equation for a plane wave in the small amplitude approximation [23]. The refractive index of high-frequency electromagnetic wave propagation in unmagnetized plasma is:

$$\mu_e = \sqrt{1 - \frac{\omega_p^2}{\omega^2}} = \sqrt{1 - \frac{n_e}{n_c}} \quad (1)$$

where $\omega = 2\pi c/\lambda$ the frequency of the electromagnetic wave, $\omega_p = (n_e e^2 / \epsilon_0 m_e)^{1/2}$ is the electron plasma frequency, and $n_c = m_e \epsilon_0 \omega^2 e^{-2}$ is the cutoff electron density for which electromagnetic wave propagation is possible. In our shadowgraphy experiments, as shown in Fig. 1, a green laser at $\lambda = 532$ nm is used as a light source due to its coherence, brightness, and narrow bandwidth. The cutoff density for 532 nm is $3.9 \times 10^{21} \text{ cm}^{-3}$, which is well above the densities encountered in our laser-focused plasma experiments.

III. Experimental Setup

A. 1064 nm Infrared Laser Induced Plasma System

The experimental setup is shown schematically in Fig. 1. In this experiment, a dual wavelength Q-switched Nd:YAG laser (Newport, INDI Quanta-ray) that outputs a 1st harmonic at $\lambda = 1064$ nm wavelength (1.17 eV per photon) and a 2nd harmonic at $\lambda = 532$ nm (2.33 eV per photon) laser radiation is used. The laser outputs a 10 ± 1 mm diameter circular cross section Gaussian distributed laser beam intensity in a 8 ± 1 ns full width at half maximum (FWHM) pulse at a rep-rate of 10 Hz and laser beam divergence of $\alpha = 1$ mrad. The maximum available laser pulse energy at 1064 nm and 532 nm is 280 ± 10 mJ and 100 ± 3 mJ, respectively. In this experiment the 2nd harmonic 532 nm laser output was minimized by detuning the second harmonic generator crystal and separating it from the 1064 nm fundamental laser wavelength using a dichroic mirror. The laser output was controlled by varying the flash lamp energy, shown schematically in Fig. 1 as a variable beam attenuator, and the laser beam energy was measured using a diffuser-equipped laser energy sensor (EnergyMax, J-50MB-YAG) coupled to a calibrated energy meter (Coherent, FieldMax II Top). A top-down laser beam path configuration using three mirrors (M1, M2 and M3) with 99% reflectivity at 45° was utilized. Laser energies were measured after each optical component to ensure optimal energy throughput. The 1064 nm laser beam was focused using a high power-handling gold coated objective lens (TECHSPEC, High Performance ReflX) with an effective focal length of $f = 13.3$ mm and a 0.28 NA. The minimum radius of the laser focal region was calculated based on the standard optical focal theory as $r = f\alpha/2 = 7 \mu\text{m}$ where f is the focal length and α is the beam divergence. The visible light emission from the laser induced plasma was collected using a 200-1100 nm broadband 1 ns high-speed optical photodetector

(Thorlabs, DET10A) and recorded using a 2.5 GS/s high speed digital oscilloscope (Tektronix, TDS3034C).

B. Optical Laser Shadowgraphy Diagnostics Setup

A high resolution 532 nm laser shadowgraphy diagnostic was setup as illustrated in Fig. 1, to study the laser induced plasma system. A computer-controlled 532 nm continuous-wave (CW) diode-pumped solid state probe laser outputs a 1 mm beam diameter TEM₀₀ laser beam with 0 – 10 mW adjustable power output that was expanded to 20 mm beam diameter using an anti-reflective (AR) coated 20X Galilean laser beam expander (Thorlabs, BE20M) with collimation adjustment. The expanded 532 nm laser beam axis was aligned to pass through the focal region of the 1064 nm laser radiation and captured using an intensified charge coupled device (ICCD; Andor, iStar 734). The ICCD is computer controlled and capable of capturing high-resolution 1024 × 1024 pixel (13.6 x 13.6 mm) images with a minimum gate width of 2 ns and a maximum gain of 10⁴. It was synchronized with the laser Q-switched triggering pulse using a digital delay generator and shutter control. The delay timings were monitored and measured using a high speed digital oscilloscope. The signal delay timings such as laser triggering delay, laser output delay, signal transmission delay, ICCD triggering, image capture and readout delay were also monitored. Optical interference filters with center wavelength at 532 ± 2 is used in front of the ICCD to suppress the plasma self-luminescence. The shadow of the laser induced plasma falls onto the ICCD sensor with a 1:1 ratio (1 pixel = 13.2 μm). The probe laser and the allied optics are well aligned with respect to the laser optical axis to minimize diffractions by setting up the lateral alignment deviation less than the 0.05 nm bandwidth probe laser coherence length of 5.7 mm.

IV. Experimental measurements, results and discussion

A. Laser plasma generation and energy measurements

As discussed earlier in the experiment section, the 1064 nm Nd:YAG laser has a maximum output of 280 mJ in a 8 ± 1 ns FWHM pulse. In this experiment laser pulses at three different stable working output energies (E) are investigated. The laser energies were measured immediately after the objective lens by placing the laser energy detector surface in contact with the output edge of the optic where the power flux density is below the damage threshold of the detector. The measured energies and pulse widths incident to the focal region were: $E_{i1} = 170 \pm 4$ mJ with 8 ns FWHM, $E_{i2} = 130 \pm 4$ mJ with 7 ns FWHM, and $E_{i3} = 65 \pm 4$ mJ with 12 ns FWHM were focused to a $7 \mu\text{m}$ radius spot size in laboratory air in 1 atm pressure, resulting in corresponding power-flux densities of $14 \text{ TW}/\text{cm}^2$, $12 \text{ TW}/\text{cm}^2$ and $4 \text{ TW}/\text{cm}^2$. These data are used as a reference level for all additional measurements in this research. The 1064 nm laser beam has a Gaussian distributed spatial profile and the temporal profiles of the three experimental laser energies are measured as shown in Fig. 2.

The temporal profiles of the laser pulses are obtained by using a high-speed broadband photodetector. Luminous plasma was observed for all three laser pulse energies at the focal spot, 23.6 mm from the edge of the objective lens. The laser energy absorbed by the plasma was measured by subtracting the laser energy transmitted through the focal volume from the incident laser energy. The transmitted laser energy (E_t) was measured by placing the 4.5 cm diameter energy meter at 5.0 cm after the focal spot. Since the maximum plasma frequency divided by the laser frequency near the focal spot is $\omega_p/\omega < 0.01$, we assume that a very small fraction of the incident laser flux is scattered by the plasma and the laser absorption is primarily due to

collisional cascade and multiphoton ionization process. The average transmitted laser energy was measured to be $E_{t1} = 15 \pm 3$ mJ for the $E_{i2} = 170 \pm 4$ mJ, $E_{t2} = 10 \pm 3$ mJ for the $E_{i2} = 130 \pm 4$ mJ, and $E_{t3} = 5 \pm 2$ mJ for the $E_{i3} = 65 \pm 4$ mJ, which corresponds to approximately 8% of the incident laser energy. Therefore the laser energies absorbed (E_a) by the plasma for the respective incident laser energies were approximately $E_{a1} = 155 \pm 4$ mJ, $E_{a2} = 120 \pm 3$ mJ and $E_{a3} = 60 \pm 3$ mJ corresponding to approximately 92% absorption of the incident laser energy.

B. Plasma spatial and temporal evolution analysis

The spatial and temporal evolution of the laser-induced plasma in air for three distinctive laser energies are measured and studied using a laser shadowgraphy diagnostic in order to understand the dynamic processes of the plasma expansion and relaxation as well as the dynamics of the resulting shock waves by laser heated neutral gas densities. In this technique, a probe laser operating at $\lambda_g = 532$ nm passed through the 1064 nm laser focal region test section where the plasma is formed and then directly falls on to the gated ICCD imaging sensor with a 1:1 ratio on the image plane. Electron densities ranging from $10^{14} - 10^{18} \text{ cm}^{-3}$ in the test section may result in refractive index gradients and appear as bright or dark regions on the shadowgram depending on the sign of the Laplacian of the refractive index. The shadowgraphy diagnostic technique is used to investigate the spatial and temporal evolution of the laser induced plasma obtained to measure the plasma volume, shockwave velocities, and hot core air pressure.

A series of 16 shadowgrams is shown in Fig. 3 for the 170 mJ incident laser energy. Each shadowgram in Fig. 3 has a spatial extent of $13.6 \text{ mm} \times 13.6 \text{ mm}$ and was obtained in the horizontal direction, perpendicular to the axis of 1064 nm IR laser beam that is incident from the top as indicated by the downward arrow in Fig. 3.a. The shadowgrams were obtained over a broad time range, from 35 ns to 800 μs , in order to study the plasma expansion, relaxation,

shockwave propagation as well as the hydrodynamic processes. Experimental time for this study begins with the rise of the laser pulse ($t = 0$). The signal delay timings between the triggering and laser output pulse were measured using a fast oscilloscope and taken in to consideration. The intensity of the shadowgram images acquired at different times was adjusted to enhance the hydrodynamic details of the plasma and neutral density shock. Laser profiles were highly reproducible for each of the energy levels studied and, based on the analysis of extensive time resolved shadowgraphy images, we observe that the laser induced plasma and its hydrodynamic behavior are highly reproducible with variations less than the resolution of the imaging system.

The earliest spatially resolvable data from the shadowgrams was observed at 35 ns. At times earlier than 35 ns, high Bremsstrahlung emission inhibits quality data acquisition. At $t = 35$ ns a ~ 1.6 mm asymmetrically shaped plasma was imaged as shown in Fig. 3.a. The plasma continues to expand asymmetrically up to $\sim 1 \mu\text{s}$ as shown in Fig. 3.a – 3.f. The aspherical shape exhibited by the laser induced plasma along the z-axis exhibits a distinctly smaller radius of surface curvature along the lower edge. The asymmetrical shape of the plasma can be explained by the changing absorption conditions during the initial formation of the system, i.e. during the laser pulse. The initially transparent medium begins to absorb laser radiation at a position in the focusing cone of ionization-threshold power-flux density. The plasma then causes energy deposition to shift toward the incoming laser radiation during the pulse due to three main factors [14]: the inhomogeneity of the incident energy flux causes a spreading of the region in which the localized energy flux exceeds the ionization requirement, the initial shock wave propagates in all directions causing increased absorption, and thermal interaction between the hot plasma region and the air through which the laser energy is passing. The majority of the energy is therefore deposited in the upper region of the plasma nearest to the laser. This effect is clearly observed in

all laser-induced plasma experiments presented here as a distinctly reduced radius of curvature along the lower edge of the plasma and shock wave at $t < 7 \mu\text{s}$. The gas in this focal region gets heated due to the collision of energetic electrons with heavy particles leading to the generation of shock wave as the temperature and pressure in the focal region are higher than that of the surroundings at the end of plasma formation. Because of the asymmetry of the region of the optical discharge propagating along the laser beam the heated neutral gas also encompass an asymmetric volume.

In addition, the presence of ponderomotive force in laser focused plasmas of certain high intensity and short-pulse widths regime was also considered for the cause of plasma asymmetry. The amount of contribution to the plasma volume asymmetry by the ponderomotive force can significantly vary based on the experimental conditions. As referred by several others as summarized by Mulser and Bauer [33], in order for significant presence of ponderomotive force it requires laser intensities of the order of 10^{14} W/cm^2 and tighter focus and very high electron density (10^{20} cm^{-3}) and temperature 1000 eV. Our experimental conditions are clearly not in these regimes rather our laser conditions still appear in the low to moderate intensity and long pulse regime with respect to ponderomotive effects. Therefore in our experimental condition the aspherical nature of the plasma and shock front at early time predominantly caused by a phenomenon of translation absorption [13]. Laser plasma asymmetry dominated by Ponderomotive effects would be expected to produce conical shocks from the focusing cone [33] whereas our shadowgraphy images indicate that the shock fronts appear to be of two colliding spherical shocks, which is consistent with absorption translation [13]. Spherical shock waves were observed even when the plasma remain in conical shape indicating minimal or less ponderomotive forces compared to translation absorption in our experimental regime.

Based on the shadowgrams it is observed that the plasma and the shock wave continue to expand at the same rate up to $t = 1 - 2 \mu\text{s}$. At $t > 1 \mu\text{s}$ (Fig. 3.f – 3.g) an outgoing neutral density shockwave separating from the hot plasma core into the surrounding cold air is clearly visible in the shadowgrams. As shown in Fig. 3.g – 3.k, the shock wave becomes spherically symmetric; however the hot core plasma remains asymmetric along the z-axis. Spherical symmetry is attained by the primary upper shock by overtaking the lower asymmetrical shock. This effect can be observed in Fig. 3.e – 3.g as two bright regions between the two shock waves. This effect was previously quantified by interferometric analysis [30]. The positions and differential velocities of the shock wave are monitored and recorded up to $t = 15 - 20 \mu\text{s}$. At $t > 20 \mu\text{s}$ the shock wave leaves the $13.6 \times 13.6 \text{ cm}^2$ field of view.

The hot core plasma subjects to a sharp deformation soon after the separation of the expanding neutral density shock wave, suggesting that the neutral density shockwave plays an important role for the stability of the hot core plasma expansion by enclosing it as a pressure barrier. At $t = 6 \mu\text{s}$ the deformation of the hot core plasma collapsing inwards at the smaller radius of curvature along the z-axis is observed. The protruding, lower portion of the central hot gas is surrounded by relatively cold air and collapses as it cools during $t = 10 - 50 \mu\text{s}$ (Fig. 3.j – 3.n) leading to inflow of the surrounding colder and denser air in to the hot central core along the z-axis leading to the ultimate destabilization of the system over time, during this time frame the penetration velocities of the cold air influx into the hot core are measured to be $7 - 14 \text{ m/s}$. At times around $60 \mu\text{s}$ and up to $100 \mu\text{s}$ the formation of the vortex-ring type structure is clearly visible and thereafter turbulence begins to dominate.

A series of 16 shadowgrams are shown in Fig. 4 and 5 for the incident laser energies 130 mJ and 70 mJ respectively. For these experimental conditions the laser induced plasma and the

shadowgraphy diagnostics field of view is slightly off centered in the vertical direction such that the displacements of the spherically expanding shockwave can be captured at later delay times. As seen from the shadowgraphy in Fig. 4 and 5, the dynamic processes observed are similar to those observed in Fig. 3 for 170 mJ incident laser energy. This result indicates that the same fundamental physical processes dominating the formation and evolution of the higher energy system are also dominating the lower energy regime. The development of these lower-energy systems, such as shock front positions and velocities, follow the same overall profile pattern as the 170 mJ system with apparently different initial conditions. This is inferred from later figures due to apparently staggered timings, i.e. lower energy velocity profiles appear to be shifted to earlier times. This effect would be expected for similar systems with lower initial velocity, temperature, and pressure conditions induced by the lower energy input from the IR laser.

C. Plasma pressure and volume analysis

The laser induced plasma in air as seen from the shadowgrams is similar to a strong explosion in a homogeneous atmosphere. Such a case is an example of a self-similar flow, in which the flow variables change with time in such a manner that their distributions with respect to the coordinate variable remain similar in time [34]. When a significant amount of laser energy E is deposited in a small focal volume of a gas such as air with pressure $p_0 = 1$ atm, constant specific heat ratio $k = 1.4$ and density ρ_0 during a short time interval creates a plasma and neutral density gas shock with pressure p_1 and ρ_1 behind the shock front expanding and propagating through the gas from the point where the energy is released. Based on the shadowgrams it is evident that both plasma and neutral density gas shock are expanding at the at the same rate until the shock wave separates from the hot core, thus the flow parameters behind the shock front is equivalent to that

of the plasma during the initial expansion stages. The radius R of the expanding plasma and shock front can be governed the relationship $r \propto (E/\rho_0)^{1/5} t^{2/5}$ [14].

At a time t the wave reaches a radius r and encompasses a volume V , whose mass is $M = V\rho_0$. The expanding volume of the laser induced plasma was measured from the shadowgram images and shown in Fig. 6. The plasma volume increases rapidly at early times $t < 1 \mu s$ and plateau at times $t > 2 \mu s$, which corresponds to the separation of the shock from the hot core. The propagation velocity v of the plasma and shock front is

$$v = \frac{\delta r}{\delta t} \sim \frac{2}{5} \left(\frac{E}{\rho_0} \right)^{\frac{1}{5}} t^{\frac{-3}{5}} \quad (2)$$

The pressure behind the shock front can be expressed as [14]

$$p_1 = \left(\frac{2}{k} + 1 \right) \rho_0 v^2 \quad (3)$$

Thus based on the measured velocity of the shock front from the shadowgrams the pressure behind it was obtained and shown in Figure 6 as a function of time. At times $t < 100$ ns pressures of 100 - 1000 atm were observed. These pressures rapidly decreased from 100 to 10 atm during $t = 100$ ns - $1 \mu s$, then at times $t > 1 \mu s$ pressure approaches one atmosphere.

D. Plasma temperature analysis

The decaying shock wave by spherical expansion represents a gas-dynamic discontinuity and it can be clearly monitored from the shadowgrams obtained at small time increments. For each of the three absorbed laser energies 155 mJ, 120 mJ, and 60 mJ, the radial position of the expanding laser induced plasma and neutral gas density spherical shock front is measured as shown in Fig. 7 in logarithmic time scale. The focal point of the focusing objective lens is used as the reference

center and from which the position of the shock wave was measured as a function of time. In a coordinate system moving radially along with the shock wave away from the center is quasi-steady, in which the time δt during which the shock wave travels through a distance of δr . The expansion velocity v of the laser induced plasma and neutral gas density shock front for the three laser energies are measured from the shadowgrams by calculating $v = \delta r / \delta t$ and is shown in Fig. 7. High hypersonic shock wave velocities of 22 - 24 km/s were observed at the earliest times $t < 15$ -35 ns and it rapidly slows down to near-hypersonic velocities of 2 - 4 km/s at $t = 100$ ns. Supersonic velocities of 1.7 km/s were observed at times $t = 120$ to 150 ns and then at $t > 20 \mu s$ the velocities reach sonic velocities. The shock wave reached sonic velocity around $t = 20 \mu s$ after leaving the experimental field of view. Using a 532 nm laser interferometry diagnostics [17, 30, 35], we have measured the plasma density of $\sim 10^{18} \text{ cm}^{-3}$ at 125 ns the earliest time possible (detailed density analysis are presented elsewhere). The measurements of the shock position and velocity were validated by comparing with the Taylor-Sedov scaling theory [34, 36, 37], in which we have mapped our experimental results on to the Taylor-Sedov scaling theory of plasma expansion based on the energy deposited. We have plotted the theoretical curve with the series-1 measurements in the sub-plot of Fig. 7. We have obtained very close results comparing with the theory confirming a very minimal backscattering and majority of the energy ($\sim 90\%$ of incident energy) is being absorbed in the focal region. In this comparison with the Taylor-Sedov scaling theory, the analytical expression for the distance R between the center of the blast and the shock front is given by the Taylor-Sedov scaling [34, 36, 37] $R = \lambda(E/\rho)^{0.2} t^{0.4}$ is used. In which λ is a scaling factor near unity, E is the energy absorbed, and ρ is the density of the medium into which the shock is propagating. The Taylor-Sedov blast-wave scaling approximates result close match indicating that the coupled energy values are acceptable

[36]. On the other hand, the theoretical models for the laser air plasma creation at much shorter laser pulse widths (femtoseconds) and much higher laser fluxes (10^{16} W/cm²) have shown that the laser beam focusing and scattering can be substantially modified [38].

In a gas such as air with constant specific heat, the temperatures behind the shock wave T is proportional to the square of the shock wave propagation velocity v . Zel'dovich and Raizer [14] have tabulated the flow quantities behind a shock wave such as the temperature and velocity in air such as the with standard conditions ahead of the shock wave with pressure $p_0 = 1$ atmosphere and temperature $T_0 = 293^\circ$ K. Fig. 8 shows the temperature decay based on the measured velocities of the plasma and gas shock. The electron temperature behind the shock front approach values of 4 - 5 eV at $t = 15 - 20$ ns and the temperature decays rapidly to 0.3 - 0.5 eV at 100 ns and continues to drop to 0.1 eV at 300 ns.

E. Plasma luminosity and lifetime analysis

The temporal decay of the light emission from the laser induced plasma can be an indicator of the plasma electron temperature decay as the excited atoms lose excitation energy through photon emission. A higher emission coefficient indicates higher number of excited atoms and thus a higher temperature. The visible luminosity of the laser induced plasma for the three laser energies are collected using the 1 ns response high-speed visible wavelength photodetector shown in Fig. 1. A clear distinguishable drop in the light intensity can be observed in all three cases and in which higher the laser energy longer the plasma luminosity lasts. The luminosity can also be used as an indicator of plasma lifetime and the distinctive drop in light intensity is observed at distinctive times for each of the laser energies. The timings at which the plasma

luminosity suddenly drops approximately corresponds to the plasma and shock wave expansion velocities decaying and transiting from near-hypersonic velocity regime to supersonic velocity regime. The light intensity after the significant drop is still above the background noise level as seen in Fig. 9, however it decays at a much slower rate and reaches the background level near 2 μ s.

Summary

Laser-induced plasmas were created in laboratory air at 760 Torr by a pulsed Nd:YAG laser operating at the 1064 nm fundamental. Three experimental laser energies and pulse widths were examined such as 170 mJ at 8 ns, 130 mJ at 7 ns and 65 mJ at 12 ns. The laser beam was focused downwards to a $\sim 7 \mu\text{m}$ spot size using IR coated optics and 15x objective lens, and the resulting laser flux densities range from 4-14 TW/cm². The downward laser focusing configuration will facilitate our future work on laser plasmas in liquids. The laser induced air plasma was studied using high-speed laser shadowgraphy, an optical diode and a wavelength-calibrated energy measuring system. A laser shadowgraphy diagnostics was setup to investigate the spatio-temporal evolution and hydrodynamic behavior of the 1064 nm laser induced plasma and neutral density shock during the formation, expansion and collapsing stages. The laser shadowgraphy diagnostics was realized using a 10 mW 532 nm probe optical laser beam expanded by a magnification factor of 20X and passed through the 1064 nm laser focused plasma. The transmitted probe laser beam was captured at 5 ns gating time with high spatial resolution using a gated ICCD. Shadowgraphy images of the laser plasma were taken for the three laser energy levels from 15 ns to 1 ms.

Results quantifying shock propagation velocity and plasma volume indicate similarly shaped profiles at different expansion velocities and shifting later in time for lower input energy with longer pulse width. This effect would be expected for similar systems with lower initial velocity, temperature, and pressure conditions induced by the lower energy input from the 1064 nm laser. The observed plasma and shock formations were aspherical due to absorption translation during the initial laser-energy coupling. Absorption translation occurs due to the spreading on the ionization region caused by inhomogeneous incident laser radiation and the

propagation of the absorption front toward the laser occurs due to shock propagation and radiative interaction between the plasma and the air through which the laser is propagating. The aspherical feature apparently seeded the hydrodynamic instability leading to the ultimate destabilization of the hot gaseous core after approximately $10\ \mu\text{s}$. During the first microsecond of experiments, the hot plasma core expands at the same rate as the shock wave. Shock propagation velocity and plasma volume for three laser pulse series indicate the similarly shaped profiles at different expansion velocities. Early plasma expansion velocities of $20\ \text{km/s}$ were measured and using Hugoniot relations the neutral shock pressures and temperatures were inferred and the results at the early plasma expansion stage were found to be over 1000 atmospheres and $4\ \text{eV}$. The shock front separates from the system $1 - 2\ \mu\text{s}$ after formation in rough correlation with the luminosity profile dropping to noise level. After $2\ \mu\text{s}$ the plasma is considered to be a hot gaseous core. The temporal plasma luminosity was measured using a fast $2\ \text{ns}$ optical diode to determine plasma lifetime. The active plasma lifetime through plasma self-luminescence measurements indicate significantly varied plasma lifetimes for each of the input energies and the intensity profiles decayed exponentially until a rapid decrease to near-noise levels between $200\ \text{ns}$ and $500\ \text{ns}$. Further optical diagnostics such as two-wavelength laser interferometry and optical emission spectroscopy will be carried out to further investigate the laser induced plasma characteristics.

Acknowledgements

This work was partially supported by the College of Science and Engineering, School of Engineering and Computing Sciences at the Texas A&M University-Corpus Christi, Texas Research and Development Fund (TRDF) and the Department of Defense (DOD) /Army grant (W81XWH-10-1-0923) administered by the U.S. Army Medical Research & Materiel Command (USAMRMC) and the Telemedicine & Advanced Technology Research Center (TATRC), at Fort Detrick, MD.

List of figure captions

Figure 1. Schematic of the experimental and diagnostic setup: A - power control attenuator, BE – 20x beam expander, BS - beam splitter, EM – energy meter, F – 532 nm dichroic filter, ICCD - intensified charge-couple device, M – high-power infrared mirror, ND – Neutral density filter, Obj – 15x objective lens, PD – photodiode.

Fig. 2: An overlay of three experimental laser intensities - series 1: 170 mJ (solid), series 2: 130 mJ (dash) black and series 3: 65 mJ (dot).

Fig. 3. Shadowgraphy images of 1064 nm laser focused plasma in air with 170 mJ, 8 ns laser pulse (Series 1). Gating time $t_g = 5$ ns time and spatial extent of each image is 13.6 x 13.6 mm.

Fig. 4. Shadowgraphy images of 1064 nm laser focused plasma in air with 130 mJ, 7 ns laser pulse (Series 2). Gating time $t_g = 5$ ns time and spatial extent of each image is 13.6 x 13.6 mm.

Fig. 5. Shadowgraphy images of 1064 nm laser focused plasma in air with 65 mJ, 12 ns laser pulse (Series 3). Gating time $t_g = 5$ ns time and spatial extent of each image is 13.6 x 13.6 mm.

Fig. 6. Temporal decay of downstream shock pressure (neutral density) and expansion of plasma volume for series 1 (170 mJ), series 2 (130 mJ) and series 3 (65 mJ).

Fig. 7: Velocity and radial position of the shock front for series 1 (170 mJ), series 2 (130 mJ) and series 3 (65 mJ). Subplot- comparison of experimental measurements with Taylor-Sedov blast-wave scaling (solid square – experimental series 1, short-dash – Taylor-Sedov theory).

Fig. 8: Shock front temperature decay for series 1 (170 mJ), series 2 (130 mJ) and series 3 (65 mJ) with equivalent inset in log-log plot. Subplot- comparison of experimental measurements with Taylor-Sedov blast-wave scaling (solid square – experimental series 1, short-dash – Taylor-Sedov theory).

Fig. 9: Temporal optical emission intensity from laser-induced plasma for series 1 (170 mJ), series 2 (130 mJ) and series 3 (65 mJ) with equivalent inset in log-scale plot.

References

- [1] A. N. Panchenko, *et al.*, "Pulsed IR laser ablation of organic polymers in air: Shielding effects and plasma pipe formation," *Journal of Physics D: Applied Physics*, vol. 44, 2011.
- [2] T. T. Mon, *et al.*, "Experimental micromachining of silicon with Nd-YAG laser," in *International Conference on Experimental Mechanics 2010, ICEM10, November 29, 2010 - December 1, 2010*, Malaysia, 2011, pp. 244-248.
- [3] P. G. Ashmore, *Photochemistry and reaction kinetics*. London: Cambridge Univ. Press, 1967.
- [4] P. U. Andersson and L. Holmlid, "Fusion Generated Fast Particles by Laser Impact on Ultra-Dense Deuterium: Rapid Variation with Laser Intensity," *Journal of Fusion Energy*, pp. 1-8, 2011.
- [5] R. G. Adelgren, *et al.*, "Axisymmetric jet shear-layer excitation by laser energy and electric arc discharges," *AIAA Journal*, vol. 43, pp. 776-791, Apr 2005.
- [6] R. G. Adelgren, *et al.*, "Control of Edney IV interaction by pulsed laser energy deposition," *AIAA Journal*, vol. 43, pp. 256-269, Feb 2005.
- [7] D. W. Riggins and H. F. Nelson, "Hypersonic flow control using upstream focused energy deposition," *AIAA Journal*, vol. 38, pp. 723-725, Apr 2000.
- [8] L. N. Myrabo, *et al.*, "Reduction of drag and energy consumption during energy release preceding a blunt body in supersonic flow," *High Temperature*, vol. 42, pp. 901-910, Nov-Dec 2004.
- [9] D. Riggins, *et al.*, "Blunt-body wave drag reduction using focused energy deposition," *AIAA Journal*, vol. 37, pp. 460-467, Apr 1999.
- [10] T. X. Phuoc, "Laser spark ignition: experimental determination of laser-induced breakdown thresholds of combustion gases," *Optics Communications*, vol. 175, pp. 419-423, Mar 1 2000.
- [11] K. Toyoda, *et al.*, "Thrust performance of a CW laser thruster in vacuum," *Vacuum*, vol. 65, pp. 383-388, May 27 2002.

- [12] B. Dromey, *et al.*, "The plasma mirror - A subpicosecond optical switch for ultrahigh power lasers," *Review of Scientific Instruments*, vol. 75, pp. 645-649, 2004.
- [13] Y. P. Raizer, *Gas Discharge Physics*. Berlin, Germany: Springer-Verlag, 1991.
- [14] Y. B. Zeldovich and Y. P. Raizer, *Physics of Shock Waves and High-Temperature Hydrodynamic Phenomena* vol. 1. New York: Academic Press, 1966.
- [15] N. Kroll and K. M. Watson, "Theoretical Study of Ionization of Air by Intense Laser Pulses," *Physical Review A*, vol. 5, pp. 1883-1905, 1972.
- [16] I. P. Shkarofsky, "Review of gas-breakdown phenomena induced by high-power lasers," *RCA Review*, vol. 35, pp. 48-78, 1974 1974.
- [17] M. Thiagarajan and J. Scharer, "Experimental investigation of ultraviolet laser induced plasma density and temperature evolution in air," *Journal of Applied Physics*, vol. 104, 2008.
- [18] M. Thiagarajan and J. E. Scharer, "Experimental Investigation of 193-nm Laser Breakdown in Air," *Ieee Transactions on Plasma Science*, vol. 36, pp. 2512-2521, Oct 2008.
- [19] R. Giar and J. Scharer, "Focused excimer laser initiated, radio frequency sustained high pressure air plasmas," *Journal of Applied Physics*, vol. 110, Nov 15 2011.
- [20] J. S. Hummelt and J. E. Scharer, "Excitational energy transfer enhancing ionization and spatial-temporal evolution of air breakdown with UV laser radiation," *Journal of Applied Physics*, vol. 108, Nov 1 2010.
- [21] J. Way, *et al.*, "Experimental measurements of multiphoton enhanced air breakdown by a subthreshold intensity excimer laser," *Journal of Applied Physics*, vol. 106, Oct 15 2009.
- [22] G. Bekefi, *Principles of Laser Plasmas*. New York: Wiley, 1976.
- [23] C. H. Chan, *et al.*, "Signifi ant loss me hanisms in gas breakdown at 10.6 μ ," *Journal of Applied Physics*, vol. 44, pp. 1179-1188, 1973 1973.
- [24] H. Yan and M. e. a. Adलगren, "Laser Energy Deposition in Quiescent Air," *AIAA Aerospace Sciences Meeting*, vol. 41, p. 1988, 2003.

- [25] A. D. MacDonald, *Microwave Breakdown in Gases*. New York: Wiley, 1966.
- [26] J. Stricker and J. G. Parker, "Experimental investigation of electrical breakdown in nitrogen and oxygen induced by focused laser radiation at 1.064 μ ," *Journal of Applied Physics*, vol. 53, pp. 851-855, 1982.
- [27] U. Jordan, *et al.*, "On the effective diffusion length for microwave breakdown," *IEEE Transactions on Plasma Science*, vol. 34, pp. 421-430, Apr 2006.
- [28] M. Thiyagarajan and S. Thompson, "Optical breakdown threshold investigation of 1064 nm laser induced air plasmas," *Journal of Applied Physics*, vol. 111, p. 073302, 2012.
- [29] M. Villagran-Muniz, *et al.*, "Shadowgraphy and interferometry using a CW laser and a CCD of a laser-induced plasma in atmospheric air," *Ieee Transactions on Plasma Science*, vol. 29, pp. 613-616, Aug 2001.
- [30] H. Zhang, *et al.*, "Optical interferometric analysis of colliding laser produced air plasmas," *Journal of Applied Physics*, vol. 106, pp. 063308-1-063308-5, 2009.
- [31] G. S. Settles, *Schlieren and shadowgraph techniques: visualizing phenomena in transparent media*: Springer, 2001.
- [32] H. Hutchinson, *Principles of Plasma Diagnostics*: Cambridge University Press, 2002.
- [33] P. Mulser and D. Bauer, *High power laser matter interaction*: Springer, 2010.
- [34] L. Sedov and F. Jafari, "Similarity and dimensional methods in mechanics, tenth edition," *Applied Mechanics Reviews*, vol. 47, pp. B21-B21, 1994.
- [35] B. V. Weber and S. F. Fulghum, "A high sensitivity two-color interferometer for pulsed power plasmas," *Rev. Sci. Instrum*, vol. 68, p. 02, 1997.
- [36] X. Zeng, "Energy deposition and shock wave propagation during pulsed laser ablation in fused silica cavities," *Journal of Physics D: Applied Physics*, vol. 37, pp. 1132-1136, 2004.
- [37] G. Callies, *et al.*, "Time-Resolved Observation of Gas-Dynamic Discontinuities Arising during Excimer-Laser Ablation and Their Interpretation," *Journal of Physics D-Applied Physics*, vol. 28, pp. 794-806, Apr 14 1995.

- [38] J. H. Shin, *et al.*, "Non-linear plasma effects on laser-induced terahertz emission from the atmosphere," *Physics of Plasmas*, vol. 19, Feb 2012.

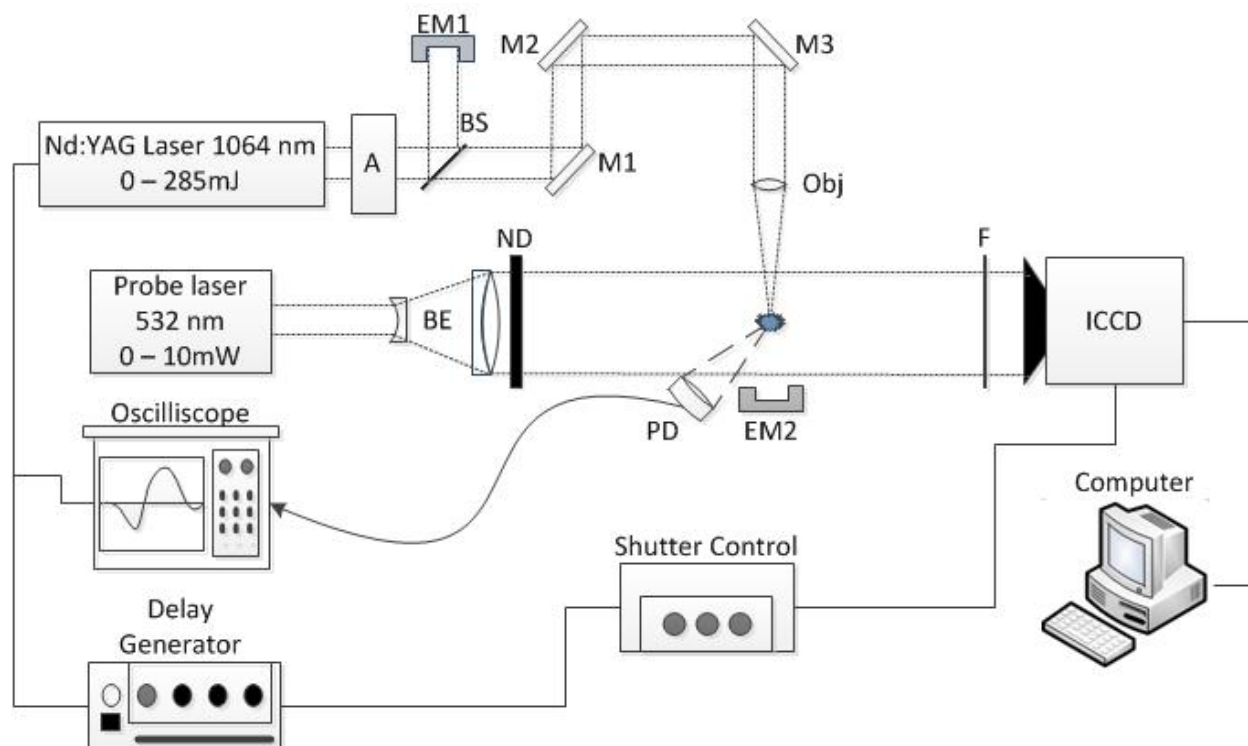


Fig 1. Schematic of the experimental and diagnostic setup: A - power control attenuator, BE – 20x beam expander, BS - beam splitter, EM – energy meter, F – 532 nm dichroic filter, ICCD - intensified charge-couple device, M – high-power infrared mirror, ND – Neutral density filter, Obj – 15x objective lens, PD – photodiode.

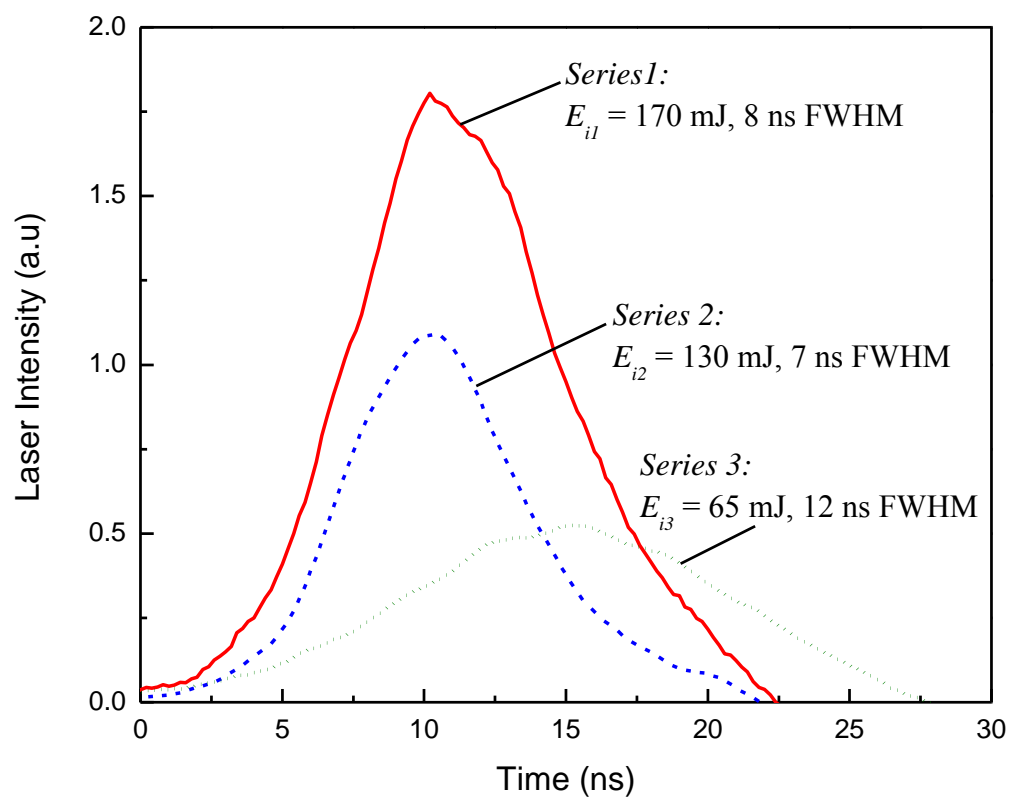


Fig. 2. An overlay of three experimental laser intensities - series 1: 170 mJ (solid), series 2: 130 mJ (dash) black and series 3: 65 mJ (dot).

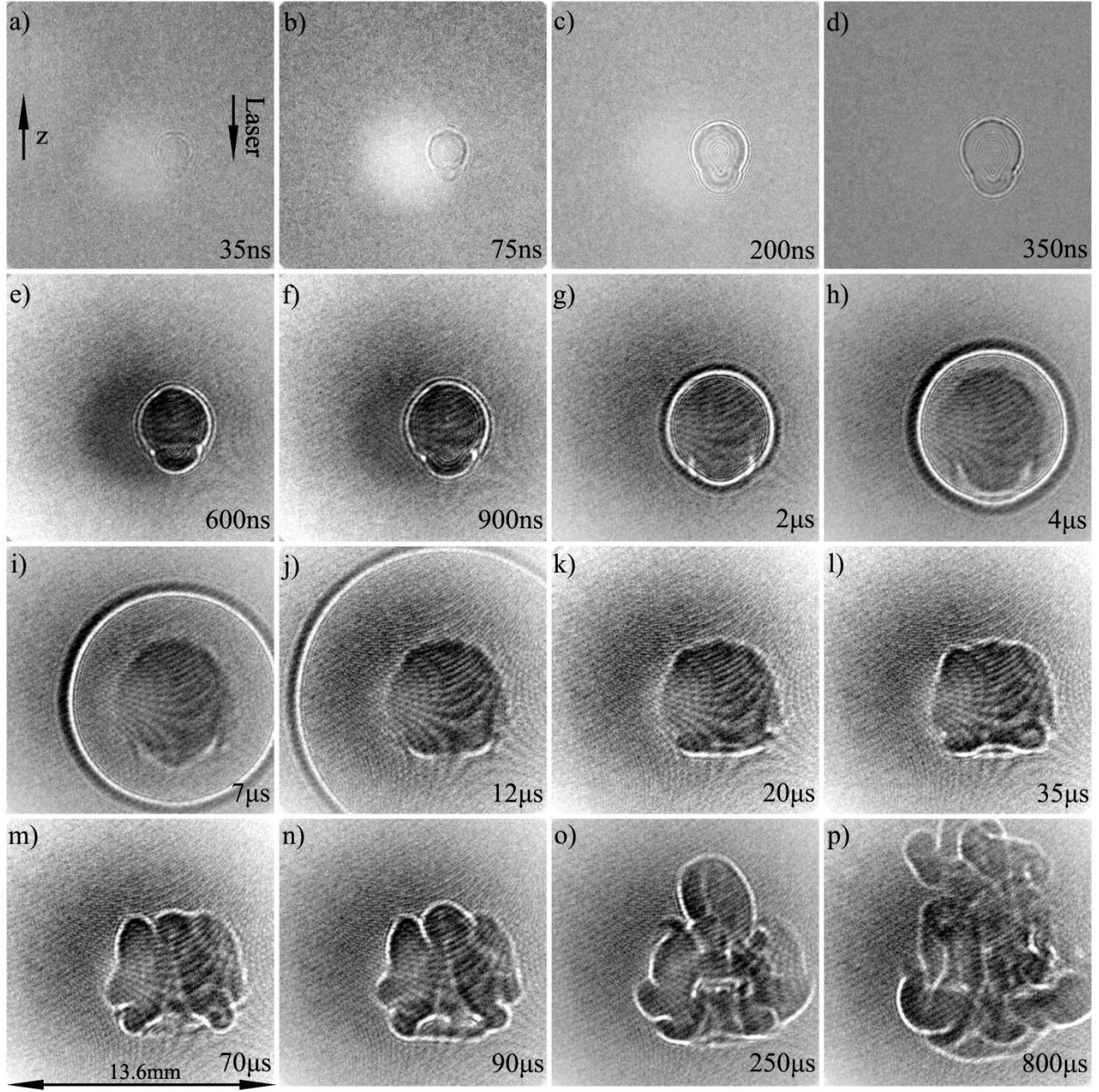


Fig. 3. Shadowgraphy images of 1064 nm laser focused plasma in air with 170 mJ, 8 ns laser pulse (Series 1). Gating time $t_g = 5$ ns time and spatial extent of each image is 13.6 x 13.6 mm.

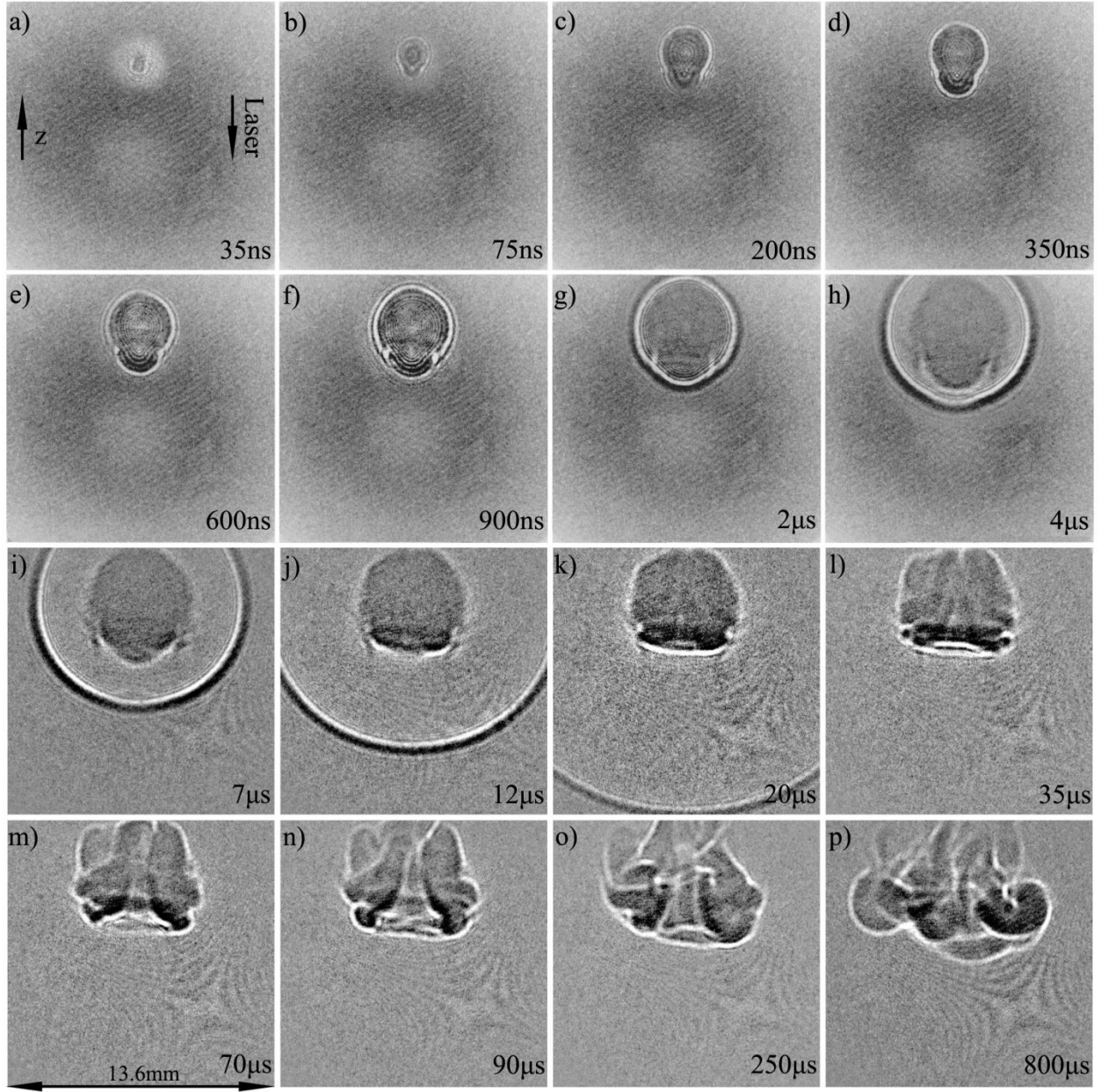


Fig. 4. Shadowgraphy images of 1064 nm laser focused plasma in air with 130 mJ, 7 ns laser pulse (Series 2). Gating time $t_g = 5$ ns time and spatial extent of each image is 13.6 x 13.6 mm.

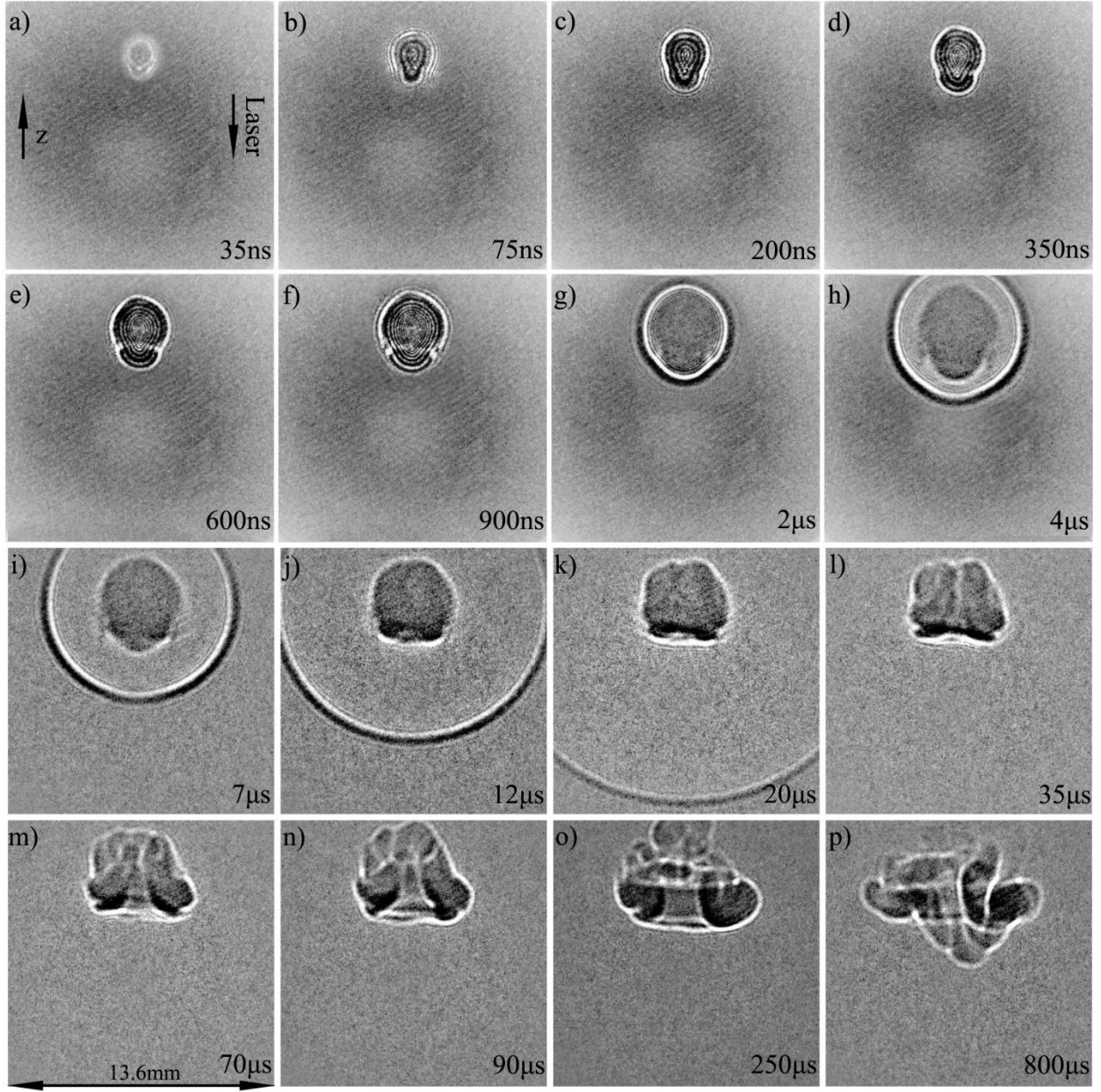


Fig. 5. Shadowgraphy images of 1064 nm laser focused plasma in air with 65 mJ, 12 ns laser pulse (Series 3). Gating time $t_g = 5$ ns time and spatial extent of each image is 13.6 x 13.6 mm.

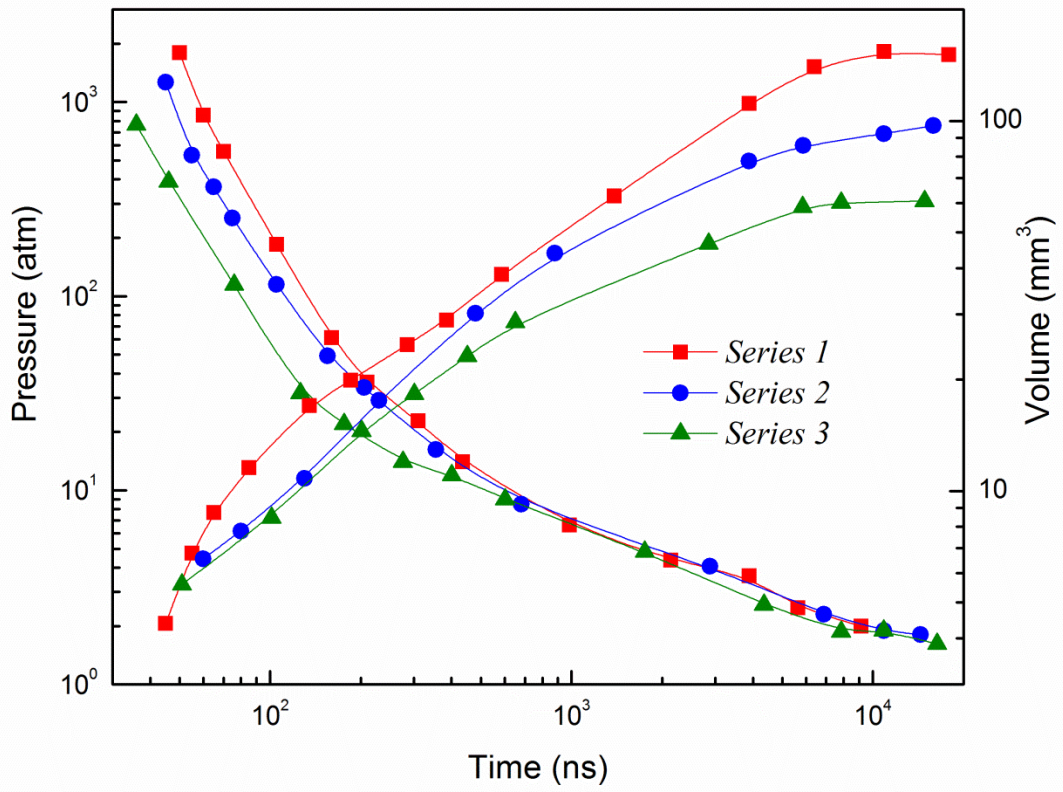


Fig. 6. Temporal decay of downstream shock pressure (neutral density) and expansion of plasma volume for series 1 (170 mJ), series 2 (130 mJ) and series 3 (65 mJ).

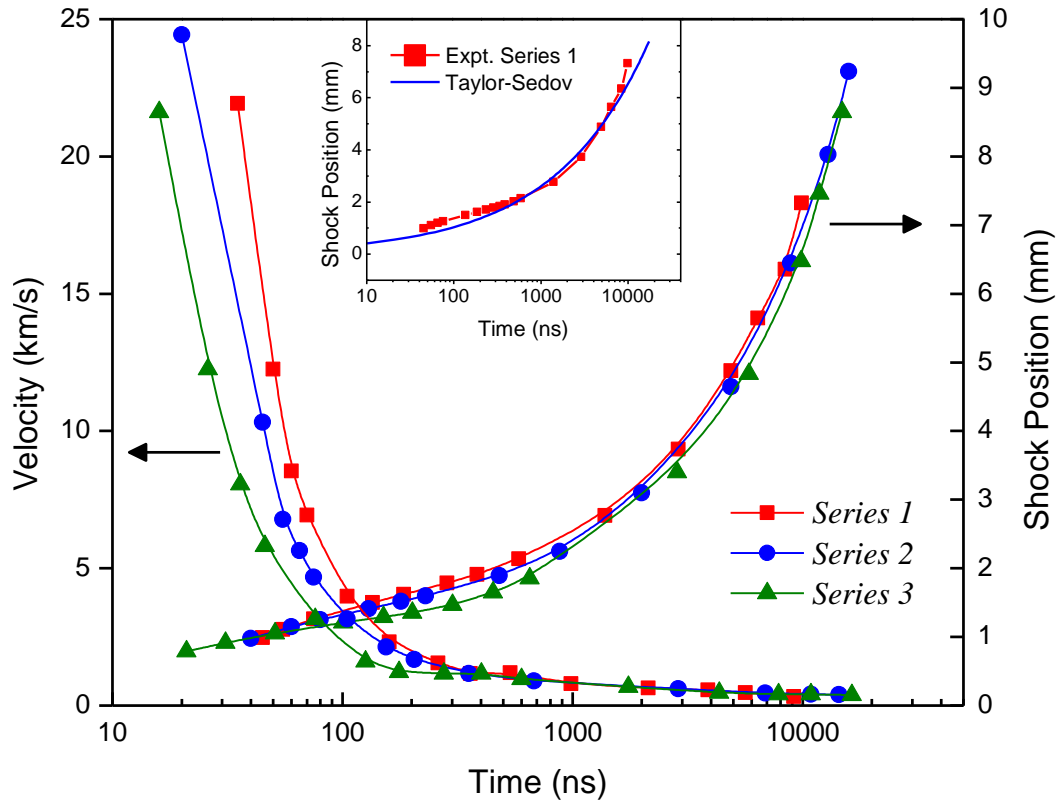


Fig. 7: Velocity and radial position of the shock front for series 1 (170 mJ), series 2 (130 mJ) and series 3 (65 mJ). Subplot- comparison of experimental measurements with Taylor-Sedov blast-wave scaling (solid square – experimental series 1, short-dash – Taylor-Sedov theory).

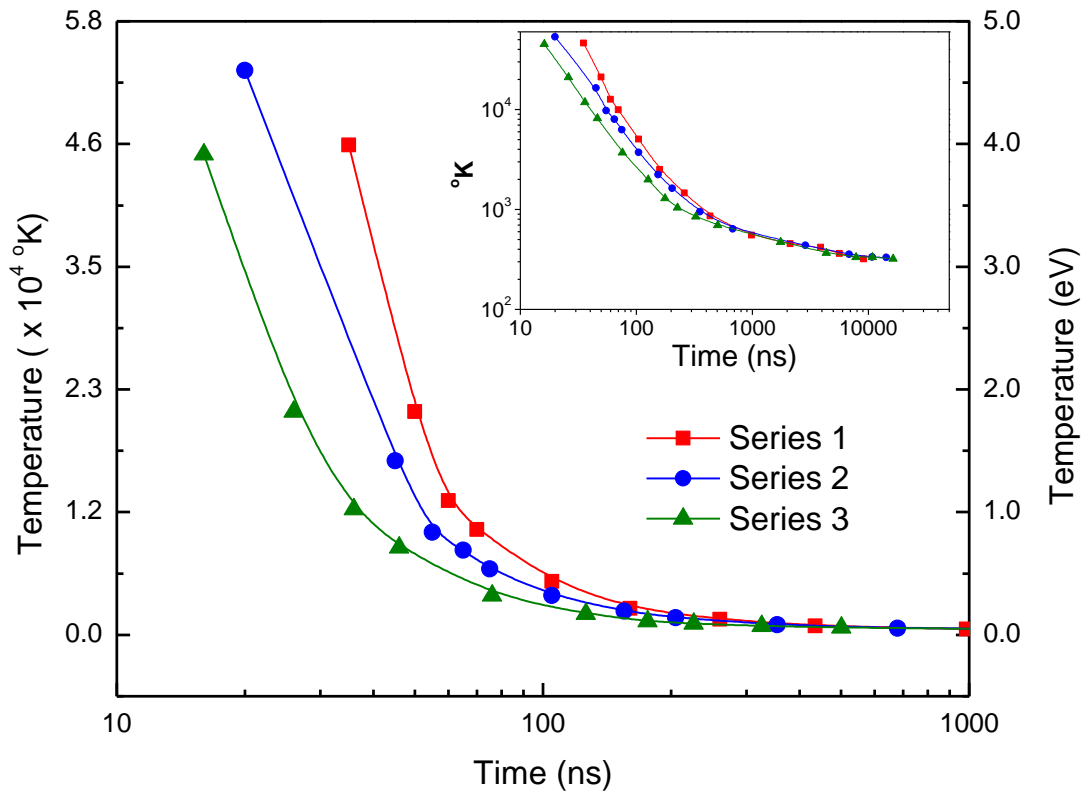


Fig. 8: Shock front temperature decay for series 1 (170 mJ), series 2 (130 mJ) and series 3 (65 mJ) with equivalent inset in log-log plot.

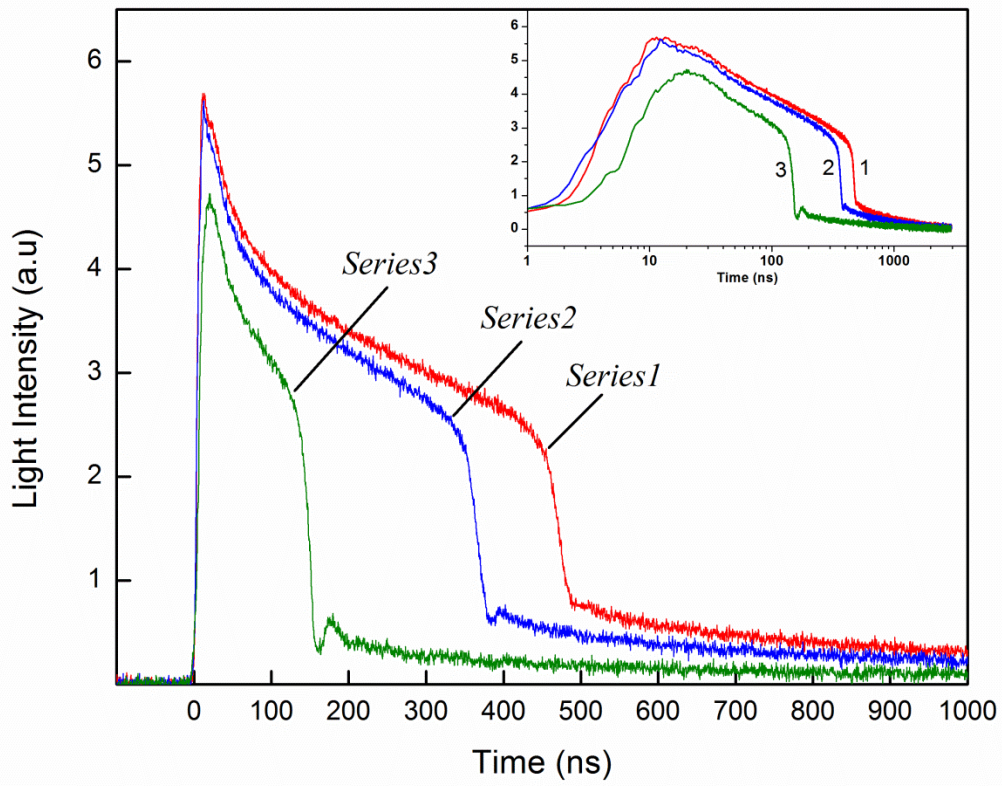


Fig. 9: Temporal optical emission intensity from laser-induced plasma for series 1 (170 mJ), series 2 (130 mJ) and series 3 (65 mJ) with equivalent inset in log-scale plot.

Dr. Magesh Thiagarajan is the Director of Plasma Engineering Research Lab (PERL) and Assistant Professor of Engineering at the Texas A&M University – Corpus Christi (TAMUCC) since 2009. Earlier he was a lead engineer for the Global Research Center - General Electric Company in Albany, N.Y. He received his Ph.D. in 2008 (work completed December 2007) from University of Wisconsin-Madison and M.S. from the University of Tennessee Knoxville and B.S. from University of Madras. His current research is focused on laser plasmas in gases, liquids and at phase boundaries, laser shadowgraphy, laser interferometry, optical emission spectroscopy, non-thermal plasma jets and its applications in materials processing, microbial deactivation and cancer treatment. He has published two books on laser induced plasmas and its optical diagnostics. He is a recipient of the UTK Citation Award for professional promise, IEEE Fellowship Award, University of Madras Gold Medalist Award, Wisconsin Governor's and Texas Coastal Bend Best Technology Business Award.

Kenneth Williamson

Kenneth Williamson is a postdoctoral research associate at the Plasma Engineering Research Lab (PERL) at the Texas A&M University at Corpus Christi since 2011. He received his Ph.D. in Experimental High Energy Density Plasma Physics in 2011 and B.S. in 2004 from University of Nevada Reno.

Anudeep Reddy Kandi

Anudeep Reddy Kandi is a graduate student in Computer Science at the School of Engineering and Computing Sciences at the Texas A&M University Corpus Christi.

Atmospheric pressure resistive barrier air plasma jet induced bacterial inactivation in aqueous environment

Magesh Thiagarajan^{a)}, Abdollah Sarani and Xavier Gonzales

Plasma Engineering Research Lab (PERL), College of Science and Engineering,
Texas A&M University-Corpus Christi, Texas 78412, USA

(Received

An atmospheric pressure resistive barrier air plasma jet is designed to inactivate bacteria in aqueous media in direct and indirect exposure modes of treatment. The resistive barrier plasma jet is designed to operate at both DC and standard 50-60 Hz low frequency AC power input and the ambient air at 50% humidity level was used as the operating gas. The voltage-current characteristics of the plasma jet were analyzed and the plasma power was measured to be 26 Watt. The plasma jet rotational temperatures (T_{rot}) are obtained from the optical emission spectra, from the $N_2C-B(2+)$ transitions by matching the experimental spectrum results with the SPECAIR simulation spectra. The reactive oxygen and nitrogen species were measured using optical emission spectroscopy and gas analyzers, for direct and indirect treatment modes. The nitric oxides (NO) were observed to be the predominant long lived reactive nitrogen species produced by the plasma. Three different bacteria including *Staphylococcus aureus* (Gram-positive), *Escherichia coli* (Gram-negative) and *Neisseria meningitidis* (Gram-negative) were suspended in an aqueous media and treated by the resistive barrier air plasma jet in direct and indirect exposure modes. The results show that a near complete bacterial inactivation was achieved within 120 second for both direct and indirect plasma treatment of *S. aureus* and *E. coli* bacteria. Conversely, a partial inactivation of *N. meningitidis* was observed by 120 second direct

plasma exposure and insignificant inactivation was observed for the indirect plasma exposure treatment. Plasma induced shifts in *N. meningitidis* gene expression was analyzed using *pilC* gene expression as a representative gene and the results showed a reduction in the expression of the *pilC* gene compared to untreated samples suggesting that the observed protection against NO may be regulated by other genes.

^{a)} Author to whom correspondence should be addressed. Electronic mail: magesh@tamucc.edu.

I. INTRODUCTION

In recent years, there has been a significant interest in the development of new atmospheric pressure plasma sources and their characterization for integration in various biomedical applications.¹⁻⁴ Particularly the bacterial inactivation in aqueous media by atmospheric pressure plasmas is gaining significant and widespread importance as an efficient sterilization technology compared to the current conventional decontamination methods. The bacterial contamination of water and other aqueous media is a predominantly significant concern to society as there are more than 100 different types of bacteria, viruses and microorganisms living in aqueous media.⁵ The traditional bacterial inactivation methods in liquids are based on heat treatment, or chemical treatments with exposure to chlorine, or UV radiation methods or in combinations of these. These currently used conventional sterilization methods are not suitable for heat and drug resistant bacteria and they also suffer by several drawbacks including the complex processes involved, unsuitability to heat sensitive materials accompanied with liquids, emission of toxic residual gases or radiation health safety issues.⁵ Consequently, there is a substantial need for an efficient and alternative sterilization technique for aqueous media such as water. The development of new atmospheric pressure plasma sources which produces partially ionized gases containing wide range of radicals and key inactivation chemical active species such as nitric oxides (NO_x and N_xO_y), singlet oxygen, ozone (O_3), active hydroxyl (OH) radicals, reactive oxygen species (ROS), reactive nitrogen species (RNS), UV radiation, charged particles. The plasma based inactivation of bacteria on solid surfaces is widely researched,⁶ using a range of operating gases mostly using helium or argon as the carrier gas, however there remains limited investigation on the inactivation of bacteria in aqueous environments using atmospheric pressure plasmas particularly using ambient air as the operating gas.

The antimicrobial efficacy of plasmas depends on the type of the plasma source and mechanism of plasma generation. Recently, different non-thermal atmospheric pressure plasma sources with varying geometries, excitation frequencies and operating gases have been developed for biomedical applications.⁷⁻¹⁰ The plasma sources particularly reported for biological decontamination includes DC or Pulsed coronas, capacitive coupled dielectric barrier discharges (DBD), atmospheric pressure plasma jets and microwave driven micro plasma sources.¹¹⁻¹⁴ Among these types of plasma sources the atmospheric pressure plasma jets have gained much interest in the recent past due to its ability to penetrate into narrow gaps with high aspect ratio for biomedical applications with complex 3D surface geometries, capillaries and microstructure dental cavities.¹⁵⁻¹⁸ Atmospheric pressure plasma jets can be utilized in direct or remote mode; however, most of the application works in direct plasma treatment and its high etch rate results in destruction of the microorganisms in surfaces.^{19,20} Most of the recently reported atmospheric pressure plasma jets primarily use gases such as helium or argon as the operating gas with or without oxygen/nitrogen admixtures. Conversely, there has been an increasing interest on atmospheric plasmas using ambient air as the operating gas particularly for remote and military applications intended for bacterial decontamination. Portability of the plasma source and its ability to operate in either battery (DC) powered or standard 50-60Hz low frequency AC power is also critical for such remote applications. Another key question that may arise regarding the inactivation of bacteria in liquid suspension is, if the plasma induced active species such as the nitric oxides (NO) produced by the plasma would be able to diffuse into liquid media. It was noted in a previous study that NO can diffuse into liquid media such as water and saline.²¹ Similarly, it was reported that gliding arc plasma was directed over water, which activated the water with plasma chemistries and it was successful in bacterial

inactivation.²² Another reason for utilizing the aqueous suspension model for bacterial inactivation was that bacterial growth and infection inside a wound, cavity, or nasal passage (in the case of *N. meningitidis*) would not be on a completely dry surface. This work presents the design and characterization results of our newly developed portable and light weight atmospheric pressure resistive barrier (RB) air plasma jet in direct and indirect treatment modes. The bacterial inactivation in aqueous media were tested using the RB plasma jet on three different infectious bacteria including *Staphylococcus aureus* (Gram-positive), *Escherichia coli* (Gram-negative) and *Neisseria meningitidis* (Gram-negative) in both direct and indirect modes and the results are presented.

II. EXPERIMENT

A. Atmospheric pressure resistive barrier air plasma jet

The schematic representation of the atmospheric pressure resistive barrier (RB) air plasma jet is shown in Fig. 1(a), together with an image of the air plasma jet. Basically, the RB plasma jet consists of central deionized water cooled cylindrical electrode surrounded by deionized water cooled high density alumina ceramic resistive coating. The central electrode which is approximately 1 cm diameter and 10 cm long is surrounded by a double layer hollow ground electrode separated by an electrode gap space of 2 mm. Discharge streamers are formed between the high-voltage resistive electrode and the ground electrode. With applying enough voltage, the air passing through the RB plasma jet gets ionized and exits through a 2 mm pinhole type opening at the tip of the plasma source generating a stable plasma jet and a continuous flow of active species such as ROS and RNS. The discharge streamers formed in the cylindrical hollow electrode configuration are dynamic with respect to its location between the electrodes,

which also assists in preventing localized heating and arc formation. The presented RB plasma jet is developed based on the principles of large volume non-thermal resistive barrier discharge (RBD)²³⁻²⁵ and can be used in both direct and indirect plasma exposure modes as shown in Fig. 1(b). Direct exposure of plasma involves, exposure of plasma directly on to a target treatment surface whereas the indirect plasma exposure involves, exposure of only the ROS and RNS generated by the plasma instead of the plasma itself, thus eliminating the effect of any possible UV radiation produced by plasma. For the indirect exposure method the concentrations of the nitric oxides are preserved by reducing the plasma temperature rapidly through a separate external small efficient cooling unit.

The RB plasma jet operates in both DC and low frequency AC, such as the standard operating voltages 120 V/60 Hz and 230 V/50 Hz. The power supply is stepped-up with using a transformer (6 kV, 30 mA (max)). In addition, the power supply unit also houses transistor-transistor logic (TTL) and relay controls to select between AC and DC, and power levels and flow controls. The RB plasma jet uses atmospheric pressure air as the operating gas. A 12 V DC air compressor is used to force the air through the electrode gap space of the RB plasma jet. Thus, the plume length, plasma power and ROS including nitric oxides at the tip of the handheld plasma jet tip are controlled and maintained. The power supply unit also contains a mini 12 V DC water pump (Geo-Inline) for cooling the electrodes in the handheld plasma probe unit as well as the optional external cooling unit. The entire RB plasma source is very compact, portable and light weight. It is constructed to fit within $12 \times 10 \times 10$ inch³ portable metallic case and the entire power supply and RBS plasma source weighs approx. 20 lbs.

B. Diagnostics

The voltage applied to the high-voltage electrode is measured using a high voltage probe (Tektronix P6015A) and the discharge current is measured using a current probe (Tektronix TCP202). The voltage–current waveforms are recorded using a 2 GHz digital oscilloscope (Tektronix TDS3034C). Accurate measurement of gas temperatures of the RB plasma jet is a significant experimental challenge. Due to electrical interference using conventional thermocouple inside the discharge can lead to inaccurate measurements. Therefore, the optical emission spectroscopy^{26,27} was employed to measure the rotational gas temperature (T_{rot}) of the plasma jet using a high resolution narrow band (0.004 nm resolution) monochromator (Acton Research, Model: SP-2750) coupled with a fast gating Andor iStar ICCD (ANDOR, DH 734). This system has a near-Lorentzian slit function with a half-maximum width of 0.2 nm when the grating density was set to 1200 lines/mm. A high-temperature ceramic fiber-insulated-wire thermocouple probe capable of measuring temperatures up to 1400 °C was used to measure the temperature of the downstream jet when plasma emission ends after approximately 2.5 cm. The parts per million (ppm) concentration of the ROS and RNS including nitric oxides at different spatial distances from the tip of the plasma jet was measured using two gas sensors namely NOXCANg and Testo 350 M/XL gas analyzers.

C. Bacterial sample preparation and plasma treatment procedure

Bacterial samples of *S. aureus* (ATCC 259231), *E. coli* (ATCC 117751), and *N. meningitidis* serogroup C (ATCC 700532) were obtained from ATCC (Manassas, VA). Bacterial cultures of *S. aureus* (ATCC 259231) and *E. coli* (ATCC 117751) were grown overnight on Tryptic Soy agar (BD, Franklin Lakes, NJ) plate overnight at 37°C in 5% CO₂. *N. meningitidis*

was grown overnight on GC medium (BD, Franklin Lakes, NJ) plate supplemented with Thayer-Martin supplement I and supplement II (Sigma-Aldrich, St. Louis MO) overnight at 37°C in 5% CO₂. Bacteria was collected from overnight cultures using an inoculating loop and placed into 20 ml of Mueller Hinton broth (MHB) (BD, Franklin Lakes, NJ). Bacterial cultures in suspension were adjusted with sterile MHB to an OD at 595 nm (OD_{595}) = 0.2 (Spectronic Genesys 5 Spectrophotometer, Madison, WI) and allowed to incubate (37°C, 5% CO₂) till reaching an OD_{595} = 0.4. *N. meningitidis* suspensions included agitation by a plate mixer (~100 rpm). After reaching the selected density, 13x100 glass culture tube were filled with 5ml of bacterial suspension and treated to regime of either 0, 30, 60, or 120 seconds of maximum power and flow rate of RB plasma jet in direct or indirect treatment modes by fixing the plasma jet exit above the surface of the media at a distance of approximately 5cm. Control suspension samples pH was monitored before and after 30, 60, and 120 seconds of direct and indirect RB plasma jet treatment using S20 SevenEasy pH meter (Mettler-Toledo, Columbus, OH). Bacterial density was monitored over a period of 24 hours and OD_{595} readings were recorded. The efficacy of the inactivation was determined by making serial dilutions of untreated and treated samples and plating them on agar plates. Three independent experiments were performed and data were collected for the analysis of post-treatment bacterial growth means over time.

D. Messenger RNA analysis by quantitative real time-PCR

Real time polymerase chain reaction (RT-PCR) analysis can provide information about the presence and quantity of a specific gene within a cell. Cells such as bacteria can recognize external stimuli such as NO produced by the RB plasma jet and react accordingly to alter its metabolic processes through gene regulation to respond to the stimuli. Cultures of *N. meningitidis* were prepared as described above and the untreated and 60 second direct plasma

treated samples were incubated at 37°C, 5% CO₂. Bacterial RNA was harvested from each sample culture at 2 hour post treatment using a Qiagen RNeasy minikit. Purified mRNA was quantitated via Nanodrop with appropriate standards. cDNA synthesis and quantitative PCR were done using the Superscript III Platinum SYBR Green two-step qRT-PCR kit (Invitrogen) on an Cepheid Smart Cycler. The relative expression of *pilC* was normalized to that of 16S gene, which served as an internal control. The qRT-PCR experiments were done in triplicate with independently isolated RNA samples.

III. RESULTS AND DISCUSSION

A. Electrical characterization of the RB plasma jet

The electrical properties of the discharge are obtained using voltage-current characterization. The discharge is initiated by applying a sufficient voltage between electrodes at which the air between electrodes breaks down and results in a self-sustained plasma jet maintained by applied voltage of the power supply. Figure 2 shows the voltage-current waveform of the RB plasma jet. The positive and negative half periods of the applied voltage are not symmetrical due to the existence of only one resistance between the electrodes. It can be seen from Fig. 2 that breakdown of air in atmospheric pressure resistive barrier plasma jet resulting in several current filaments called micro-discharges which are randomly spread in time and space. The maximum voltage and current values are approximately 20 kV and 3 mA on the positive half period of the applied voltage, correspondingly. Using the voltage–current waveforms, the average power dissipated in the discharge is calculated by integrating the product of the discharge voltage and current over one cycle; according to the following equation (T = period of the discharge).²⁸

$$W = \frac{1}{T} \int_t^{t+T} I(t)V(t)dt \quad (1)$$

and the average plasma power is measured to be 26 W.

B. Optical emission spectroscopy

The rotational temperature (T_{rot}) of the RB plasma jet was measured using the optical emission spectroscopy. The rotational temperature and plasma gas temperature can be considered equivalent if there is a small energy gap between the rotational levels compared with that of the vibrational or electronic energy levels and in the presence of thermal equilibrium between the translational and rotational degrees of freedom.²⁹ A local thermodynamic equilibrium (LTE) condition has been assumed and emission spectra of the plasma jet were used for gas temperature determination.

The commonly used technique to estimate rotational temperature is based on finding the best fit between experimental and simulated emission spectra of the second positive system of N_2 and considering the plasma gas temperature equivalent with rotational temperature of N_2 (T_{rot}). In this section, the spectral lines of the nitrogen second positive system (SPS), ($N_2(C-B)$ ($C^3\Pi B^3\Pi$) ($2+$)), is used to determine the rotational temperature distribution of nitrogen SPS with SPECAIR software.³⁰ SPECAIR is computer simulation software developed by Laux et. al. on the basis of the Non-Equilibrium Air Radiation code (NEQAIR) by Park.³⁰ The rotational temperature distribution of the N_2 SPS, in the afterglow of the RB plasma jet was determined on the basis of simulation of experimental spectra in the range of region 364-383 nm. Fitting of the spectra is carried out with one rotational temperature, and taking into account the instrumental function of the spectrometer. The experimental spectra were compared to the simulated spectra with various rotational temperatures. The rotational temperature for the best fitting between

simulated and experimental spectra was determined as the gas temperature. The experimental and simulated spectra of N₂ second positive system are presented in Fig. 3.

The results indicate the rotational temperature for air discharge at a distance of 0.2 cm from the nozzle is 3050 °C. The T_{rot} drops to 2100 °C at 0.8 cm and continue to decrease to 1500 C at 1.5 cm and to 1050 °C at 2 cm away from the nozzle. The rotational temperature of nitrogen is significantly smaller at 2 cm away from the nozzle than the one of 0.2 cm from the jet exit. This clearly indicates that the nozzle acts as an efficient heat source for the plasma jet. Nitrogen line emissions drop significantly after 2 cm (plasma plume length is 2.5 cm) from the tip of electrode along the axis and beyond which the gas temperature estimation by OES based rotational temperature estimation is challenging. However, the long life active species such as the ROS and RNS produced by the plasma jet can still propagate further in to the surrounding air (NO_x concentration was measured to be ~900 ppm at 10 cm away from nozzle) and are important active species particularly for the biomedical applications. Therefore the downstream gas temperatures beyond the plasma emission, which is from 2 cm of the plasma jet exit onwards, were measured by using a high-temperature ceramic fiber-insulated-wire thermocouple probe. The Fig. 4 shows the axial temperature measurements of the RB plasma jet before attaching the cooling unit. As seen in Fig. 4, the gas temperatures decrease at a much slower rate after approximately 5 cm from the nozzle. The high gas temperatures obtained from N₂ rotational temperature is due to excitation of N₂ to high rotational/vibrational levels and the excited N₂ species are generated in the plasma jet. However, plasma gas temperature drops down very fast at the end of the jet's plume. The temperature of the plasma plume at the exit reaches >2500 °C sufficient enough to generate nitric oxides. When the external cooling units were added the gas

temperatures were brought close to room temperature at the tip of the handheld plasma source unit.

C. Measurements of long lived active plasma species

RB plasma jet produces wide range of active species such as radicals, electrons, atoms, ions, molecules, ROS and RNS etc. These plasma species contributes to the biological cell interactions and inactivation of the bacteria. The concentrations of the ROS and RNS produced by the plasma jet with and without the cooling unit are measured using gas analyzers. The majority of the short lived ions will recombine before it exits through the cooling unit and at this stage several long lived gas species and other parameters were monitored, including O₂, O₃, CO, CO_{low}, NO/NO₂, NO_{low}, NO_X, CO₂(Infrared), SO₂, HC, H₂S, temperature, pressure, flow, velocity, efficiency, mass, etc. Based on the results we observed that nitric oxides are the predominant long lives species produced by the RB plasma jet and some trace of O₃. The nitric oxide formation is a reversible plasma chemical reaction and it can be expressed as



The decaying concentration of the nitric oxides from the plasma jet can be used as reference for the treatment distance between the biological cells and the plasma source tip. The background NO_x concentration are measured using NO_xCANg module at various timings and at standard laboratory conditions well before the plasma source was operated and it was measured to be less than 0.5 ppm.

The NO_x concentration measurements are carried out at 20 data sets separated by 1 min with 1 second acquisition time at different distances. For consistency in the concentration measurements, three other sampling timings such as 10, 30 and 60 second are tested in addition

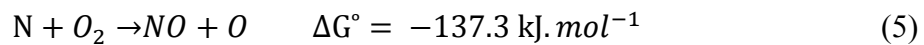
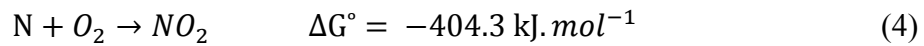
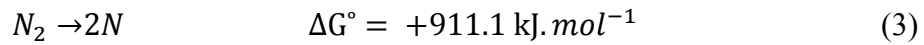
to 1 second acquisition time. Figure 5 shows the NO_x concentration at different distance with different acquisition times. As can be seen, the concentration of NO_x species is consistent for various gas acquisition integration times at various distances from plasma jet's nozzle.

The NO_x concentrations of the plasma jet with and without the cooling unit are measured at various axial distances from the tip and the results are shown in Fig. 6. The measurements show that the NO_x concentration peaks at the electrode tip as expected and the NO_x concentration was measured to be in the range of 500-660 ppm at 5 cm from the plasma jet exit without the cooling unit. The concentration drops to half of its initial value at ~20cm and it continues to drop to ~100 ppm at 60 cm and at 100 cm distance from the tip the concentration was very low (<10 ppm). In addition, the Fig. 6 shows the NO_x concentrations for plasma jet with cooling unit (circles) and it was observed that the NO_x concentration after the cooling unit was higher (~950 ppm) compared to that of plasma jet without cooling unit (~615 ppm), this was due to the fact that plasma jet diffuses out after it exits from the nozzle whereas the probe diameter after the cooling unit is very small like a pinhole arrangement with 1 mm diameter opening leading to increased concentration.

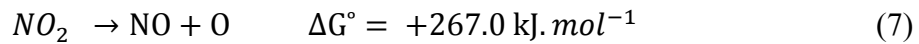
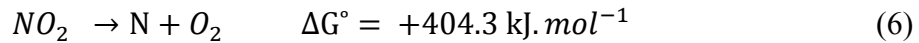
NO_x is composed of two components such as the mono-nitrogen oxides or nitric oxides (NO) and nitrogen dioxide (NO_2). In order to measure the individual concentration levels of NO and NO_2 a different diagnostic tool was realized using a gas analyzer (Testo 350 M/XL) capable of identifying and characterizing over several molecular gases including NO and NO_2 . Table 1 shows the concentrations of NO and NO_2 produced by the plasma jet without the cooling unit and the Table 2 shows the concentrations of NO and NO_2 produced by the plasma jet with external cooling unit. In both cases, the concentration of NO_2 was much lesser compared to that of NO by an order of magnitude or higher. The ppm concentration of NO is at the preferred level for a

wide range of standard biomedical treatment applications. The ppm concentration of NO₂ is below the OSHA safety standards.

The formation of different active species produced in air plasmas involves very complex plasma chemistries. At such a relatively high gas temperature different nitrogen oxides products are formed from N₂ and O₂ reactions.³¹ The O₂ concentration affects the production of NO_x species air discharges and it has been shown that a threshold value of O₂ concentration (5%) is necessary for production of different NO_x species.^{31,32} In such a plasma condition, NO₂ will be produced from N₂ and O₂ in the discharge based on the following reactions.



Although NO₂ production is more favorable than NO production, NO₂ decomposes according to following reactions and produces additional NO species.



Thus, considering both process of NO formation; such as from N₂ and O₂ (according to reactions 3 and 5) and from decomposition of NO₂ (reaction 7), results in a higher NO concentration compared to NO₂ along the plasma jet (see Table 1-2). Such processes are observed in other thermal plasmas as well.³²

D. Direct versus indirect bacterial inactivation in liquid environment

Plasma treatments on bacterial cultures of *S. aureus*, *E. coli*, and *N. meningitidis* were done using direct and indirect methods. The demonstration of bacterial inactivation and its quantitative

analysis were done by optical density (OD) measurements using UV-VIS spectrometer tested at 595 nm. Considering the OD value proportional with the concentration of the detected bacteria, we determined the inactivation of the bacterial growth. The pH measurements of the plasma treated samples showed similar values as the untreated samples.

The Fig. 7(a) demonstrate that with direct plasma treatment, *S. aureus* suspensions reached a mean maximum density over a 24 hour period of $OD_{595} = 1.418$, $OD_{595} = 1.283$, and $OD_{595} = 0.137$, with increasing direct treatment of RB plasma jet times of 30s, 60s, and 120s, respectively, while untreated *S. aureus* bacterial suspensions resulted with a mean maximum density measurement of $OD_{595} = 1.964$. The results show that the *S. aureus* suspended in aqueous media were inactivated with 60s of direct exposure of RB plasma jet. Similarly, *E. coli* displayed similar trends as *S. aureus* suspensions as shown in Fig. 7(b). The untreated *E. coli* suspensions reached a mean maximum density over a 24 hour period of $OD_{595} = 3.305$. The OD_{595} mean maximum density readings over a 24 hour period of *E. coli* with 30s and 60s of direct treatment of RB plasma jet reached $OD_{595} = 2.77$ and $OD_{595} = 1.084$, respectively, showing partial inactivation. Whereas, the *E. coli* suspensions with direct treatment of RB plasma jet for 120s displayed a radically lower OD_{595} with the mean maximum density reading over a 24 hour period reaching $OD_{595} = 0.259$. The inactivation efficacy of the *S. aureus* and *E. coli* by the RB plasma jet direct treatment of 120s at 5 cm distance was further corroborated with 1×10^{-6} serial dilution and 100 μ l plating of cultures on agar plates as shown in Fig. 8(a) and (b). As shown in Fig 7(c), the direct treatment of RB plasma jet on *N. meningitidis* suspensions showed a different density pattern compared to *E. coli* and *S. aureus* suspensions. The OD_{595} mean maximum density readings over 24 hour period of *N. meningitidis* with 30s, 60s, and 120s of direct treatment of RB plasma jet reached $OD_{595} = 1.26$, $OD_{595} = 1.32$, and $OD_{595} = 0.451$, respectively. Untreated

suspensions of *N. meningitidis* displayed a mean maximum density measurement of $OD_{595} = 1.185$.

The indirect plasma treatment involves exposure of only the long lived active species (ROS and RNS) generated by the plasma instead of the plasma itself, thus excluding the effect of any possible UV radiation produced by plasma. It has been researched that under same treatment condition, a direct plasma treatment is an order of magnitude faster than indirect treatment by plasma active agents such as bombardment of the surface of a microorganism by charged particles in the primary inactivation mechanism.³³ In the RB plasma jet indirect exposure method the concentrations of the nitric oxides are preserved by reducing the plasma temperature rapidly through a separate external small efficient cooling unit. Utilizing the maximum time of direct exposure of RB plasma jet treatment at which the lowest densities were seen in *S. aureus*, *E. coli*, and *N. meningitidis* suspensions, we found that 120s of indirect exposure of RB plasma jet treatment greatly reduced the densities of *S. aureus* and *E.coli* and with mean maximum densities over a 24 hour period reaching $OD_{595} = 0.693$ and $OD_{595} = 0.130$, respectively; as compared to untreated controls as shown in Fig. 9(a) and (b). As suspected, the 120s of indirect RB plasma jet treatment of *N. meningitidis* suspensions did not impact the density as determined with the mean maximum density over a 24 hour period reading of $OD_{595} = 1.187$, similar to the untreated control as shown in Fig 9(c). Eventually the inactivation of *N. meningitidis* can be expected since its close relative *N. gonorrhoea* with similar characteristics was effectively inactivated after at least 4 min of plasma treatment.³⁴

The comparative bacterial growth inactivation results by the direct and indirect RB plasma jet treatments are presented in Fig. 10. Variable differences in the amount of plasma exposure required to inactivate different strains of bacteria has been repeatedly reported but of

greater interest is variable resistance to inactivation amongst bacteria of the same species as seen with *S. aureus*³⁵ and determined in *N. gonorrhoea*³⁶. The identified variability in bacterial resistance to plasma as seen in this study and previously reported studies suggest that some bacteria may be incorporating mechanisms to ameliorate some of the plasma effect. In the use of direct plasma inactivation of bacterial growth, *N. meningitidis* required greater plasma exposure to allow for its inactivation, while there was no apparent inactivation by indirect plasma treatment. As indicated in Table 1 and 2, NO is a major component of the long lived species produced by the RB plasma jet. *N. meningitidis* is normally found in the moist tissues of the NO rich environment of the nasal passages.³⁷ Furthermore *N. meningitidis* is known for its ability to impede host cell defenses against removing the bacteria through inhibition of NO induction cell suicide.³⁸ We can only allude to the incorporation of these mechanisms as a factor that provided tolerance toward indirect plasma treatment consisting of high levels of nitric oxide for *N. meningitidis* as compared to successful decreases in densities seen in *E. coli* and *S. aureus*. Although the results signify that *N. meningitidis* might be metabolizing NO, further metabolic measurements may be required in order to confirm. Alternately, the ability of plasma to affect bacterial gene expression has been previously described with *E. coli* treated with direct plasma demonstrating significant changes in gene expression of genes that control the bacterial defense against oxidative stress.^{39,40} Similarly, a *pilC* gene expression analysis of *N. meningitidis* was performed for 60 second direct treatment of RB plasma jet. The *pilC* gene is widely known for directing the production of *PilC* protein that is the primary adhesin allowing for the bacteria to bind to the semi-aqueous mucosal layer inside the nose and throat.⁴¹ The results indicate that, 60 seconds of direct plasma treatment has a 4 fold reduction in the relative expression of the *pilC* gene as compared to the untreated sample as shown in Fig. 11. The values were determined after

correcting the gene expression using the internal 16S control. The 16S control gene is a standard functional gene within the bacteria whose expression level is normally constant. The values represent mean \pm standard deviations. We can derive from previous reports that demonstrated an increase in the levels of NO in cultures of *N. meningitidis* results in an increase in expression of genes involved with protection against NO.⁴² Therefore, the change in gene expression of *pilC* suggests that other genes involved with protection against NO are also variably affected by direct plasma treatment. The NO detoxification mechanisms found in the bacterial species used in this study were originally detected as a bacterial defense response against host cell nitrosative stress.^{4,43} The presence of bacterial bio-physical mechanisms that may provide the capabilities to resist specific plasma chemistries as observed with *N. meningitidis* highlights a research prospect for plasma treatment of infected wounds. The authors have suggested the potential use of RB plasma jet for wound sterilization, although the increasing levels of NO may concern to treating wound tissue. So far, there have been no report of plasma treatment on bacterial infected wounds being negatively impacted in rodent⁴⁴ and porcine² models or human clinical trials⁴⁵. The RB plasma source can be extended further to personal and small scale treatment of wound infections, medical instrumentation sterilization, along with food and agricultural product sterilization and detoxification.

IV. CONCLUSION

In conclusion, we have developed a portable, light weight resistive barrier (RB) plasma jet applicable for a range of biomedical applications including bacterial inactivation in aqueous media. The RB plasma jet can be operated at both DC and standard low frequency AC, and also able to function effectively in both direct and indirect plasma exposure configurations based on

the type of treatment targets and applications. The characteristics of the RB plasma jet such as the voltage-current curves, plasma power, plasma gas temperature and RNS concentrations were characterized. The voltage-current waveform analysis resulted the plasma power to be 26 W. A high resolution optical emission spectroscopy diagnostic analysis of the N₂ second positive band system N₂C-B(2+) rotational transitions in the 364-383 nm range showed the gas temperatures equivalent to the rotational (T_{rot}) temperatures to be as 3000 °C at 0.2 cm from the exit and decayed to 2000 °C at 0.8 cm and continued to decay to 1500 °C at 1.5 cm and to 1000 °C at 2 cm and the jet temperature reached room temperature with the addition of external cooling unit for the indirect treatment mode. The parts per million (ppm) concentration of the nitric oxide (NO) at different spatial distances from the tip of the plasma jet were measured to be in the range of 500-660 ppm at 5 cm distance from the electrode and drops to ~100 ppm at 60 cm. The RB plasma jet was effective in inactivating the *S. aureus* and *E. coli* in less than 120 seconds determined by measuring the density of bacteria growing in liquid cultures, in both direct and indirect exposure treatment modes. The *N. meningitidis* appeared to show some resistance to inactivation and required extended plasma exposure as compared to *S. aureus* and *E. coli*, especially when the RB plasma jet was used in the indirect mode. The RT-PCR based *pilC* gene expression analysis was done on 60 second direct plasma treated *N. meningitidis* samples at which only partial inactivation was achieved. The results revealed that although a significant inactivation was not observed as determined by bacterial growth, the genes that control the ability of bacteria to cause an infection were being inhibited by at least 4 fold differences as compared to untreated bacteria. However, the ability of *N. meningitidis* to partially resist direct plasma and completely resist indirect plasma treatment suggest that it has incorporated processes that are regulated by genes that are directed by external stimuli such as NO from the RB plasma

jet. The findings indicate that *N. meningitidis* displayed some tolerance to plasma and the long lived reactive nitrogen species, indicating the need for further research toward the specific bacterial inactivation mechanisms of plasma derived reactive nitrogen species.

Acknowledgments

This work was supported in part by the College of Science and Engineering, School of Engineering and Computing Sciences at the Texas A&M University-Corpus Christi, Texas Research and Development Fund (TRDF) and the Department of Defense (DOD) /Army grant (W81XWH-10-1-0923) administered by the U.S. Army Medical Research & Materiel Command (USAMRMC) and the Telemedicine & Advanced Technology Research Center (TATRC), at Fort Detrick, MD. The authors would like to thank for the assistance provided in part by Dr. Lilian Waldbeser and the undergraduate research assistant Keisha Hardeman.

- 1 D. Dobrynin, G. Friedman, A. Fridman, and A. Starikovskiy, *New Journal of Physics* **13**
(2011).
- 2 L. C. Heller, C. M. Edelblute, A. M. Mattson, X. Hao, and J. F. Kolb, *Lett Appl*
Microbiol **54**, 126 (2012).
- 3 M. Laroussi, C. Tendero, X. Lu, S. Alla, and W. L. Hynes, *Plasma Processes and*
Polymers **3**, 470 (2006).
- 4 J. R. Laver, T. M. Stevanin, S. L. Messenger, A. D. Lunn, M. E. Lee, J. W. B. Moir, R.
K. Poole, and R. C. Read, *Faseb Journal* **24**, 286 (2010).
- 5 Y. Maeda, N. Igura, M. Shimoda, and I. Hayakawa, *Journal of the Faculty of Agriculture*
Kyushu University **48**, 159 (2003).
- 6 K. H. Seo, B. W. Mitchell, P. S. Holt, and R. K. Gast, *Journal of Food Protection* **64**, 113
(2001).
- 7 T. Winter, J. Winter, M. Polak, K. Kusch, U. Mader, R. Sietmann, J. Ehlbeck, S. van
Hijum, K. D. Weltmann, M. Hecker, and H. Kusch, *Proteomics* **11**, 3518 (2011).
- 8 G. Fridman, G. Friedman, A. Gutsol, A. B. Shekhter, V. N. Vasilets, and A. Fridman,
Plasma Processes and Polymers **5**, 503 (2008).
- 9 M. Laroussi, *Ieee Transactions on Plasma Science* **30**, 1409 (2002).
- 10 G. E. Morfill, M. G. Kong, and J. L. Zimmermann, *New Journal of Physics* **11** (2009).
- 11 F. Iza, G. J. Kim, S. M. Lee, J. K. Lee, J. L. Walsh, Y. T. Zhang, and M. G. Kong,
Plasma Processes and Polymers **5**, 322 (2008).
- 12 U. Kogelschatz, *Contributions to Plasma Physics* **47**, 80 (2007).
- 13 K. H. Becker, K. H. Schoenbach, and J. G. Eden, *Journal of Physics D-Applied Physics*
39, R55 (2006).
- 14 K. Becker, A. Koutsospyros, S. M. Yin, C. Christodoulatos, N. Abramzon, J. C. Joaquin,
and G. Brelles-Marino, *Plasma Physics and Controlled Fusion* **47**, B513 (2005).
- 15 A. Sarani, A. Y. Nikiforov, and C. Leys, *Ieee Transactions on Plasma Science* **39**, 2358
(2011).
- 16 K. D. Weltmann, R. Brandenburg, T. von Woedtke, J. Ehlbeck, R. Foest, M. Stieber, and
E. Kindel, *Journal of Physics D-Applied Physics* **41** (2008).
- 17 G. Daeschlein, T. von Woedtke, E. Kindel, R. Brandenburg, K. D. Weltmann, and M.
Junger, *Plasma Processes and Polymers* **7**, 224 (2010).
- 18 H. W. Lee, S. H. Nam, A. A. H. Mohamed, G. C. Kim, and J. K. Lee, *Plasma Processes*
and Polymers **7**, 274 (2010).
- 19 K. Fricke, H. Steffen, T. von Woedtke, K. Schroder, and K. D. Weltmann, *Plasma*
Processes and Polymers **8**, 51 (2011).
- 20 J. Y. Jeong, S. E. Babayan, V. J. Tu, J. Park, I. Henins, R. F. Hicks, and G. S. Selwyn,
Plasma Sources Science & Technology **7**, 282 (1998).
- 21 I. G. Zacharia and W. M. Deen, *Annals of Biomedical Engineering* **33**, 214 (2005).

- 22 M. Naitali, G. Kamgang-Youbi, J. M. Herry, M. N. Bellon-Fontaine, and J. L. Brisset, *Applied and Environmental Microbiology* **76**, 7662 (2010).
- 23 M. Thiyagarajan and I. Alexeff, in *A Dual Mode – Steady State Atmospheric Pressure Nonthermal Resistive Barrier Plasma Discharge*, San Francisco, California, 2003.
- 24 M. Thiyagarajan, I. Alexeff, S. Parameswaran, and S. Beebe, in *Ambient pressure resistive barrier cold plasma discharge for biological and environmental applications*, Baltimore, MD, United states, 2004 (Institute of Electrical and Electronics Engineers Inc.), p. 197.
- 25 M. Thiyagarajan, I. Alexeff, S. Parameswaran, and S. Beebe, *IEEE Transactions on Plasma Science* **33**, 322 (2005).
- 26 M. Thiyagarajan and J. E. Scharer, *Ieee Transactions on Plasma Science* **36**, 2512 (2008).
- 27 M. Thiyagarajan and J. Scharer, *Journal of Applied Physics* **104** (2008).
- 28 F. Massines and G. Gouda, *Journal of Physics D-Applied Physics* **31**, 3411 (1998).
- 29 V. Linss, H. Kupfer, S. Peter, and F. Richter, *Journal of Physics D-Applied Physics* **37**, 1935 (2004).
- 30 C. O. Laux, T. G. Spence, C. H. Kruger, and R. N. Zare, *Plasma Sources Science & Technology* **12**, 125 (2003).
- 31 S. Futamura, A. H. Zhang, and T. Yamamoto, *Ieee Transactions on Industry Applications* **36**, 1507 (2000).
- 32 S. Futamura, A. H. Zhang, and T. Yamamoto, *Journal of Electrostatics* **42**, 51 (1997).
- 33 G. Fridman, A. D. Brooks, M. Balasubramanian, A. Fridman, A. Gutsol, V. N. Vasilets, H. Ayan, and G. Friedman, *Plasma Processes and Polymers* **4**, 370 (2007).
- 34 Y. T. Tu, L. Xu, Y. Yu, M. Tan, J. A. Li, and H. X. Chen, *Journal of Huazhong University of Science and Technology-Medical Sciences* **30**, 226 (2010).
- 35 S. A. Ermolaeva, A. F. Varfolomeev, M. Y. Chernukha, D. S. Yurov, M. M. Vasiliev, A. A. Kaminskaya, M. M. Moisenovich, J. M. Romanova, A. N. Murashev, I. I. Selezneva, T. Shimizu, E. V. Sysolyatina, I. A. Shaginyan, O. F. Petrov, E. I. Mayevsky, V. E. Fortov, G. E. Morfill, B. S. Naroditsky, and A. L. Gintsburg, *Journal of Medical Microbiology* **60**, 75 (2011).
- 36 I. Gusarov and E. Nudler, *Proceedings of the National Academy of Sciences of the United States of America* **102**, 13855 (2005).
- 37 B. Kimberly, B. Nejadnik, G. D. Giraud, and W. E. Holden, *Am J Respir Crit Care Med* **153**, 829 (1996).
- 38 A. J. Tunbridge, T. M. Stevanin, M. Lee, H. M. Marriott, J. W. Moir, R. C. Read, and D. H. Dockrell, *Infect Immun* **74**, 729 (2006).
- 39 A. Sharma, G. Collins, and A. Pruden, *Journal of Applied Microbiology* **107**, 1440 (2009).
- 40 A. R. Krapp, M. Victoria Humbert, and N. Carrillo, *Microbiology-Sgm* **157**, 957 (2011).

- 41 I. Scheuerpflug, T. Rudel, R. Ryll, J. Pandit, and T. F. Meyer, *Infect Immun* **67**, 834
(1999).
- 42 K. Heurlier, M. J. Thomson, N. Aziz, and J. W. B. Moir, *J Bacteriol* **190**, 2488 (2008).
- 43 A. R. Richardson, S. J. Libby, and F. C. Fang, *Science* **319**, 1672 (2008).
- 44 A. B. Shekhter, V. A. Serezhenkov, T. G. Rudenko, A. V. Pekshev, and A. F. Vanin,
Nitric Oxide-Biology and Chemistry **12**, 210 (2005).
- 45 G. Isbary, G. Morfill, H. U. Schmidt, M. Georgi, K. Ramrath, J. Heinlin, S. Karrer, M.
Landthaler, T. Shimizu, B. Steffes, W. Bunk, R. Monetti, J. L. Zimmermann, R. Pompl,
and W. Stolz, *British Journal of Dermatology* **163**, 78 (2010).

LIST OF FIGURE CAPTIONS

FIG 1. The schematic set up of: (a) the RB air plasma jet, (b) direct and indirect plasma exposure.

FIG 2. Voltage-current waveform of the RB air plasma jet.

FIG. 3. Experimental and simulated air plasma emission spectra of N₂ SPS for fixed power of 26 Watt without cooling unit and at distances: (a) 0.2 cm, (b) 0.8 cm, (c) 1.5 cm, and (d) 2 cm after the nozzle.

FIG. 4. Gas temperature as a function of distance from the tip of the RB plasma jet. Air discharge and fixed power of 26 Watt (No cooling unit).

FIG. 5. NO_x concentration (ppm) at different distances from plasma jet's nozzle without the cooling unit.

FIG. 6. NO_x concentrations of the RB plasma jet with and without cooling unit.

FIG.7. Inactivation efficacies of RB plasma jet as a function of direct plasma exposure treatment. Density measurements over 24 hr post treatment on: (a) *S. aureus*, (b) *E. coli*, (c) *N. meningitidis*.

FIG. 8. Bacterial growth represented in terms of CFUs on agar plates for (a) *S. aureus*, (b) *E. coli*. (left)-control without plasma treatment, (right)-120s direct RB plasma jet treated.

FIG. 9. Inactivation efficacies of RB plasma jet as a function of indirect plasma exposure treatment. Density measurements over 24 hr post treatment on: (a) *S. aureus*, (b) *E. coli*, (c) *N. meningitidis*.

FIG. 10. Comparative 24-hr post treatment inactivation results for *S. aureus*, *E. coli* and *N. meningitidis* by RB plasma jet exposure in: (a) direct plasma treatment, (b) indirect plasma treatment –modes.

FIG 11. Quantitative PCR analysis of relative expression of *pilC* in *N. meningitidis* untreated and 60 second of RB plasma jet direct treatment.

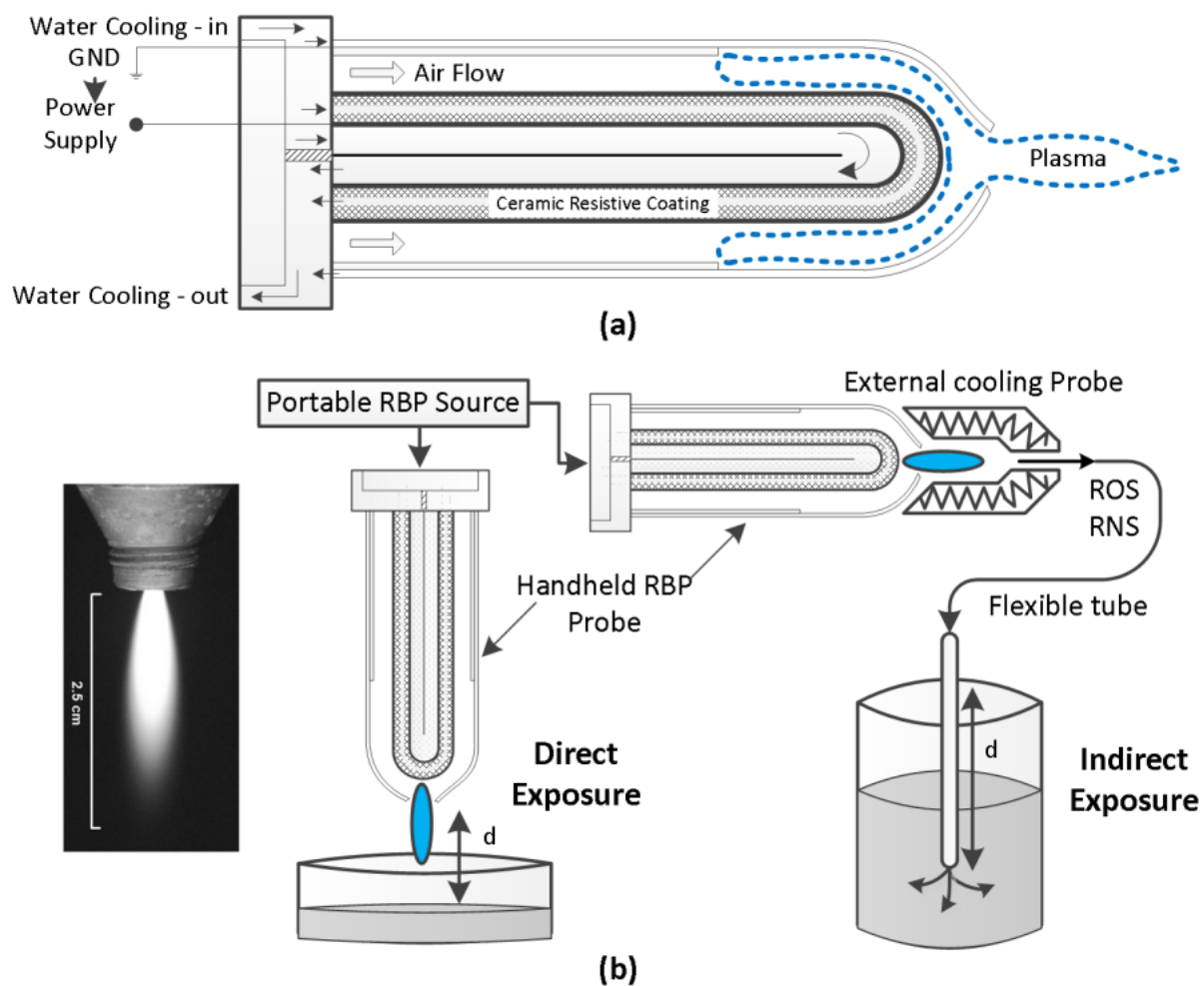


FIG 1. The schematic set up of: (a) the RB air plasma jet, (b) direct and indirect plasma exposure.

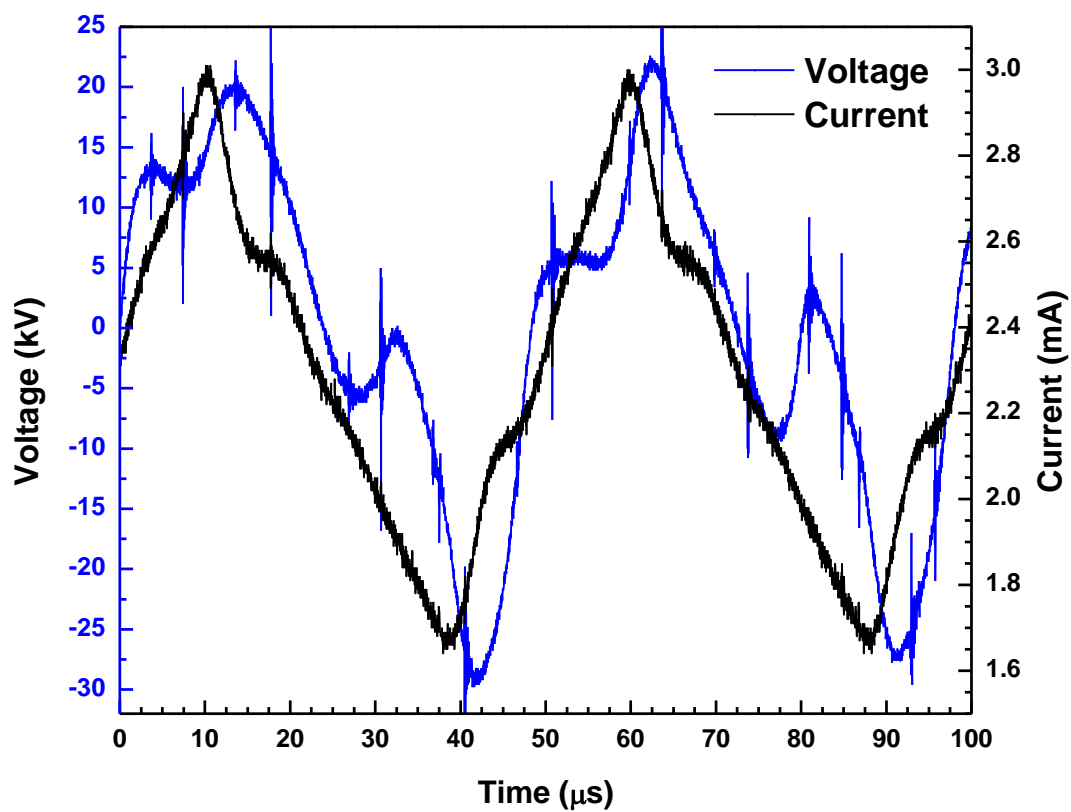


FIG 2. Voltage-current waveform of the RB air plasma jet.

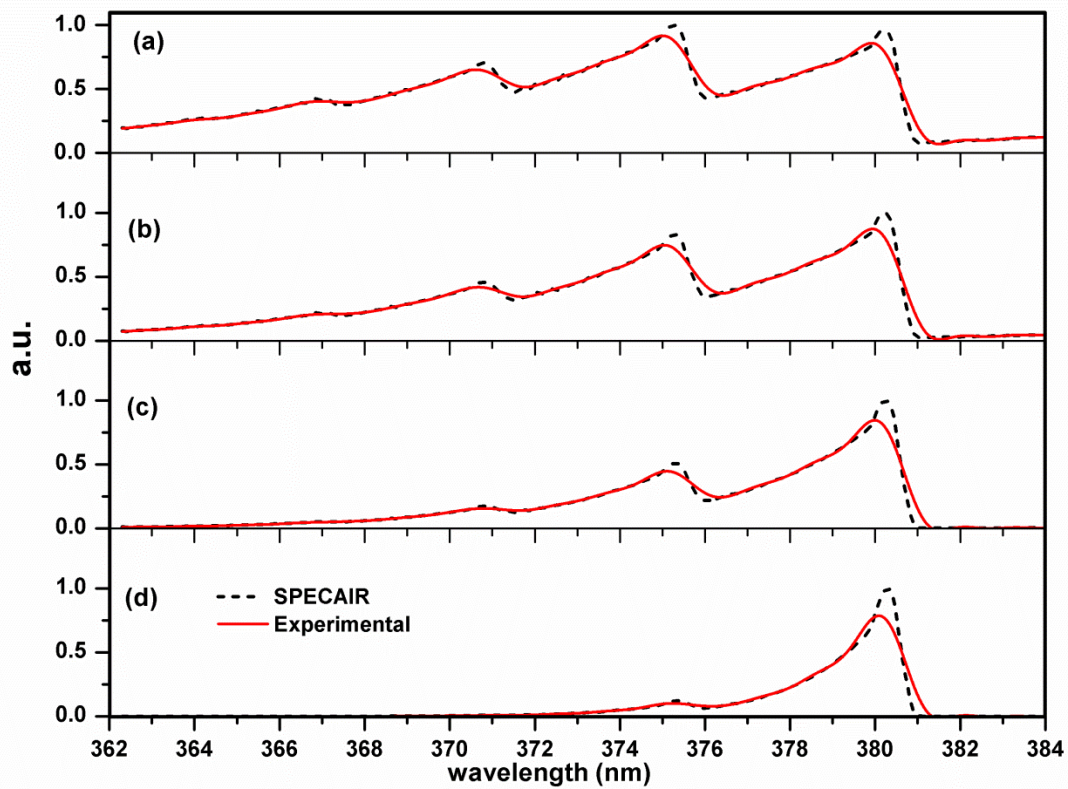


FIG. 3. Experimental and simulated air plasma emission spectra of N_2 SPS for fixed power of 26 watt without cooling unit and at distances: (a) 0.2 cm, (b) 0.8 cm, (c) 1.5 cm, and (d) 2 cm after the nozzle.

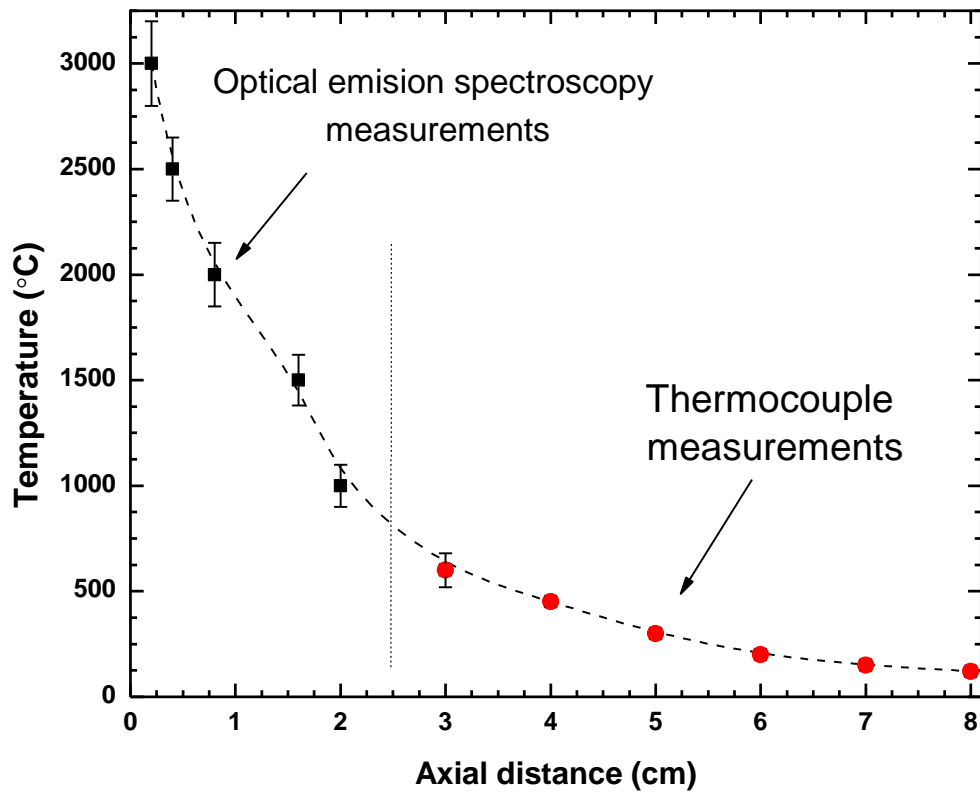


FIG. 4. Gas temperature as a function of distance from the tip of the RB plasma jet. Air discharge and fixed power of 26 watt (No cooling unit).

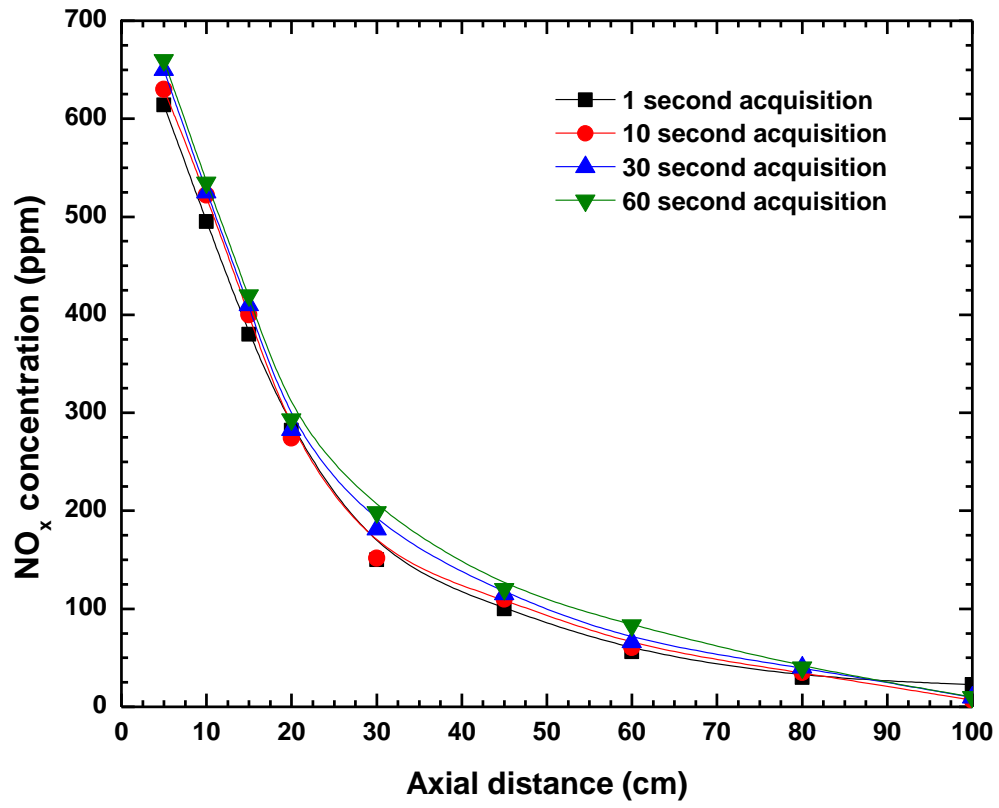


FIG. 5. NO_x concentration (ppm) at different distances from plasma jet's nozzle without the cooling unit.

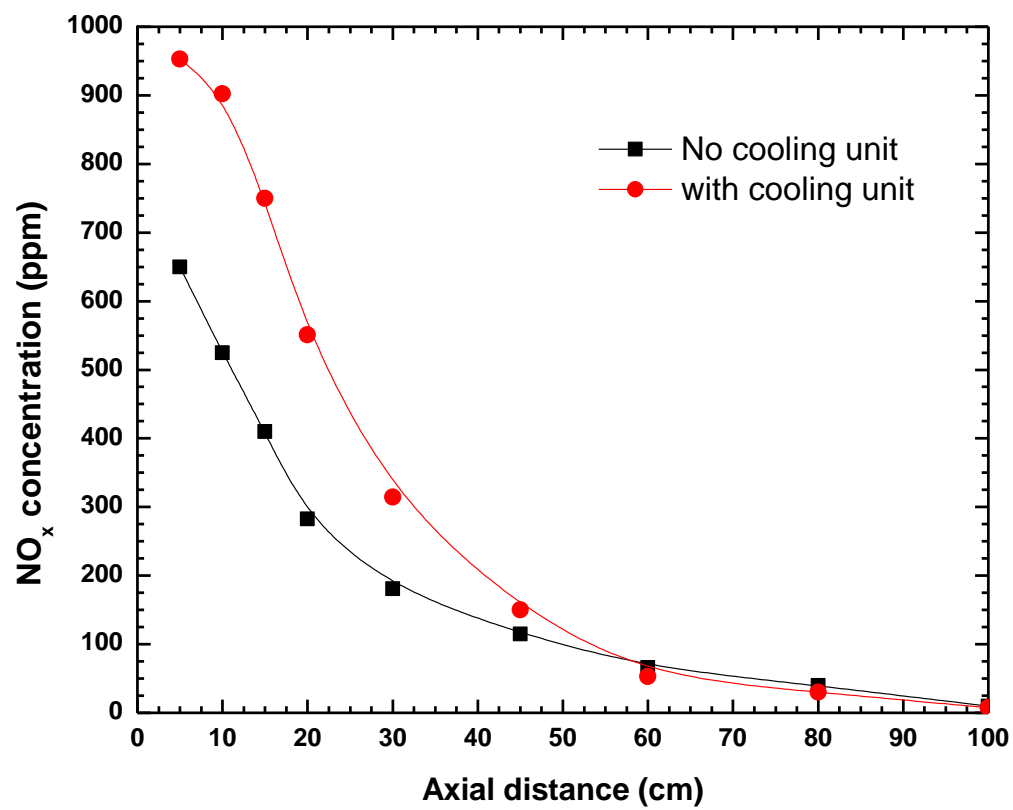


FIG. 6. NO_x concentrations of the RB plasma jet with and without cooling unit.

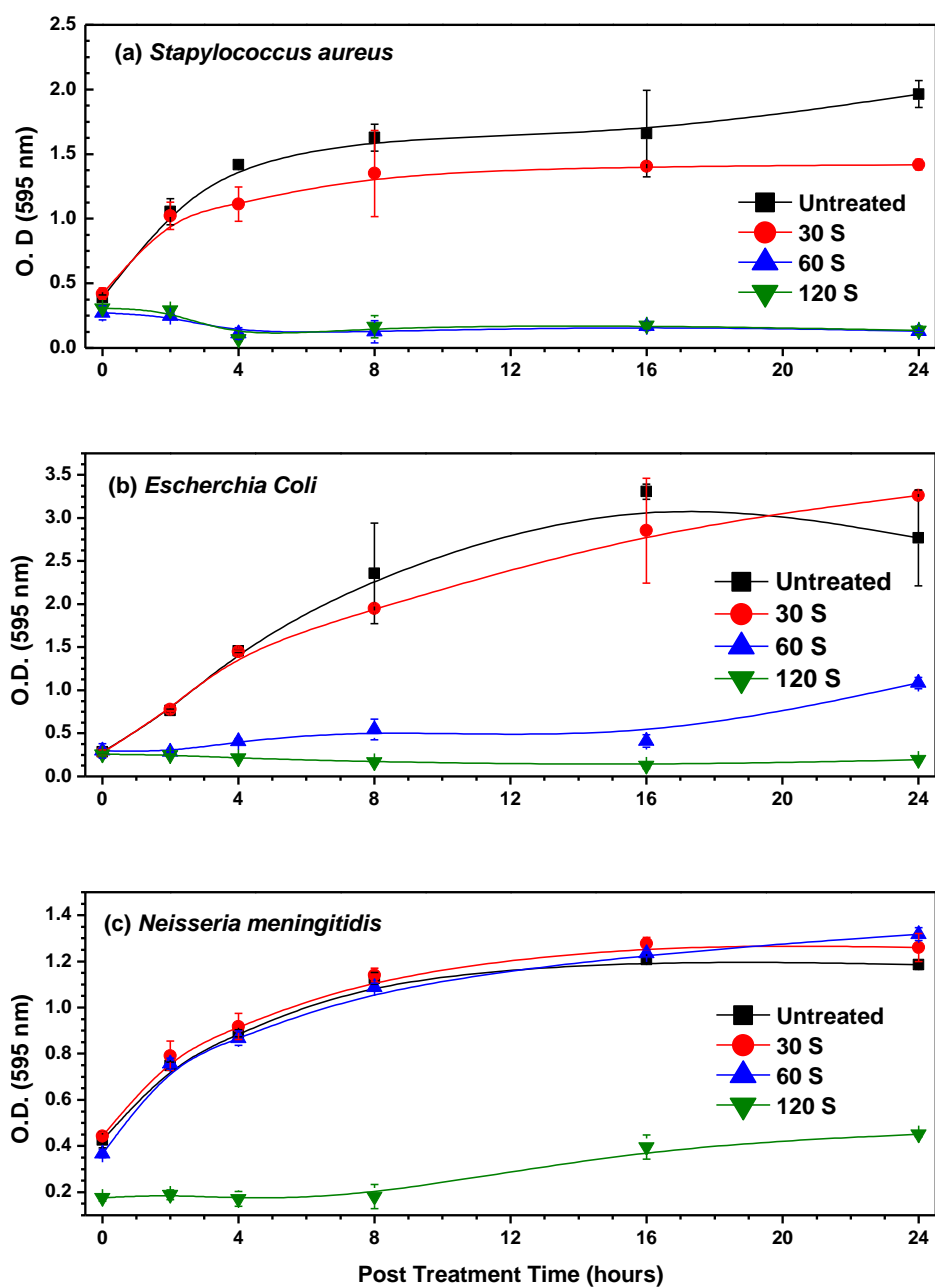
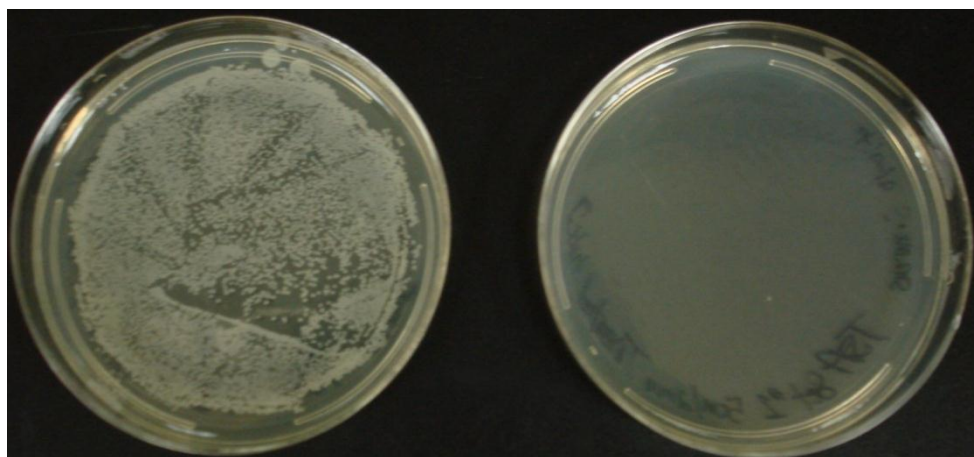
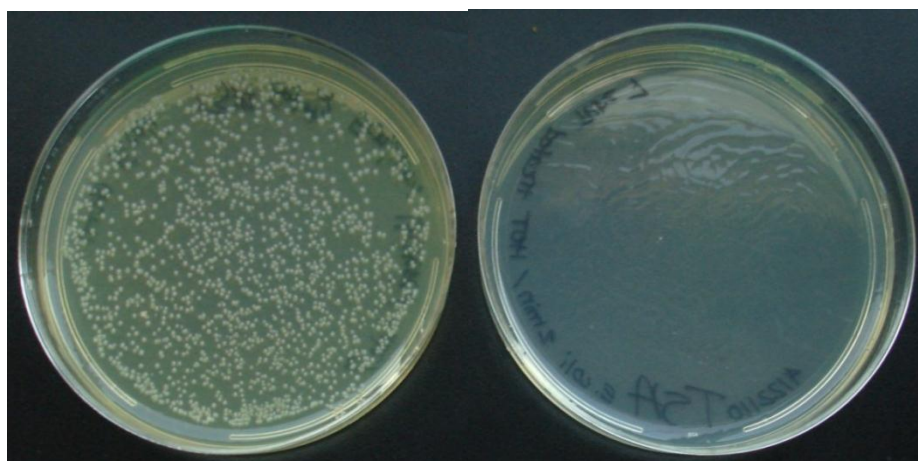


FIG.7. Inactivation efficacies of RB plasma jet as a function of direct plasma exposure treatment. Density measurements over 24 hr post treatment on: (a) *S. aureus*, (b) *E. coli*, (c) *N. meningitidis*.



(a)



(b)

FIG. 8. Bacterial growth represented in terms of CFUs on agar plates for (a) *S. aureus*, (b) *E. coli*. (left)-control without plasma treatment, (right)-120s direct RB plasma jet treated.

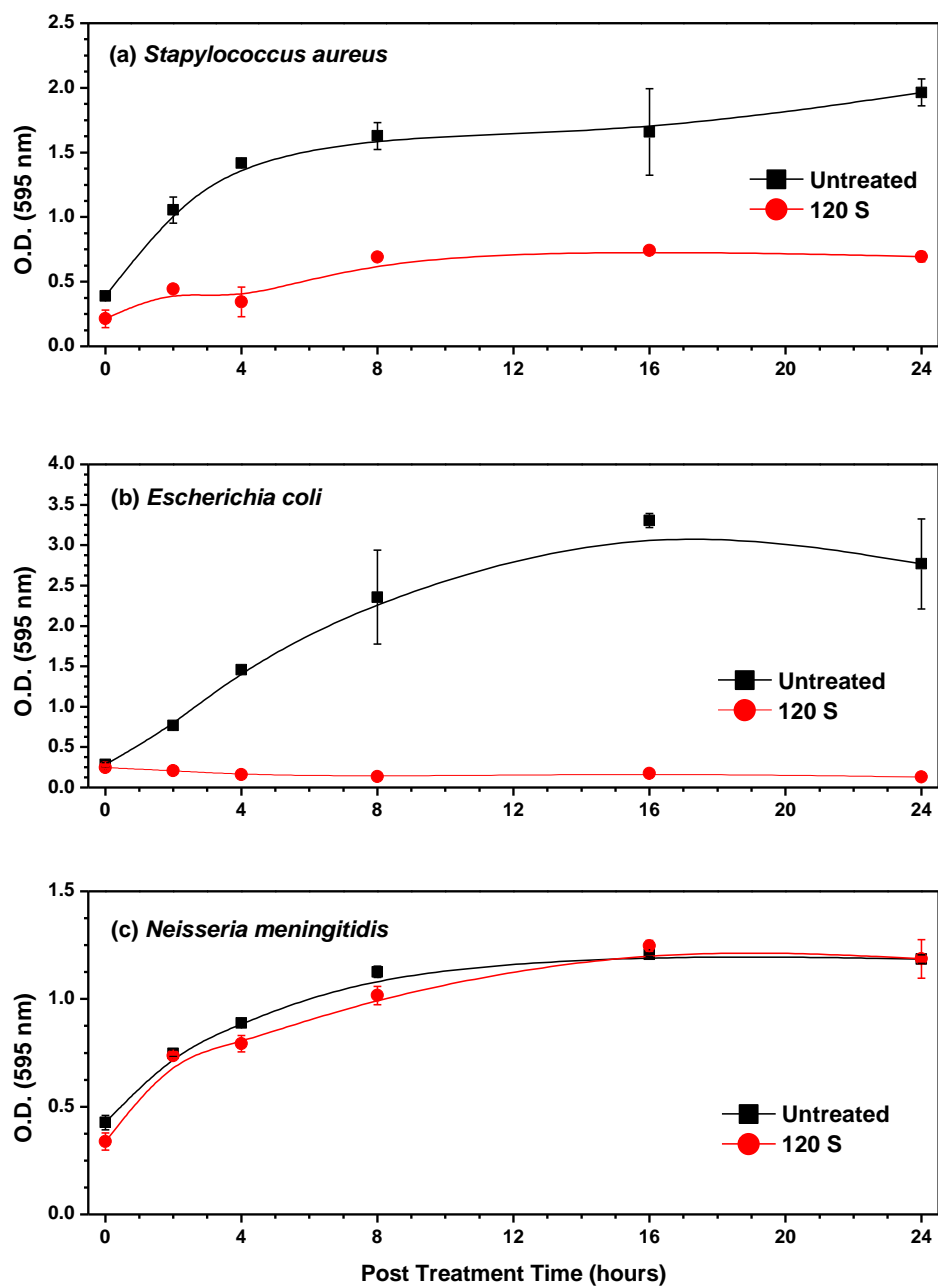


FIG. 9. Inactivation efficacies of RB plasma jet as a function of indirect plasma exposure treatment. Density measurements over 24 hr post treatment on: (a) *S. aureus*, (b) *E. coli*, (c) *N. meningitidis*.

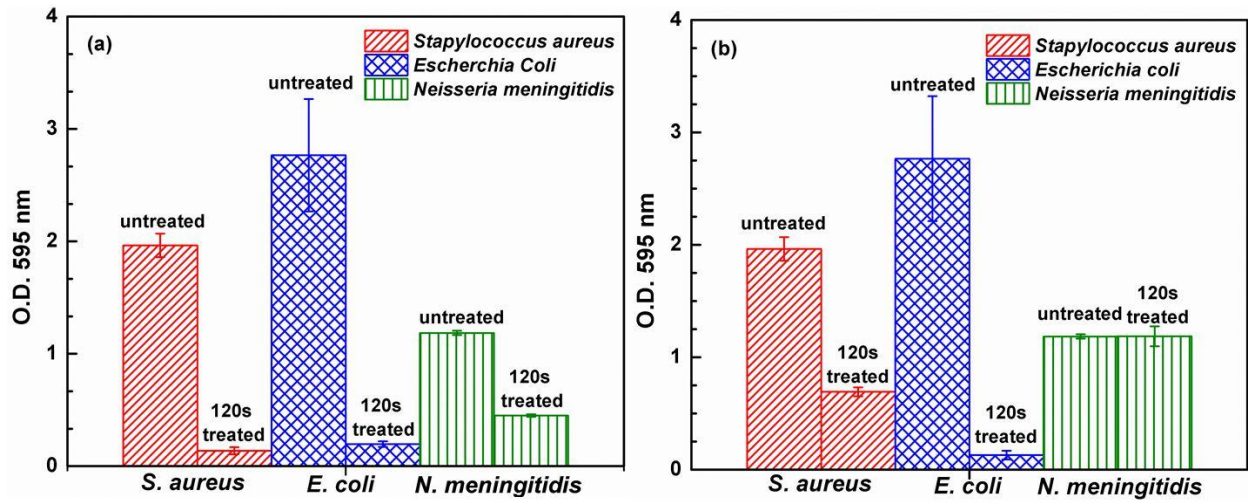


FIG. 10. Comparative 24-hr post treatment inactivation results for *S. aureus*, *E. coli* and *N. meningitidis* by RB plasma jet exposure in: (a) direct plasma treatment, (b) indirect plasma treatment –modes.

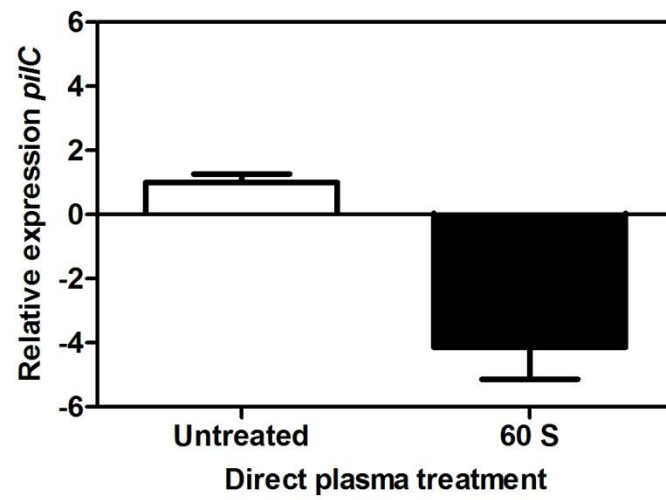


FIG 11. Quantitative PCR analysis of relative expression of *pilC* in *N. meningitidis* untreated and 60 second of RB plasma jet direct treatment.